

Advanced Nanohybrid Materials: Surface Modification and Applications

Guest Editors: Li-Hong Liu, Rémi Métivier, Shanfeng Wang,
and Hui Wang





Advanced Nanohybrid Materials: Surface Modification and Applications

**Advanced Nanohybrid Materials:
Surface Modification and Applications**

Guest Editors: Li-Hong Liu, Rémi Métivier, Shanfeng Wang,
and Hui Wang



Copyright © 2012 Hindawi Publishing Corporation. All rights reserved.

This is a special issue published in "Journal of Nanomaterials." All articles are open access articles distributed under the Creative Commons Attribution License, which permits unrestricted use, distribution, and reproduction in any medium, provided the original work is properly cited.

Editorial Board

Katerina Aifantis, Greece
Nageh K. Allam, USA
Margarida Amaral, Portugal
Xuedong Bai, China
L. Balan, France
Enrico Bergamaschi, Italy
Theodorian Borca-Tasciuc, USA
C. Jeffrey Brinker, USA
Christian Brosseau, France
Xuebo Cao, China
Shafiul Chowdhury, USA
Kwang-Leong Choy, UK
Cui ChunXiang, China
Miguel A. Correa-Duarte, Spain
Shadi A. Dayeh, USA
Ali Eftekhari, USA
Claude Estournes, France
Alan Fuchs, USA
Lian Gao, China
Russell E. Gorga, USA
Hongchen Chen Gu, China
Mustafa O. Guler, Turkey
John Zhanhu Guo, USA
Smrati Gupta, Germany
Michael Harris, USA
Zhongkui Hong, USA
Michael Z. Hu, USA
David Hui, USA
Y.-K. Jeong, Republic of Korea
Sheng-Rui Jian, Taiwan
Wanqin Jin, China
Rakesh K. Joshi, India
Zhenhui Kang, China
Fathallah Karimzadeh, Iran
Do Kyung Kim, Republic of Korea
Kin Tak Lau, Australia
Burtrand Lee, USA
Benxia Li, China
Jun Li, Singapore
Shijun Liao, China
Gong Ru Lin, Taiwan
J. -Y. Liu, USA
Jun Liu, USA
Tianxi Liu, China
Songwei Lu, USA
Daniel Lu, China
Jue Lu, USA
Ed Ma, USA
Gaurav Mago, USA
Sanjay R. Mathur, Germany
A. McCormick, USA
Vikas Mittal, UAE
Weihai Ni, Germany
Sherine Obare, USA
Edward Andrew Payzant, USA
Kui-Qing Peng, China
Anukorn Phuruangrat, Thailand
Ugur Serincan, Turkey
Huaiyu Shao, Japan
Donglu Shi, USA
Suprakas Sinha Ray, South Africa
Vladimir Sivakov, Germany
Marinella Striccoli, Italy
Bohua Sun, South Africa
Saikat Talapatra, USA
Nairong Tao, China
Titipun Thongtem, Thailand
Somchai Thongtem, Thailand
Valeri P. Tolstoy, Russia
Tsung-Yen Tsai, Taiwan
Takuya Tsuzuki, Australia
Raquel Verdejo, Spain
Mat U. Wahit, Malaysia
Shiren Wang, USA
Yong Wang, USA
Ruibing Wang, Canada
Cheng Wang, China
Zhenbo Wang, China
Jinquan Wei, China
Ching Ping Wong, USA
Xingcai Wu, China
Guodong Xia, Hong Kong
Zhi Li Xiao, USA
Ping Xiao, UK
Shuangxi Xing, China
Yangchuan Xing, USA
N. Xu, China
Doron Yadlovker, Israel
Ying-Kui Yang, China
Khaled Youssef, USA
Kui Yu, Canada
William W. Yu, USA
Haibo Zeng, China
Tianyou Zhai, Japan
Renyun Zhang, Sweden
Yanbao Zhao, China
Lianxi Zheng, Singapore
Chunyi Zhi, Japan

Contents

Advanced Nanohybrid Materials: Surface Modification and Applications, Li-Hong Liu, Rémi Métivier, Shanfeng Wang, and Hui Wang
Volume 2012, Article ID 536405, 2 pages

Nanobioprobe for the Determination of Pork Adulteration in Burger Formulations, M. E. Ali, S. Mustafa, U. Hashim, Y. B. Che Man, and K. L. Foo
Volume 2012, Article ID 832387, 7 pages

Patterning Luminescent Nanocrystalline $\text{LaPO}_4 : \text{Eu}$ and $\text{CePO}_4 : \text{Tb}$ Particles Embedded in Hybrid Organosilica with Soft-Lithographic Techniques, Sajid U. Khan and Johan E. ten Elshof
Volume 2012, Article ID 279810, 11 pages

Effect of Particle Morphology on Sinterability of SiC-ZrO_2 in Microwave, Lydia Anggraini and Kei Ameyama
Volume 2012, Article ID 741214, 8 pages

Synthesis of a Layered Organic-Inorganic Nanohybrid of 4-Chlorophenoxyacetate-zinc-Layered Hydroxide with Sustained Release Properties, Mohd Zobir Hussein, Nor Farhana binti Nazarudin, Siti Halimah Sarijo, and Mohd Ambar Yarmo
Volume 2012, Article ID 860352, 9 pages

Engineered Hybrid Scaffolds of Poly(vinyl alcohol)/Bioactive Glass for Potential Bone Engineering Applications: Synthesis, Characterization, Cytocompatibility, and Degradation, Hermes S. Costa, Alexandra A. P. Mansur, Marivalda M. Pereira, and Herman S. Mansu
Volume 2012, Article ID 718470, 16 pages

Topical Review: Design, Fabrication, and Applications of Hybrid Nanostructured Array, Shaoli Zhu and Wei Zhou
Volume 2012, Article ID 206069, 8 pages

Making Organic-Inorganic Nanocomposites via Selective Dispersion of PS-Tethered SiO_2 Particles in Polystyrene-Block-Polymethylmethacrylate Copolymer, Chia-Hong Liu, Li-Ko Chiu, Je-Yuan Yeh, and Raymond Chien-Chao Tsiang
Volume 2012, Article ID 327583, 7 pages

A Review on Nanofluids: Preparation, Stability Mechanisms, and Applications, Wei Yu and Huaqing Xie
Volume 2012, Article ID 435873, 17 pages

Editorial

Advanced Nanohybrid Materials: Surface Modification and Applications

Li-Hong Liu,¹ Rémi Métivier,² Shanfeng Wang,^{3,4} and Hui Wang⁵

¹ Department of Chemistry, Portland State University, Portland, OR 97207, USA

² Macromolecular and Supramolecular Photophysics and Photochemistry Laboratory (PPSM Laboratory), CNRS UMR8531, Ecole Normale Supérieure de Cachan, 61 Avenue du Président Wilson, 94235 Cachan Cedex, France

³ Department of Materials Science and Engineering, The University of Tennessee, 306D Dougherty Engineering Building, Knoxville, TN 37996-2200, USA

⁴ Biosciences Division, Oak Ridge National Laboratory, Oak Ridge, TN 37831, USA

⁵ Department of Chemistry, University of Massachusetts Lowell, Olney Hall 510, Lowell, MA 01854, USA

Correspondence should be addressed to Li-Hong Liu, lihongl@pdx.edu

Received 25 December 2011; Accepted 25 December 2011

Copyright © 2012 Li-Hong Liu et al. This is an open access article distributed under the Creative Commons Attribution License, which permits unrestricted use, distribution, and reproduction in any medium, provided the original work is properly cited.

The field of functional nanoscale hybrid materials is one of the most promising and rapidly emerging research areas in materials chemistry. Nanoscale hybrid materials can be broadly defined as synthetic materials with organic and inorganic components that are linked together by noncovalent bonds (Class I, linked by hydrogen bond, electrostatic force, or van der Waals force) or covalent bonds (Class II) at nanometer scale. The unlimited possible combinations of the distinct properties of inorganic, organic, or even bioactive components in a single material, either in molecular or nanoscale dimensions, have attracted considerable attention. This approach provides an opportunity to create a vast number of novel advanced materials with well-controlled structures and multiple functions. The unique properties of advanced hybrid nanomaterials can be advantageous to many fields, such as optical and electronic materials, biomaterials, catalysis, sensing, coating, and energy storage. In this special issue, the breadth of papers shows that the hybrid materials is attracting attention, because of both growing fundamental interest, and a route to new materials. Two review articles and seven research papers that report new results of hybrid materials should gather widespread interest.

One review paper presents an overview of the recent developments in the study of nanofluids, which has interaction with hybrid materials. The review discusses the preparation methods, the evaluation methods for their stability, the ways to enhance their stability, the stability mechanisms, and their potential applications in different areas, such as heat

transfer intensification, mass transfer enhancement, energy fields, mechanical fields, and biomedical fields.

In another paper, a zinc-layered hydroxide-4-chlorophenoxy acetate (4CPA) organic-inorganic nanohybrid was prepared via a simple direct reaction of 4CPA anions with ZnO under an aqueous environment. The concentration of 4CPA was found to be a controlling factor in determining the formation of a pure phase and well-ordered nanolayered hybrid material. The nanohybrid showed a controlled release property that could be used as a controlled release formulation of herbicides, and the releasing was governed by pseudo-second-order kinetics. The authors on one paper report selective dispersion of SiO₂ nanoparticles in the polystyrene (PS) domain of polystyrene-block-polymethylmethacrylate (PS-b-PMMA) block copolymer via blending PS-b-PMMA with PS-tethered SiO₂. Another paper reviews the fabrication of Au-coated Ag nanoarrays as biosensors.

The authors in another paper synthesized hybrid scaffolds of poly(vinyl alcohol)/bioactive glass (PVA/BaG) and investigated the effect of glutaraldehyde as the crosslinker on mechanical properties, degradation, and cytocompatibility. The authors of one paper investigated the effect of the particle morphology on sinterability of the SiC-ZrO₂ in microwave. They pointed out the possible good microwave absorption of ZrO₂. In another paper, Eu³⁺-doped LaPO₄ and Tb³⁺-doped CePO₄ luminescent nanoparticles embedded in hybrid organosilica were patterned by two soft lithographic techniques. The role of various parameters, such

as solution chemistry, thermal protocols, and modification of the mold-substrate surface energies related to pattern shape formation and adhesion to the substrates, have been studied. In another paper, species-specific hybrid nanobio-probe based on gold nanoparticles was developed by a covalent integration of a fluorophore-labeled 27-nucleotide Alu fragment of swine cytochrome b gene to a 3 nm gold nanoparticle for determination of pork adulteration in processed meat products.

Li-Hong Liu
Rémi Métivier
Shanfeng Wang
Hui Wang

Research Article

Nanobioprobe for the Determination of Pork Adulteration in Burger Formulations

M. E. Ali,¹ S. Mustafa,² U. Hashim,¹ Y. B. Che Man,² and K. L. Foo¹

¹Institute of Nano Electronic Engineering (INNE), Universiti Malaysia Perlis, Kangar, 01000 Perlis, Malaysia

²Halal Products Research Institute, Universiti Putra Malaysia, Serdang, 43400 Selangor, Malaysia

Correspondence should be addressed to S. Mustafa, shuhaimi@biotech.upm.edu.my

Received 6 October 2011; Revised 11 November 2011; Accepted 12 November 2011

Academic Editor: Shanfeng Wang

Copyright © 2012 M. E. Ali et al. This is an open access article distributed under the Creative Commons Attribution License, which permits unrestricted use, distribution, and reproduction in any medium, provided the original work is properly cited.

We report the development of a swine-specific hybrid nanobioprobe through a covalent integration of a fluorophore-labeled 27-nucleotide *AluI*-fragment of swine cytochrome b gene to a 3 nm gold nanoparticle for the determination of pork adulteration in processed meat products. We tested the probe to estimate adulterated pork in ready-to-eat pork-spiked beef burgers. The probe quantitatively detected 1–100% spiked pork in burger formulations with $\geq 90\%$ accuracy. A plot of observed fluorescence against the known concentration of *AluI*-digested pork DNA targets generated a concave curve, demonstrating a power relationship ($y = 2.956x^{0.509}$) with a regression coefficient (R^2) of 0.986. No cross-species detection was found in a standard set of pork, beef, chicken, mutton, and chevon burgers. The method is suitable for the determination of very short-length nucleic acid targets which cannot be estimated by conventional and real-time PCR but are essential for the determination of microRNA in biodiagnostics and degraded DNA in forensic testing and food analysis.

1. Introduction

In the recent decades, a multitude of reports have been built outlining the detection of meat species in foods [1–13]. These reports clearly reveal that mitochondrial (mt) DNA is the analyte of choice and that real-time PCR is the analytical method of preference [1–13]. Maternal inheritance, multiple copy numbers, and additional protection by specialized shape of mitochondrial membrane have given mt genes extraordinary stability to survive in harshly processed food and feeds or compromised samples [3, 6]. On the other hand, real-time PCR technique is highly automated and allows simultaneous detection and quantification of potential targets from a complex background, eliminating the need of laborious electrophoresis or blotting that are required for conventional PCR [1–13].

A real-time PCR assay with a short-length amplicon is preferred since it provides better amplification and recovery of target DNA from a compromised sample processed under harsh physical and chemical treatments which break down DNA into small fragments [2–8]. Following this observation,

real-time PCR assays with amplicon as short as 66 or 76 bps were developed [2]. However, this was achieved with a compromise of assay specificity [5]. A compromised assay leads to artefacts in the final results by cross-amplifying an alien species in heterogeneous mixtures of processed foods. A cross-amplifying assay cannot determine whether there has been a real or contaminated target identification [3, 5, 6]. This has raised the concerns of validity and applicability of PCR assays to authenticate species in highly processed meat products where DNA fragmentation is observed.

Hybrid biomaterials composed of functionalized nanoparticles, covalently [14–17] or noncovalently [18, 19] linked to biomolecules, such as peptides, proteins, and polynucleotides, are particularly interesting and promising for their size-dependent optoelectronic properties and dimensional similarities to biomacromolecules [14–19]. These conjugated biomaterials are potential agents for multiplexed bioassays, material synthesis, ultrasensitive optical detection and imaging, *in vivo* magnetic resonance imaging (MRI), long-circulating carriers for targeted drug release, and structural scaffolds for tissue engineering [14–19].

Thiol-capped gold nanoparticles (GNPs) covalently linked to fluorophore-labeled oligonucleotide through metal-sulfur bonds are shown to detect specific sequences and single-nucleotide mismatches in shorter oligos [14–17]. However, such studies are limited to the laboratory level model experiments with synthetic oligotargets. No studies so far have been conducted on the sequence and mismatch detecting power of the fluorophore-labeled-oligonanoparticle conjugates in heterogeneous biological or commercial samples. Hybridization profile of such nanobioconjugates is also needed to be explored.

Burger is a special type of restructured comminuted meat products and very popular all over the world [3]. It can be prepared by mixing emulsified ground meat of pork, beef, chicken, lamb, or fish with certain ratios of starch, seasonings, and salts [3]. Replacement of higher value meats by lower value ones is a wide-spread problem in food industry to realize extra economic benefit and also to survive in a highly competitive market [1–13, 16–21]. Pork is a potential adulterant in beef burger since it is similar in color and texture and also available at cheaper prices [3]. The mixing of pork or its derivatives in food products is a serious matter in the platforms of religions and health because it is not permitted by the Kosher and Halal food laws, its unconscious consumption might ignite allergic reactions, and its high content of cholesterol and saturated fats may initiate cardiovascular diseases [3–13, 16–20]. Thus, reliable, easy-to-perform, and cost-effective methodologies are highly appreciated for the verification of pork adulteration in processed foods.

In this paper, we structurally and functionally integrated a 27-nucleotide *AluI*-cut segment of swine mitochondrial (mt) *cytb* gene to a 3 nm diameter citrate-tannate-coated gold nanocrystal to fabricate a novel class of species-specific nanobioprobe to determine pork in ready-to-consume burger formulations. The method is comparatively cheaper than the real-time PCR and can be applied to analyze highly compromised heterogeneous samples where PCR methods may not work due to breakdown of longer DNA template into smaller fragments.

2. Materials and Methods

2.1. Design of Swine-Specific Oligoprobe. We chose a 27-nt *AluI*-cut fragment (428–454 bp) of swine (*Sus scrofa*) *cytb* gene (GenBank accession no. Gu135837.1 in NCBI data base) as a porcine-specific marker. This fragment demonstrated a high degree of polymorphism between the species and similarities within the species by NCBI-BLAST analysis against nonredundant nucleotide collections and also by ClustalW alignment analysis. The probes were custom-synthesized with a tetramethyl rhodamine (TMR) dye at the 5'-end and a thiol (SH) function at the 3'-end with a hexyl-A (A6) spacer between them by the Integrated DNA Technologies, USA. The synthetic targets (complementary, noncomplementary, and single mismatched) were supplied by the 1st Base, Malaysia. The probe and oligosequences are shown in Table 1.

2.2. Synthesis of Colloidal Gold Nanoparticles. Small gold nanoparticles (GNPs) were prepared according to Ali et al. [16]. The colloidal sol was characterized by Hitachi 7100 transmission electron microscope and PerkinElmer Lambda 25 UV-vis spectroscopy. The average size of the particles was assigned to 3 ± 0.2 nm in diameter by measuring 500 particles [16]. The approximate number and concentration of the particles were determined according to Haiss et al. and were found to be 2.01×10^{11} NPS μL^{-1} and 335 pmol mL^{-1} [22].

2.3. Preparation of Hybrid Nanobioprobe. The custom-made probes were mixed with GNPs in a ratio of 3:1, and the mixture was incubated overnight at 20°C in a shaking water bath. The oligoconjugated particles were aged and purified according to Maxwell et al. [15]. The average number of attached oligoprobe per particle was determined by 2-mercaptoethanol digestion following Maxwell and coworkers [15]. The approximate ratio of the single-to-double probe-bound particles was 1:1.

2.4. Preparation of Burger Meats. Separate aliquots of 500 g of pork-beef binary admixtures were prepared by mixing fresh pork and beef in a ratio of 100:0, 50:50, 25:75, 10:90, 5:95, 1:99, and 0:100 (w/w). The burger meats were prepared according to Ali et al. [3]. Briefly, to a 500 g portion of deboned minced mixed meats of the above composition, 1 g finely chopped onion, 1 g of egg, 6 g of finely chopped sundried tomato, one teaspoon of cumin seed, and 1/4 teaspoon of cayenne pepper were added and mixed well. Each mixture was divided into four equal portions and each portion, was given a burger shape. The produced burger was kept in a fridge for 1 h and then grilled on both sides in an electrical oven at 220°C for 15 min.

2.5. Calibration and Validation Standard. The calibration set was prepared by spiking 1, 3, 5, 10, 25, and 50% (w/w) of pork in beef burger meats. Burger meats of 100% pork and 100% beef were also formulated to see the differences in fluorescence signal. A different set of burgers was prepared with similar composition for the validation or prediction experiment [3]. Both the calibration and validation sets were prepared in triplicates.

2.6. DNA Extraction. For DNA extraction, 1 mL of cell and tissue lysis solution (Epicenter Biotechnologies, Madison, USA) was added to a 100 mg portion of finely chopped burger meats and was incubated in a shaking water bath at 65°C for 12 h. The subsequent steps of the extraction protocol were performed according to the Epicenter Biotechnologies. The purity and concentration of the extracted DNA samples were determined by spectrophotometric analysis (Biophotometer, Eppendorf, Germany) of absorbance at $A_{260/280}$ and $A_{260\text{ nm}}$ [3, 6, 16–19].

2.7. Specificity and Sensitivity of the Hybrid Nanobioprobe. An aliquot of the purified nanobioprobe was diluted to 10 pmol mL^{-1} (9.01×10^{12} copies mL^{-1}) with hybridization

TABLE 1: Oligonucleotide sequences used in the study.

Name	Sequences (5' → 3')
Probe	TMR ^a -A ₆ CTGATAGTAGATTTGTGATGACCGTAG-A ₆ (CH ₂) ₆ SH
Complementary target	CTACGGTCATCACAA ATCTACTATCAG
Noncomplementary target	ACGTAAGTCTGCTGTGGCCTGGTCGCTGA
Single-mismatched target	CTACGGTCATCACAAAT ^b TACTATCAG

^a 6-Carboxy tetramethyl rhodamine flanked by hexyl A (A₆) spacer, ^b mismatched base.

buffer (90 mM KCl, 10 mM Tris, pH 8) [14]. To determine specificity, the hybrid probes were incubated with a 4-fold excess (60 pmol mL⁻¹ and 3.6×10^{13} copies mL⁻¹) of complementary, noncomplementary, and single-mismatch targets (Table 1) at 70°C for 5 min to allow strand separation and then at 40°C for 30 min to allow hybridization.

2.8. Specificity and Sensitivity in Mixed Biological Samples. The extracted total DNA (500 µg mL⁻¹) was digested with *AluI* (New England Biolabs, UK) restriction enzymes to create fragments of decisive lengths that could easily match with the size and length of the developed nanobioprobe. The fragments that are produced under natural heat or pressure-induced degradation may not be suitable for biosensor-based detection due to their uncontrolled sizes and shapes. The digestions were performed in a total volume of 1 mL, containing 600 µL of total DNA, 200 U of restriction enzymes, and 100 µL of digestion buffer (New England Biolabs, UK) for 1 h at 37°C in a shaking water bath. After 1 h, nonspecific digestion was stopped by heating the mixture for 10 min at 65°C that inactivates the enzymatic functions of *AluI* [6]. The digestions were confirmed by electrophoresis on 3% agarose gel. The hybridization reaction was performed in a total volume of 2.5 mL in triplicates with 10 pmol mL⁻¹ of probe and 60 µg mL⁻¹ of *AluI*-digested mixed DNA.

2.9. Fluorescence Measurement. The emission spectra were collected in 10 mm cuvette with 2 mL volume in PerkinElmer LS55 fluorescence spectrometer with excitation at 545 nm. Each spectrum was an average of 5 scans with the speed of 200 nm min⁻¹ and 5 nm slit widths. The background was subtracted by replacing sample with 2 : 1 ratio of 10 mM PBS and hybridization buffer. In order to see the hybridization kinetics, a series of fluorescence spectra were obtained in triplicates, and average fluorescence intensity at 579 nm was plotted as a function of target concentration.

3. Results and Discussions

3.1. Detection and Quantification Mechanisms. The operation and quantification principles of the hybrid nanobioprobe are represented in Figure 1. Earlier studies reported that hybrid materials composed of single-stranded DNA (ssDNA), covalently linked to a small gold nanoparticle (2–3 nm in diameter) *via* sulfur-gold bond at one extremity and a fluorescent dye to the other, can assume one of the two distinct conformations: (1) a constrained conformation with a stem-loop or arch-like appearance before target

binding or (2) a straight conformation with a rod-like appearance after target binding. In the closed structure, the fluorophore and the GNP are held in close proximity, and the fluorescence is quenched by nonradiative energy transfer from fluorophore to the metal. Conversely, in the open state, the fluorophore is far enough (>2 nm) from the metal particle to emit fluorescence [14–16]. As such, we assumed that the degree of fluorescence emission depends on the degree of target binding. The maximum fluorescence is observed when the probe is saturated with the targets, and the base-line fluorescence is realized in the absence of any targets. A relationship might be found if fluorescence intensity is plotted against the target concentration, and such a relationship may be used to determine the target DNA concentration.

3.2. Specificity of the Hybrid Nanobiosensor. The fluorescence spectra of 10 pmol mL⁻¹ porcine nanobioprobe with 4-fold molar excess (60 pmol mL⁻¹) of complementary (blue curve: top one), single mismatch (red curve: 2nd from the top), noncomplementary targets (pink curve: 3rd from the top) and no targets (green curve: bottom one) are shown in Figure 2. Only base-line fluorescence was observed with the noncomplementary targets. However, single-mismatched targets (2nd from the top) lost 60–70% observed fluorescence of the perfectly matched targets. Thus, it clearly demonstrated that the fabricated nanobioprobe was highly specific in discriminating complementary, non-complementary, and single-mismatch sequences. Maxwell et al. [15] achieved 55% quenching with 2.5 nm diameter gold nanoparticle probes where gold nanoparticles were produced by reducing sodium borohydride. On the other hand, Dubertret et al. [14] achieved 75% reduction of fluorescence intensity with molecular beacon and 1.4 nm diameter gold nanocrystals. The former group used 4-fold and the latter 10-fold molar excess of targets, probably to produce crowding effect to realize maximum emission of fluorescence. According to Dubertret et al., the discrimination of perfectly matched and mismatched sequences can be clearly observed if low ionic strength hybridization buffer (90 mM KCl, 10 mM Tris, pH 8.0) is used. However, the gold particles, they used, were too small and unstable above 50°C. We used highly stable citrate-tannate-coated GNPs with relatively large diameter (~3 nm), 4-fold, molar excess of targets, and also the low ionic strength hybridization buffer. Thus, we achieved sensitivity which is higher than that of Maxwell et al. [15] and close to Dubertret's [14].

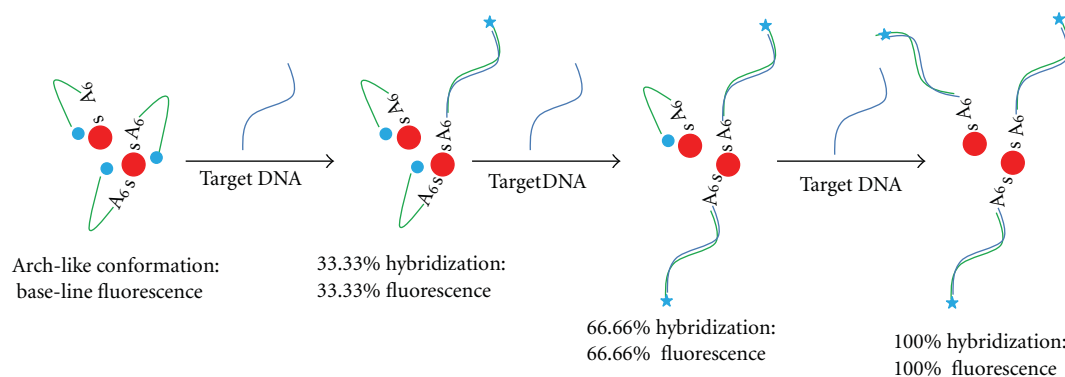


FIGURE 1: Schematic presentation of the operating and quantification principles of the swine nanobiosensor probes. Three oligonucleotides probes flanked by a hexyl-A spacer and linked to a gold nanocrystal through a gold-thiol bond at one end and fluorophore (TMR) to the other are shown to be self-organized in a constrained arch-like structure where the fluorophore is quenched by the nanoparticle in the absence of any complementary targets. Upon target binding, the closed structure is opened into a rod-like conformation separating the fluorescent dye from the nanoparticle to allow fluorescence emission. The degree of fluorescence emission is shown to proportionate to the degree of target hybridization. Gold nanoparticle is demonstrated by a red sphere. The quenched and emission state of the fluorophore is represented by a sky-blue sphere and a sky-blue star. Single-stranded probe DNA and target DNA are shown by green- and blue-curved line, respectively.

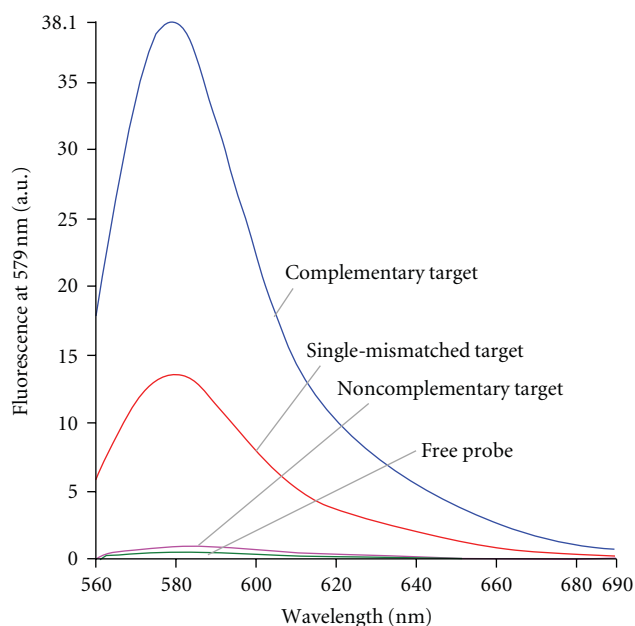


FIGURE 2: Detection of specific DNA sequences and single-nucleotide mismatches by swine-specific nanobiosensor probes. The corresponding emission spectra collected at λ_{545} excitation are shown by labels.

3.3. Pork Detection in Mixed Burger Formulations. The fluorescence spectra of burgers prepared from pork-beef binary admixtures containing various percentages of spiked pork are shown in Figure 3. Fluorescence spectra of commercial burgers of beef, chicken, chevon, and mutton are also demonstrated in the same figure. The swine-specific biosensor probe clearly detected 1% pork containing $0.6 \text{ ng } \mu\text{L}^{-1}$ of swine DNA (yellowish green curve: 7th from

the top) in ready-to-eat burger prepared from pork-beef binary mixtures. This clearly reflects the high sensitivity and specificity of the hybrid nanobioprobe to trace out target DNA in food products processed by severe heat and pressure which degrades DNA [2, 3, 5–8]. No significant change in the sensitivity was observed with uncooked burger preparations (not shown), demonstrating the high stability of the potential targets in processed food products.

Commercial burgers from other species (beef, chicken, mutton, and chevon) showed fluorescence that is comparable to the base-line fluorescence of the free probes (Figure 3). We retrieved the nucleotide sequence of *cytb* genes of these species and aligned with the probe by ClustalW alignment program. The number of mismatches and mismatched nucleotides of each species is shown in the inset of Figure 3. Only the *Sus scrofa* (pig) species showed 100% matching, and all the other species showed 5–8 nucleotide (shown in red) mismatching, reflecting the extraordinary specificity of the designed probe, and supporting the experimental findings.

Rodríguez et al. [4] quantified 0.5% pork adulteration in pork-beef binary mixtures under raw states using TaqMan probe real-time PCR targeting 411 bp template DNA of mt-12S ribosomal RNA gene. In contrast, using a comparatively shorter fragments (<120 bp) of different mt genes, Frezza et al. [7] quantitatively detected 0.2% adulteration of bovine, ovine, swine, and chicken DNAs in feedstuffs by conventional and FRET-based real-time PCR. Recently, Farrokhi et al. [11] detected 0.1 ng pork DNA from commercial meat extracts targeting 234 bp mt-DNA using SYBR green real-time PCR. The detection limit of the molecular beacon real-time PCR assay developed by Yusop et al. [12] that targeted a 119 bp mt-*cytb* gene was 0.1% (w/w) pork in pork-beef binary mixtures under raw states. The highest detection limit of 0.01% of pork in beef burger has recently been reported by Ali et al. [3, 6] who targeted a 109 bp fragment of mt-*cytb* gene using a TaqMan probe real-time PCR [3]

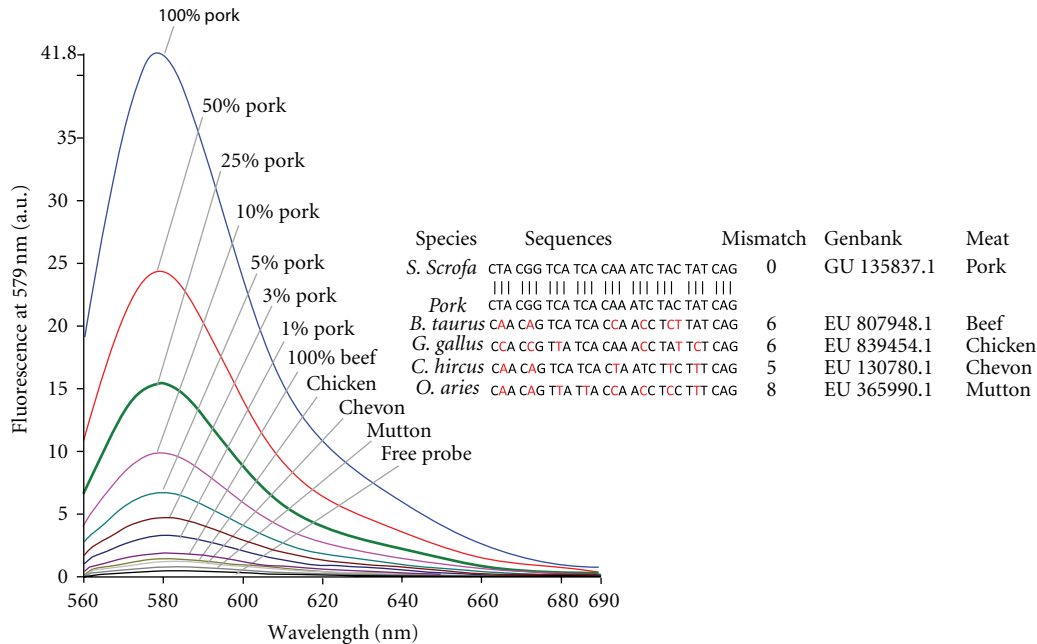


FIGURE 3: Pork detection in ready-to-eat mixed (pork-beef) and commercial burgers of various species. The corresponding emission spectra collected at λ_{545} excitation are shown by labels. The inset is the comparison of nucleotide sequences of different species with swine oligoprobe. The mismatched bases are shown in red.

and conventional PCR coupled with microfluidic analysis of the amplified PCR products [6]. While these studies clearly demonstrate improved sensitivity with the reduction of the length of template DNA, too much reduction of the template DNA length is reported to compromise specificity, making the PCR assay unreliable [2, 5]. Additionally, the PCR assays as short as 27 bp cannot be possible as they reflect the equivalence of the size of a PCR primer [1–13, 20]. Thus, although the detection limit of this assay is far below the conventional and real-time PCR, still the assay has important applications for the detection of shorter-length nucleic acid targets which can survive in the harsh conditions that extensively breakdown DNA into smaller fragments causing amplification failure in PCR reactions [3, 6]. In short-length (15–30 nucleotides) nucleic acids, such as microRNAs, detection is increasingly important in the diagnosis of cancer and other hereditary diseases at an earlier stage, and the present assay is a suitable candidate for this job [20].

Conventional and real-time PCR assays not only have limitations in detecting short-length nucleic acid targets, but also incur huge cost of instrumentations and consumables and involves laborious electrophoresis and handling of hazardous chemicals such as ethidium bromide [16–19]. In contrast, the present method only involves the initial cost of fluorescence spectrophotometer, reusable cuvette, and fluorescence-labeled probe. GNP preparation is easy and also commercially available at reasonable prices.

Detection of pork in meat products by Fourier transform infrared spectroscopy is interesting as it apparently looks simple and does not involve huge cost that is incurred by real-time PCR [9]. However, the method is flawed by

itself as it depends on the analysis of fat which can be extensively manipulated during the cooking process [3, 6]. Colorimetric detection of PCR amplified and nonamplified swine genomic DNA in a mixed background [18, 19] is quite interesting because it does not need any instrument, and detection is also rapid. However, the method is solely qualitative, cannot provide any quantitative information, and also suffers from the interference of single-stranded nucleic acid species. Quantification of specific nucleic acid species helps to draw a boundary between the permissible and nonpermissible limits of adulteration in food analysis and also to monitor the progression of infectious and hereditary diseases in molecular diagnostics [3]. The present assay has a strong potential to be used for these purposes because of its simplicity and lower cost compared with the other existing methods such as real-time PCR.

3.4. Hybridization Kinetics and Target Quantification. When the logarithmic value of *AluI*-digested target DNA (% w/w) was plotted against the fluorescence intensity at a fixed concentration of nanobioprobe (10 pmol mL^{-1}), a concave-shaped curve reflecting a power relationship ($y = 2.956x^{0.509}$) between the observed fluorescence and target concentration was obtained (Figure 4(a)). The regression coefficient (R^2) of this curve was 0.986, meaning the dependant variable (y -axis = observed fluorescence) can explain 98.6% values of the independent variable (x -axis = target DNA concentration). The plot reflects very little changes in emitted fluorescence at the two extremes demonstrating that at too low concentration of target (<1% w/w), probe-target collision is too low to open the closed structure (Figure 1), and at too high concentration of target (>100% w/w), the

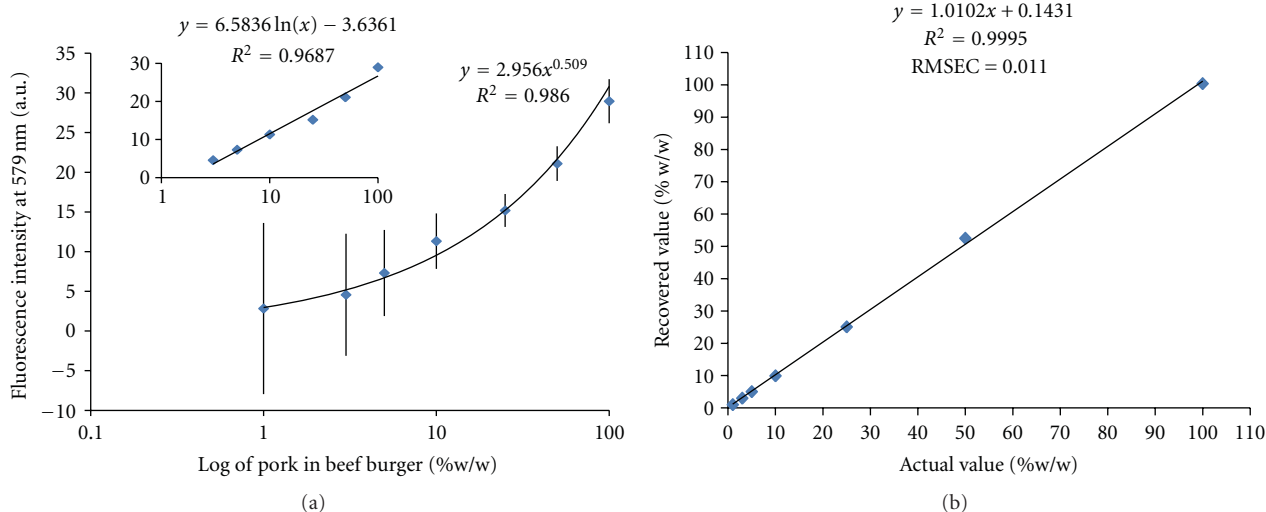


FIGURE 4: Pork estimation in ready-to-eat beef burgers of 1%, 3%, 5%, 10%, 25%, and 100% pork adulterations (a) and relationship between the actual (x -axis) and recovered values (y -axis) obtained from the standard and validation sets of the above mixtures (b). The standard errors (%) are shown by the error bars, and the linear part of the curve (3–100%) is displayed in the inset (a).

probe is supersaturated with the targets resulting in very little or no change in spectral intensity [16, 17]. At low concentration ($\leq 3\%$) of targets, the standard deviation of the observed fluorescence was also higher ($\leq 10\%$). However, over a moderate range of target DNA concentration (3–100%), a linear curve were appeared with $R^2 = 0.968$ (Figure 4(a), inset). This part of the curve also showed $\leq 10\%$ deviation in interreplicates, interday, and interanalyst analysis, indicating its potential uses in target DNA quantification. When pork concentration (% w/w) in beef burger over the range of 5–100% was plotted against the fluorescence intensity, a linear curve (not shown) with $R^2 = 0.998$ resulted. Linearity was considerably destroyed when less than 5% pork was used, again reflecting the scarcity of available targets to interact with the probe to open the closed conformation in an efficient manner at low concentration.

We further validated our findings by plotting experimentally determined value against the actual concentration of pork in burger formulations (Figure 4(b)). We observed a linear curve over the range of 1–100% pork in beef burger with $R^2 = 0.999$. R^2 value reflects how close the experimentally determined value to the actual concentration. The closer the value to unity, the better the accuracy [3, 9]. The accuracy of the method as shown by error bar was 90–95% over the range of 5–100% adulteration. However, the accuracy was drastically fallen down ($< 90\%$) in $\leq 3\%$ pork mixed in beef burger, reflecting low level of probe-target collision.

4. Conclusion

Species-specific hybrid nanobioprobe based on gold nanoparticles was developed to authenticate pork adulteration as low as 1% in ready-to-consume beef burger preparations with spiked pork. The cross-testing results with various formulations of commercial burgers also revealed the high

specificity and sensitivity of the hybrid biosensor for the pork DNA. The hybridization kinetics of the nanobioprobe reflected a power relationship of observed fluorescence with target concentration (1–100% w/w). However, a linear curve was realized over the moderate concentration of the target (3–100%) and used to quantify potential targets in processed mixed meat products with more than 90% accuracy. The method eliminated the need of expensive real-time PCR, time-consuming electrophoresis, and laborious blotting techniques for target DNA identification. We believe our approach would find application in food analysis, genetic screening, biodiagnostics, and forensic investigations.

Acknowledgments

M. E. Ali is a recipient of Universiti Malaysia Perlis graduate fellowship. The authors like to acknowledge funds “RUGS no. 9031” to Professor Y. B. C. Man and “MOSTI no. 05-01-35-SF-1030” to Professor U. Hashim.

References

- [1] R. Meyer, U. Candrian, and J. Lüthy, “Detection of pork in heated meat products by the polymerase chain reaction,” *Journal of AOAC International*, vol. 77, no. 3, pp. 617–622, 1994.
- [2] P. D. Brodmann and D. Moor, “Sensitive and semi-quantitative TaqMan real-time polymerase chain reaction systems for the detection of beef (*Bos taurus*) and the detection of the family Mammalia in food and feed,” *Meat Science*, vol. 65, no. 1, pp. 599–607, 2003.
- [3] M. E. Ali, U. Hashim, Th. S. Dhahi, S. Mustafa, Y. B.C. Man, and Md. A. Latif, “Analysis of pork adulteration in commercial burgers targeting porcine-specific mitochondrial cytochrome b gene by TaqMan probe real-time polymerase chain reaction,” *Food Analytical Methods*. In press.

- [4] M. A. Rodríguez, T. García, I. González, P. E. Hernández, and R. Martín, "TaqMan real-time PCR for the detection and quantitation of pork in meat mixtures," *Meat Science*, vol. 70, no. 1, pp. 113–120, 2005.
- [5] H. Hird, J. Chisholm, A. Sanchez et al., "Effect of heat and pressure processing on DNA fragmentation and implications for the detection of meat using a real-time polymerase chain reaction," *Food Additives and Contaminants*, vol. 23, no. 7, pp. 645–650, 2006.
- [6] M. E. Ali, U. Hashim, S. Mustafa, and Y. B. Che Man, "Swine-specific PCR-RFLP assay targeting mitochondrial cytochrome B gene for semiquantitative detection of pork in commercial meat products," *Food Analytical Methods*. In press.
- [7] D. Frezza, V. Giambra, F. Chegdani et al., "Standard and Light-Cycler PCR methods for animal DNA species detection in animal feedstuffs," *Innovative Food Science and Emerging Technologies*, vol. 9, no. 1, pp. 18–23, 2008.
- [8] M. Rojas, I. González, M. A. Pavón et al., "Novel taqman real-time polymerase chain reaction assay for verifying the authenticity of meat and commercial meat products from game birds," *Food Additives and Contaminants A*, vol. 27, no. 6, pp. 749–763, 2010.
- [9] A. Rohman, Sismindari, Y. Erwanto, and Y. B. Che Man, "Analysis of pork adulteration in beef meatball using Fourier transform infrared (FTIR) spectroscopy," *Meat Science*, vol. 88, no. 1, pp. 91–95, 2011.
- [10] A. Doosti, P. Ghasemi Dehkordi, and E. Rahimi, "Molecular assay to fraud identification of meat products," *Journal of Food Science and Technology*. In press.
- [11] R. Farrokhi and R. Jafari Joozani, "Identification of pork genome in commercial meat extracts for Halal authentication by SYBR green I real-time PCR," *International Journal of Food Science and Technology*, vol. 46, no. 5, pp. 951–955, 2011.
- [12] M. H. M. Yusop, S. Mustafa, Y. B. Che Man, A. R. Omar, and N. F. K. Mokhtar, "Detection of raw pork targeting porcine-specific mitochondrial cytochrome B gene by molecular beacon probe real-time polymerase chain reaction," *Food Analytical Methods*. In press.
- [13] Y. B. Che Man, S. Mustafa, N. F. K. Mokhtar, R. Nordin, and A. Q. Sazili, "Porcine-specific polymerase chain reaction assay based on mitochondrial D-loop gene for the identification of pork in raw meat," *International Journal of Food Properties*. In press.
- [14] B. Dubertret, M. Calame, and A. J. Libchaber, "Single-mismatch detection using gold-quenched fluorescent oligonucleotid," *Nature Biotechnology*, vol. 19, no. 4, pp. 365–370, 2001.
- [15] D. J. Maxwell, J. R. Taylor, and S. Nie, "Self-assembled nanoparticle probes for recognition and detection of biomolecules," *Journal of the American Chemical Society*, vol. 124, no. 32, pp. 9606–9612, 2002.
- [16] M. E. Ali, U. Hashim, S. Mustafa et al., "Nanobiosensor for detection and quantification of DNA sequences in degraded mixed meats," *Journal of Nanomaterials*, vol. 2011, Article ID 781098, 11 pages, 2011.
- [17] M. E. Ali, U. Hashim, S. Mustafa, Y. B. Che Man, and M. H.M. Yusop, "Nanobiosensor for the detection and quantification of specific DNA sequences in degraded biological samples," *IFMBE Proceedings*, vol. 35, pp. 384–387, 2011.
- [18] M. E. Ali, U. Hashim, S. Mustafa, Y. B. Che Man, and K. N. Islam, "Gold nanoparticle sensor for the visual detection of pork adulteration in meatball formulation," *Journal of Nanomaterials*, vol. 2012, Article ID 103607, 7 pages, 2012.
- [19] M. E. Ali, U. Hashim, S. Mustafa et al., "Nanoparticle sensor for label free detection of swine DNA in mixed biological samples," *Nanotechnology*, vol. 22, no. 19, 2011.
- [20] S. Catuogno, C. L. Esposito, C. Quintavalle, L. Cerchia, G. Condorelli, and V. de Franciscis, "Recent advance in biosensors for microRNAs detection in cancer," *Cancers*, vol. 3, no. 2, pp. 1877–1898, 2011.
- [21] J. M. Regenstein, M. M. Chaudry, and C. E. Regenstein, "The Kosher and Halal Food laws," *Comprehensive Reviews in Food Science and Food Safety*, vol. 2, pp. 111–127, 2003.
- [22] W. Haiss, N. T. K. Thanh, J. Aveyard, and D. G. Fernig, "Determination of size and concentration of gold nanoparticles from UV-Vis spectra," *Analytical Chemistry*, vol. 79, no. 11, pp. 4215–4221, 2007.

Research Article

Patterning Luminescent Nanocrystalline LaPO_4 :Eu and CePO_4 :Tb Particles Embedded in Hybrid Organosilica with Soft-Lithographic Techniques

Sajid U. Khan^{1,2} and Johan E. ten Elshof²

¹ Faculty of Materials Science and Engineering, Institute of Space Technology, P.O. Box 2750, Islamabad 44000, Pakistan

² MESA+ Institute for Nanotechnology, University of Twente, P.O. Box 217, 7500 AE Enschede, The Netherlands

Correspondence should be addressed to Sajid U. Khan, sajid.ullah@ist.edu.pk

Received 29 September 2011; Revised 3 November 2011; Accepted 3 November 2011

Academic Editor: Shanfeng Wang

Copyright © 2012 S. U. Khan and J. E. ten Elshof. This is an open access article distributed under the Creative Commons Attribution License, which permits unrestricted use, distribution, and reproduction in any medium, provided the original work is properly cited.

Eu^{3+} -doped LaPO_4 and Tb^{3+} -doped CePO_4 luminescent nanoparticles embedded in hybrid organosilica were patterned by two soft lithographic techniques. The role of various parameters such as solution chemistry, thermal protocols, and modification of the mold-substrate surface energies related to pattern shape formation and adhesion to the substrates have been studied. The shrinkage of the oxide patterns and shape evolution during the process was also examined. The patterns were characterized with optical and photoluminescence (PL) microscopy, X-ray diffraction (XRD), and scanning electron microscopy (SEM). Compositional analyses were carried out with X-ray photoelectron spectroscopy (XPS), low-energy ion scattering (LEIS), and secondary ion mass spectroscopy (SIMS). The results indicated that the final patterns obtained with these two techniques for the same material have different shapes and adherence to the substrates.

1. Introduction

Oxide materials doped with lanthanide ions comprise a class of materials that have great technological importance in areas such as phosphor lamps, displays, sensors, lasers, and optical amplifiers [1–3]. At nanometer scale, these materials have high surface-to-volume ratio and enhanced structural, electronic, and optical properties in comparison to the bulk phase. Generally, oxide materials are known to be good hosts for lanthanide ions, since they provide good quantum yields. For example, lanthanum orthophosphate (LaPO_4) is an excellent host for ions such as europium, cerium, and terbium in the fabrication of photoluminescent materials [3, 4].

At present, the most common technologies used for the deposition of these materials are electrophoretic deposition [5–7], screen printing [8], pulsed laser deposition [9, 10], and traditional photolithography [11]. In fact, the patterning techniques used for phosphor screens are known to have a great effect on the resolution of flat panel displays [12].

Soft-lithographic techniques [13] could be used as alternative techniques, when simplicity, ease of use, and cost

effectiveness is targeted. They are cheap, easy, and simple and most importantly, they need no clean room conditions or complicated and lengthy processing steps. So far, relatively little work has been reported on the use of soft-lithographic techniques for the patterning of luminescent materials. Yu et al. applied micromoulding in capillaries (MIMIC) to pattern a Pechini sol-gel-based nanocrystalline $\text{YVO}_4:A$ ($A = \text{Eu}^{3+}$, Dy^{3+} , Sm^{3+} , Er^{3+}) phosphor films [12]. Pisignano et al. employed mechanical lithographic techniques to print 1D patterns of light emitting materials embedded in organic films [14]. They reported that patterned films exhibited enhanced luminescence (by more than a factor of two) as compared to nonpatterned films. Similarly, Han and coworkers [15] applied the technique of MIMIC to sol-gel-based phosphor patterned lines having various line widths. The patterned and nonpatterned films exhibited the same optical properties.

Here we report the use of two soft-lithographic techniques, namely, MIMIC [13, 16] and microtransfer moulding (μTM) [13, 17] for the patterning of two types of

luminescent nanoparticles. A comparison between the two techniques has been made based on the degree of filling of the channels, adhesion of the patterned films to the substrate, their shape profiles, and shrinkage behavior. This paper will focus on two important fundamental questions (a) what will be the outcome of applying two different soft-lithographic techniques to one material? (b) What will be the result of patterning two different materials with one technique? This paper will make a great contribution and a step forward towards selecting an appropriate soft-lithographic technique for the right material and applications.

2. Experimental

2.1. Materials. Unless otherwise stated, reagents were used as received without further purification. The organosilane precursor 1,2-bis(triethoxysilyl)ethane (99.999%) abbreviated as BTESE, nitric acid (65%), polyoxyethylene 20 cetyl ether (Brij 58), and ethanol (99.8%) were all purchased from Aldrich. N, N-dimethylformamide (99.8%) (DMF) was purchased from Merck.

2.2. Synthesis of Luminescent Lanthanide Phosphate Nanoparticles. Two types of luminescent nanoparticles (NPs), namely, $\text{LaPO}_4:\text{Eu}$ and $\text{CePO}_4:\text{Tb}$, having particle diameters (Φ) of 5–8 nm, were used for patterning in the present work. The synthesis route adopted was according to Riwozki et al. and was scaled down to 10 mmol and slightly modified as follows [18]. To a solution of lanthanide chloride hydrate salts (10 mmol) in methanol (50 mL), tris(2-ethylhexyl) phosphate (TEHP, 60 mL) was added. Under reduced pressure (10 mbar at 60°C), methanol and water were evaporated. Depending on the lanthanide ions used for the synthesis, the remaining solution sometimes remained slightly colored.

In parallel, a solution of crystalline phosphoric acid (980 mg, 10 mmol) in tris(2-ethylhexyl) phosphate (30 mL) and tri-*n*-octylamine (TOA, 13.1 mL, 30 mmol) was prepared. The dissolved acid solution was heated to 80°C, and water and oxygen were removed in the vacuum. The solution was flushed with argon three times before the lanthanide-ion solution was added. Again, the flask was evacuated and flushed with argon three times before the mixture was heated to 200°C for 20 h in order to minimize the oxidation of cerium(III) to cerium(IV). During the reaction, the temperature decreased by 30° to 170–175°C. The heating was stopped at this point, and the colloidal solution was cooled to room temperature. Then, the solution was added to methanol (400 mL) in a separating funnel to precipitate the nanocrystals as a white solid. The nanocrystals were separated from the solution into centrifuge tubes. After centrifuging down the nanocrystals at 1500 g for 5 min, they were suspended in methanol and centrifuged again. This step was repeated three times. The nanocrystals were transferred into a flask and dried with a rotary evaporator yielding a white to yellowish powder (average yield 7.2 mmol, 72%), depending on the composition of the nanocrystals.

2.2.1. Preparation of Nanoparticles Solution Embedded in Hybrid Silica

Solution (a). 10 mg of the $\text{LaPO}_4:\text{Eu}$ NPs were dissolved in 5 mL of DMF and stirred at 100°C for 1 h. In case of $\text{CePO}_4:\text{Tb}$, the NPs were dissolved in ethanol and stirred for 1 h at room temperature. When needed, the amount of solvent was varied for the adjustment of viscosity.

Solution (b). Aqueous nitric acid (0.5 mL concentrated HNO_3 in 1.8 mL of water) was added dropwise to 1.8 mL of 1,2-bis(triethoxysilyl)ethane (BTESE), and 5.0 mL of ethanol while stirring in an ice bath. The mixture was refluxed for 2–3 h at 60°C.

Solutions of various concentrations were made by mixing solutions (a) and (b) in various proportions. The viscosity was adjusted by adding small amounts of Brij 58 to the final solution and stirring for 2–3 h. The viscosity of the final solution was measured to be 4.210 mPa·s.

3. Results and Discussion

3.1. Patterning of $\text{LaPO}_4:\text{Eu}$ by Micromoulding in Capillaries (MIMIC). Micromoulding in capillaries (MIMIC) technique was applied to pattern $\text{LaPO}_4:\text{Eu}$ nanoparticles (NPs) embedded in hybrid silica. First of all, the Si substrates were cleaned with a fine jet of CO_2 crystals to blow away the dust particles. Then both substrates and PDMS moulds were treated with oxygen plasma (Harrick Plasma, 200 W) at a pressure of 80 Pa using molecular oxygen [19]. Figure 1 shows SEM and AFM images of line- and pit-patterned films. The complete filling of the capillaries took 10–15 min. The wet patterns were then left for 10–60 min. (with the mould) at 80°C on a hot plate in order to evaporate the solvents and were annealed at 300°C for 30 min in nitrogen. Figure 1(a) shows an example of such a line pattern having a line width (w_l) of 6 μm and spacing between the lines (s_l) of 12 μm . The adhesion of the filled mould to the substrate after drying was found to be stronger. In some cases, the strong adhesion resulted in detachment of a residue layer from the mould and stayed on the substrate. An example is shown in Figure 1(b), where the darkest lines, which are mostly located in the lower part of the picture, are the residue lines of PDMS, while the less dark lines between the PDMS residues are actual patterned organosilica lines obtained from a mould having both w_l and s_l of 1.5 μm , respectively. The resulting shapes of the organosilica pattern are not perfect replicas of the PDMS master from which they are obtained, as can be seen in Figure 1(c), having similar dimensions as in Figure 1(b). The patterned lines have a single peak unlike the double-peak profile as reported somewhere else [20]. Figure 1(d) shows an AFM image showing line pattern of the same dimensions as shown in Figures 1(b) and 1(c) and illustrates the surface roughness between the patterned features due to PDMS residues.

The strong adhesion between mould, pattern, and substrate can have two consequences. It may either result in the detachment of PDMS from the mould and its adhesion to the substrate (Figure 1(b)) or in the detachment of

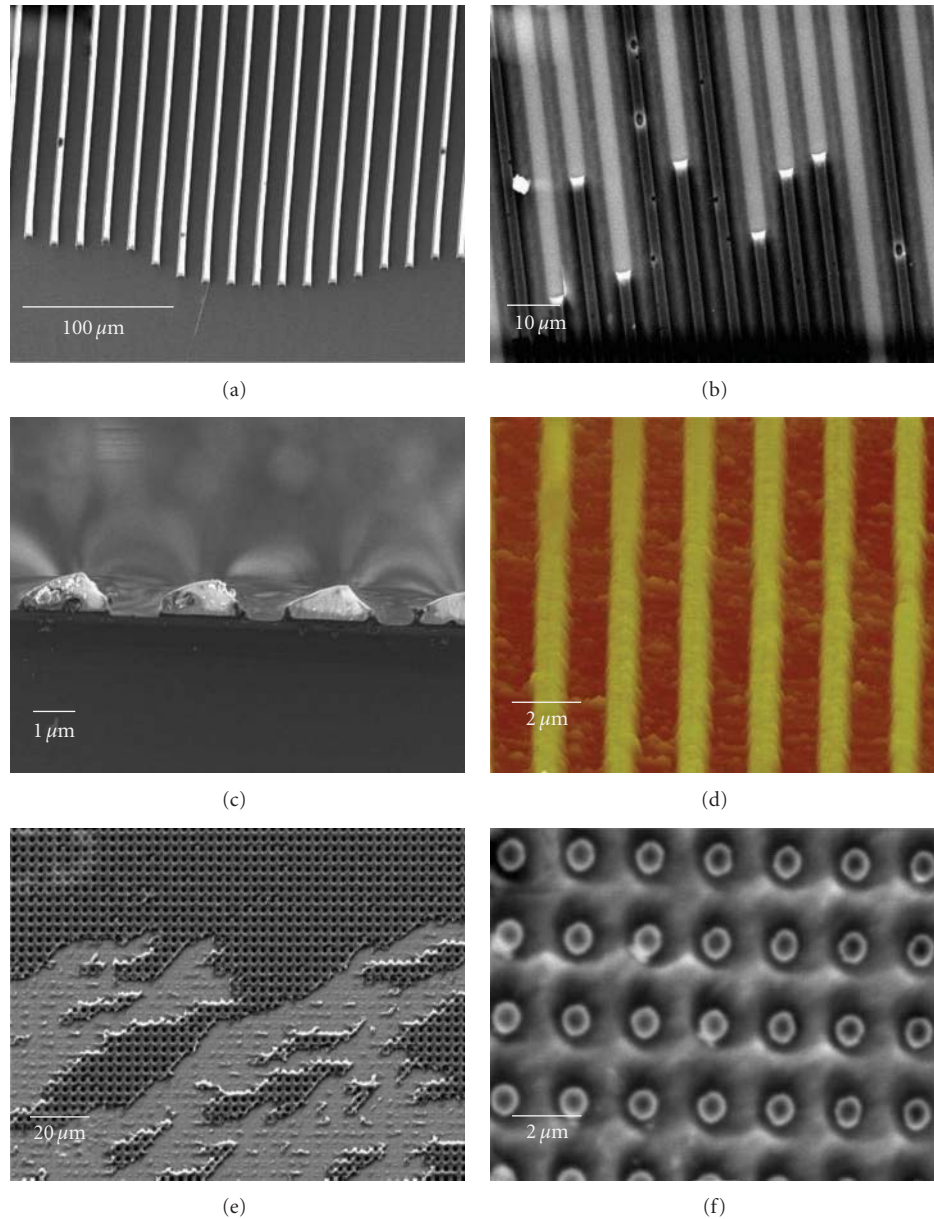


FIGURE 1: SEM and AFM images of $\text{LaPO}_4:\text{Eu}$ NPs embedded in hybrid organosilica and made with the MIMIC technique. (a) SEM image of line patterns having $w_l = 6 \mu\text{m}$ and $s_l = 12 \mu\text{m}$; (b) SEM image of a nonannealed line pattern showing patterned lines and PDMS residue having $w_l = 1.5 \mu\text{m}$ and $s_l = 1.5 \mu\text{m}$; (c) Cross-sectional SEM image of $1.5 \mu\text{m}$ patterned lines; (d) AFM image of $1.5 \mu\text{m}$ wide lines showing surface roughness due to residual PDMS layer; (e) SEM image of pit-patterned film having $P_d = 800 \text{nm}$, depicting the detachment of the pattern due to strong adhesion of the film to the mould; (f) pit pattern showing white PDMS residues inside the pit pattern. Here w_l , s_l , and P_d mean the width of the lines, spacing between the lines, and diameter of the pit, respectively.

the patterned film from the substrate. An example of the latter effect is shown in Figure 1(e), where a pit-patterned film having pit diameter P_d of 800nm was removed together with the mould. This problem can be solved by careful adjustment of the surface energy of the mould by varying the time of plasma treatment, as shown elsewhere [19]. The white areas inside the holes in the pit-patterned film in Figure 1(f) also show the residue layer.

3.2. Patterning of $\text{LaPO}_4:\text{Eu}$ by Microtransfer Moulding. As discussed in the previous section, the adhesion of

MIMIC-derived patterned films was too strong that it resulted in the partial detachment (removal) of the patterned material. In order to circumvent this problem we applied microtransfer moulding (μTM). A tiny drop of solution containing NPs was gently placed on a PDMS mould after it had been treated with oxygen plasma for $20\text{--}60 \text{s}$. After removing the excess material from the protruding parts of the mould with a clean PDMS or steel block, the mould was placed and pressed carefully onto a clean Si substrate. Mould and pattern were then placed on a hot plate at 80°C for $10\text{--}30 \text{min}$ to solidify the wet pattern. Figures 2(a) and 2(b)

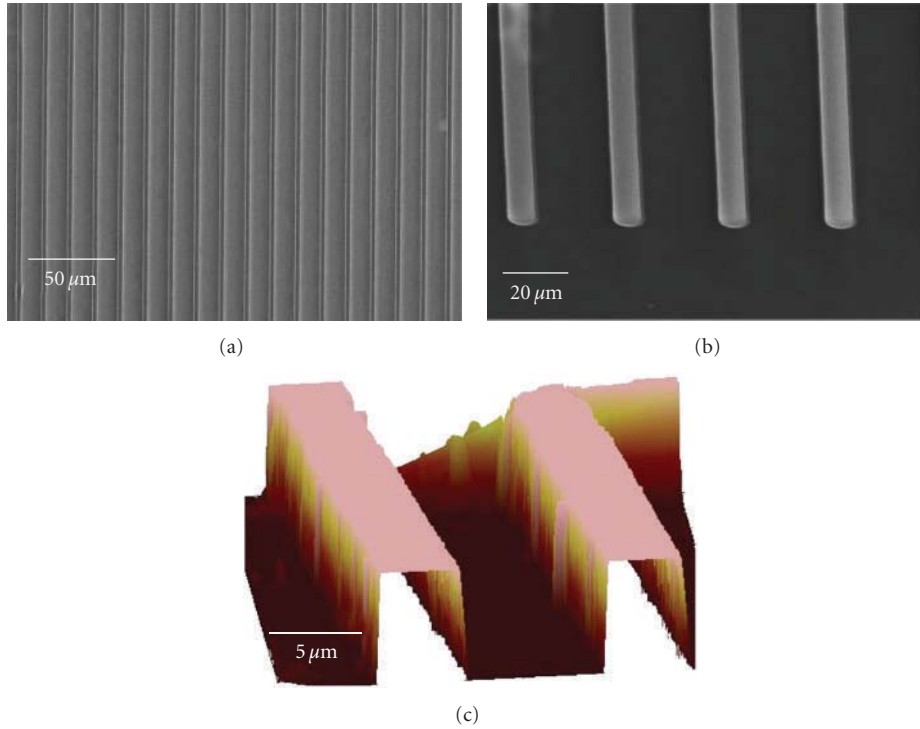


FIGURE 2: Images of $\text{LaPO}_4:\text{Eu}$ lines having $w_l = 6\ \mu\text{m}$ and $s_l = 12\ \mu\text{m}$ patterned with μTM ; (a) and (b) SEM images; (c) topographic AFM. The shape of the line is more rectangular than those derived from MIMIC.

show line patterns having w_l and s_l of $6\ \mu\text{m}$ and $12\ \mu\text{m}$, respectively, and obtained with μTM . Similarly, Figure 2(c) shows an AFM height image of the shape of the pattern. The shape profile is more rectangular than those derived from MIMIC.

The main reason that the shape of the pattern is replicated well with μTM is probably that the channels of the mould are filled prior to replication and exposed to air, to which solvents can evaporate faster and more homogeneously than through the mould as in MIMIC. In μTM the channels are filled with a block unlike MIMIC, where they are filled by capillary action. In other words, the filling phenomenon in MIMIC is rather a spontaneous process whereas in μTM it is a mechanical process.

3.3. Patterning of $\text{CePO}_4:\text{Tb}$ Nanoparticles (NPs). MIMIC and μTM were also applied to pattern $\text{CePO}_4:\text{Tb}$ NPs of various dimensions and shapes. These NPs were stabilized in solvent ethanol unlike $\text{LaPO}_4:\text{Eu}$ NPs which were stabilized in DMF. Figure 3(a) shows a MIMIC-made line-patterned film having w_l of $6\ \mu\text{m}$. The filling length of the channels was higher, and the evaporation was comparatively faster than that of $\text{LaPO}_4:\text{Eu}$ NPs, which were stabilized in DMF, since ethanol evaporates faster than DMF does. Furthermore, DMF was observed to be less compatible with PDMS, since it is a strong solvent. It degraded the PDMS mold when left in contact for longer periods of time. Figure 3(b) shows a μTM -derived line-patterned film having w_l $3\ \mu\text{m}$ before annealing. Residue PDMS lines between the actual patterned lines can be observed. This was found to happen when the

PDMS mould was treated in oxygen plasma for more than 30 s. Longer plasma treatment times increase the surface energy of the mould by oxidizing PDMS to amorphous SiO_x , which is brittle. The surface energy increased the bonding strength between mould and substrate, and the brittleness of the oxidized PDMS layer.

Moulds treated within oxygen plasma for shorter periods of 20–30 s were found to be suitable for replication of features (Figure 3(c)). On the other hand, a mould treated with plasma for a too short period of time reduces the adhesion of the patterned material with the substrate. In that case, the patterned material may detach from the substrate. An example is shown in Figure 3(d), where the displacement of line patterns and their detachment from the substrate can be observed.

An advantage of μTM over MIMIC is the possibility of patterning isolated features. Examples of patterned isolated pillars having diameters (P_d) of 800 and 1500 nm are shown in the lower and upper part of Figure 3(e), respectively. In Figure 3(f), the residue layer between the patterned features is visible. This occurs when the excess solution was not completely removed from the mould prior to their registration onto the substrate.

3.4. Important Aspects of Microtransfer Moulding. Although μTM has some advantages over MIMIC, the adhesion of μTM -made patterned features to the substrate is weaker than that of MIMIC. When patterning line structures, the excess solution should be removed at right angle to the lines. Otherwise, it may cause the removal of the solution from

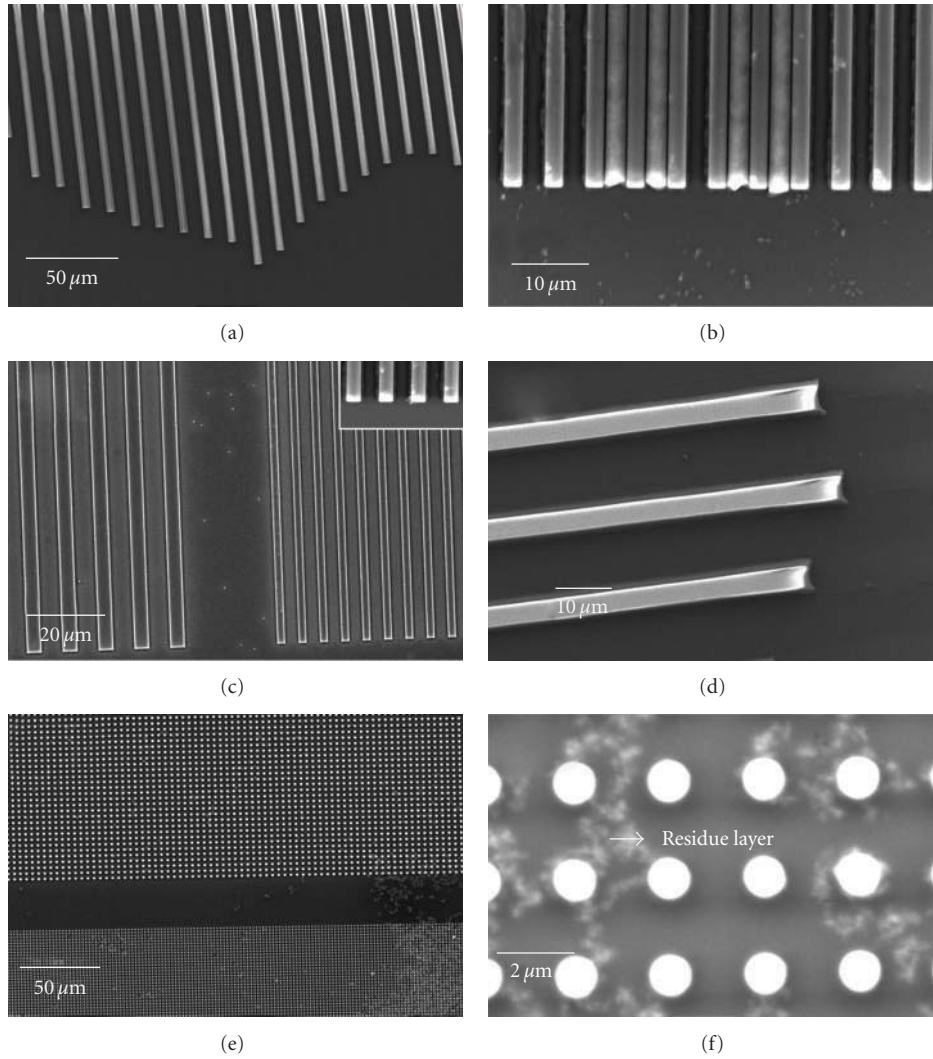


FIGURE 3: SEM images of $\text{CePO}_4 : \text{Tb}$ fluorescence NPs in hybrid silica; (a) line pattern made with MIMIC having $w_l = 6 \mu\text{m}$; (b) line pattern made with μTM showing residue of PDMS lines between the patterned lines as a result of strong adhesion; (c) line pattern made with μTM having $w_l = 5 \mu\text{m}$ (left) and $w_l = 3 \mu\text{m}$ (right); (d) μTM -derived line pattern showing displacement and detachment of the lines due to poor adhesion to the substrate; (e) μTM -derived pillars pattern having diameter of $P_d = 800 \text{ nm}$ (lower part), and $P_d = 1500 \text{ nm}$ (upper part); (f) pillar pattern showing the residue layer between the pillars.

the lines and results in the formation of partially filled M-shaped lines. See Figure 4(a).

The force exerted on a cleaning block to remove excess solution from the mould is also of importance. Application of too large force can cause the partial or complete removal of solution from the patterned area and may lead to incomplete pattern replication. An example is shown in Figure 4(b) (left), where the broken lines resulted from too large forces on the mould. The force applied with a hard material such as steel should be smaller when a soft material is used, such as PDMS. Finally, the excess materials should be removed thoroughly from the mould, or it will be transferred to the substrate and may affect the pattern (Figure 4(c)). All line patterns shown in Figure 4 have w_l and s_l of $6 \mu\text{m}$ and $12 \mu\text{m}$, respectively, and were obtained from a solution of $\text{LaPO}_4 : \text{Eu}$ nanoparticles embedded in hybrid silica.

3.5. D Layer-by-Layer Type Patterning. Both techniques can also be applied to produce 3D layer-by-layer type patterns. As discussed in the introduction part that these 3D wood pile patterns may find application in photonics for waveguiding and photonic crystals. Figure 5 depicts the step-by-step schematic procedure adopted for patterning these 3D structures. The first layer can be patterned with the conventional MIMIC or μTM method (Figure 5(a)). The pattern is then dried at some elevated temperature. After drying, a thin film of some degradable polymer is spin coated on top (Figure 5(b)). In the present work, we applied a thin film of commercially available UV-curable polyurethane (PU) with a speed of 1500 rpm for a period of 1 min. The PU film was cured by exposure to UV light with a wavelength of 350 nm for 2 h. Subsequently, the PU film was treated in oxygen plasma for 5–10 min in order to improve its adhesion

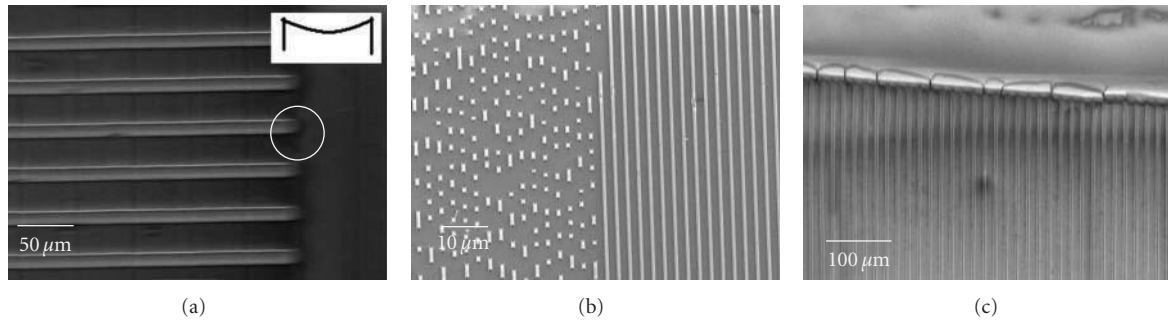


FIGURE 4: SEM images showing the effects of various processing variables in μ TM (a) removal of the excess material in a direction parallel to the lines results in M-shaped lines; (b) application of strong force during the removal of excess material may result in incomplete filling of features of the mould; (c) reservoir (bulk) of excess material at the edge of the patterned lines resulting from incomplete removal of excess solution.

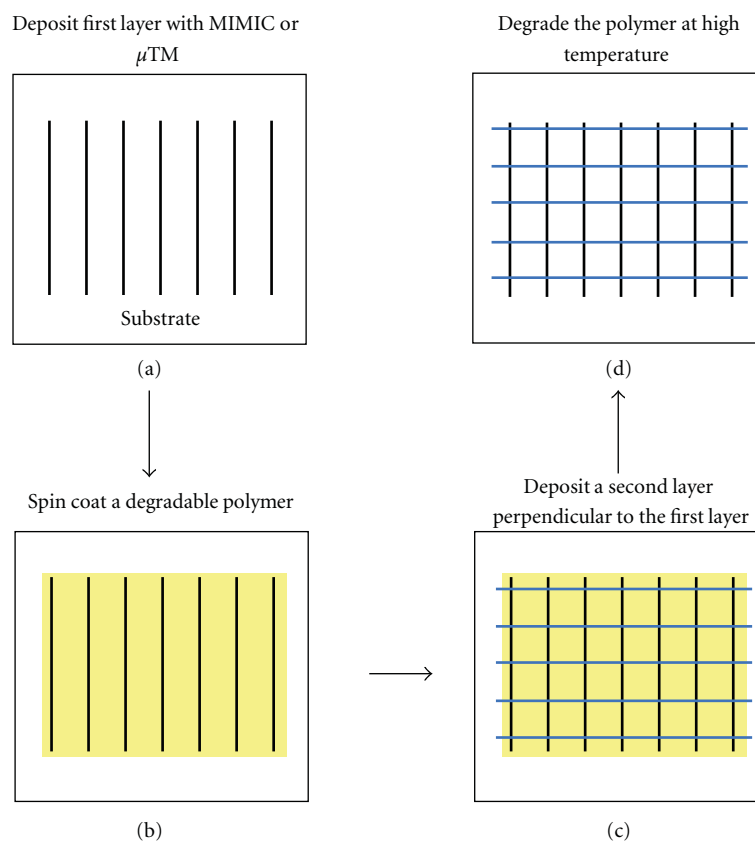


FIGURE 5: Schematic illustration of the procedure adopted for 3D wood pile pattern fabrication.

to the PDMS mould for the next layer to be deposited. A fresh PDMS mould was also treated in oxygen plasma for 5 min and placed very carefully on top of the PU film in such a way that channels of the mould were oriented perpendicular to the lines of the first layer. Then a second layer was patterned on top of the PU film (Figure 5(c)). Finally, after drying, the buried PU film can be degraded by annealing the sample at 550°C in air for 2 h. This yielded a 3D wood pile pattern (Figure 5(d)).

In principle, the same procedure is expected to be applicable to stack a third or more layers. However, defects and errors that occur in one layer will be transmitted to the layers

above. Thus, increasing the number of layers also promotes the number of defects in the final pattern, especially in the upper layers. Furthermore, the weight of the mould while placing it on top of the green body may also produce defects. It was found that the adhesion of the second layer to the underlying PU/titania substrate was weaker than the adhesion of the first layer to the substrate. The adhesion was improved by oxygen plasma treatment of the polymer film for 5 min prior to deposition of the second layer.

While the MIMIC-derived patterns showed good adhesion to the substrate, the final line shapes were not perfectly rectangular; this is an undesirable feature when 3D type

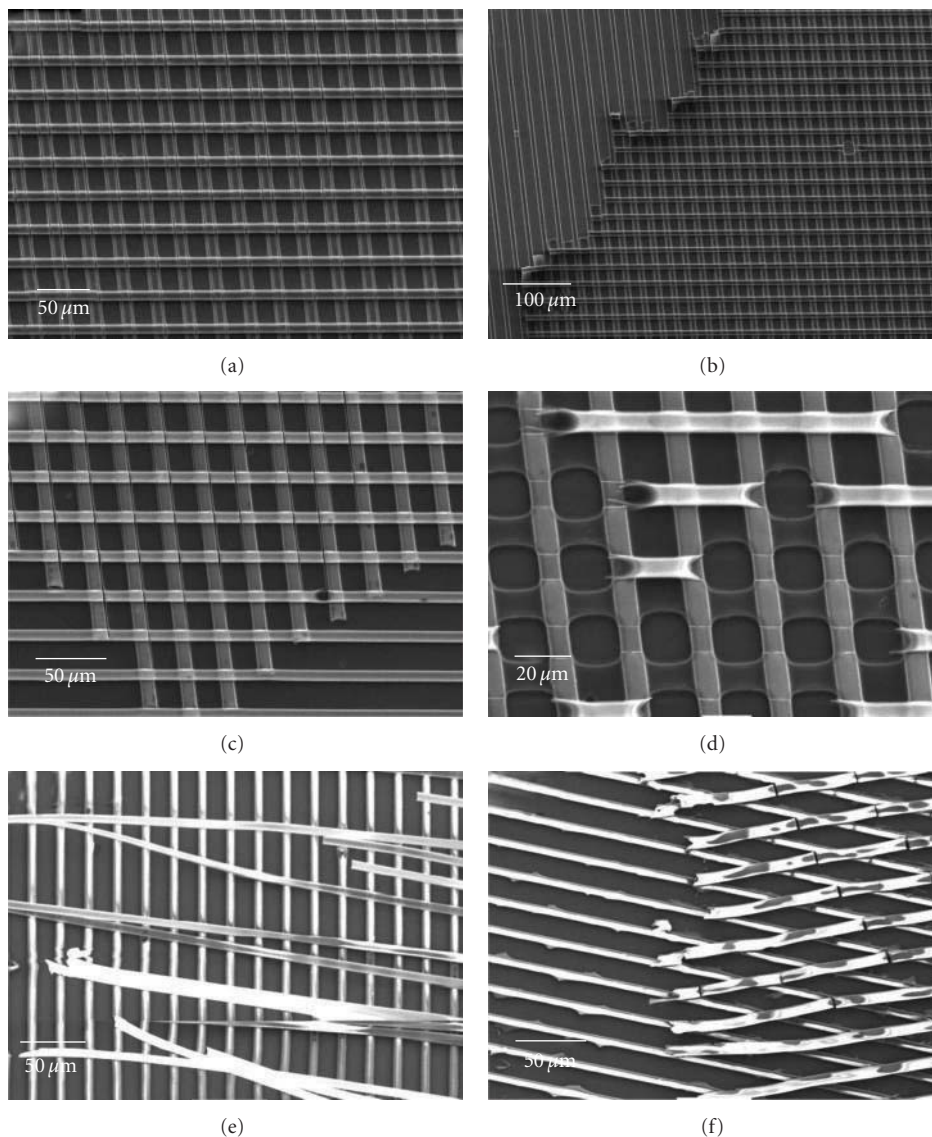


FIGURE 6: SEM images of 3D patterns. (a) μ TM-derived dual layer pattern; (b) detached second layer of a pattern showing the residue layer; (c) 3D pattern showing cracks at the point of contact; (d) effect of incomplete drying of the second layer on pattern coherence and adhesion; (e) dual layer pattern where first layer was made with MIMIC and second layer with μ TM; (f) μ TM-derived dual layer patterns. The lines are at ca. 120° with respect to the others. Fractures are visible at the points of contact.

patterning is targeted. Formation of a residue layer is another limitation of MIMIC, even though absence of residue layers was one of the underlying reasons to develop MIMIC in the first place. These two problems were avoided by using μ TM for 3D patterning.

Figure 6(a) shows μ TM-made 3D pattern having a w_l of $6\ \mu\text{m}$ derived of hybrid organosilica-embedded $\text{LaPO}_4:\text{Eu}$ NPs. Care must be taken to remove the excess solution before bringing it onto the substrate. Otherwise, some residue layer will stay on top of the first layer; this undesirable layer can be seen in Figure 6(b) near the area of detachment of the second layer. Prior to the deposition of the second layer in μ TM, the wet solution in the channels should be dried for a period of time, that is, partially gelled. Otherwise, it may penetrate into the underlying layer and result in defected

pattern (Figures 6(c) and 6(d)). This should be done before the solution bond to the mould channels, since in that case it might not transfer to the substrate. The time period may vary for different materials and solvents; however, in the present scenario a time interval of 2-3 min was found to be the optimum.

The adhesion of the μ TM-derived second layer to the underlying layer was found to be weak as compared to those derived from MIMIC. Eventually, this leads to detachment of the top layer, as illustrated in Figure 6(e). The second layer was also deposited under other angles to see if that might improve the adhesion of the second layer, but this also resulted in cracked lines (Figure 6(f)). The cracking of lines probably result from stresses that occur due to shrinkage of the second layer when the pattern dries.

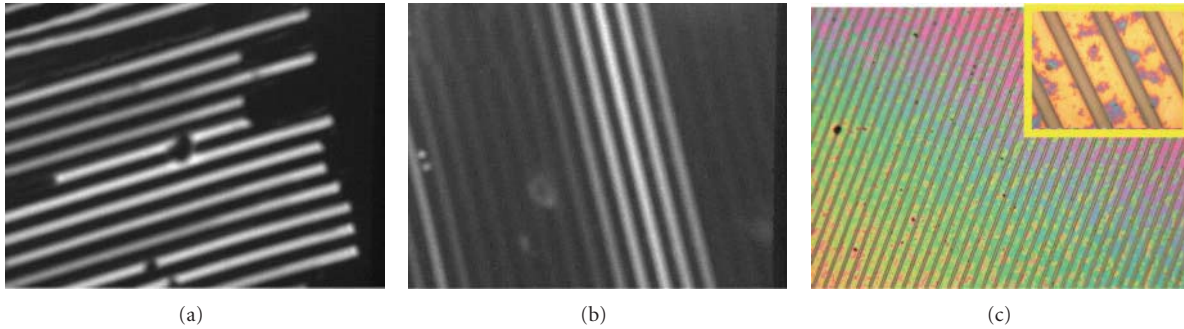


FIGURE 7: (a) and (b) Photoluminescence micrographs of $\text{LaPO}_4:\text{Eu}$ line patterns with $w_l = 4\ \mu\text{m}$, excited with 260 nm UV light, showing reduced luminescence intensity; (c) optical micrograph of a $\text{CePO}_4:\text{Tb}$ patterned film with $w_l = 6\ \mu\text{m}$, depicting residues and color contrast due to thickness variations of a few nanometers.

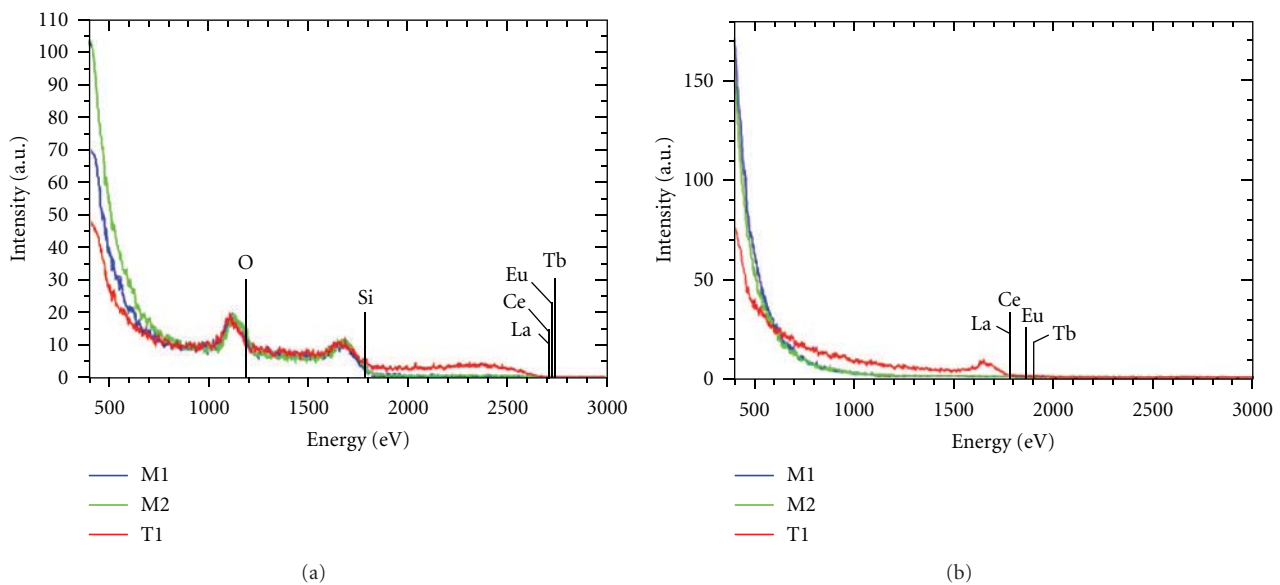


FIGURE 8: LEIS spectra of (a) He and (b) Ne scattering of $\text{LaPO}_4:\text{Eu}$ NPs (M1) patterned by MIMIC; $\text{CePO}_4:\text{Tb}$ NPs (M2) patterned by MIMIC; $\text{LaPO}_4:\text{Eu}$ NPs (T1) patterned by μTM . All lines were made with same mould having $w_l = 6\ \mu\text{m}$, and NPs were embedded in hybrid organosilica.

3.6. Photoluminescence Microscopy. Eu has maximum luminescence (fluorescence) at $\lambda = 393\ \text{nm}$, whereas for $\text{LaPO}_4:\text{Eu}$ the best excitation is at 260 nm [1–5]. Figures 7(a) and 7(b) show the photoluminescence (fluorescence) micrographs of a $\text{LaPO}_4:\text{Eu}$ patterned film made with MIMIC. These patterned films were studied with optical microscopy using an excitation wavelength of 260–300 nm. The photoluminescence intensity, however, was very low as can be seen in the figure. X-ray photoelectron spectroscopy (XPS) was performed to study the presence of the NPs in the patterned films. However, the results (not presented here) did not show indications for the presence of NPs in the patterned lines. The following possible reasons can be sum up about the reduced luminescence intensities.

Firstly, that the NPs are not present in the upper layers of the patterned lines, since XPS can give information up to 20 Å with an exponential decay towards the depth. The sensitivity of XPS is limited to 0.1–0.2 at%, depending on material. Lower concentrations will not be detected.

Furthermore, the microscope lenses were made from glass, which absorbs UV light. Thus, the microscope itself may have reduced the observed intensity drastically. A mercury lamp ($\lambda = 254\ \text{nm}$) was also tried, but the intensity remained low. The excitation and emission wavelengths may also be affected by the matrix material. The hybrid organosilica matrix may reduce the optical yield by several orders of magnitude. Other reasons might include quenching effects such as phonon emission, where the energy of the excited state is consumed in the form of vibrational energy. Nevertheless, a detailed investigation into this effect was not within the scope of this research work. Figure 7(c) shows optical micrograph of a MIMIC-patterned film of $\text{CePO}_4:\text{Tb}$. The color spectrum indicates the presence of a residue layer, and the color contrast is indicative of thickness variation. The dark spots are small dust particles.

3.7. Low Energy Ion Scattering Analysis. To look in more detail to the surface composition than is possible with XPS,

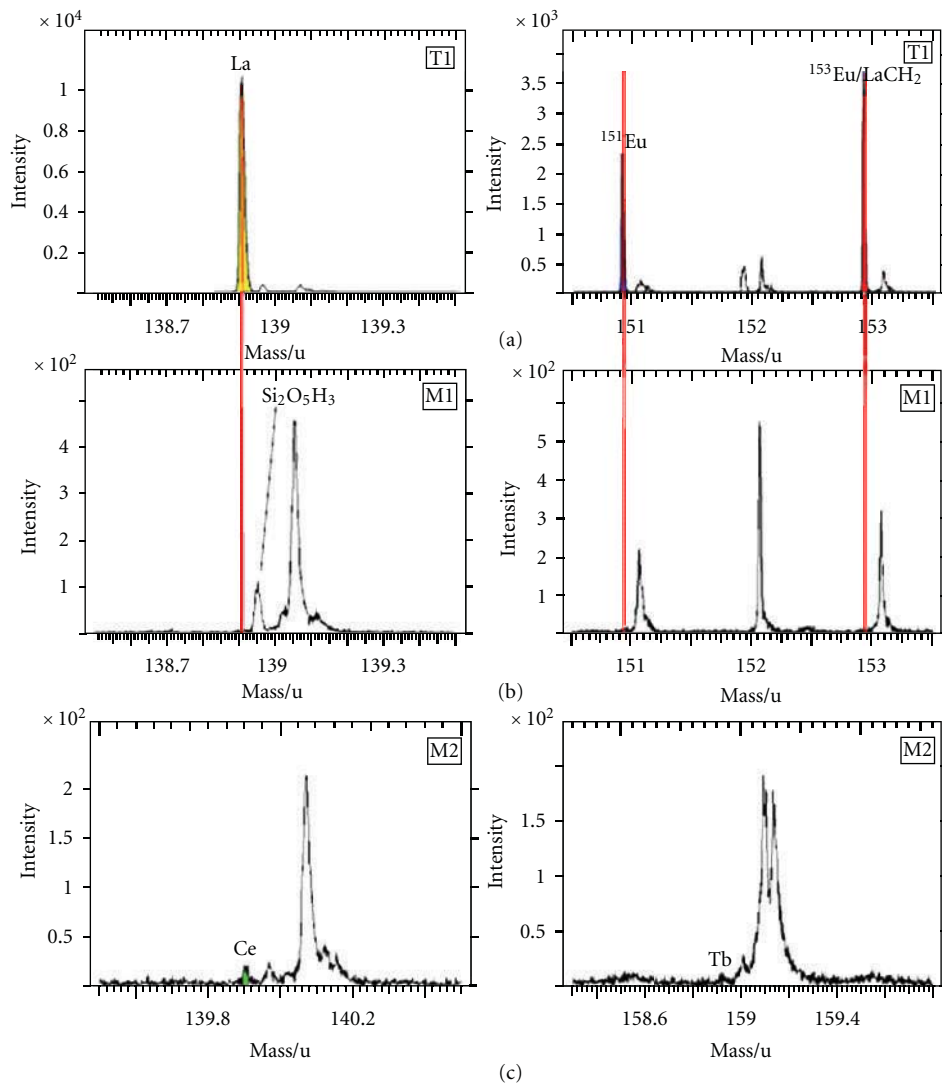


FIGURE 9: TOF-SIMS spectra of (a) T1 (LaPO₄:Eu NPs lines by μ TM); (b) M1 (LaPO₄:Eu NPs patterned by MIMIC); (c) M2 (CePO₄:Tb NPs patterned by MIMIC).

compositional analyses of other three representative samples were done with the low energy ion scattering (LEIS) technique. LEIS can register lower element concentrations, but only in the upper atomic layer. One of the samples (M1), shown in Figure 1(a), is a MIMIC-derived line patterned film of LaPO₄:Eu NPs. The second sample (M2) is shown in Figure 3(a) and is a MIMIC-made CePO₄:Tb-patterned film. The third sample (T1) is shown in Figure 2. It is a μ TM-made LaPO₄:Eu-line patterned film. Henceforth, these samples will be represented by M1, M2, and T1, respectively.

LEIS was performed using helium for the identification of low mass elements, followed by neon scattering for the identification of high mass elements. This way the composition of the first atomic layer was studied by ion scattering. Figures 8(a) and 8(b) show the He and Ne LEIS spectra of the above three samples.

In samples M1 and M2, no rare earth elements were detected. A likely reason is that the concentration of NPs is below the detection limit, at least in the top most layers.

Since LEIS is sensitive only to the top atomic layer and cannot detect elements below a few atomic layers. On the other hand, Sample T1 showed the presence of lanthanum (La) in the outermost monolayer. The difference between the samples lies only in the use of the applied patterning technique, which suggests that the NPs are not present in the upper top layer of MIMIC-derived samples. Major differences resulting from the two soft-lithographic techniques are related to differences in filling behavior and differences in evaporation rates of solvent, and so forth. These may affect the concentration of NPs in the upper most regions of the patterned lines.

3.8. Secondary Ion Mass Spectroscopy Analysis. Time of flight (TOF) secondary ion mass spectroscopy (SIMS) was performed on the same samples as mentioned in the above section.

In all three samples, clear signs of SiOH compounds were detected. Sample T1 showed the presence of La and Eu along with the phosphates (Figure 9(a)). However, for sample M1

neither La nor Eu could be detected (Figure 9(b)). Similarly, for sample M2, a limited amount of Ce and Tb was detected (Figure 9(c)). Furthermore, no phosphates were found in the two samples (Figures 9(b) and 9(c)). Aliphatic and aromatic hydrocarbons were detected in these two samples. The aromatic compounds probably may have resulted from the initial synthesis of the NPs and, therefore, indirectly suggests their presence in the materials under investigation here.

On the basis of compositional analysis with LEIS and SIMS, some indications for the reasons for the reduced intensities observed with PL microscopy can be deduced. Firstly, the NPs are not near to the surface region. The path that photons have to travel to escape from the organosilica matrix is therefore relatively long; this affects the degree of absorption by the organosilica matrix. Furthermore, the sample patterned with μ TM showed the presence of NPs very near to the external surface. This suggests that the patterning technique also has an influence on the location of NPs in the matrix material in the given pattern. Silica is known to be a good host material for lanthanide ions such as europium and cerium; however, quenching effects may reduce the photoluminescence intensity.

4. Conclusions

MIMIC and μ TM techniques were applied successfully to pattern $\text{LaPO}_4 : \text{Eu}$ and $\text{CePO}_4 : \text{Tb}$ NPs embedded in hybrid silica. The shape of the patterned lines derived from MIMIC was found to be different from those derived with μ TM. The adhesion of the patterned material to the substrate and to the mould was very challenging, and further work is needed to be done for a variety of other materials system to be able to reproduce the results. Furthermore, the adhesion of MIMIC-derived patterns to the substrate and the underlying pattern was stronger than that of μ TM-made patterns. This is probably due to the fact that the residue layer in MIMIC is thicker, which improves bonding to the substrate. Also, in MIMIC the bonding is stronger due to the fact that in μ TM the sol is jellified (semi-dried) before it is transferred. On the other hand, the shape of patterns is better replicated with μ TM than with MIMIC.

By comparison of the two techniques, it can be concluded that both techniques have their own advantages and limitations. The selection of an appropriate technique may depend on the applications of the patterned films. MIMIC is a good technique for applications where residue layer is not undesirable. Similarly, μ TM is good for the patterning of isolated features and as well as when exact replication of the mould is desired.

Photoluminescence properties in the encapsulated NPs were studied. Their intensities were low. This may be either due to some quenching effects, and/or due to the fact that the NPs are buried away from the external surface. Other possibility could be that their amount is low. Nevertheless, the experiments show that both techniques can be used to pattern similar or other complex materials with these techniques.

Acknowledgments

Financial support from the Netherlands Technology Foundation STW within the framework of the VIDI Innovational Research Scheme is greatly acknowledged. The authors thank the Dutch Organization for Scientific Research (NWO) for the financial contribution to publish this work. They gratefully acknowledge Professor Karst and his group at the University of Münster for providing fluorescent nanoparticles and helping in the characterization of patterned films.

References

- [1] H. Meyssamy, K. Riwotzki, A. Kornowski, S. Naused, and M. Haase, "Wet-chemical synthesis of doped colloidal nanomaterials: particles and fibers of $\text{LaPO}_4 : \text{Eu}$, $\text{LaPO}_4 : \text{Ce}$, and $\text{LaPO}_4 : \text{Ce, Tb}$," *Advanced Materials*, vol. 11, no. 10, pp. 840–844, 1999.
- [2] J. W. Stouwdam and F. C. J. M. van Veggel, "Near-infrared emission of redispersible Er^{3+} , Nd^{3+} , and Ho^{3+} doped LaF_3 nanoparticles," *Nano Letters*, vol. 2, no. 7, pp. 733–737, 2002.
- [3] K. Riwotzki, H. Meyssamy, H. Schnablegger, A. Kornowski, and M. Haase, "Liquid-phase synthesis of colloids and redispersible powders of strongly luminescing $\text{LaPO}_4 : \text{Ce, Tb}$ nanocrystals," *Angewandte Chemie International Edition*, vol. 40, no. 3, pp. 573–576, 2001.
- [4] W. Li and J. Lee, "Microwave-assisted sol-gel synthesis and photoluminescence characterization of $\text{LaPO}_4 : \text{Eu}^{3+}, \text{Li}^+$ nanophosphors," *Journal of Physical Chemistry C*, vol. 112, no. 31, pp. 11679–11684, 2008.
- [5] J. W. Stouwdam, *Lanthanide-doped nanoparticles as the active optical medium in polymer-based devices*, Ph.D. thesis, University of Twente, 2004.
- [6] E. Sluzky and K. Hesse, "Electrophoretic preparation of phosphor screens," *Journal of the Electrochemical Society*, vol. 136, pp. 2724–2727, 1989.
- [7] J. B. Talbot, E. Sluzky, and S. K. Kurinec, "Electrophoretic deposition of monochrome and color phosphor screens for information displays," *Journal of Materials Science*, vol. 39, no. 3, pp. 771–778, 2004.
- [8] M. A. Santana-Aranda and M. Meléndez-Lira, "Screen printed $\text{CdS}_x\text{Te}_{1-x}$ films, structural and optical characterization," *Applied Surface Science*, vol. 175–176, pp. 538–542, 2001.
- [9] M. B. Korzenski, P. Lecoeur, B. Mercey, and B. Raveau, "Nd:YVO₄ thin films grown by pulsed laser deposition: effects of temperature and pressure on the grain morphology and microstructure," *Chemistry of Materials*, vol. 13, no. 5, pp. 1545–1551, 2001.
- [10] P. Lecoeur, M. B. Korzenski, A. Ambrosini, B. Mercey, P. Camy, and J. L. Doualan, "Growth of $\text{Er:Y}_2\text{O}_3$ thin films by pulsed laser ablation from metallic targets," *Applied Surface Science*, vol. 186, no. 1–4, pp. 403–407, 2002.
- [11] E. W. Bohannan, X. Gao, K. R. Gaston, C. D. Doss, C. Sotiriou-Leventis, and N. Leventis, "Photolithographic patterning and doping of silica xerogel films," *Journal of Sol-Gel Science and Technology*, vol. 23, no. 3, pp. 235–245, 2002.
- [12] M. Yu, J. Lin, Z. Wang et al., "Fabrication, patterning, and optical properties of nanocrystalline $\text{YVO}_4 : \text{A}$ (A = Eu^{3+} , Dy^{3+} , Sm^{3+} , Er^{3+}) phosphor films via sol-gel soft lithography," *Chemistry of Materials*, vol. 14, no. 5, pp. 2224–2231, 2002.
- [13] Y. Xia and G. M. Whitesides, "Soft lithography," *Angewandte Chemie International Edition*, vol. 37, no. 5, pp. 550–575, 1998.

- [14] D. Pisignano, M. F. Raganato, L. Persano et al., "The luminescence quantum yield of organic one-dimensional periodic nanostructures," *Nanotechnology*, vol. 15, no. 8, pp. 953–957, 2004.
- [15] X. M. Han, J. Lin, J. Fu et al., "Fabrication, patterning and luminescence properties of $X_2\text{-Y}_2\text{SiO}_5\text{:A}$ ($A=\text{Eu}^{3+}$, Tb^{3+} , Ce^{3+}) phosphor films via sol-gel soft lithography," *Solid State Sciences*, vol. 6, no. 4, pp. 349–355, 2004.
- [16] E. Kim, Y. Xia, and G. M. Whitesides, "Micromolding in capillaries: applications in materials science," *Journal of the American Chemical Society*, vol. 118, no. 24, pp. 5722–5731, 1996.
- [17] X. M. Zhao, Y. Xia, and G. M. Whitesides, "Fabrication of three-dimensional micro-structures: microtransfer molding," *Advanced Materials*, vol. 8, no. 10, pp. 837–840, 1996.
- [18] K. Riwotzki, H. Meyssamy, A. Kornowski, and M. Haase, "Liquid-phase synthesis of doped nanoparticles: colloids of luminescing $\text{LaPO}_4\text{:Eu}$ and $\text{CePO}_4\text{:Tb}$ particles with a narrow particle size distribution," *Journal of Physical Chemistry B*, vol. 104, no. 13, pp. 2824–2828, 2000.
- [19] S. U. Khan, O. F. Göbel, J. E. ten Elshof, and D. H. A. Blank, "Patterning lead zirconate titanate nanostructures at sub-200-nm resolution by soft confocal imprint lithography and nanotransfer molding," *ACS Applied Materials & Interfaces*, vol. 1, no. 10, pp. 2250–2255, 2009.
- [20] C. R. Martin and I. A. Aksay, "Topographical evolution of lead zirconate titanate (PZT) thin films patterned by micromolding in capillaries," *Journal of Physical Chemistry B*, vol. 107, no. 18, pp. 4261–4268, 2003.

Research Article

Effect of Particle Morphology on Sinterability of SiC-ZrO₂ in Microwave

Lydia Anggraini¹ and Kei Ameyama²

¹ Graduate School of Science and Engineering, Ritsumeikan University, 1-1-1 Noji-Higashi, Kusatsu 525-8577, Japan

² College of Science and Engineering, Ritsumeikan University, 1-1-1 Noji-Higashi, Kusatsu 525-8577, Japan

Correspondence should be addressed to Lydia Anggraini, gr040069@ed.ritsumei.ac.jp

Received 2 August 2011; Revised 26 October 2011; Accepted 27 October 2011

Academic Editor: Li-Hong Liu

Copyright © 2012 L. Anggraini and K. Ameyama. This is an open access article distributed under the Creative Commons Attribution License, which permits unrestricted use, distribution, and reproduction in any medium, provided the original work is properly cited.

The effect of particle morphology on the sinterability of microwave-sintered SiC-ZrO₂ was evaluated in this paper. A comparison was also made against the electric furnace and resulted in faster heating rate because of the difference of heat transfer in the sintering processes. High-energy mechanical milling process has been applied to obtain the homogeneous particle morphology and finer particles size. The microstructure of finer particles of SiC-ZrO₂ after milling was better in the region sintered by microwave. The microstructure in the sintered region was smaller for the coarser particles which were obtained by heterogeneous nonmilled powder mixture. The result of the Vickers hardness test was higher for the powder homogeneously dispersed SiC-ZrO₂ after milling and sintering by microwave. These are influenced by the difference of individual electric properties of the initial SiC and ZrO₂ which have an effect on the absorption of the microwave energy.

1. Introduction

The principal advantages of ceramics are high hardness, extremely high melting point, high compressive strength and stiffness, and wear resistance [1, 2]. Silicon-carbide-(SiC-) based ceramics are also very promising high-temperature structural materials owing to their excellent thermal and mechanical properties, such as hardness and flexural strength [3–7]. One of the applications of SiC is in gas turbines. Mechanical properties of SiC, especially fracture toughness, can be improved by the addition of other phases into a material matrix to form a composite structure [8–12]. SiC-based ceramics are generally produced by cold die compaction with subsequent sintering or by hot isostatic pressing and finishing [13]. Among these procedures, the usage of sintering is the most important process for fabricating ceramics. One of the sintering technologies is microwave, which was initially used only in food production but now is also used in the powder processing. However, monolithic SiC is a highly covalently bonded silicon and carbon compound that is difficult to sinter without additives by any method [14] including microwaves [15]. Besides, SiC-based ceramics

have low-dielectric-loss factor, that is, the materials with such properties are not easy to heat up by microwave, especially at lower temperature, as reported by Agrawal et al. [16, 17].

Dispersion of zirconia (ZrO₂) particles in silicon carbide and other low dielectric loss ceramics is an effective method to enhance the absorption of energy in microwave sintering in room temperature. The preparation of ultrafine ZrO₂-based ceramic particles by microwave sintering has been studied extensively [18, 19]. Dispersing of ultrafine particles is expected to improve the sintering ability in ceramics. This is because the specific surface area of the particles provides additional driving force for densification during sintering. Ultra-fine initial size of the particles normally results in higher densities, and in some cases may lead to lower firing temperatures due to faster sintering kinetics [20]. Ultra-fine ZrO₂-based ceramic particles are usually known to contain agglomerates. One of most important factors in sintering is the agglomerate size. In microwave sintering, when the powders are milled and refined to nanometer-sized particles, the microwave absorption properties may be changed. Ruan et al. compared the microwave attenuation between the particles of different sizes of 5 μm and 65 nm and showed that

the dielectric loss of nanometer-sized particles is larger than that of micrometer-sized particles [21].

Although SiC and ZrO₂ have been sintered individually by microwave by many researchers, the formation of the particles morphology and its effect on the microstructure and mechanical properties have not been previously reported. Thus, the objective of this paper is to evaluate the two different formations of the particle morphology on the microstructure of SiC-ZrO₂. The differences in the formation of the particles morphology were obtained by mechanical milling and compacted by microwave or electric furnace sintering. The hardness tests of SiC-ZrO₂ with different particles morphology were also measured.

2. Experimental Procedure

2.1. Mechanical Milling. In this study, a fine α -SiC of 2~3 μ m and an ultra-fine ZrO₂ of 30 nm were used, as shown in Figure 1(a). Both ceramics were manually mixed with a weight ratio of 1:1. In another set, both ceramics were subjected to vibratory ball milling (Super Misuni NEV-MA-8, Nishin Gikken, Japan). Dense tungsten carbide-cobalt (WC-Co) of 5 mm in diameter was used as a grinding media and of 60 mm in diameter was used as a grinding pot. Figure 1(b) shows the illustration of vibration ball mill. A constant vibration frequency of 12.5 Hz and a total time of 144 ks were used to mill SiC and ZrO₂ with the same ratio, 1:1. The milling time was chosen to achieve different morphology of the particles. The ratio of the grinding ball to milled powder was 5:1 by weight. After mixing and milling, the SiC-ZrO₂ was precompact in a 10 mm diameter stainless steel die under 50 MPa pressure, and then consolidated by nonconventional microwave and conventional electric furnace sintering.

2.2. Sintering. The schematic illustration of microwave sintering is shown in Figures 2(a) and 2(b) (IDX, MSS-TE0004, Japan) with a single-mode cavity and linked to a magnetron that delivers a variable forward power of up to 2 kW at a frequency of 2.45 GHz. Figure 2(a) shows the temperature measurement of the microwave sintering process. It was continuously measured by an infrared radiation thermometer camera cold air intake (Chino, IR-CAI). The microwave sintering was carried out in nitrogen atmosphere at a temperature of 1273 K for 600 s. The microwave heating was generated by 800 W power. The specimen was set upon a silica plate inside a silica tube for thermal insulation, as shown in the front view in Figure 2(b). An alumina stage was used as the susceptor for the purpose of thermally heating the low-dielectric-loss ceramic specimens to a certain temperature. The ceramic specimens directly absorb microwave energy to self-heat to the desired temperature at high heating rates, and the main function of the susceptor is to maintain a uniform temperature. The specimen was heated in the electric- (E-) field, which was controlled via a three-stub tuner. The maximum setting of the specimens on the E-field plunger was set to 142 mm.

For the conventional electric furnace sintering, the temperature of SiC-ZrO₂ was controlled to the same value as the microwave, 1273 K. The sintering temperature was measured using an R-type thermocouple with a constant soak time of 600 s, which was generated by applying a nominal power of 2000 W.

2.3. Characterizations. The impurities of the powders, before and after mechanical milling, were investigated by X-ray diffraction analysis (XRD, RINT-2000, Japan). The morphology of the particles was characterized using a field-emission scanning electron microscope (FE-SEM S-4800, Hitachi, Japan). The sintered samples were cut in half and their cross-sections carefully polished. These were used for microstructure characterization by means of FE-SEM. The mechanical properties were examined using hardness testing. The hardness was measured with an HMV-1 (Shimadzu Corp., Japan) using the Vickers indents obtained by applying a 98.1 N load for 5 s. The measurement was conducted at 30 random points on each specimen.

3. Results and Discussion

3.1. Characterization of Particle Morphology. Figure 3 shows FE-SEM images of SiC-ZrO₂. As shown in the non-milled powder mixing in Figure 3(a), the shape of the SiC was irregular and the ZrO₂ was agglomerate, which is similar to the initial one (Figure 1(a)). Before mixing, the amount of ZrO₂ particles that attach on the surface of the SiC powders is very limited. As a result of mixture, there is no change in the appearance of both SiC and ZrO₂. From this image, it appears that the particle morphology is heterogeneous.

After mechanical milling, the surface of the SiC powders becomes finer and almost fully covered with ZrO₂ particles, as shown in Figure 3(b). In order to achieve homogeneous particle morphology, control of the milling time was very important. If the milling time was too short, the particle morphology of ZrO₂ on the surface of SiC would remain heterogeneous. The homogeneous particle morphology could be fully achieved for a milling time of 144 ks. The size of the SiC powders was not significantly reduced, and their shape became somewhat spherical. In the case of ZrO₂, the size was refined and the shape of the particles was deformed. These morphological changes are attributed to a fragmentation of the particle agglomerates which was caused by the high-energy mechanical milling.

The refinement of the particle size is consistent with the broadening of X-ray diffraction peaks in Figure 4. In the case of the nonmilled powder mixture (heterogeneous particle morphology), the diffraction peaks were slightly narrower than for the milled powders (homogeneous particle morphology). According to Scherrer's formula,

$$\tau = \frac{K\lambda}{\beta \cos \theta}, \quad (1)$$

where K is the shape factor, λ is the X-ray wavelength of the radiation used ($\text{CuK}\alpha$), β is the line broadening at half the maximum intensity (FWHM) in radians, θ is

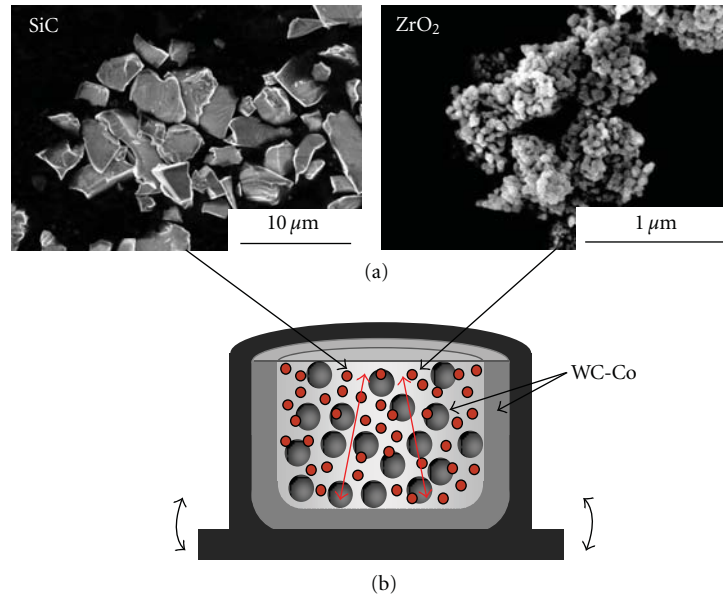


FIGURE 1: (a) Appearance of initial silicon carbide powders with the size $2\sim 3\ \mu\text{m}$ and zirconia particles with the size $30\ \text{nm}$ (b) Illustration of Super Misuni vibration ball mill with dense WC-Co of $5\ \text{mm}$ in diameter used as a grinding media and of $60\ \text{mm}$ in diameter used as a grinding pot.

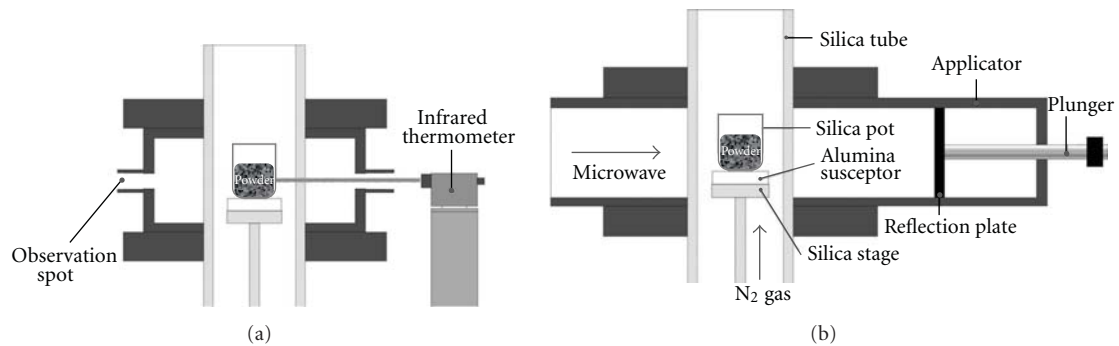


FIGURE 2: Schematic of (a) side and (b) front view of single-mode microwave sintering. The microwave sintering was carried out in nitrogen atmosphere at a temperature of $1273\ \text{K}$ for $600\ \text{s}$ and was generated by $800\ \text{W}$ power.

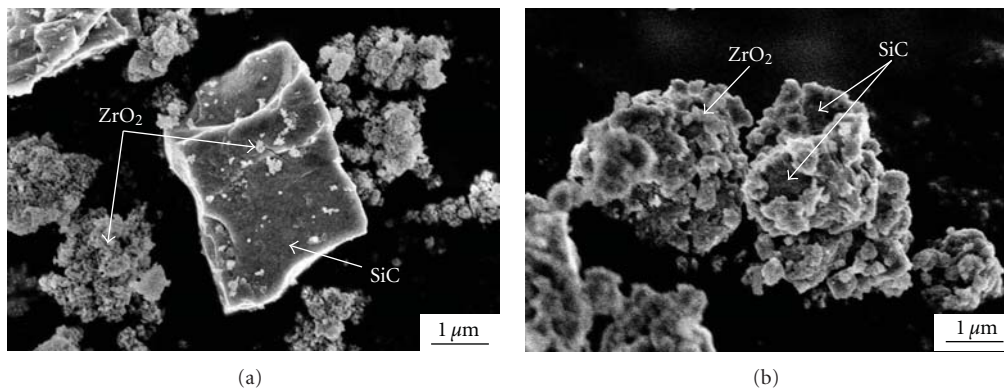


FIGURE 3: FE-SEM micrographs of particles morphology appearance of SiC-ZrO₂ with (a) nonmilled powder mixture (heterogeneous) with the amount of ZrO₂ particles that attach on the surface of the SiC powders is very limited (b) milled powder (homogeneous) particle morphology with the surface of the SiC powders becoming finer and almost fully covered with ZrO₂ particles.

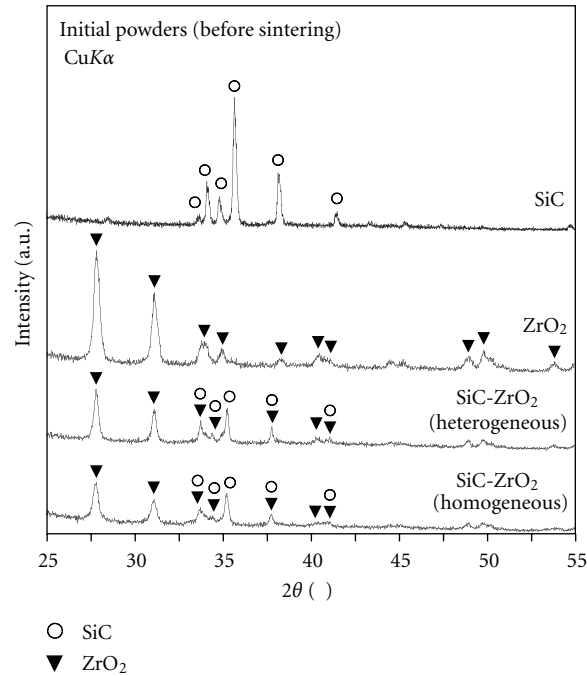


FIGURE 4: X-ray diffraction pattern of initial SiC and ZrO₂, for the nonmilled powder mixture (heterogeneous); the diffraction peaks were slightly narrower than those for the milled powders (homogeneous distribution).

the Bragg angle, and τ is the mean size of the crystalline domains, which may be smaller or equal to the particle size; the broadening of diffraction peaks indicates a reduction in crystalline size [22]. No phase transformation or new phase formation for both SiC-ZrO₂ was found in the heterogeneous and homogeneous powder mixtures such that SiC and ZrO₂ maintain their rhombohedral and monoclinic structures, respectively.

3.2. Sintering Behaviors. The microwave heating profiles of SiC-ZrO₂ separated into electric and magnetic fields are shown in Figure 5(a). The plot shows different heating results in microwave fields. In the E-field, SiC-ZrO₂ powders could be sintered, unlike in the H-field. The temperature increased to around 40 s. To achieve the desired temperature of 1273 K, the time required in microwave heating is less than 60 s. It means that the heating rate in the microwave sintering is very rapid, 25 K/s on average.

In case of electric furnace sintering, the temperature remained almost constant at room temperature from 1 s to 30 s time. Then, the temperature increased until around 160 s, as shown in the heating profile in Figure 5(b). The heating rate in the electric furnace is slower than in microwave sintering, which is only 8 K/s on average. To achieve the temperature of 1273 K, the time required is as much as 200 s.

3.3. Sinterability and Microstructure of SiC-ZrO₂. Figure 6 shows FE-SEM images of SiC-ZrO₂ specimens sintered by microwave and electric-furnace sintering at the constant temperature of 1273 K. In low magnification of microwave

sintering microstructures, there is an obvious difference in the microstructure of samples derived from heterogeneous and homogeneous particle morphology. It is clearly showed that the sintering ability of heterogeneous particle of SiC-ZrO₂ in microwave is lower than that of the homogeneous one. In heterogeneous particle morphology microstructure, only a few scattered sintered regions are present, as shown in Figure 6(a). After mechanical milling for 144 ks, the particles morphology was changed, the particle morphology was homogeneous, and the average grain size was refined, as shown in Figure 6(b), the better homogeneity of ZrO₂ particle on SiC surface, improve the sintering region in microwave. The grain size of SiC-ZrO₂ is clearly shown in the FE-SEM micrographs at higher magnification in Figures 6(c) and 6(d). In the non-milled powder mixture (heterogeneous), the SiC size is bigger and coarser than the milled powder (homogeneous particle morphology).

The microstructures of the SiC-ZrO₂ at 1273 K temperature, sintered by the conventional electric furnace, are shown in Figures 6(e) and 6(f). In this case, a very different appearance, as compared to the microstructure of microwave sintered powder, is shown for all electric furnace sintered specimens. The SiC-ZrO₂ shows a coarse-grained aspect with high porosity. From the micrographs, there is almost no difference in the heterogeneous and homogeneous particles morphology of the SiC-ZrO₂ after sintering by electric furnace.

3.4. Vickers Hardness. SiC-ZrO₂ specimens sintered by microwave and electric furnace were measured by the Vickers hardness. Those specimens were tested on random points from top to bottom section. In the case of electric

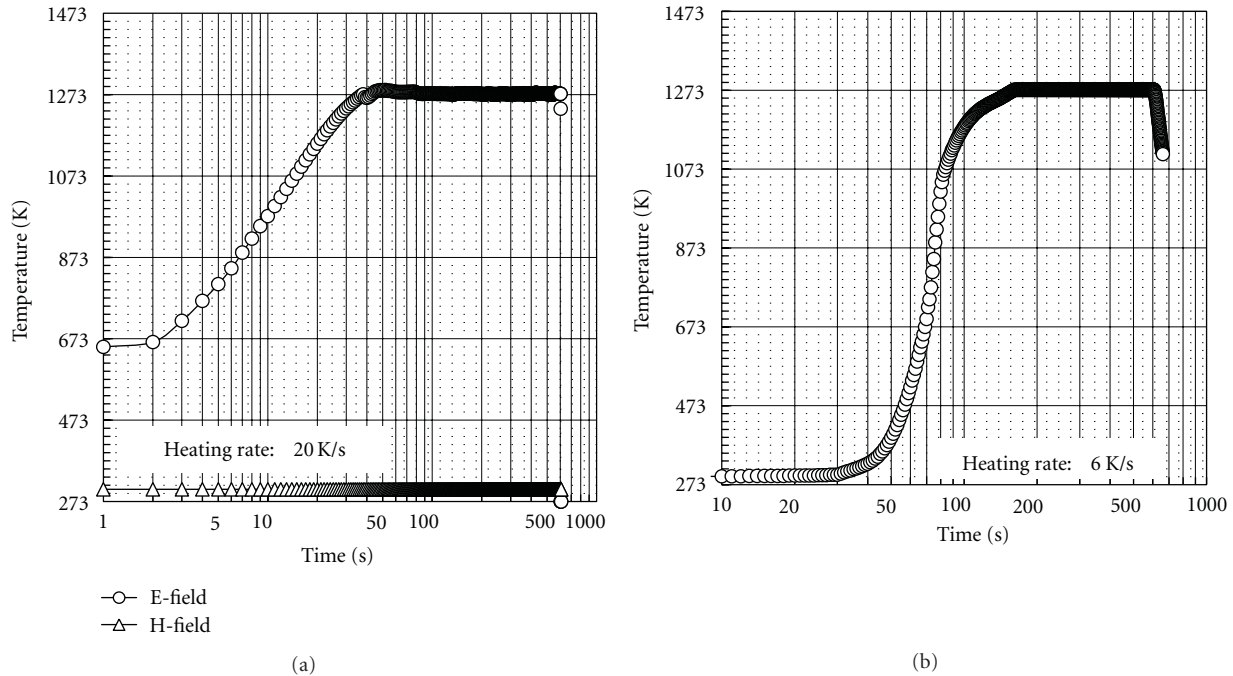


FIGURE 5: Heating profile of (a) microwave and (b) electric furnace sintering. The heating rate in the microwave sintering is 25 K/s on average and in the electric furnace is 8 K/s on average.

furnace sintering, both the heterogeneous and homogeneous particles morphology specimens showed very similar results, as shown in Figure 7. This result indicates that the sintering ability of SiC-ZrO₂ in electric furnace is very low, regardless of grain size and/or particle morphology.

In the case of microwave sintering, the Vickers hardness of the homogeneous is higher than that of the heterogeneous particle morphology specimens. This is consistent with the microstructures of heterogeneous particle morphology of SiC-ZrO₂ in microwave-sintered compacts which shows lower sintering ability than homogeneous particles morphology specimens.

3.5. Discussion. In microwave sintering, the 800 W applied power and E-field were chosen evaluation. In the E-field, SiC and ZrO₂ ceramic powders could be sintered unlike the magnetic H-field; this indicates that the initial ceramics such as SiC and ZrO₂ do not have the magnetic properties. Therefore, the E-field can be used to evaluate the effect of particle morphology of SiC-ZrO₂ in microwave.

The heating profiles of microwave and electric furnace sintering show that for conventional electric furnace sintering, the heating rate required is 8 K/s on average from room temperature to 1273 K. For microwave sintering, the total time was only 50 s on average to reach 1273 K temperature. During electric furnace sintering, the heating rate is limited by the capability of the machine to achieve fast heating rates because of the slow resistive heating of the heating elements and heat transfer via thermal radiation to the material and also to prevent large thermal variation within the compacts

to avoid cracking [23]. The slower heating rate, the need for holding at intermittent temperature to reduce thermal variation, and long soaking time for sintering increase the total processing time of the compacts [23]. For microwave, heating coupled with susceptors, rapid heating rates in excess of 25 K/s on average can be easily achieved since the powder compact can absorb microwave energy directly and can be heated rapidly from within. The susceptors provide radiant heating to the samples externally, thereby reducing the thermal variation in the compacts [23]. The rapid heating rate in microwave will activate the ion exchange and chemical reaction as material transport, thereby reducing the activation energy [24]. Rapid heating minimizes grain growth and enhances the mechanical properties of materials. Those rapid heating rates in microwave resulted in larger sintered regions of microstructure than in the case of electric furnace-sintered compact specimens.

The microwave sintering response in microstructure is not only caused by the rapid heating rates. The better response in microwave for mechanical milling powder is also due to ultrafine ZrO₂ particles dispersed homogeneously on the SiC surface. It is known that smaller particle can enhance the sintering kinetics. Another important factor in the microstructure of SiC-ZrO₂ is the absorption of microwave energy in each material. The absorption of ultrafine ZrO₂ particles is better than that of fine SiC powders, considering the dielectric loss factor of ZrO₂ is higher than that of SiC. As reported by Ruan et al., the dielectric loss of nanometer-sized particles is larger than that of micrometer-sized particles [21]. When the ultra-fine ZrO₂ particles are dispersed homogeneously on the SiC surface, the absorption of the

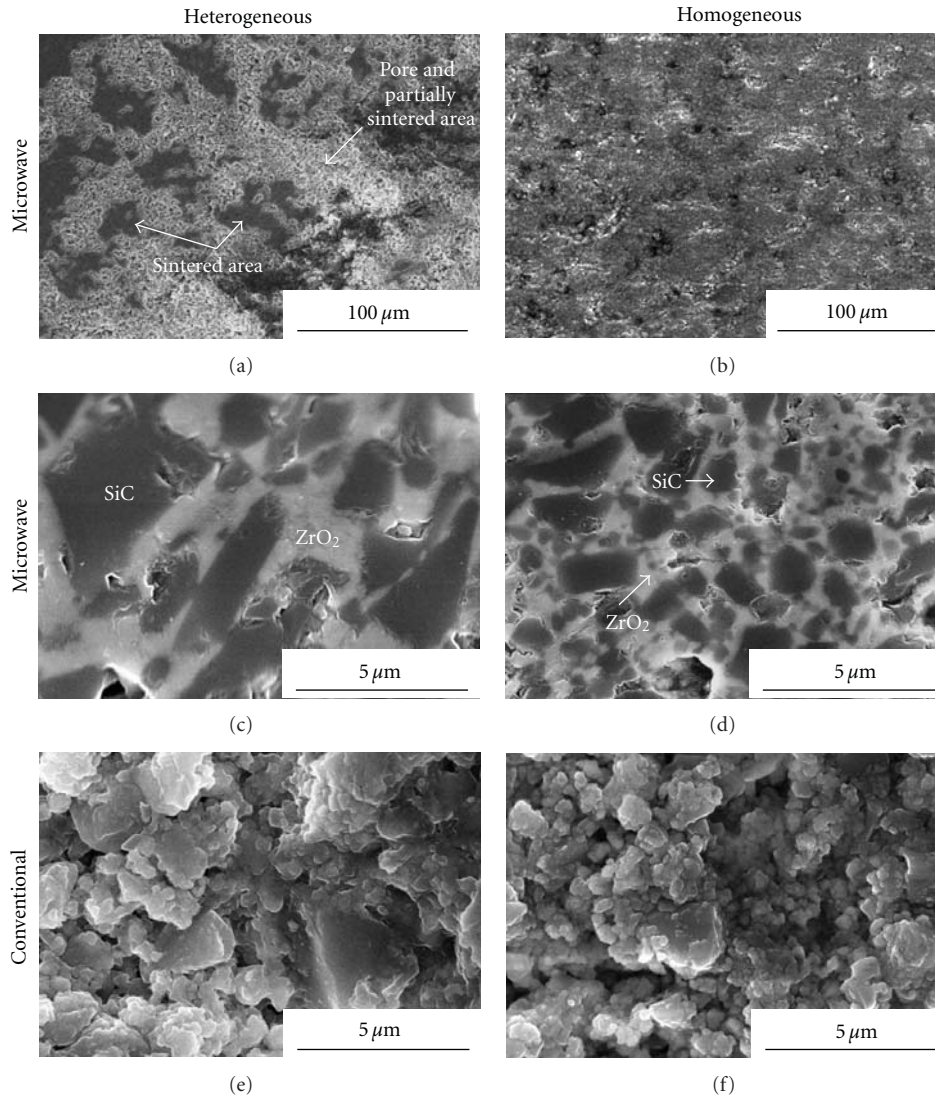


FIGURE 6: (a) and (b) are low magnification and (c) and (d) are high magnification of FE-SEM micrographs of nonmilled powder mixture (heterogeneous) and milled powder (homogeneous) particle morphology of SiC-ZrO₂ sintered by microwave sintering. (e) and (f) are FE-SEM micrographs of SiC-ZrO₂ sintered by conventional electric furnace with heterogeneous and homogeneous particle morphology and homogeneous particle morphology.

microwave energy is further increased. The homogeneous particle morphology and finer crystalline size that were obtained by high-energy mechanical milling leads to higher dielectric loss compared with the non-milled powder mixture (heterogeneous particle morphology). Therefore, larger sintered regions by microwave sintering could be obtained as an effect of the homogeneous particle morphology of SiC-ZrO₂ ceramic composites.

Although the effects of the particle size and morphology of SiC-ZrO₂ on the microwave sintering response were clearly mentioned, we still have a problem with microwave sintering that was performed in single-mode, 2.45 GHz microwave with small chamber, easy to maintain and to use. The drawback of these single-mode chambers is that they are relatively small, which only allows the heating of one small specimen at a time. Unfortunately, this method has a critical

drawback since the electro magnetic field in the chamber is not uniform [25], resulting in inhomogeneous heating and the unavoidable formation of hot spots. One approach to achieve a uniform electro-magnetic field distribution in a single-mode chamber is to design a chamber with at least one of the major dimensions 100 times greater than the wavelength. A higher frequency is more convenient than using a huge chamber to enlarge the uniform field region. For this reason, higher microwave frequencies such as 28 GHz and 80 GHz could be used [26–28].

In the present study, specimens were sintered by microwave single-mode furnace with a small chamber, in which the field distribution at the center of the chamber is not completely uniform and specimens sintered using the alumina susceptor show regional microstructures. The susceptor can also have a compensating or correcting effect

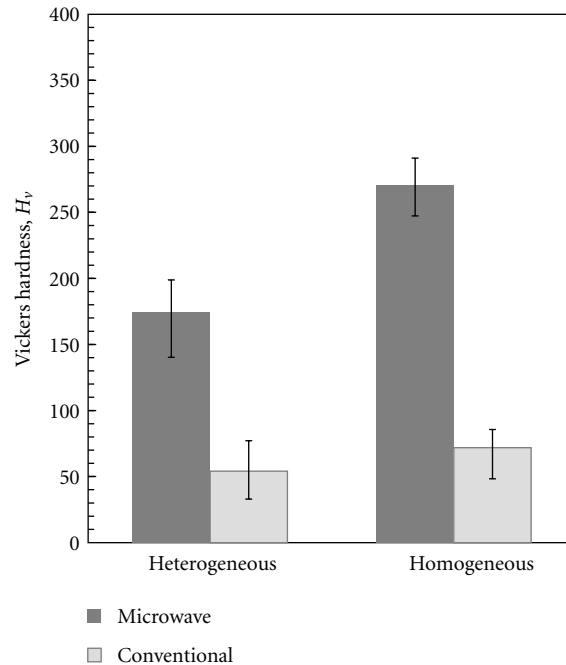


FIGURE 7: The vickers hardness of non-milled powder mixture (heterogeneous) and milled powder (homogeneous) particle morphology of SiC-ZrO₂ sintered by microwave and conventional electric furnace. The lower hardness of specimen sintered by conventional electric furnace compared with that sintered by microwave indicates that the sintering ability of SiC-ZrO₂ in electric furnace is also very low, regardless of grain size and/or particle morphology.

with respect to the inhomogeneous electric field. In our experiments, the response of microwave sintering of SiC-ZrO₂ with alumina susceptor shows excellent repeatability in microstructure and hardness test results, while sintering without susceptor resulted in differences in the repeatability of microstructure and hardness test results because of an extreme sensitivity to the materials response in the chamber.

4. Summaries

The effects of particles morphology of SiC-ZrO₂ have been evaluated using microwave and electric furnace sintering. Several summaries obtained are as follows.

- (1) The heating rate obtained in the microwave furnace was faster compared with the electric furnace sintering.
- (2) The ZrO₂ particles were refined and the morphology, of the ZrO₂ particles was homogenized on the SiC surface by mechanical milling.
- (3) The homogeneous particle morphology resulted in larger sintered regions in microstructure and higher hardness values after sintering by microwave, compared with the nonmilled powder mixture (different particle morphology).

References

- [1] R. J. Brook, "Superhard-ceramics," *Nature*, vol. 400, no. 6742, pp. 312–315, 1999.
- [2] J. M. Léger and J. Haines, "The search for superhard materials," *Endeavour*, vol. 21, no. 3, pp. 121–124, 1997.
- [3] A. Maître, A. V. Put, J. P. Laval, S. Valette, and G. Trolliard, "Role of boron on the Spark Plasma Sintering of an α -SiC powder," *Journal of the European Ceramic Society*, vol. 28, no. 9, pp. 1881–1890, 2008.
- [4] M. Singh and J. A. Salem, "Mechanical properties and microstructure of biomorphic silicon carbide ceramics fabricated from wood precursors," *Journal of the European Ceramic Society*, vol. 22, no. 14-15, pp. 2709–2717, 2002.
- [5] Q.-W. Huang and L.-H. Zhu, "High-temperature strength and toughness behaviors for reaction-bonded SiC ceramics below 1400°C," *Materials Letters*, vol. 59, no. 14-15, pp. 1732–1735, 2005.
- [6] J. Sánchez-González, A. L. Ortiz, F. Guiberteau, and C. Pascual, "Complex impedance spectroscopy study of a liquid-phase-sintered α -SiC ceramic," *Journal of the European Ceramic Society*, vol. 27, no. 13-15, pp. 3935–3939, 2007.
- [7] F. M. Varela-Feria, J. Martínez-Fernández, A. R. De Arellano-López, and M. Singh, "Low density biomorphic silicon carbide: microstructure and mechanical properties," *Journal of the European Ceramic Society*, vol. 22, no. 14-15, pp. 2719–2725, 2002.
- [8] N. Claussen, "Fracture toughness of Al₂O₃ with an unstabilized ZrO₂ dispersed phase," *Journal of the American Ceramic Society*, vol. 59, no. 1-2, pp. 49–51, 1976.
- [9] S. E. Dougherty, T. G. Nieh, J. Wadsworth, and Y. Akimune, "Mechanical properties of a 20 vol% SiC whisker-reinforced, yttria-stabilized, tetragonal zirconia composite at elevated temperatures," *Journal of Materials Research*, vol. 10, no. 1, pp. 113–118, 1995.

- [10] N. Claussen, K. L. Weisskopf, and M. Ruehle, "Tetragonal zirconia polycrystals reinforced with SiC whiskers," *Journal of the American Ceramic Society*, vol. 69, no. 3, pp. 288–292, 1986.
- [11] X. Miao, W. Mark Rainforth, and W. E. Lee, "Dense zirconia-SiC platelet composites made by pressureless sintering and hot pressing," *Journal of the European Ceramic Society*, vol. 17, no. 7, pp. 913–920, 1997.
- [12] H. L. Lee and H. M. Lee, "Effect of SiC on the mechanical properties of 3Y-TZP/SiC composites," *Journal of Materials Science Letters*, vol. 13, no. 13, pp. 974–976, 1994.
- [13] H. Park and K. T. Kim, "Consolidation behavior of SiC powder under cold compaction," *Materials Science and Engineering A*, vol. 299, no. 1-2, pp. 116–124, 2001.
- [14] Y. W. Kim, M. Mitomo, H. Emoto, and J. G. Lee, "Effect of initial α -phase content on microstructure and mechanical properties of sintered silicon carbide," *Journal of the American Ceramic Society*, vol. 81, no. 12, pp. 3136–3140, 1998.
- [15] S. Mandal, A. Seal, S. K. Dalui, A. K. Dey, S. Ghatak, and A. K. Mukhopadhyay, "Mechanical characteristics of microwave sintered silicon carbide," *Bulletin of Materials Science*, vol. 24, no. 2, pp. 121–124, 2001.
- [16] J. Cheng, R. Roy, and D. Agrawal, "Radically different effects on materials by separated microwave electric and magnetic fields," *Materials Research Innovations*, vol. 5, pp. 170–177, 2002.
- [17] K. H. Brosnan, G. L. Messing, and D. K. Agrawal, "Microwave sintering of alumina at 2.45 GHz," *Journal of the American Ceramic Society*, vol. 86, no. 8, pp. 1307–1312, 2003.
- [18] S. Sano, S. Kawakami, Y. Takao, S. Takayama, and M. Sato, "Microwave absorptency change of zirconia powder and fiber during vacuum heating," *Advances in Science and Technology*, vol. 63, pp. 85–90, 2010.
- [19] Y. Fang, J. Cheng, R. Roy, D. M. Roy, and D. K. Agrawal, "Enhancing densification of zirconia-containing ceramic-matrix composites by microwave processing," *Journal of Materials Science*, vol. 32, no. 18, pp. 4925–4930, 1997.
- [20] M. W. Barsoum, *Fundamentals of Ceramics*, McGraw Hill series in Materials Sciences, McGraw-Hill, 1997.
- [21] S. Ruan, B. Xu, H. Suo, F. Wu, S. Xiang, and M. Zhao, "Microwave absorptive behavior of ZnCo-substituted W-type Ba hexaferrite nanocrystalline composite material," *Journal of Magnetism and Magnetic Materials*, vol. 212, no. 1, pp. 175–177, 2000.
- [22] M. V. Zdujić and O. B. Milošević, "Mechanochemical treatment of ZnO and Al₂O₃ powders by ball milling," *Materials Letters*, vol. 13, no. 2-3, pp. 125–129, 1992.
- [23] W. W. L. Eugene and M. Gupta, "Characteristics of aluminum and magnesium based nanocomposites processed using hybrid microwave sintering," *Journal of Microwave Power and Electromagnetic Energy*, vol. 44, pp. 14–27, 2010.
- [24] R. M. German, *Sintering Theory and Practice*, John Wiley & Sons, New York, NY, USA, 1996.
- [25] W. H. Sutton, "Microwave processing of ceramic materials," *American Ceramic Society Bulletin*, vol. 68, no. 2, pp. 376–386, 1989.
- [26] B. Swain, "Advanced materials and processing," *Advanced Materials and Processes*, vol. 134, p. 75, 1988.
- [27] A. Birnboim, D. Gershon, J. Calame et al., "Comparative study of microwave sintering of zinc oxide at 2.45, 30, and 83 GHz," *Journal of the American Ceramic Society*, vol. 81, no. 6, pp. 1493–1501, 1998.
- [28] T. Kimura, H. Takizawa, K. Uheda, T. Endo, and M. Shimada, "Microwave synthesis of yttrium iron garnet powder," *Journal of the American Ceramic Society*, vol. 81, no. 11, pp. 2961–2964, 1998.

Research Article

Synthesis of a Layered Organic-Inorganic Nanohybrid of 4-Chlorophenoxyacetate-zinc-Layered Hydroxide with Sustained Release Properties

Mohd Zobir Hussein,^{1,2} Nor Farhana binti Nazarudin,¹
Siti Halimah Sarijo,³ and Mohd Ambar Yarmo⁴

¹ Department of Chemistry, Faculty of Science, Universiti Putra Malaysia (UPM), Selangor, 43400 Serdang, Malaysia

² Advanced Materials and Nanotechnology Laboratory, Institute of Advanced Technology (ITMA), Universiti Putra Malaysia (UPM), Selangor, 43400 Serdang, Malaysia

³ Faculty of Applied Science, MARA University of Technology (UiTM), Selangor, 40450 Shah Alam, Malaysia

⁴ Department of Chemistry, Faculty of Science and Technology, National University of Malaysia (UKM), Selangor, 43400 Bangi, Malaysia

Correspondence should be addressed to Mohd Zobir Hussein, mzobir@science.upm.edu.my

Received 27 July 2011; Accepted 26 August 2011

Academic Editor: Li-Hong Liu

Copyright © 2012 Mohd Zobir Hussein et al. This is an open access article distributed under the Creative Commons Attribution License, which permits unrestricted use, distribution, and reproduction in any medium, provided the original work is properly cited.

A zinc-layered hydroxide-4-chlorophenoxy acetate (4CPA) organic-inorganic nanohybrid was prepared using a simple direct reaction of 4CPA anions with ZnO under an aqueous environment to be used as a controlled release formulation of the herbicide, 4CPA. The concentration of the active agent, 4CPA, was found to be a controlling factor for the formation of a pure phase well-ordered nanolayered hybrid in which it could be synthesised at 0.2 M 4CPA. ZnO shows a well-defined grain structure of variable size in the nanometre range. However, the formation of the 4CPA-ZLH nanohybrid resulted in a flake-like fibrous structure. On heating at 500°C for 5 h under atmospheric conditions, the nanohybrid transformed back to a well-defined grain structure, as previously observed with the starting material, ZnO. The release of 4CPA was found to occur in a controlled manner and was generally governed by pseudo-second-order kinetics.

1. Introduction

Layered metal hydroxide compounds with inorganic brucite-like structures can be generally classified into two major types, layered double hydroxides (LDHs) and layered metal hydroxides (LMHs). They can be represented by the general formula, $[M^{2+}_{1-x}M^{3+}_x(OH)_2]^{x+}(A^{m-})_{x/m} \cdot nH_2O$ and $M^{2+}(OH)_{2-x}(A^{n-})_{x/n} \cdot mH_2O$, respectively, where M^{2+} is a divalent cation (Ca^{2+} , Mg^{2+} , Zn^{2+} , Co^{2+} , Ni^{2+} , Cu^{2+} , Mn^{2+}), M^{3+} is a trivalent cation (Al^{3+} , Cr^{3+} , Fe^{3+} , Co^{3+} , Ni^{3+} , Mn^{3+}) and A^{m-} is an interlayer anion (Cl^- , NO_3^- , ClO_4^- , CO_3^{2-} , SO_4^{2-} , and many other inorganic anions). For LDH, the x value is the charge density, that is, the molar ratio of $M^{3+}/(M^{2+} + M^{3+})$ [1, 2]. LMH consists of two parts: positively charged brucite-like inorganic layers and exchangeable anions and water molecules in the interlayer.

These properties give LMH wide applications in industrial and environmental research from catalysts [3] to antacids [4] and from magnetic materials [5, 6] to controlled release formulations of various active agents such as DNA [7], drugs [8, 9], and agrochemicals [10–15].

One LMH which has been the subject of intense research lately is zinc-layered hydroxide (ZLH). This is due the fact that ZLH has very similar properties to those of LDH. The 2D layered inorganic material is composed of layers with octahedral coordinated zinc cations, in which 1/4 of them are displaced out of the layer, leaving an empty octahedral site which forms cationic centres tetrahedrally coordinated to the top and bottom of the octahedral sheet. Water molecules occupy the apices, and nitrate counter ions are free between the interlayers [16].

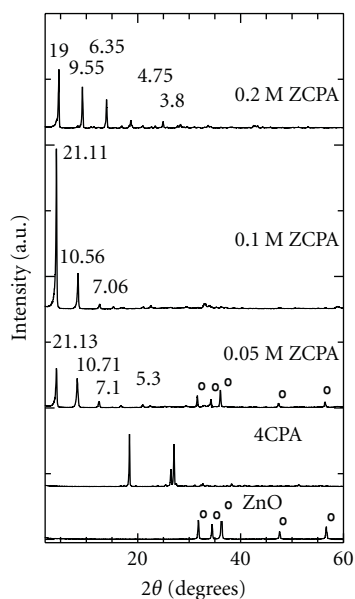


FIGURE 1: PXRD patterns of ZnO, 4CPA, and ZCPA nanohybrids prepared at 0.05, 0.10, and 0.20 M 4CPA (o = ZnO phase, peak from left to right is for 100, 002, 101, 102, 110 reflection. Assignment of other peaks is given in Table 1).

Controlled release formulations (CRF) have been used as an approach to exploit the most effective use of herbicides and at the same time to prevent environmental pollution [17]. Ideally, the CRF should be able to release herbicides at a level required to manage the crops, therefore preventing problems such as leaching, evaporation, degradation, and excessive use of harmful chemicals [18]. Various matrices have been proposed for use as pesticide CRF. The active agent should be immobilised or intercalated into an inert matrix and gradually released over time [19]. The use of natural and synthetic clay-type materials in the preparation of CRF is of current interest due to their tailor-made properties and relatively low cost of preparation.

In this study, we discuss our work on the intercalation of 4CPA, an herbicide, into the interlayer of ZLH by a simple synthesis method, that is, by the direct reaction of ZnO with 4CPA under an aqueous environment for the formation of a new controlled release formulation of the organic-inorganic-layered nanohybrid type. In addition, the controlled release property of the resulting nanohybrid will be also discussed.

2. Materials and Methods

All chemicals used in this synthesis were obtained from various chemical suppliers and used without further purification. All solutions were prepared using deionised water with resistivity of 18.2 MΩ-cm.

In this study, 0.05 g ZnO (Acros), was discharged into 100 mL deionised water. Solutions of 4CPA (Aldrich) with concentrations of 0.025–0.1 M were added to the ZnO solutions and aged at 70°C in an oil bath shaker for 18 hours. The synthesised material was centrifuged, thoroughly washed with deionised water and dried in an oven at 70°C.

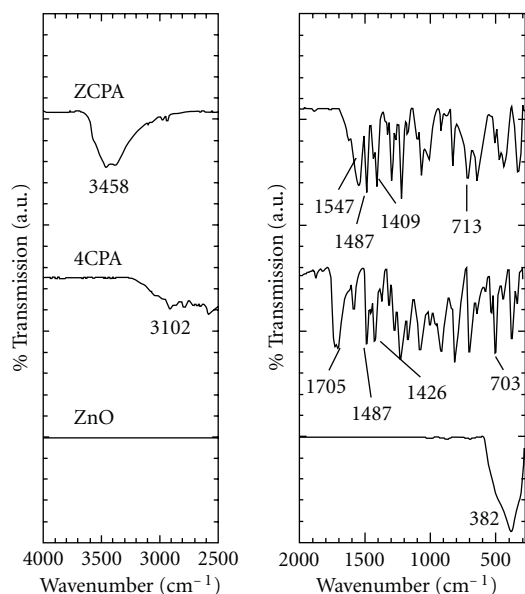


FIGURE 2: FTIR spectra of ZnO, 4CPA, and the nanohybrid, ZCPA.

The resulting material was then powdered and stored in a sample bottle for further use and characterisation.

Powder X-ray diffraction patterns were recorded at 2–60° on a Shimadzu diffractometer XRD-6000 using Cu K α radiation at 40 kV and 30 mA. FTIR spectra of the materials were recorded over the range 400–4000 cm $^{-1}$ on a Perkin-Elmer 1752X spectrophotometer using the KBr disc method. A CHNS analyser, model CHNS-932 of LECO Instruments was used for CHNS analyses. Thermogravimetric and differential thermogravimetric analyses (TGA/DTG) were carried out using a Mettler Toledo instrument. Surface characterisation of the material was carried out using a nitrogen gas adsorption-desorption technique at 77 K using a Micromeritics ASAP 2000. The surface morphology of the samples was observed by a field emission scanning electron microscope (FESEM), using a JOEL JSM-6400. UV-vis spectra were obtained using a Perkin Elmer UV-Visible Spectrophotometer, Lambda 35. Surface analysis of the nanohybrid in powder form was studied using an X-ray Photoelectron Spectrometer (XPS), Kratos Ultra. Samples were analysed at 1×10^{-9} torr using monochromatic AlK α as the X-ray source and data were collected based on wide and narrow scans of the elements of interest.

3. Results and Discussion

3.1. Powder X-Ray Diffraction. The powder X-ray diffraction (PXRD) patterns of ZnO, 4CPA, and the nanohybrids prepared using 0.05, 0.10, and 0.20 M 4CPA are shown in Figure 1. The PXRD patterns of ZnO show that the sample was of a pure phase with good crystallinity as shown by the presence of typical ZnO peak patterns (Table 1).

The resulting materials obtained by direct reaction between ZnO and 4CPA (0.05–0.20 M) showed well-ordered 2D-layered nanohybrids, labelled as ZCPAs. The average basal spacing of 21.26 and 21.14 Å was observed when 0.05

TABLE 1: Carbon and hydrogen content, surface area and thermal property of ZnO, 4CPA, and ZCPA nanohybrid and the kinetic equations used for the fitting.

(a)

Sample	Mass (%)		Loading (%)	BET surface area/m ² g ⁻¹	BJH pore diameter/Å
	Carbon	Hydrogen			
4CPA	51.2	4.089	—	—	—
ZCPA(ZnO)	21.9	3.141	45.4	6.1 (3.9)	138 (208)

(b) XPS analysis (value in Ev)

	C _{1s}	O _{1s}	Zn _{p_{3/2}}	Zn _{p_{1/2}}	Cl _{p_{3/2}}	Cl _{p_{1/2}}
ZCPA	284.5	531.3	1021.7	1044.8	200.2	201.8
	286.0	533.1	—	—	—	—
	288.4	—	—	—	—	—

(c) Thermal property

	$T_{max}/^{\circ}C$	$\Delta m/\%$						
4CPA	—	—	—	—	243.5	97.5	—	—
ZnO	100.6	0.9	—	—	—	—	—	—
ZCPA	92.6	6.8	155.0	6.2	294.4	30.1	952.1	20.5

(d) ^aKinetic equations

Zerth order	First order	Pseudo-second-order	Parabolic diffusion
$x = kt + c$	$-\log(1 - x) = kt + c$	$t/M_i = 1/k_2 M_f^2 + (1/M_f) \cdot t$	$M_i/M_f = kt^{0.5} + c$

^a x is the percentage release of 4CPA at time, t (min), and c is a constant. k , M_i , and M_f are the rate constant, the initial, and final concentration of 4CPA, respectively.

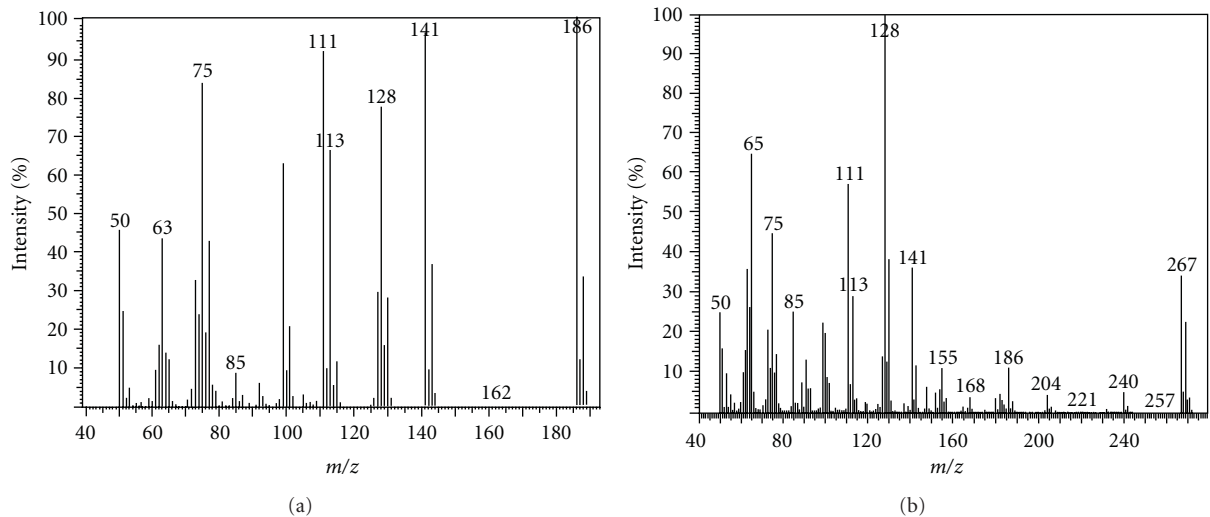


FIGURE 3: Direct injection mass spectra for 4-chlorophenoxyacetic acid, 4CPA (a), and its nanohybrid, ZCPA (b).

and 0.10 M 4CPA was used, respectively, in the synthesis, compared to 19.03 Å when 0.20 M 4CPA was used (see Figure 1) with 4, 3, and 5 harmonics, respectively. This confirmed the formation of layered nanohybrids in which ZnO under an aqueous environment was transformed into a metal layered hydroxide, and at the same time, the intercalation of the 4CPA anion into the interlayer of the zinc-layered hydroxide took place.

It is believed that a “dissociation-deposition” mechanism governs the formation of the nanohybrid synthesised by a direct reaction between 4CPA and ZnO under an aqueous environment. ZnO was first hydrolysed followed by the formation of Zn(OH)₂ on the surface of solid particles. The formation of Zn(OH)₂ then subsequently formed thin layers on the oxide particle surfaces. The dissociation of Zn(OH)₂ occurred at the solution-solid interface and formed Zn²⁺

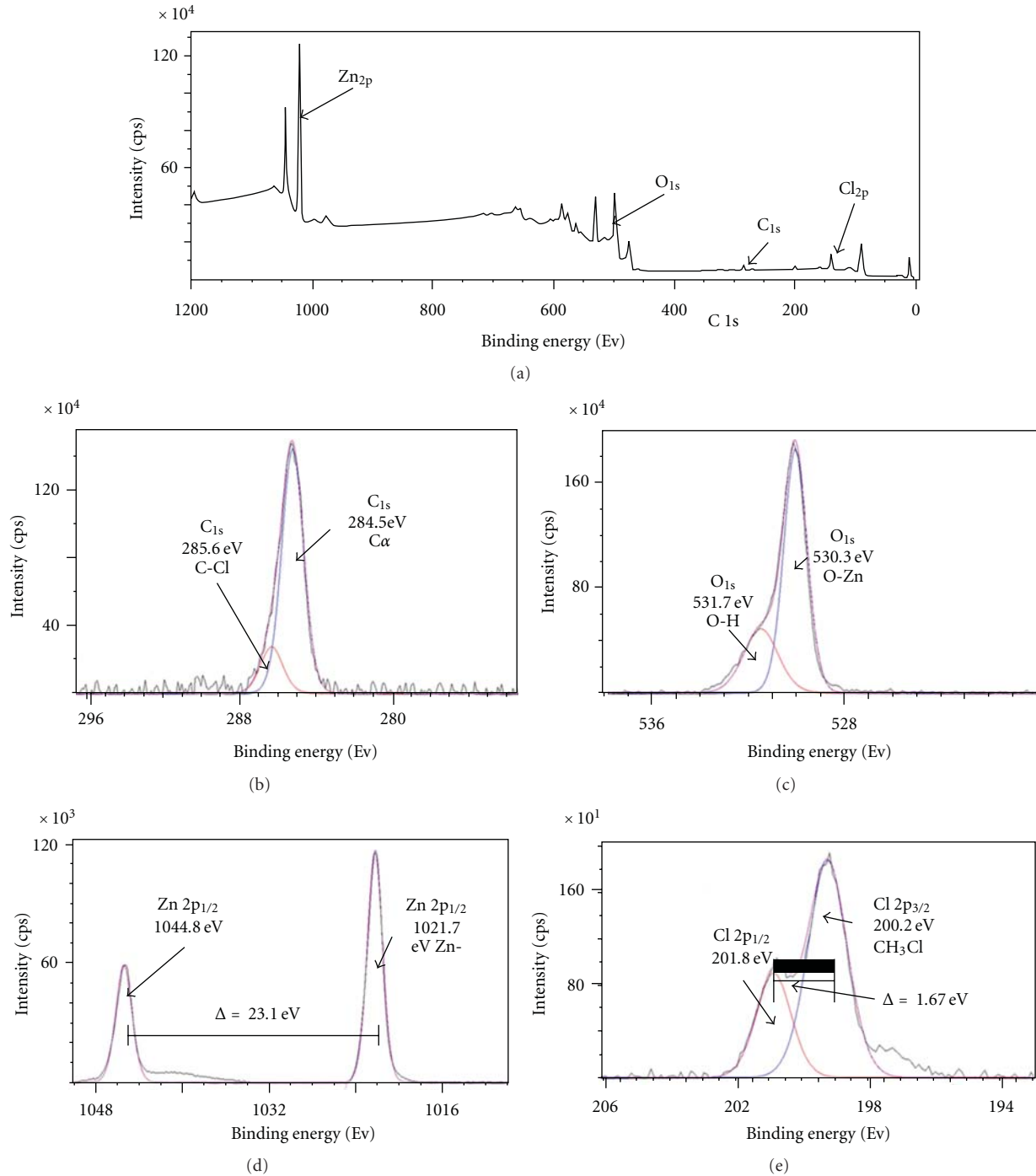


FIGURE 4: Wide (a) and narrow scan of XPS spectra of the nanohybrid, ZCPA for C_{1s} (b), O_{1s} (c), Zn_{2p} (d), and Cl_{2p} (e).

species. This species was then reacted with the hydroxyl group of 4CPA anions and water in solution, to generate the layered ZCPA nanohybrid. As a result, a nanolayered hybrid in which 4CPA was intercalated into the interlayer of zinc-layered hydroxides was formed [20]. Also, shown in Figure 1, ZCPA nanohybrids synthesised using 0.10 and 0.20 M 4CPA showed a relatively purer phase than the one synthesised at 0.05 M. The latter showed the presence of ZnO, indicated by an incomplete reaction which resulted in the remaining ZnO

phase. In contrast, no ZnO phase could be observed for the nanohybrids prepared at 0.10 M and 0.20 M 4CPA, indicating that a complete reaction between the 4CPA anion and ZnO had taken place. As a result, the formation of phase pure zinc-layered hydroxide nanohybrid in which the 4CPA anion was completely intercalated into the inorganic interlayer host could be observed. The PXRD pattern of ZCPA synthesised at 0.20 M 4CPA showed a well-ordered nanolayered hybrid with up to five harmonics, from which the average basal spacing

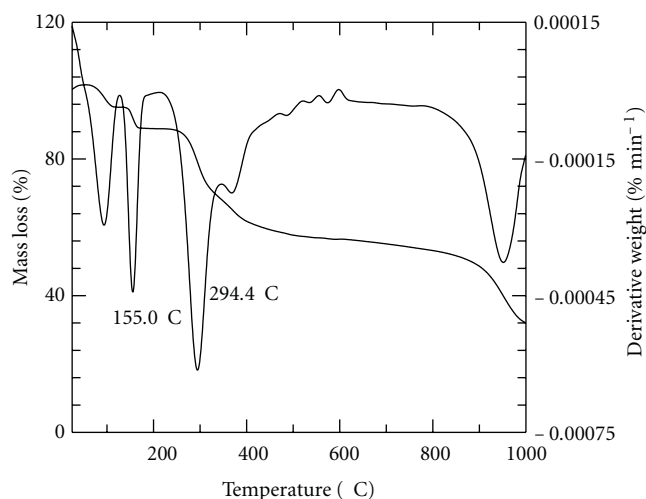


FIGURE 5: TGA/DTG thermogram of the ZCPA nanohybrid.

of 19.03 Å of the material was deduced, showing a long-range order of the layer packing. The basal spacing was very similar to that of the 4CPA-Zn/Al-LDH nanohybrid, which is 20.1 Å [21].

3.2. Fourier Transform Infrared. Figure 2 shows the FTIR spectra of ZnO, 4CPA, and ZCPA. The FTIR spectrum of pure ZnO showed a band at 382 cm^{-1} , which was due to zinc-oxygen sublattices [22]. For 4CPA, a broad absorption band at 3102 cm^{-1} was due to O–H stretching vibration of the hydrogen-bonded and nonhydrogen-bonded hydroxyl groups from the hydroxide layers and interlayer water in 4CPA. The band at 2911 cm^{-1} was due to the presence of C–H stretching vibrations of aromatic compounds. In addition, H–O–H bending vibration in 4CPA could be observed at 1873 cm^{-1} and a sharp, strong, and distinct band at 1705 cm^{-1} indicated the C=O functional group. Both bands at 1487 cm^{-1} and 1426 cm^{-1} were attributed to the C=C stretching vibration of the aromatic ring. The C–O–C stretching vibration was observed at 1230 cm^{-1} and a band at 703 cm^{-1} was due to the C–Cl stretching vibration.

As shown in the figure, the nanohybrid ZCPA showed a broad absorption band at 3458 cm^{-1} which corresponded to the O–H stretching vibration due to adsorbed and/or interlayer water. The band at 2970 cm^{-1} was due to the C–H stretching vibration of the aromatic group while the H–O–H bending vibration for ZCPA was observed at 1888 cm^{-1} . A band at 1547 cm^{-1} was due to the stretching vibration of aromatic compounds. Bands at 1487 cm^{-1} and 1409 cm^{-1} were attributed to the C=C stretching vibration of the aromatic ring. Furthermore, the C–O–C stretching vibration was observed at 1220 cm^{-1} and a band at 713 cm^{-1} corresponded to the C–Cl stretching band.

The FTIR spectrum of the ZCPA nanohybrid generally showed characteristic bands, indicating the contribution of 4CPA and ZnO. These data demonstrate that the 4CPA anion had been intercalated into the interlayer of ZLH. However, some of the bands shown were slightly shifted in position, which indicated the existence of interactions between the

4CPA anionic guest and the ZLH host as a result of the formation of new bonds due to the intercalation process.

3.3. Organic Content, XPS, MS, and Thermal Studies. The organic loading of the ZCPA nanohybrid gave an indication of the degree of intercalation of 4CPA, $\text{C}_8\text{H}_6\text{ClO}_3$. If only adsorption of 4CPA occurred, then the XRD pattern of the resulting material should have been composed of the component phases separately, ZnO and 4CPA. The carbon and hydrogen contents of 4CPA and ZCPA nanohybrid obtained by CHNS analysis are shown in Table 1. The results show that 4CPA contained 51.2% carbon compared to 21.9% for the nanohybrid, ZCPA. Therefore, the loading percentage of 4CPA in the nanohybrid of ZCPA was estimated to be 45.4% (w/w). This result also confirmed the intercalation episode of the 4CPA anion into the inorganic interlayer of ZLH. Otherwise, adsorption of 4CPA occurred, resulting in the observation of the 4CPA phase in the resulting XRD patterns.

In order to confirm that the organic moiety that was actually intercalated into the ZLH interlamellae was 4CPA, the direct injection mass spectra (DIMS) were studied. The DIMS of 4CPA (Figure 3) showed major peaks at m/z values of 186, 141, 128, 111, 75, 50, and 28 and similar peaks could be also observed for the nanohybrid, ZCPA. The molecular ion at m/z 186 and 267 corresponded to the molecular formula of 4CPA ($\text{C}_8\text{H}_7\text{ClO}_3$) and $\text{C}_8\text{H}_6\text{ClO}_3\text{-ZnO}$, respectively. The latter particularly showed the formation of a bond between 4CPA and Zn–O in the ZLH. Again, this demonstrated that the intercalation of 4CPA into ZLH had been successfully accomplished and confirmed the formation of the ZCPA nanohybrid in which the 4CPA organic moiety was bound with the inorganic ZLH cation, Zn, in the interlamellae of ZLH.

XPS spectra of ZCPA nanohybrid are given in Figure 4 and the analysis is presented in Table 1. Generally, expected elements such as C, O, Zn, and Cl were detected from a wide scan of the photoelectron peaks of the C_{1s} , O_{1s} , Zn_{2p} , and Cl_{2p} spectra of the sample. The related binding energies were compared with references for their elemental chemical states [23]. Carbon (C_{1s}) was observed mainly as a terminal hydrocarbon ($\text{C}_{1s} = 284.5\text{ eV}$) and C–Cl from 4CPA. Oxygen (O_{1s}), observed at 530.3 and 531.7 eV was due to Zn–O and –OH, respectively. There was only one chemical state of Zn ($\text{Zn}_{2p_{3/2}}$) at 1021.7 eV that could be observed in the XPS spectrum, which could be attributed to the Zn of Zn–O–H. Chlorine ($\text{Cl}_{2p_{3/2}}$) in the form of a single organochlorine was observed at a binding energy of 200.26 eV, which was expected from the 4CPA compound. In general, all the expected elements and their chemical states were in agreement with the assumption that organocompounds were bonded to Zn. This shows that the organic moiety, 4CPA was directly bonded to Zn, and that it was intercalated between ZLH interlayers in agreement with the DIMS study.

Thermogravimetric analysis of 4CPA showed a strong, intense, and sharp peak at a temperature maximum of 243.5°C with weight loss of 97.5% (Table 1). This corresponded to complete decomposition of the organic

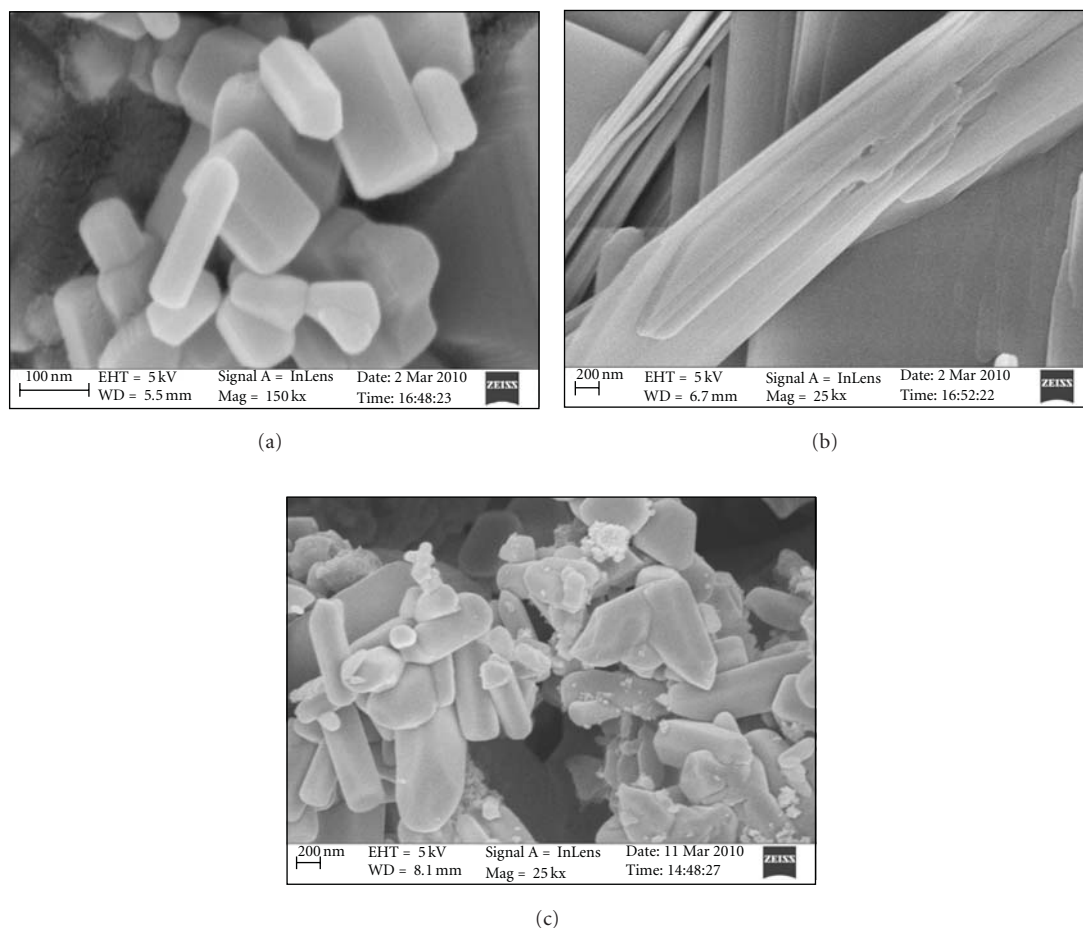


FIGURE 6: Field emission scanning electron micrographs of ZnO (a), the nanohybrid (b), and the nanohybrid heated at 500°C for 5 h (c).

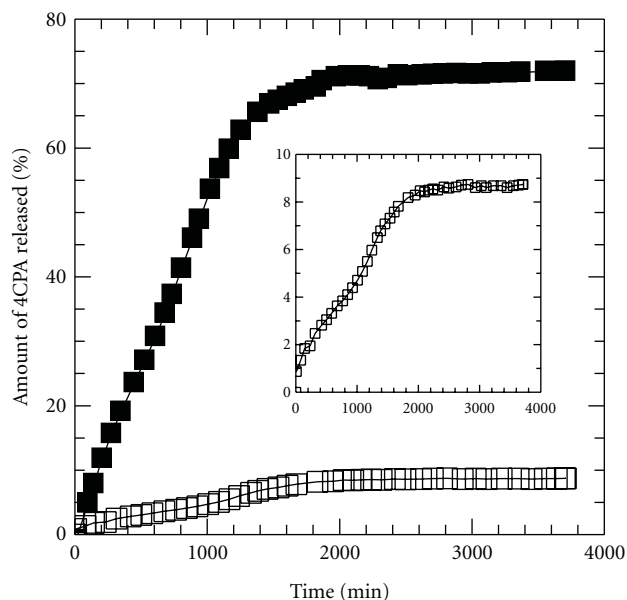


FIGURE 7: Release profiles of 4CPA from the interlamellae of the ZCPA nanohybrid into Na₂CO₃ aqueous solutions, 0.001 M (opened symbol, also, shows in the inset with y-axis expanded) and 0.002 M (closed symbol).

compound, 4CPA. For ZCPA, there were four intense and sharp peaks that could be seen clearly. The first temperature maximum was at 92.6°C with a weight loss of 6.8%. This was due to the removal of surface physisorbed water molecules. The weight loss of 6.2% at 155.0°C was attributed to the removal of interlayer anions and dehydroxylation of the hydroxyl layer. About 30.1% weight loss at 294.4°C was due to the decomposition of the intercalated organic moiety, the 4CPA anion, between the inorganic-ZLH layers (Figure 5).

The thermal study showed that 4CPA intercalated into the inorganic host, ZLH was thermally more stable than its counterpart in the nonintercalated form. TGA/DTG thermograms of ZnO showed that it was a very stable compound thermally with weight loss of 0.9% at 100.6°C, attributed to surface-adsorbed water molecule from the atmosphere.

3.4. Surface Morphology and Surface Area. Field emission scanning electron microscope (FESEM) was used to study the surface morphology of the materials. The surface morphology of ZnO showed well-defined hexagonal and square-like structures with various shapes and sizes at the nanometre scale. This structure was transformed into a thin, sheet-like structure when the ZCPA nanohybrid was formed

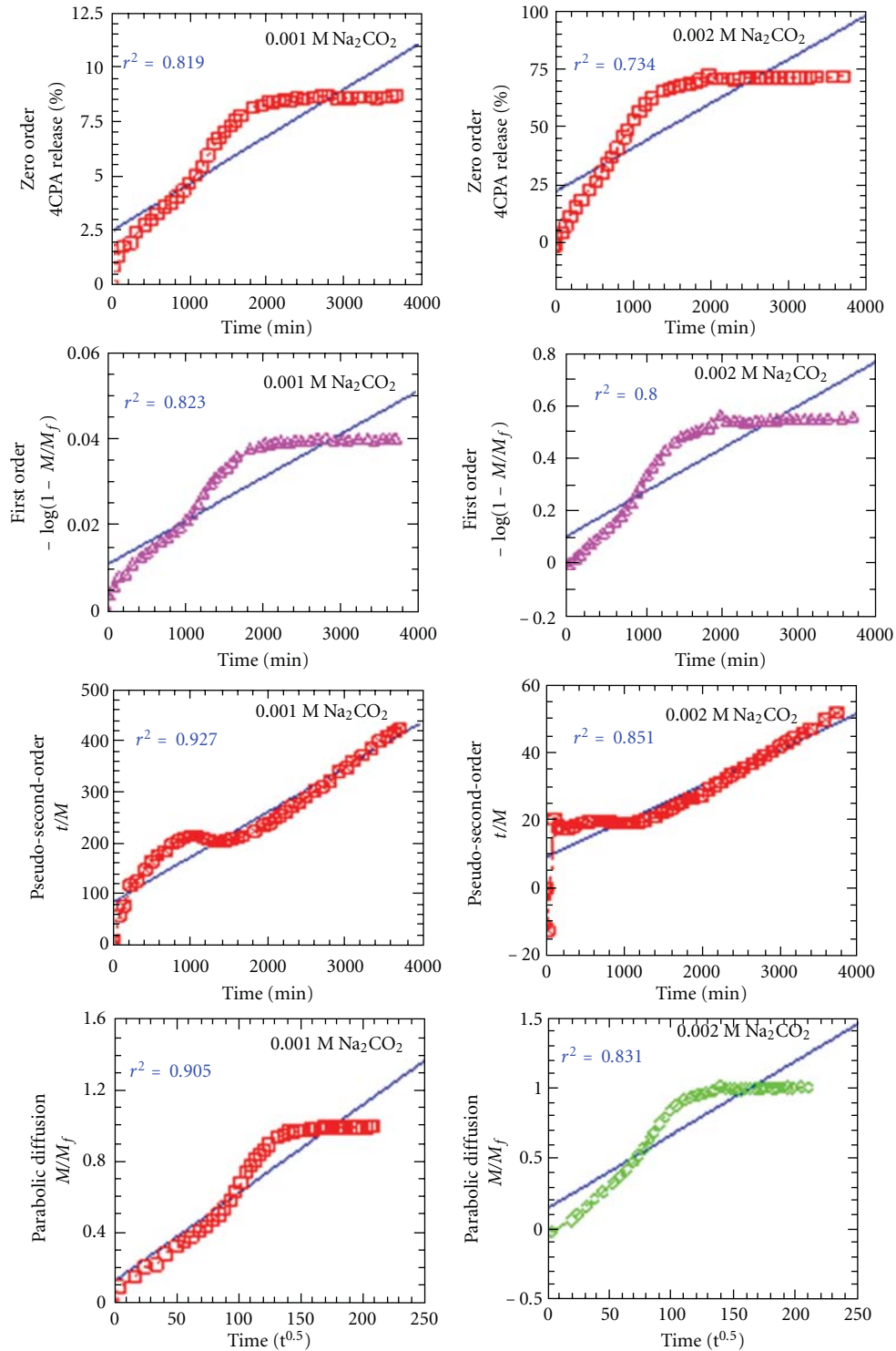


FIGURE 8: Fitting of the data of 4CPA released from the nanohybrid into Na_2CO_3 aqueous solutions to the zeroth-, first-, pseudo-second-order, and parabolic diffusion using 0.001 M and 0.002 M.

by a direct reaction of ZnO with 4CPA under an aqueous environment, as shown in Figure 6. This showed that the intercalation of 4CPA into the interlayer of zinc-layered hydroxide resulted in a change of the surface morphology from a well-defined fine hexagonal- and square-like structure

to a thin, sheet-like structure with a thickness in the nanometre range. This is slightly different compared to the rosette-like structure that has been observed for the [4-(2,4-dichlorophenoxybutyrate)-zinc-layered hydroxide] nanohybrid [23].

When the ZCPA nanohybrid was calcined at 500°C for 5 h, the structure of thin, sheet-like nanostructures was transformed back to the original ZnO structure (Figure 6(c)) reverting back to the irregular hexagonal- and square-like structure. This indicated that the organic moiety, 4CPA, intercalated into the interlayer of inorganic ZLH and was completely decomposed by heating at 500°C. At the same time, the Zn component was oxidised, resulting in the formation of ZnO.

The BET surface area was measured for ZnO and ZCPA by the gas adsorption technique and the surface areas were determined to be 4 and 6 m²/g, respectively, (Table 1). Relative to ZnO, the intercalation resulted in an increase of the BET-specific surface area by about 50%. This is in agreement with the formation of mesopores (Type IV isotherm) created by the formation of a layered ZCPA nanohybrid.

3.5. Controlled Release and Kinetics. Figure 7 shows the release profiles of 4CPA from the interlamellae of the ZCPA nanohybrid into 0.001 and 0.002 M Na₂CO₃ aqueous solutions. As shown in the figure, the accumulated 4CPA released into the aqueous solution increased with contact time when ZCPA was placed in the aqueous solutions. For the 0.002 M Na₂CO₃ solution, the release rate was found to be rapid for the first 1400 minutes, followed by a sustained release thereafter. Equilibrium was achieved at around 1685 minutes with 65% of the 4CPA released from the interlayer of ZCPA. On the other hand, for the 0.001 M Na₂CO₃ aqueous solution, the amount of 4CPA released was found to be about 12% with a rapid release rate for the first 1450 minutes, followed by a slow release thereafter. Equilibrium was achieved at 1720 minutes. This result indicates that the higher the concentration of aqueous solution used, the higher the percentage release of 4CPA from the interlamellae of ZCPA nanohybrid. This was due to the higher concentration of carbonate from the aqueous solution to be ion-exchanged with 4CPA from the interlamellae of ZCPA nanohybrid material.

The release kinetics of 4CPA from the interlamellae of ZLH were evaluated using various kinetics models, namely, zeroth-, first-, pseudo-second order, as well as parabolic diffusion equations (Table 1).

An attempt was made to fit the data for 4CPA release into these equations, and the obtained results are shown in Figure 8. Linear regression (r^2) showed that a pseudo-second-order kinetic model fit better than the other models used in this work with an r^2 value of 0.927 and 0.851 for 0.001 M and 0.002 M sodium carbonate, respectively. This shows that the release of the organic moiety from the inorganic ZLH interlamellae involved the dissolution of the nanohybrid as well as ion exchange between the intercalated anions in the interlamellae host and the carbonate anions in the aqueous solution which was controlled by pseudo-second-order kinetics. These results are very similar to the results of a previous study [21].

4. Conclusions

An organic-inorganic nanohybrid of zinc-layered hydroxide-4-chlorophenoxyacetate can be prepared using a simple direct reaction of the 4CPA anion with ZnO under an aqueous environment. The concentration of 4CPA was found to be a controlling factor in determining the formation of a pure phase, well-ordered nanolayered hybrid material. The nanohybrid showed a controlled release property, and the release was governed by pseudo-second-order kinetics. Therefore, such a material could be used as a controlled release formulation of herbicides.

Acknowledgments

Funding for this research was provided by the Ministry of Higher Education of Malaysia (MOHE) under the FRGS Grant no. 02-11-08-615FR. N. F. Nazarudin thanks Jabatan Perkhidmatan Awam Malaysia for the scholarship.

References

- [1] F. Cavani, F. Trifirò, and A. Vaccari, "Hydrotalcite-type anionic clays: preparation, properties and applications," *Catalysis Today*, vol. 11, no. 2, pp. 173–301, 1991.
- [2] G. G. C. Arizaga, K. G. Satyanarayana, and F. Wypych, "Layered hydroxide salts: synthesis, properties and potential applications," *Solid State Ionics*, vol. 178, no. 15–18, pp. 1143–1162, 2007.
- [3] S. Hamada, S. Hibarino, K. Ikeue, and M. Machida, "Preparation of supported Pt-M catalysts (M = Mo and W) from anion-exchanged hydrotalcites and their catalytic activity for low temperature NO-H₂-O₂ reaction," *Applied Catalysis B*, vol. 74, no. 3–4, pp. 197–202, 2007.
- [4] C. S. Cordeiro, G. G. C. Arizaga, L. P. Ramos, and F. Wypych, "A new zinc hydroxide nitrate heterogeneous catalyst for the esterification of free fatty acids and the transesterification of vegetable oils," *Catalysis Communications*, vol. 9, no. 11–12, pp. 2140–2143, 2008.
- [5] P. Nalawade, B. Aware, V. J. Kadam, and R. S. Hirlekar, "Layered double hydroxides: a review," *Journal of Scientific and Industrial Research*, vol. 68, no. 4, pp. 267–272, 2009.
- [6] L. Poul, N. Jouini, and F. Fievet, "Layered hydroxide metal acetates (metal = zinc, cobalt, and nickel): elaboration via hydrolysis in polyol medium and comparative study," *Chemistry of Materials*, vol. 12, no. 10, pp. 3123–3132, 2000.
- [7] M. J. Masarudin, K. Yusoff, R. A. Rahim, and M. Z. Hussein, "Successful transfer of plasmid DNA into in vitro cells transfected with an inorganic plasmid-Mg/Al-LDH nanobiocomposite material as a vector for gene expression," *Nanotechnology*, vol. 20, no. 4, Article ID 045602, 2009.
- [8] V. Ambrogi, G. Fardella, G. Grandolini, and L. Perioli, "Intercalation compounds of hydrotalcite-like anionic clays with antiinflammatory agents-I. Intercalation and in vitro release of ibuprofen," *International Journal of Pharmaceutics*, vol. 220, no. 1–2, pp. 23–32, 2001.
- [9] H. Zhang, K. Zou, S. Guo, and X. Duan, "Nanostructural drug-inorganic clay composites: structure, thermal property and in vitro release of captopril-intercalated Mg-Al-layered double hydroxides," *Journal of Solid State Chemistry*, vol. 179, no. 6, pp. 1792–1801, 2006.

- [10] M. Z. B. Hussein, N. Hashim, A. H. Yahaya, and Z. Zainal, "Controlled release formulation of agrochemical pesticide based on 4-(2,4-dichlorophenoxy)butyrate nanohybrid," *Journal of Nanoscience and Nanotechnology*, vol. 9, no. 3, pp. 2140–2147, 2009.
- [11] M. Z. Hussein, A. M. Jaafar, A. H. Yahaya, and Z. Zainal, "The effect of single, binary and ternary anions of chloride, carbonate and phosphate on the release of 2,4-dichlorophenoxyacetate intercalated into the Zn-Al-layered double hydroxide nanohybrid," *Nanoscale Research Letters*, vol. 4, no. 11, pp. 1351–1357, 2009.
- [12] M. Z. Bin Hussein, Z. Zainal, A. H. Yahaya, and D. W. V. Foo, "Controlled release of a plant growth regulator, α -naphthaleneacetate from the lamella of Zn-Al-layered double hydroxide nanocomposite," *Journal of Controlled Release*, vol. 82, no. 2-3, pp. 417–427, 2002.
- [13] M. Z. B. Hussein and C. W. Long, "Synthesis of organo-mineral nanohybrid material: indole-2-carboxylate in the lamella of Zn-Al-layered double hydroxide," *Materials Chemistry and Physics*, vol. 85, no. 2-3, pp. 427–431, 2004.
- [14] M. Z. B. Hussein, S. H. Sarijo, A. H. Yahaya, and Z. Zainal, "Synthesis of 4-chlorophenoxyacetate-zinc-aluminium-layered double hydroxide nanocomposite: physico-chemical and controlled release properties," *Journal of Nanoscience and Nanotechnology*, vol. 7, no. 8, pp. 2852–2862, 2007.
- [15] W. Stählin and H. R. Oswald, "The crystal structure of zinc hydroxide nitrate, $Zn_5(OH)_8(NO_3)_2 \cdot 2H_2O$," *Acta Crystallographica*, vol. 26, pp. 860–863, 1970.
- [16] S. M. Lu and S. F. Lee, "Slow release of urea through latex film," *Journal of Controlled Release*, vol. 18, no. 2, pp. 171–180, 1992.
- [17] M. A. Teixeira, W. J. Paterson, E. J. Dunn, Q. Li, B. K. Hunter, and M. F. A. Goosen, "Assessment of chitosan gels for the controlled release of agrochemicals," *Industrial and Engineering Chemistry Research*, vol. 29, no. 7, pp. 1205–1209, 1990.
- [18] G. G. Allan, C. S. Chopra, A. N. Neogi, and R. M. Wilkins, "Design and synthesis of controlled release pesticide-polymer combinations," *Nature*, vol. 234, no. 5328, pp. 349–351, 1971.
- [19] L. P. Cardoso, R. Celis, J. Cornejo, and J. B. Valim, "Layered double hydroxides as supports for the slow release of acid herbicides," *Journal of Agricultural and Food Chemistry*, vol. 54, no. 16, pp. 5968–5975, 2006.
- [20] Z. Xingfu, H. Zhaolin, F. Yiqun, C. Su, D. Weiping, and X. Nanping, "Microspheric organization of multilayered ZnO nanosheets with hierarchically porous structures," *Journal of Physical Chemistry C*, vol. 112, no. 31, pp. 11722–11728, 2008.
- [21] S. H. Sarijo, M. Z. Hussein, A. H. J. Yahaya, and Z. Zainal, "Effect of incoming and outgoing exchangeable anions on the release kinetics of phenoxyherbicides nanohybrids," *Journal of Hazardous Materials*, vol. 182, no. 1–3, pp. 563–569, 2010.
- [22] R. Muñoz-Espí, A. Chandra, and G. Wegner, "Crystal perfection in zinc oxide with occluded carboxyl-functionalized latex particles," *Crystal Growth and Design*, vol. 7, no. 9, pp. 1584–1589, 2007.
- [23] X-ray Photoelectron Spectroscopy (XPS) Database, 2010, <http://srdata.nist.gov/xps/selectEnergyType.aspx>.

Research Article

Engineered Hybrid Scaffolds of Poly(vinyl alcohol)/Bioactive Glass for Potential Bone Engineering Applications: Synthesis, Characterization, Cytocompatibility, and Degradation

Hermes S. Costa, Alexandra A. P. Mansur, Marivalda M. Pereira, and Herman S. Mansur

Laboratory of Biomaterials and Tissue Engineering, Department of Metallurgical and Materials Engineering, School of Engineering, Federal University of Minas Gerais, Avenida Antônio Carlos 6627, 31270-901 Belo Horizonte, MG, Brazil

Correspondence should be addressed to Herman S. Mansur, hmansur@demet.ufmg.br

Received 31 July 2011; Revised 1 September 2011; Accepted 1 September 2011

Academic Editor: Shanfeng Wang

Copyright © 2012 Hermes S. Costa et al. This is an open access article distributed under the Creative Commons Attribution License, which permits unrestricted use, distribution, and reproduction in any medium, provided the original work is properly cited.

The synthesis, characterization, preliminary cytocompatibility, and degradation behavior of the hybrids based on 70% Poly(vinyl alcohol) and 30% bioactive glass (58SiO₂-33CaO-9P₂O₅, BaG) with macroporous tridimensional structure is reported for the first time. The effect of glutaraldehyde covalent crosslinker in the organic-inorganic nanostructures produced and, as a consequence, tailoring the hybrids properties was investigated. The PVA/BaG hybrids scaffolds are characterized by Fourier transform infrared spectroscopy (FTIR), scanning electron microscopy (SEM), X-ray diffraction (XRD), and X-ray Microcomputed tomography analysis (μ CT). Cytotoxicity assessment is performed by the MTT method with VERO cell culture. Additionally, the hybrid *in vitro* degradation assay is conducted by measuring the mass loss by soaking in deionized water at 37°C for up to 21 days. The results have clearly shown that it is possible to modify the PVA/BaG hybrids properties and degradation behavior by engineering the structure using different concentrations of the chemical crosslinker. Moreover, these hybrid crosslinked nanostructures have presented 3D hierarchical pore size architecture varying within 10–450 μ m and a suitable cytocompatibility for potential use in bone tissue engineering applications.

1. Introduction

Essentially, the aim of tissue engineering is to restore diseased or damaged tissue to its original state and function, reducing the need for transplants and joint replacements. One of the challenges in tissue engineering is associated with the development of suitable scaffold materials that can act as templates for cell adhesion, growth, and proliferation [1–3]. More specifically, bone tissue engineering combines cells and biodegradable 3D scaffolds to repair bone tissues. The scaffolds must present an adequate pore size and interconnectivity to promote cell ingrowth, good biocompatibility, and controlled degradation kinetics to match the ratio of replacement by new tissue. Also, the scaffolds should provide an initial biomechanical support until cells generate the extracellular matrix. During the formation, deposition, and organization of that matrix, the scaffold is continuously

degraded and metabolized. Thus, the degradation behavior of the produced scaffold is a critically important requirement to be used in tissue engineering applications [3–11]. Nevertheless, most attention has been paid to the synthesis and characterization of the material structure and properties, but comparatively few reports have dealt with the degradation kinetics of the entire system [3–11]. In the last 2–3 decades, a variety of biomaterials have been developed to act as synthetic scaffolds that may guide and stimulate the three-dimensional tissue growth [3–14]. Among them, bioactive glasses and related biomaterials have been mostly studied for bone tissue engineering due to their recognized osteoconductive and osteoinductive properties [15–22]. Furthermore, the dissolution products of bioactive glass exert control over genetic factors of bone growth [23]. However, bioactive glasses, compared to cortical and cancellous bones, usually present low mechanical properties, especially in porous

forms [10, 18]. This disadvantage significantly restricts the use of these materials in a very broad range of applications. Fortunately, one solution came from mimicking nature, which provides the inspiration to design materials and systems with highly organized structures under dynamically changing conditions. Many of these structures are composed of an intrinsically complex matrix based on organic and inorganic components which produce a natural hybrid material, usually referred to as composites (or nanocomposites). By combining two or more materials in a predesigned manner, a system can be created with properties that are not possible to be attained when considering each of the individual components separately. In addition, the modification of the surface has been used as an alternative route for producing materials with very specific properties for biological applications such as immune diagnosis and protein recognition [24–26]. The development of inorganic-organic composites attempts to create a balance between strength and toughness, in turn improving the characteristics commonly found in the individual components [27]. These composites can be synthesized through a hybridization route, in which two or more components, usually organic and inorganic, are combined [28]. Sol-gel technology allows for the incorporation of polymers of different natures within an inorganic silica bulk, thus producing organic-inorganic hybrid materials [28–31]. Among several choices of polymers, poly(vinyl alcohol) (PVA), a hydrophilic semicrystalline polymer, has been frequently explored as an implant material in wide array of biomedical applications such as drug delivery systems, membranes, wound dressings, artificial skin, and surgical repairs, mainly due to its excellent mechanical strength, biocompatibility, and nontoxicity [32, 33]. PVA is produced by the polymerization of vinyl acetate to poly(vinyl acetate) (PVAc), and successive hydrolysis to PVA. This reaction, however, is incomplete, resulting in polymers with different degrees of hydrolysis (DH), that is, a copolymer of poly(vinyl alcohol) and poly(vinyl acetate) referred to as poly(vinyl alcohol-co-vinyl acetate). The degree of hydrolysis in PVA affects its physical-chemical properties, such as solubility, hydrophilic/hydrophobic interactions, pH-sensitivity, and viscosity. Additionally, PVA can be crosslinked under acid conditions producing hydrogels with a wide range of swelling and degradation properties for biomedical applications [34].

Recently, hybrid organic-inorganic scaffolds in the poly(vinyl alcohol)/bioactive glass (PVA/BaG) system have been prepared through the sol-gel process [30, 35–38], by hydrolysis of tetraethyl orthosilicate in the presence of an acid solution and a subsequent addition of calcium chloride. A solution of PVA, surfactant, and hydrofluoric acid were added to the sol, and the mixture vigorously agitated until the foam had formed. The foam was placed in containers, where gelation occurred, and subsequently dried at low temperatures to avoid polymer thermal degradation. They usually contain unreacted species that may cause some cytotoxicity. This concern was also addressed in previous works in which potentially toxic species remaining within the hybrid structure were blocked by immersion in buffered solutions [37, 38]. Afterward, focusing on applying these materials in tissue

engineering, it is crucial to control their degradation behavior based on the designed nanostructure. A versatile method to obtain biomaterials with controlled degradation rates involves the chemical crosslinking of the polymer network [34]. Recent results have demonstrated that an appropriate breakdown of the synthetic biomaterial, as compared to nondegradable hydrogel constructs, can improve healing and increase tissue functions [39]. In addition, the ability to alter physical properties, such as porosity, permeability, and mechanical strength of degradable hydrogels and hybrids, is an integral part of biomaterials design, as they influence cellular growth required for tissue engineering applications [40].

As previously mentioned, our research group has been very active in studying the synthesis and characterization of hybrids based on PVA-modified polymeric networks [25, 30, 35–38, 41] to be used as scaffolds aimed at tissue engineering applications. Nevertheless, to the best of our knowledge, no research has been published which addresses the degradation behavior of hybrids made of polymer (PVA) and bioceramic (bioactive glass, BaG) with a rather complex nanostructured network. This approach was used in this work in an attempt to modulate the chemical stability of PVA/BaG hybrids. Thus, the main objective of this study was to develop novel organic-inorganic hybrids with different degrees of chemical crosslinking of their nanostructures and characterize the effect on their properties and preliminary degradation behavior.

2. Materials and Methods

2.1. Preparation of Hybrid Samples. The processing route used for synthesizing the inorganic-organic hybrids was based on PVA and sol-gel-derived bioactive glass (BaG) as illustrated in Figure 1. The PVA was selected (Aldrich-Sigma) considering key aspects such as the degree of hydrolysis (DH = 80%) and molecular weight ($M_w = 9,000\text{--}10,000\text{ g/mol}$) appropriate for biomedical purposes. Deionized water (DI-water, Millipore Simplicity) with resistivity of $18\text{ M}\Omega\cdot\text{cm}$ was used in all solution preparations. A PVA aqueous solution was prepared at a 28 wt% concentration by dissolving the PVA powder in a water bath at 80°C under constant stirring for 2 h. The pH of the solution was adjusted to 2.0 ± 0.1 by hydrofluoric acid (HF) 2 N solution.

2.1.1. Preparation of the Starting Bioactive Glass Solution. The synthesis of hybrids based on PVA and inorganic glass has been the subject of investigation of our group in previous reports [30, 36–38]. Here, for clarity sake, just the most relevant parameters will be described. Thus, the starting sol solution with a designed composition of 58 wt% SiO_2 –33 wt% CaO –9 wt% P_2O_5 was synthesized by mixing tetraethoxysilane (TEOS), DI water, triethylphosphate (TEP), and calcium chloride together with the hydrofluoric acid 2 N solution. The $\text{H}_2\text{O}:\text{TEOS}$ molar ratio used was 12 : 1.

2.1.2. Preparation of the PVA-Bioactive Glass Hybrid Foams. The prepared hybrid composition consisted of 30 wt% glass

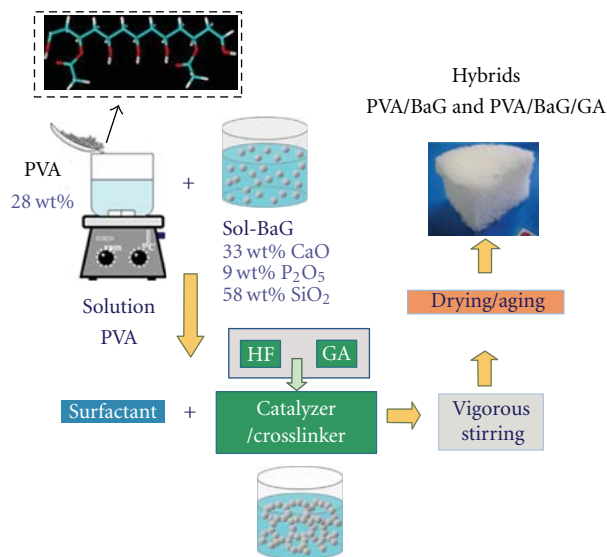


FIGURE 1: Flow chart of the procedure to synthesize PVA/BaG/GA hybrids.

and 70 wt% polymer. The hybrids were obtained using a procedure similar to that described in previous work from our research group [36, 38]. In short, an appropriate amount of the starting glass precursors was added to the PVA solution and stirred for five minutes. The surfactant, sodium laureate sulfate (SLS, Oxiteno 27% v/v) as a foaming agent, and HF 10% v/v solution as a gelling agent were added to the resulting solution. The mixture was foamed by vigorous agitation. The foams were cast shortly before gelation in plastic containers and sealed. The samples were aged at 40°C for 3 days and then dried at 40°C for 7 days. These hybrids were referred to as PVA/BaG samples.

2.1.3. Crosslinking and Stabilization. Glutaraldehyde (GA, Sigma 25 wt% aqueous solution) was used as a bifunctional chemical crosslinker. Calculated amounts of GA were added, resulting in concentrations of 1.0% and 5.0% regarding to the mass of PVA. So, PVA/GA solutions were used to prepare the PVA/BaG/GA samples in a similar procedure as described above for the PVA/BaG foams, as they were casted and dried in the same way. Another set of samples was prepared utilizing a stabilizing step to reduce the acidity of the hybrids that can lead to less cytotoxic biomaterials [29, 30]. Briefly, samples prepared with 5.0% of GA (PVA/BaG/GA-5.0%) were immersed for 10 hours in an NH₄OH solution 0.3 mol·L⁻¹. The neutralization process was carried out based on the proportion of 100 mL of stabilizing solution per 1.0 g of dried hybrid sample at the temperature of 25 ± 2°C. Prior to biological assays, all synthesized samples were washed three times in DI water and dried at room temperature. In the sequence, the hybrids were sterilized with ethylene oxide.

2.2. Structural and Mechanical Characterization of Hybrids

2.2.1. Chemical Characterization by FTIR Spectroscopy. FTIR spectra were obtained within the range 600–4000 cm⁻¹

(Perkin-Elmer, Paragon 1000), using the attenuated total reflectance spectroscopy method (ATR-FTIR). Hybrid samples were placed on the ATR crystal prism (ZnSe), and 64 scans were acquired at 2 cm⁻¹ resolution with the subtraction of background.

2.2.2. Crystallinity and Phase Characterization by X-Ray Diffraction. X-ray diffraction (XRD) patterns were obtained from hybrid PVA/BaG and PVA/BaG/GA using CuK α radiation with $\lambda = 1.54056 \text{ \AA}$ (PHILIPS, PW1710). XRD analyses were conducted in the 2θ range from 3.03 to 89.91° with steps of 0.06°. The major peaks were identified using the “Joint Committee on Powder Diffraction Standards.” Samples for XRD analysis were obtained as films, at a thickness of approximately 100 μm , by pressing 1 mm thick foams.

2.2.3. Scanning Electron Microscopy (SEM). To evaluate the pore morphology and macropore size distribution, SEM images were taken from organic-inorganic hybrids with a JSM 6360LV (JEOL/NORAN) microscope. Prior to examination, samples were coated with a thin gold film by sputtering. Images of secondary electrons (SE) were obtained using an accelerating voltage of 10–15 kV. Pore size distribution analysis was performed using the Quantikov (Version.1.0, Dr. L. C. M. Pinto, CDTN-Brazil) image analysis software.

2.2.4. X-Ray Microcomputed Tomography Analysis (μCT). The structural analysis of cylindrical samples (4 mm diameter) of PVA/BaG/5% GA was performed on a 3D microtomographer (Phoenix X-Ray Systems and Services GmbH), with a 7 mm voxel resolution. The 3D image analysis involved the μCT image conversion from the gray-scale images, according to the proper development and use of mathematical operators, which were developed to verify the sample morphology.

2.2.5. Mechanical Properties. Bones are often submitted to compression stress in the body. It has been broadly accepted by the research community to perform compression assays for evaluating biomaterials for potential use as bone repair. For that reason, the mechanical behavior of the composites was evaluated by compression tests. Specimens were evenly cut from the most homogeneous region of the foam to form blocks measuring 10 × 10 × 10 mm³. These samples were positioned between parallel plates using equipment EMIC DL 3000 and compressed with a crosshead speed of 0.5 mm·min⁻¹ and a 2.0 kN load cell. At least five samples ($n = 5$) of each hybrid system were measured and the results averaged. The elastic modulus was calculated as the slope of the initial linear portion of the stress-strain curve. The yield strength was determined from the cross point of the two tangents on the stress-strain curve at the yield point.

2.3. Degradation Behavior—In Vitro Assay. The extent of the degradation process is usually estimated from measurements of mass loss. Thus, the evaluation of the effect of crosslinking on the degradation behavior of the hybrid foams was performed by measuring the mass loss of samples that had

been chemically modified with different amounts of GA (0%, 1.0%, and 5.0%) upon immersion in water for different time periods. In addition, hybrids previously neutralized with NH_4OH solution were also analyzed (GA = 5.0%). The samples were prepared as discs with dimensions of 40 mm diameter by 2 mm thickness and a diameter/thickness ratio of 20. The solution volume was chosen to provide a surface of circular section/volume at a solution ratio of 0.1 cm^{-1} . Three samples for each composition ($n = 3$) and time period were cut and weighed six times, the average being considered the equilibrium humid mass. Samples were then kept in a desiccator with silica gel for 24 hours under vacuum, at a temperature of $25 \pm 5^\circ\text{C}$. The samples were weighed again, and the procedure was repeated until the equilibrium had been reached. Samples were immersed in DI water and maintained for periods of 2, 7, 14, and 21 days, after which time they were again dried under vacuum and weighed until the equilibrium had been reached. The mass loss was calculated according to

$$\Delta M = \frac{M_{\text{Si}} - M_{\text{Sf}}}{M_{\text{Si}}} \times 100\%, \quad (1)$$

where, M_{Si} is the dried weight before immersion, and M_{Sf} is the dried weight after a given immersion time in the degradation medium.

2.4. Cytotoxicity Assessment—*In Vitro*

2.4.1. MTT Assay. The preliminary cytocompatibility response of the produced hybrids was accessed by the MTT [3-(4,5-dimethylthiazol-2-yl)-2,5-diphenyltetrazolium bromide] assay. The MTT assay was first described by Mosmann in 1983. It is based on the ability of a mitochondrial dehydrogenase enzyme from viable cells to cleave the tetrazolium rings of the pale yellow MTT and form dark blue formazan crystals which is largely impermeable to cell membranes, thus resulting in its accumulation within healthy cells. Solubilization of the cells by the addition of a detergent results in the liberation of the crystals which are solubilized. The number of surviving cells is directly proportional to the level of the formazan product created. The color can then be quantified using a simple colorimetric assay. The results can be read on a multiwell scanning spectrophotometer (ELISA reader) [42, 43].

Thus, hybrid scaffolds disks (diameter = 5 mm, thickness = 2 mm) were presterilized by means of exposure to saturated steam of ethylene oxide before the MTT assay. The cell viability assay was performed in 5 replicates ($n = 5$) for each material. The hybrid samples were placed at the bottom of 96-well standard polystyrene microplates (Sarstedt, USA), soaked in $250 \mu\text{L}$ /well minimum essential medium eagle (MEM), and maintained in an incubator at 37°C with 5% CO_2 for 24 hours. Next, the resulting solutions were extracted from these wells, and the pH was measured (buffered medium, $\text{pH} > 5.5$) before allowing any cell contact. In the sequence, VERO cells (ATCC CCL-81 cell culture isolated from kidney epithelial cells extracted from African green monkeys) at the concentration of 5×10^5 cells/mL

were seeded to the wells in direct contact with the hybrid scaffolds. Similarly, VERO cells were also placed into the microplate wells used as the references, positive and negative controls of the experiments. Triton X-100 (0.1%, v/v) was used as negative control (medium known as highly toxic to cells) and the VERO cell culture as the positive control. Then, MEM medium supplemented with 2 mM L-glutamine and 10% fetal bovine serum (FBS) was added to all the wells, and the system was incubated at 37°C with 5% CO_2 for 24 hours. After that, the supernatant from wells was removed and replaced with $200 \mu\text{L}$ /well of fresh MEM/FBS medium and $30 \mu\text{L}$ /well of MTT reagent. Subsequently, the microplate was reincubated for 4 hours with 5% CO_2 at 37°C and protected from light. After the incubation period, $35 \mu\text{L}$ /well of sodium dodecyl sulfate (SDS) with 10% HCl was added, and the solution was carefully homogenized and reincubated for another 14–16 hours (5% CO_2 , 37°C , protected from light). Finally, the supernatant (clear of sediment or cells) from each well ($V = 100 \mu\text{L}$ /well) was collected and transferred to the respective well of a new blank 96-well microplate where the absorbance was measured at wavelength $\lambda = 595 \text{ nm}$. The absorbance background (empty well from the microplate, with no medium or cells) was subtracted from all readings. To test the significance of the observed differences between the groups, a statistical evaluation was carried out using a one-way analysis of variance (ANOVA) with 95% confidence intervals. The results are expressed as the mean value of 5 replicates \pm standard deviation (SD).

2.4.2. Cell Adhesion-Spreading Assay. Cell viability was evaluated by spreading and attachment assays in order to examine their morphology, adhesion, and spreading behavior. VERO cells were plated at 6×10^4 density on the hosting scaffolds. Cell spreading was evaluated by scanning electron microscopy (SEM, JEOL/Noran, JSM 6360LV) of the specimens after culturing for 2 hours. Before microscopy analysis, samples were fixed with 2% glutaraldehyde for 16 hours and dehydrated by passing through a series of alcohol solutions (crescent ethanol-water, 20%; 50%; 90%; 100% v/v). Then, they were dried in nitrogen flowing reactor for 4 hours and outgassed in vacuum desiccator for 12 hours. Before examination, the samples were sputtered with a thin layer of gold at low deposition rate and placed at the maximum distance from the target to prevent damages. The images were obtained using an accelerating voltage of 10–15 kV.

3. Results and Discussion

3.1. Characterization of Hybrids

3.1.1. Chemical Characterization by FTIR Spectroscopy. Fourier transform infrared spectroscopy (FTIR) was used to characterize the presence of specific chemical groups in the PVA/BaG and PVA/BaG/GA hybrid samples. IR spectra of pure PVA films, bioactive glass (BaG), and the hybrid porous scaffold (PVA/BaG) are summarized in Figure 2(a). These spectra were used as reference for the contribution of each

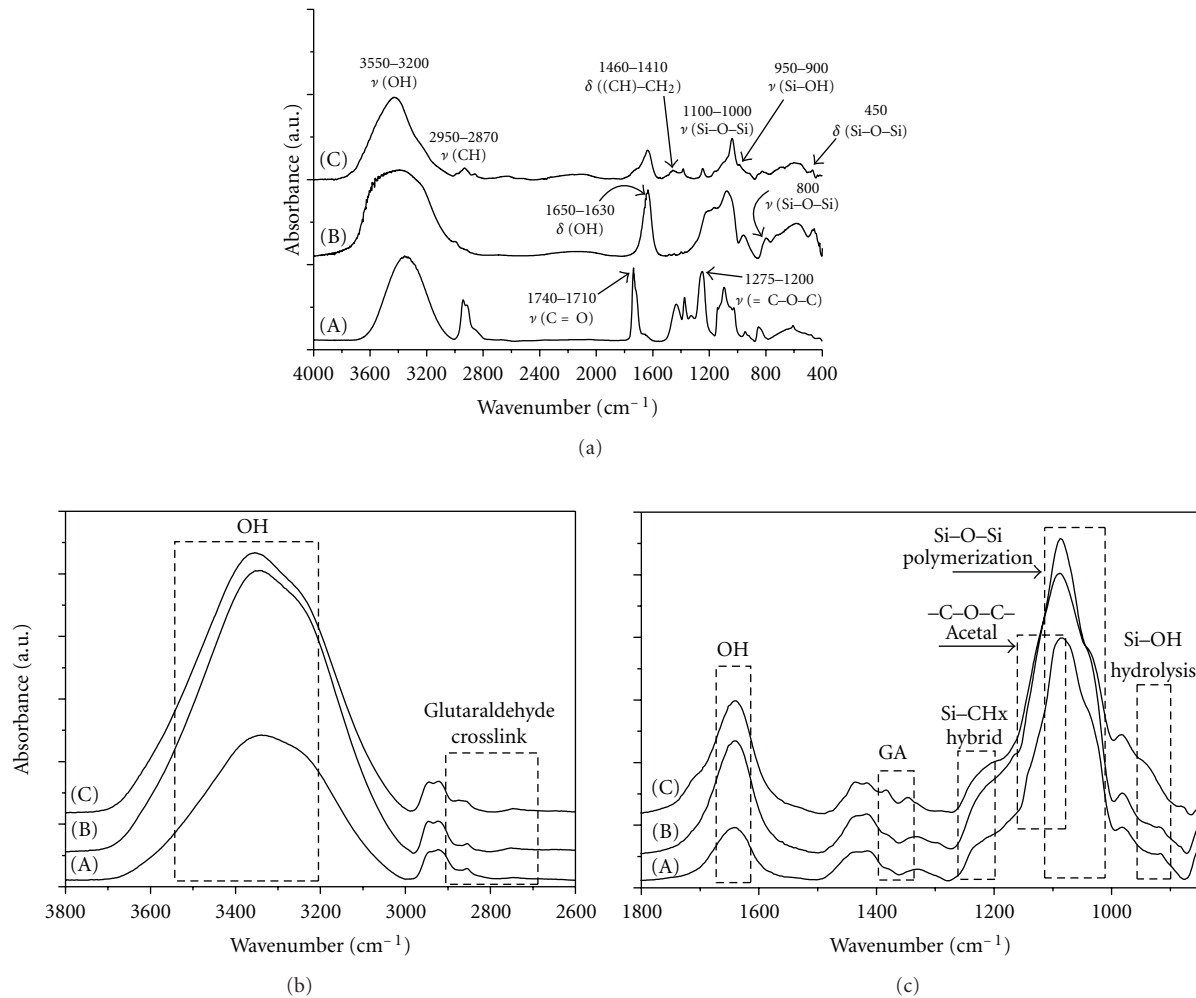


FIGURE 2: (a) FTIR spectra of (A) PVA films; (B) bioactive glass scaffold; (C) hybrid scaffold of PVA/BaG. (b) FTIR spectra range from 3800 to 2600 cm^{-1} of PVA/BaG/GA hybrids (A) uncrosslinked (0%); crosslinked with glutaraldehyde (B) 1.0% and (C) 5.0%. (c) FTIR spectra range from 1800 to 850 cm^{-1} of PVA/BaG/GA hybrids (A) uncrosslinked (0%); crosslinked with glutaraldehyde (B) 1.0% and (C) 5.0%.

and every component on the final produced hybrid network. Hence, the broad band observed from 3200 to 3550 cm^{-1} in the PVA spectra (Figure 2(a)-(A)) may be assigned to hydroxyls (ν OH) stretching due to the strong hydrogen bond of intramolecular and intermolecular type [25, 30, 41, 44]. Also, the strong band at 2870–2950 cm^{-1} was attributed to alkyl stretching mode (ν CH). The absorption bands ranging from 1710 to 1750 cm^{-1} and 1200 to 1275 cm^{-1} arise due to the stretching vibration of carbonyl (ν C=O) and ester, respectively, from the vinyl acetate group found in partially hydrolyzed PVA polymer (DH = 80%). Some other peaks which can be found related to PVA are located at 1410–1460 cm^{-1} assigned to δ (CH)CH₂; 1200–1270 cm^{-1} of group ν (C–O)–C–OH; 820–850 cm^{-1} from alkyl chain backbone [25, 30, 41, 44]. In an analogous analysis, the FTIR spectrum of the bioactive glass (BaG, Figure 2(a)-(B)) presented the bands related to Si–O–Si asymmetric and symmetric stretching modes at approximately 1100 cm^{-1} and 800 cm^{-1} , respectively [45–48]. A characteristic absorption band observed in silica gel is located at 1640 cm^{-1} and is

attributed to the deformation mode of adsorbed molecular water in the pores [45, 46]. Also, the vibrational band at 900–950 cm^{-1} has been credited to the presence of silanol groups (Si–OH) usually found in silica synthesized via sol-gel method. The overall contribution of major groups from each component on the hybrid network can be identified in Figure 2(a)-(C). The FTIR spectrum has presented broad bands in the frequency ranging from 3100 to 3650 cm^{-1} attributed to both contributions of hydroxyls (PVA) and silanols (BaG). There is an overlapping of the bands in the range from 900 to 1500 cm^{-1} derived from the bioactive glass and the PVA components [25, 30, 41, 44]. It is worth noting that the hybrid formation leads to the broadening of the bands related to vinyl acetate copolymer, that almost disappear as a consequence of the hydrogen bonds involving C=O groups and silanol groups in silicate networks [49].

The FTIR spectra of PVA/BaG hybrids before (curve (a)) and after chemical crosslinking with glutaraldehyde (1.0%, curve (b); 5.0%, curve (c)) are shown in Figures 2(b) and 2(c). The effect of the GA crosslinker was highlighted in

different regions of the spectra presented in Figure 2(b). The hydroxyls reaction with aldehydes forming hemiacetals and acetals are evidenced at the range from 3200 to 3550 cm^{-1} ($-\text{OH}$) and from 2750 to 2850 cm^{-1} (GA duplet). In the same way, Figure 2(c) shows the FTIR spectra region mostly related to the inorganic species of the hybrid network affected by the crosslinking, for instance, the $\text{Si}-\text{O}-\text{Si}$ bands from sol-gel process and the very relevant hybrid group $\text{Si}-\text{CH}_x$ (1200–1260 cm^{-1}). However, a broader absorption band (1085–1150 cm^{-1}) that is attributed to the ether ($\text{C}-\text{O}$) and acetal and hemiacetal bridges ($-\text{C}-\text{O}-\text{C}-$) bands by the crosslinking reaction of PVA with GA can be observed [25]. As mentioned, it was feasible to observe by FTIR spectroscopy the relative contribution of the organic (PVA), inorganic ($\text{Si}-\text{O}-\text{Si}$) components and the chemical crosslinker (GA) in the different hybrids produced.

It is well known that FTIR is certainly a qualitative spectroscopic method for investigating chemical functionalities in materials. Nevertheless, with some fundamentals and proper assumptions, it may be a powerful tool to conduct semiquantitative analysis by considering the ratio of intensities (height or peak areas). The FTIR spectra were normalized using CH_2 bending mode at 1450 cm^{-1} before performing the calculations with the intensities. This band associated with the CH_2 bending mode is relatively unchanged by adjacent chemical alterations [24, 25, 30, 34]. Consequently, the effect of crosslinking on the nanostructure of the hybrids was assessed by analyzing the changes on the relative intensities of relevant specific FTIR bands. This means that major bands associated with the polymer, the bioactive glass, and the network modifier were compared for different contents of crosslinking agent added.

In fact, these relative intensities of FTIR bands have offered the possibility of evaluating the actual degree of crosslinking and, as a result, the density of covalent bonds formed in the chemically modified hybrid network as presented in Figure 3. Thus, it can be observed in Figure 3(b) that the relative intensities ($I_{\text{C}-\text{O}-\text{C}}$) associated with the formation of acetal and hemiacetals (1085–1150 cm^{-1}) increased in the PVA/BaG hybrids crosslinked with glutaraldehyde (1.0 and 5.0%) compared to noncrosslinked ones. As expected, the covalent chemical crosslinking has taken place by the reaction of bifunctional aldehyde (GA) with the hydroxyls groups of PVA. Also, that effect was not evident by increasing the GA concentration from 1.0% to 5.0%, perhaps limited by some saturation of reacting sites available and the restriction in the mobility of PVA chains caused by the network crosslinking.

For the inorganic phase, the bands chosen were 1000–1100 and 900–950 cm^{-1} , associated with the bridging $\text{Si}-\text{O}-\text{Si}$ ($I_{\text{Si}-\text{O}-\text{Si}}$) and $\text{Si}-\text{OH}$ (I_{SiOH}) bonds, respectively. The intensity ratios for bands $I_{\text{Si}-\text{O}-\text{Si}}$ and I_{SiOH} as a function of the concentration of crosslinking agent added are presented in Figures 3(c) and 3(a), respectively. It can be observed that the peak intensity ratio increased due to the formation of $\text{Si}-\text{O}-\text{Si}$ bonds ($I_{\text{Si}-\text{O}-\text{Si}}$) for 1.0% GA compared to the noncrosslinked hybrids. It is suggested that the crosslinking reaction of PVA reduced the amount of hydroxyls (acetal formation = alcohol + aldehyde), reducing the sites available

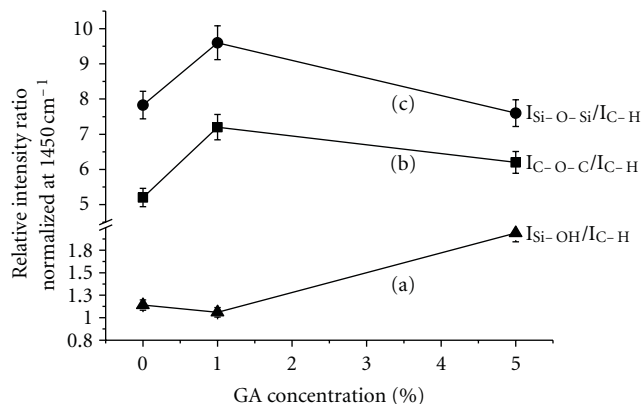


FIGURE 3: Hybrid nanostructure modification by chemical crosslinking (GA). Relative intensity ratios for specific peaks of the FTIR spectra as a function glutaraldehyde concentration in hybrids PVA/BaG/GA: (a) $I_{\text{Si-OH}}/I_{\text{C-H}}$; (b) $I_{\text{C-O-C}}/I_{\text{C-H}}$; (c) $I_{\text{Si-O-Si}}/I_{\text{C-H}}$.

for hydrogen bonds formation between PVA and silanol groups. Therefore, that would have favored an increase in the inorganic polycondensation reactions leading to the formation of silicate network ($\text{Si}-\text{OH} + \text{Si}-\text{OH} = \text{Si}-\text{O}-\text{Si}$) (Figure 3(c)). On the contrary, the peak intensity ratio related to the silanols (nonbridging oxygen, I_{SiOH}) remained practically constant for noncrosslinked and 1.0% crosslinked hybrids but drastically increased for hybrids with 5.0% GA (Figure 3(a)). This trend can be attributed to the fact that at very high GA concentration (5.0%), the crosslinking reaction has occurred very intensively, as indicated by a much lower gelation time during the synthesis (less than half the gelation time observed for hybrids produced with no addition of GA) [36, 38]. As a consequence, the fast gelation of the mixture may have affected the inorganic polycondensation reactions (“rigid frozen structure”), accounted for the reduction of $I_{\text{Si}-\text{O}-\text{Si}}$ band (Figure 3(c)) for 5.0% GA, leading to a higher amount of $\text{Si}-\text{OH}$ groups remaining within the hybrid structure and, therefore, to an increase in the value of I_{SiOH} (nonbridging in the inorganic network). Moreover, it could be assumed that at very high aldehyde concentration, the stage of the sol-gel process associated with polycondensation was significantly limited by the acetal bridges formed with PVA (alcohol hydroxyls) causing the “excess” of remaining unreacted silanol groups within the 3D hybrid network.

3.1.2. Crystallinity and 3D Morphology of PVA/BaG/GA Hybrids. The X-ray diffraction patterns for samples of PVA/BaG crosslinked with GA are presented in Figure 4. It can be observed that the noncrosslinked hybrid has shown mostly an amorphous structure most likely caused by the synergetic effect of bioactive glass and semicrystalline PVA. On the other hand, the chemically crosslinked network indicated a partially crystalline structure. In addition, a crystalline phase of calcium silicate was identified as CaSiO_3 (Figure 4(a), bottom) for the hybrid systems covalently crosslinked with the bifunctional modifier (GA). This finding can be attributed to the kinetics of the hybrid structure formation as the crosslinker has preferably reacted with

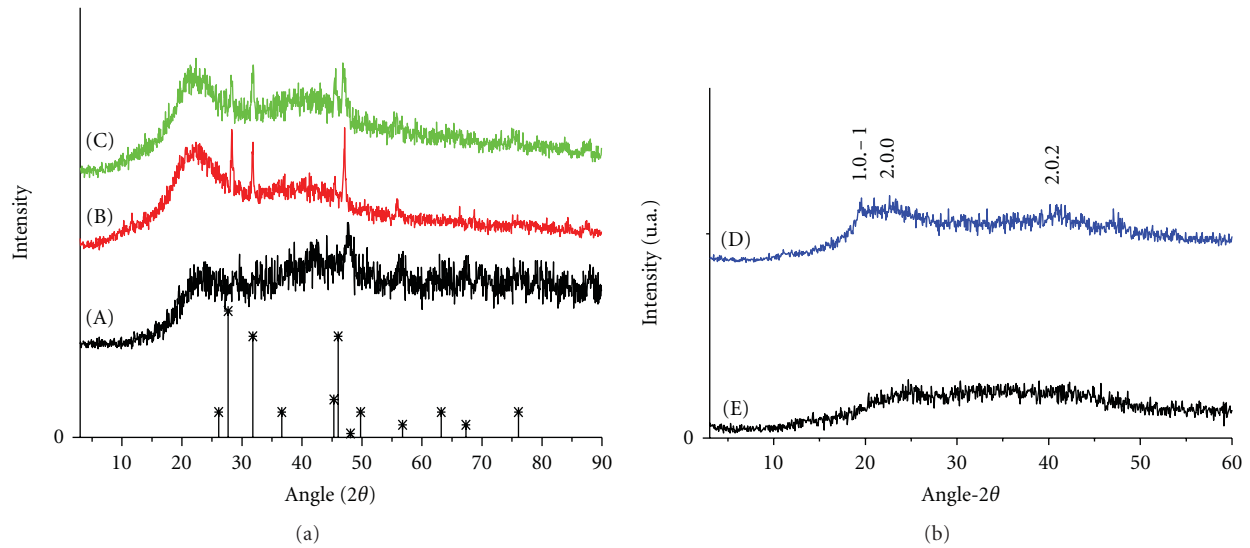


FIGURE 4: XRD patterns of hybrids. (a): (A) BaG/PVA, (B) BaG/PVA/1.0% GA, and (C) BaG/PVA/5.0% GA, (*) CaSiO_3 crystalline phase. (b): (D) PVA, and (E) bioactive glass (BaG).

TABLE 1: Pore size analyses of PVA/BaG/GA hybrids.

	Concentration glutaraldehyde (GA, %)			
	0.0	1.0	5.0	5.0*
Medium pore size (μm)	450	490	150	
Maximum pore size (μm)	1100	1000	450	450
Minimum pore size (μm)	220	180	50	100
Interconnections medium size (μm)	75	145	35	
Interconnections maximum size (μm)	285	475	100	200
Interconnections minimum size (μm)	25	35	10	60

* Values obtained by micro-CT.

alcohol groups from PVA, in turn leading to relatively richer calcium (Ca^{2+}) nanodomains, allowing for reactions with silanols (Si-OH), forming the calcium silicate phase. It should be noted that, preliminarily, this phase is not detrimental to either mechanical or biological properties.

Moving a step further, the 3D structure of the hybrid was characterized by SEM and μCT analyses. The SEM micrographs have shown the macroporous network produced for different amounts of GA added to the PVA/BaG systems (Figures 5(a), 5(b), and 5(c)). Noncrosslinked or crosslinked hybrids with 1.0% GA have shown a comparable pore structure, in which larger pores (macropore) are interconnected by smaller channels (interconnections). On the other hand, the size range of both macropores and interconnections decreased significantly when the material was crosslinked with a larger amount of GA (5.0%). The results of the quantitative assessment of the macropore and interconnection size distribution, performed using the image analysis software (Quantikov), are presented in Table 1.

The pore size range and interconnection size range are much lower for the samples crosslinked with 5.0% GA, as is qualitatively illustrated on the images. The macropore average diameter was $450 \mu\text{m}$ for the PVA/BaG sample (noncrosslinked) and $490 \mu\text{m}$ for the sample crosslinked with 1.0% GA (PVA/BaG/GA). The average pore diameter fell to $150 \mu\text{m}$ in samples crosslinked with 5.0% GA. In summary, it is reasonable to affirm that these results have evinced a pronounced effect of the network reticulation by means of covalent chemical modifiers on pore size distribution.

The pore size analysis for the sample crosslinked with 5.0% GA was also conducted using X-ray microcomputed tomography (μCT), a tool that has become more progressively used to obtain three-dimensional (3D) images of scaffold biomaterials, as it allows for a better evaluation of the 3D pore structure [50]. The 3D image obtained by μCT is shown in Figure 5(d), and the corresponding pore size distribution and interconnection distribution are presented in Figures 5(e) and 5(f). The μCT image clearly shows

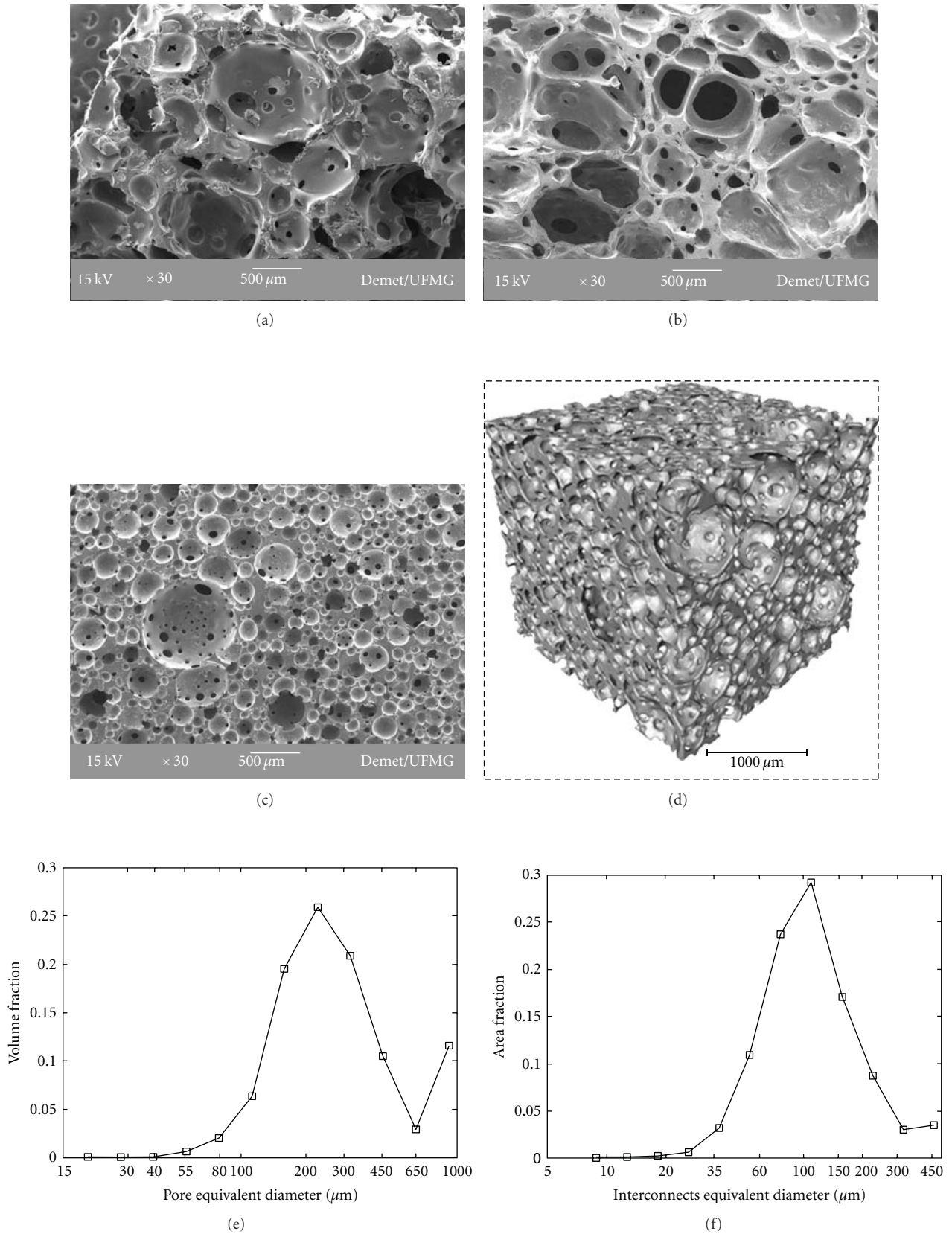


FIGURE 5: SEM of PVA/BaG/GA hybrids crosslinked with (a) 0%; (b) 1.0%; (c) 5.0% of GA. (d) X-Ray microcomputed tomography of sample crosslinked with 5.0% of glutaraldehyde. Pore size distribution (e) and interconnection size distribution (f) obtained by μCT analysis of the hybrid PVA/BaG crosslinked with 5.0% glutaraldehyde.

TABLE 2: Compression yield strength, deformation at yield stress, and elastic compression modulus for PVA/BaG/GA hybrids.

[GA]	Yield strength (MPa)	Deformation at yield stress (%)	Elastic compression modulus (MPa)
0%	2.3 ± 0.9	7.5 ± 0.3	0.6 ± 0.2
1.0%	6.7 ± 3.3	9.1 ± 2.9	0.8 ± 0.1
5.0%	9.1 ± 0.3	14.6 ± 1.1	0.8 ± 0.1
5.0%-NH ₄ OH	7.5 ± 1.1	9.9 ± 0.9	1.0 ± 0.1
Maximum stress for trabecular bone [30, 36]		2–12 MPa	

that the PVA/BaG/5.0% GA hybrid presents a 3D porous structure with interconnected pores. The distributions show that 80% of the macropore range from 100 to 450 μm with a modal pore size of 227 μm (Table 1). The interconnections also show a large distribution, with 80% ranging from 60 to 200 μm and a modal size of 110 μm . Comparing the results obtained by SEM and μCT for the PVA/BaG/5.0% GA hybrid, it can be observed that the maximum values for macropore size are similar. However, when comparing the minimum pore size, values measured by SEM and μCT are quite different. This difference may well be related to the difficulty in clearly defining, through SEM images, the difference between macropores and interconnections. As mentioned in the previous section, the reduction in pore and interconnection size for larger concentrations of the crosslinking agent may be explained by assuming that the capacity of the aldehyde groups of GA reacts with the hydroxyl groups present in PVA, thus forming bridges between the polymeric chains and contributing to the faster gelation of the solution. Upon increasing the crosslinking rate, the gelation process is then completed, in turn freezing the structure of the foam before bubbles from vigorous stirring begin to coalesce. In fact, in Figure 5 (A, B, C), an expressive amount of pores with diameters of approximately 50 μm in the sample crosslinked with 5.0% GA can be observed. This result shows that the gelation step plays a crucial role in the dynamics of pore formation. When the gelation time is increased, bubbles introduced before gelation can migrate into the foam and form groups that coalesce to originate large pores before viscosity increases at the gel point, thus stabilizing the material.

3.1.3. Mechanical Characterization. The mechanical response under compression of hybrid samples before (PVA/BaG) and after having been chemically modified by crosslinking (PVA/BaG/GA) is presented in Figure 6. In a general approach, it can be said that the mechanical behavior found for the PVA/BaG hybrids is in accordance with the reported literature for cellular (porous) materials [51]. Typically, the stress–strain curve for a cellular solid in compression is characterized by three regimes (Figure 6(a), regions I, II and III): a linear elastic regime, corresponding to cell edge bending or face stretching; a stress plateau, corresponding to progressive cell collapse by elastic buckling, plastic yielding, or brittle crushing, depending on the nature of the solid from which the material is made; densification, corresponding

to the collapse of the cells throughout the material and subsequent loading of the cell edges and faces against one another. In the produced hybrids, a marked change could be observed, particularly in the plastic regime, as the amounts of crosslinking agent increased, which can be attributed to different mechanisms leading to cell collapse. For hybrids with no crosslinking agent added or with only 1.0% GA added, the cell collapse is due to brittle crushing, although some plastic deformation might occur. The stress plateau became more defined for samples with higher added amounts of GA (5.0%), which is typical of a more plastic behavior where progressive cell collapse due to plastic yielding can be observed. For these samples, in the final stage, the compression stress increased rapidly with strain, leading to a densification of the foam due to the collapse of the cells. It should be emphasized that all samples were carefully dried in a vacuum before testing, since the high polymer content of the samples determines its hydrophilic character, and that adsorbed water acts as a plasticizer for PVA, influencing the stress–strain behavior. The mechanical properties of all hybrids are summarized in Table 2. An increase in the yield strength (Figure 6(b)), as well as in the deformation at the yield stress (Figure 6(c)), could be observed in direct proportion to the increase in the amount of crosslinking agent added. Hybrids prepared with no crosslinking agents presented a yield strength of approximately 2 MPa, close to the lower level of the range measured for the trabecular bone [30]. The addition of 1.0% GA led to a threefold ($\sim 200\%$) increase in the yield strength. The samples prepared with 5.0% GA presented a yield strength of 9 MPa, which is four times higher ($\sim 300\%$) than the value obtained for noncrosslinked hybrids. These findings are relevant as far as bone tissue engineering is concerned, where a significant improvement in mechanical properties was achieved, producing only minor changes in the overall 3D structure. At this stage, it should be emphasized that even at the highest crosslinker concentration (5.0% GA), the pore size distribution and the connectivity would make it possible to promote cell adhesion, migration, and growth mimicking the trabecular (cancellous) bone structure with comparable mechanical properties. These results are a consequence of the homogeneous 3D pore structure of the hybrids prepared with 5.0% GA which are endorsed by the low values for the standard deviation (3% at yield strength) and SEM image analysis. Nevertheless, it should also be highlighted that the most important effect of the addition of the higher content of crosslinking agents was to change the behavior of

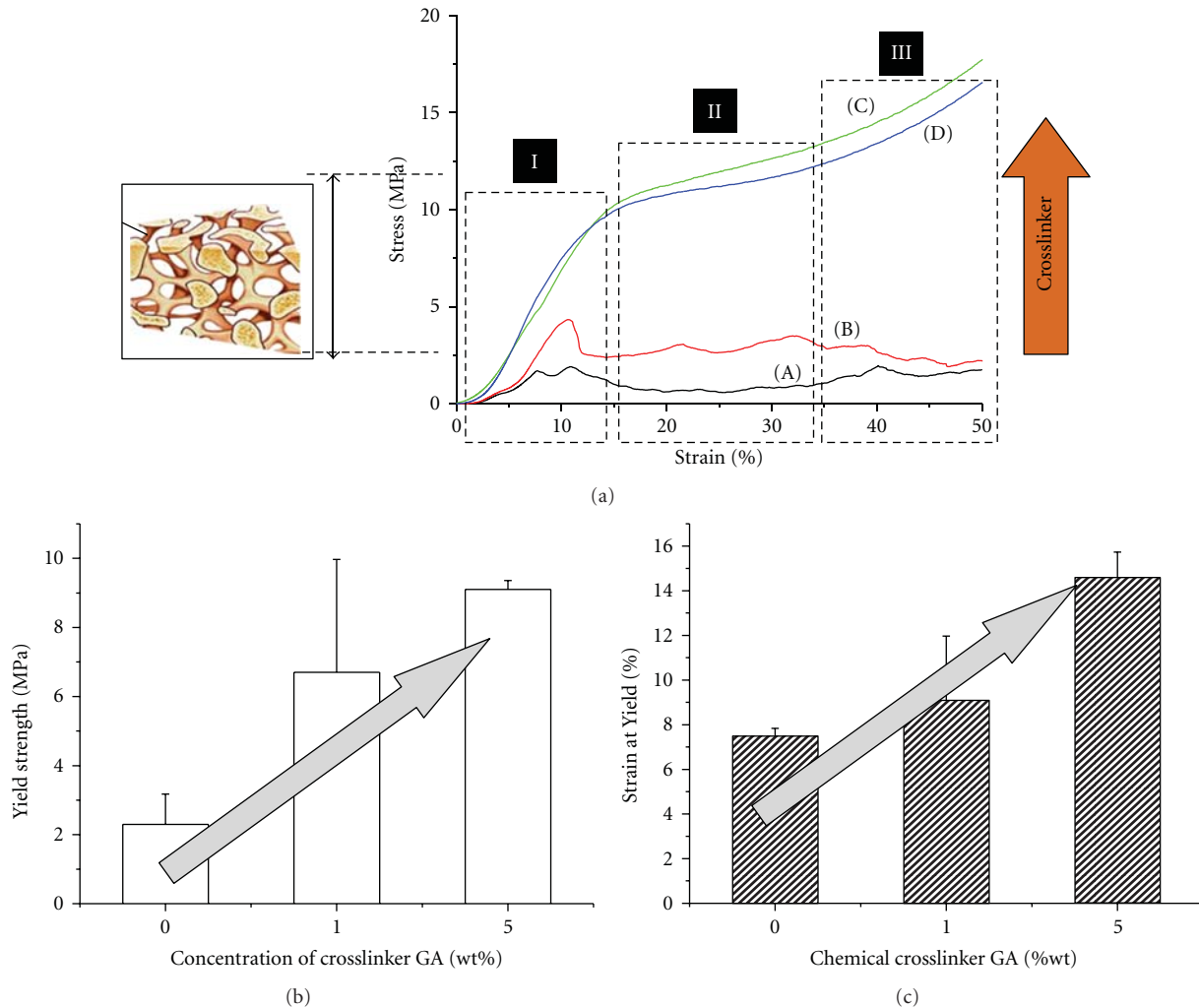


FIGURE 6: (a) Stress-strain compression curves obtained for PVA/BaG/GA hybrids crosslinked with (A) 0%, (B) 1.0%; (C) 5.0% of glutaraldehyde, and (D) crosslinked with 5.0% GA and treated with NH_4OH . Regions I, II and III related to the mechanical behavior of the nanostructured system. (b) Histogram of the yield strength results for PVA/BaG/GA hybrids crosslinked with (A) 0%; (B) 1.0%, (C) 5.0% glutaraldehyde. (c) Histogram of the strain at yield results for PVA/BaG/GA hybrids crosslinked with (a) 0%; (b) 1.0%, (c) 5.0% glutaraldehyde.

the porous hybrid to a more plastic deformation. The effect of crosslinking was similar to that observed when increasing the amount of PVA in the hybrid and under varying drying conditions, which determines the residual content of water in the material [52]. In both cases, the mechanism of cell collapse turned to plastic yielding, as the PVA and water acted as the plasticizer of the material. The mechanical characterization of the trabecular bone is very difficult.

3.2. Degradation Behavior: In Vitro Assay. At this point, it is important to present some considerations regarding to the degradation process. Despite being intensively researched, the degradation behavior of polymeric systems is a difficult theme as it may vary a lot from one system to another. One can simply classify them as degradable and “non-degradable” (inert). Nevertheless, the distinction between “degradable” and “non-degradable” polymers is unclear and

quite arbitrary, given that all materials, including polymers, will degrade within an appropriate time scale. It is the relation between the time scale of degradation and the time-scale of application that appears to make the difference between “degradable” and “non-degradable” polymers. The attribute “degradable” is commonly assigned to materials which degrade during their application or immediately after it. “Non-degradable” polymers are those that require a substantially longer time to degrade than the duration of their application. In addition, the degradation behavior of these systems is quite different, as they are commonly utilized as biomaterials in living organisms. A number of new aspects and properties must be fulfilled by the designed system in order to reach a successful performance under any clinical application. Complexity is taken to the extreme, bearing in mind the degradation process of three-dimensional porous hybrid scaffolds submitted to this dynamic physiological

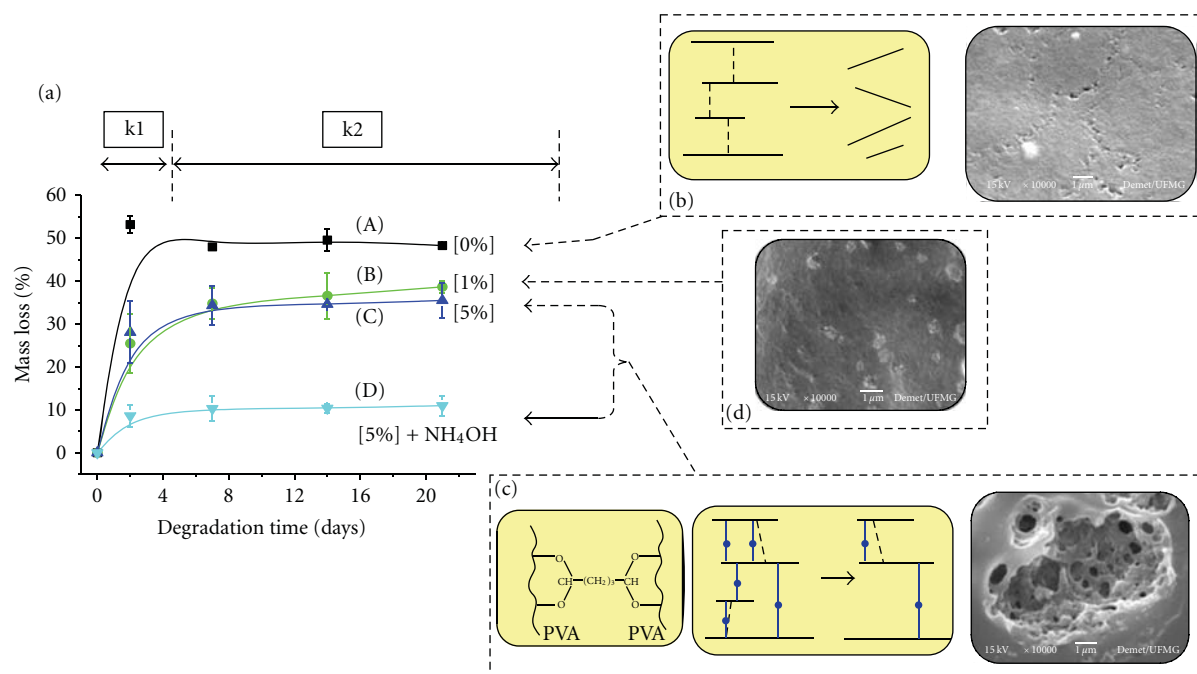


FIGURE 7: (a) Degradation assay *in vitro* for PVA/BaG/GA hybrids (A) noncrosslinked (0% GA); crosslinked with (B) 1.0% and (C) 5.0% GA; (D) crosslinked with 5.0% GA and treated with NH₄OH. (b) Schematic drawing of the degradation behavior under *in vitro* assay for PVA/BaG/GA hybrids without crosslinking with surface erosion (SEM image). (c) Schematic drawing of the degradation behavior under *in vitro* assay for PVA/BaG/GA hybrids with 5.0% GA crosslinking with bulk erosion (SEM image). (d) SEM image of the degradation behavior for PVA/BaG/GA hybrids with 1.0% GA crosslinking.

environment. There are numerous possibilities and pathways to be followed by each and every component. For instance, a component can undergo dissolution or solvation in the medium, erosion, etching, enzymatic, or hydrolytic cleavage of chains and networks into smaller species, among other possibilities. For this reason, it is beyond the focus of the present study to produce a complete in-depth investigation of the hybrids degradation process. On the contrary, it should be pointed out that a preliminary evaluation of the degradation behavior of hybrids (polymer-ceramic, PVA-BaG) was conducted in this research by performing an *in vitro* analysis based on mass loss upon immersion in aqueous medium. The main results are summarized in Figure 7. As shown in Figure 7(a), the mass loss values for all the samples proved to be higher at the beginning stages, followed by a progressive decrease in the mass loss rate according to immersion time. Moreover, the mass loss was higher for samples which were not chemically crosslinked with glutaraldehyde (PVA/BaG without GA, Figure 7(a), curve (A)). On the contrary, the mass loss was significantly reduced when the amount of chemical crosslinking agent was increased. For instance, after 21 days of *in vitro* assay, the mass loss varied from ~50% for the noncrosslinked hybrid (Figure 7(a), curve (A)) to ~35% for hybrids crosslinked with 5.0% GA (Figure 7(a), curve (C)). In a general approach, two main regions can be clearly observed in Figure 7(a), one with a relatively high degradation rate (referred to as the k1 region) and the second with a lower degradation rate (k2). This finding

may be associated with two concurrent mechanisms, one mostly dominated by solvation/dissolution (fast, k1) and the second by hydrolysis and diffusion (slow, k2) of the hybrid system. These results have given strong evidence that the original organic-inorganic network (PVA/BaG, Figure 7(c)) most likely was modified by the crosslinking reactions of PVA with the bifunctional reagent (GA), in turn causing the formation of acetal/hemiacetal bridges (Figure 7(b)) [34]. These results also suggested that the crosslinking of the hybrids improved the stability of scaffolds towards *in vitro* degradation. The PVA/BaG/GA scaffolds (1.0% and 5.0% GA) degraded slowly, while PVA/BaG (0% GA) degraded rapidly. Hence, these covalent bonds significantly altered the hybrid structure at the nanoscale level, thereby reducing the overall degradation rate. The schematic representation of the observed degradation behavior is illustrated in Figures 7(b) and 7(c), with the respective SEM images. The degradation led to some changes in the structural morphology as can be observed in the SEM micrographs (Figures 7(b) and 7(c)), which helps to explain the different degradation processes. Of course, this is a simplified approach, as many aspects are involved, such as network swelling, hydrogen bonds, hydrophobic and hydrophilic species, electrostatic balance of charges (ions), weak forces (van der Waals), among others. In fact, the choice of using water as the immersion medium rather than other degradation solutions, such as PBS (phosphate buffer saline) or SBF (simulated body fluid), was fundamentally justified by avoiding the effect of other ionic species in such already complex hybrid systems.

This element warrants future investigation, since PBS is commonly used as a physiological medium for *in vitro* assays. A similar assay was carried out with hybrids crosslinked with 5.0% GA and previously submitted to a neutralizing treatment with an NH_4OH solution before the degradation assay (Figure 7(a), curved). This assay, when compared to all samples, particularly with noncrosslinked samples, presented an even less pronounced mass loss ($\sim 10\%$ at 21 days) upon immersion. This result indicated that the treatment with an alkaline medium (NH_4OH) not only neutralizes the hybrids, but also stabilizes the samples, perhaps removing part of the material susceptible to the initial stage of degradation [38]. Hence, when these samples were submitted to the alkaline neutralizing procedure, they underwent some preliminary erosion of the more labile components, achieving a more stable network.

Figure 8 presents a schematic illustration of the novel hybrid produced aiming at moving forward and bringing some contribution to this multifaceted subject of degradation of nanostructured materials. Briefly, hybrids are considered to be an interpenetrated network (IPN) produced by the combination of organic (PVA) and inorganic (BaG) constituents that have been chemically modified by a bifunctional crosslinker (GA). The degradation process can be described by a phenomenological contribution of solvation (dissolution) and diffusion-reaction mechanisms, occurring in two stages, as represented in Figure 8(b), Scheme 1, and Scheme 2, respectively. Initially, an aqueous media diffuses into the hybrid structure which turns into a gradually swollen structure. In this stage (Figure 8(b), Scheme 1), it is expected that the effect of PVA as a water-soluble hydrophilic polymer will be mostly predominant (swelling/solvation polymeric component). It can also be said that temporary interactions (weak and strong) will be heavily affected at this stage, such as hydrogen bonds (hydroxyls of PVA and silanols), van der Waals forces (polymer chain folding), and electrostatic forces (ions, Ca^{2+} , phosphates). In the sequence, within the hybrid polymeric-inorganic matrix, hydrolytic reactions may occur, mediated by water, forming some fragments and oligomeric products which may diffuse outwards. The diffusion depends on several factors, such as porosity, pore-size distribution and connectivity, and the degree of crosslinking of the nanostructured chemically modified hybrid network (Figure 8(b), Scheme 2). The complete erosion of the polymer is known to take substantially longer than the degradation time investigated in this study. As this hybrid network was modified by the chemical crosslinker, some comparable trends may be assumed at both degradation stages, but not necessarily to the same extent. During this first phase, the aqueous solution penetrates the 3D pore structure with several phenomena taking place, including swelling, solvation, and the leaching out of ions, among others. Then, at a second moment, some hydrolytic degradation may occur at the acetal and hemiacetal bridges, converting relatively long polymer chains (PVA) into shorter water-soluble fragments. Naturally, the degradation reaction of the chemically crosslinked organic-inorganic systems will present a lower kinetic rate than will the dissolution of the noncrosslinked hybrid structure. In an

analogous mechanism, the inorganic-rich component may also be degraded, which can be regarded as an inverse of the sol-gel poly-condensation process which occurred during the hybrid synthesis. In fact, several authors have reported on the degradation behavior of polymer-based systems, but very few detailed reports dealing specifically with the degradation of 3D porous hybrid scaffolds can be observed in the literature [27, 53].

In summary, based on the results, it is valid to affirm that the produced hybrid network of PVA-BaG was engineered according to the degradation kinetics by using different concentrations of bifunctional chemical covalent modifier. Furthermore, one may be able to tailor the rate of degradation by altering some accessible parameters, such as organic/inorganic ratio, scaffold porosity, and connectivity, type of crosslinker, among others, aimed at specific biomedical applications. Ideally, the degradation and resorption kinetics of composite and hybrid scaffolds are designed to allow cells to proliferate and secrete their own extracellular matrix while the scaffolds gradually vanish, leaving space for new cell and tissue growth.

3.3. Cytotoxicity Assessment—*In Vitro*

3.3.1. MTT Assay. Safety and reliable tests including cytotoxicity analyses are required for all products to be used in contact with humans and animals. Therefore, cell viability was measured using the MTT assay and represents the active mitochondrial enzymes present in a cell capable of reducing MTT. In general, MTT assays using cell culture have been accepted as the first step in identifying active compounds and for biosafety testing. As such, all synthesized hybrids of PVA/BaG were evaluated by MTT assay. Representative results are presented in Figure 9. A higher relative cytocompatibility of PVA/BaG hybrids crosslinked with 5.0% GA, as compared to unmodified hybrids (0% GA), can be observed. Moreover, samples submitted to the *in vitro* degradation process have clearly indicated an improvement in their preliminary biocompatibility during longer immersion times (21 days). Taking into consideration all the results, the PVA/BaG/GA hybrid crosslinked with 5.0% GA presented the best performance in the MTT assay. Similar results were verified for the PVA/BaG/GA hybrid crosslinked with 5.0% GA, which had been previously neutralized by NH_4OH medium. Interestingly, these very hybrids have also shown better results in terms of structure and mechanical behavior. They presented a more homogeneous pore size distribution; a higher yield strength and strain deformation; and a lower degradation rate. Nevertheless, one should be aware that the values found in MTT results are attributed to a comparable biocompatibility under *in vitro* conditions and cannot be straightforwardly used to predict *in vivo* performance in biomedical applications.

3.3.2. Cell Viability via Adhesion-Spreading Assay. Moving beyond the MTT assay, the qualitative analysis of cell morphology was conducted by means of SEM images (Figure 9(b)) associated with its proliferation and growth in

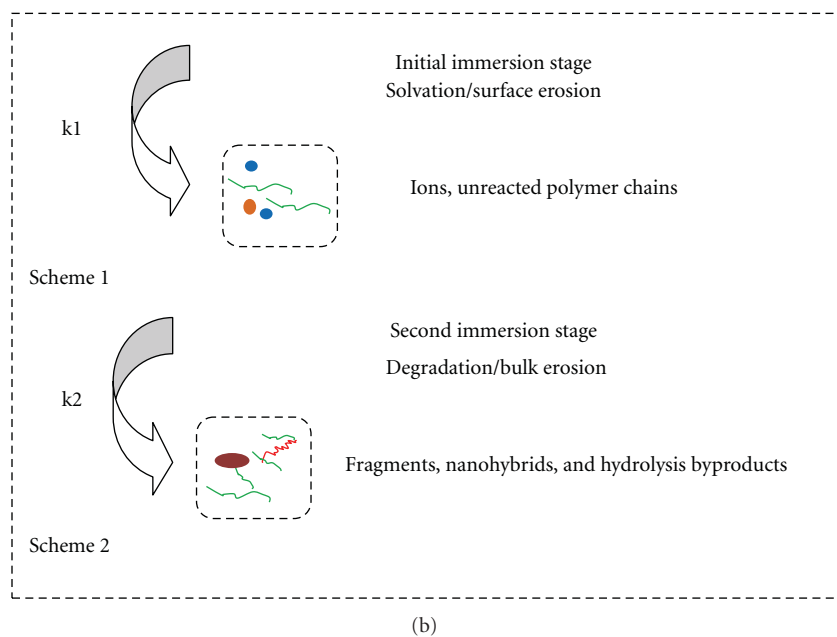
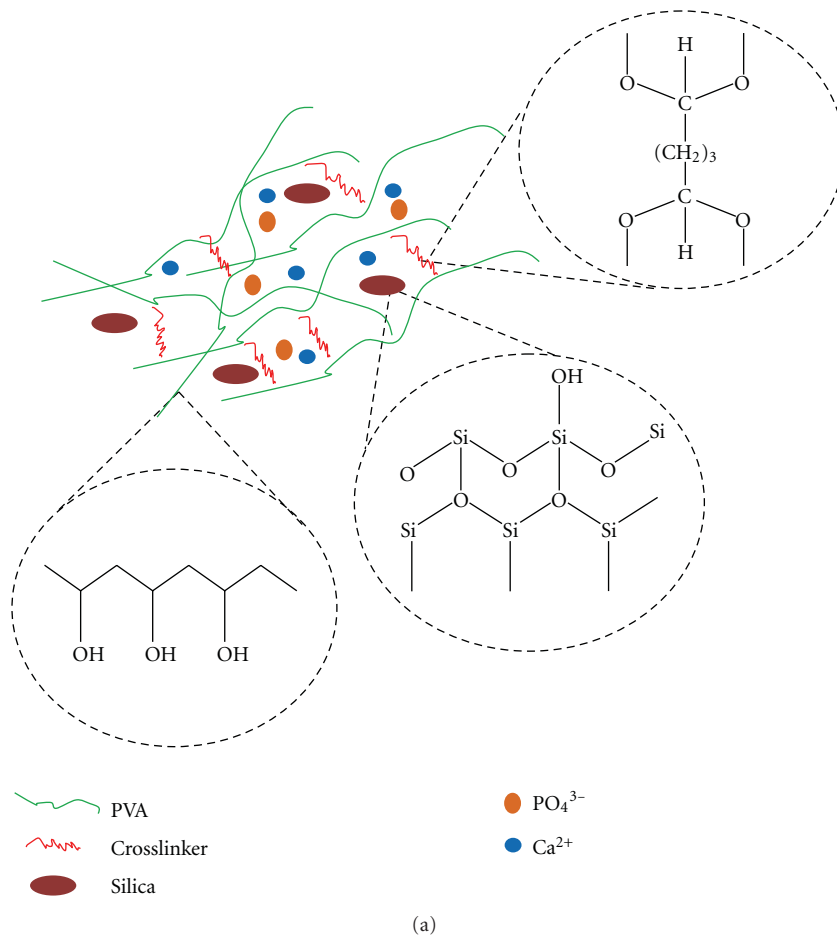


FIGURE 8: (a) Representation of the complex nanostructure of the hybrids based on PVA/BaG/GA. Surface erosion of noncrosslinked hybrids associated with solvation/dissolution at fast rate k_1 (Scheme 1); Bulk erosion of hybrids chemically modified with bifunctional crosslinker at slow rate k_2 (Scheme 2).

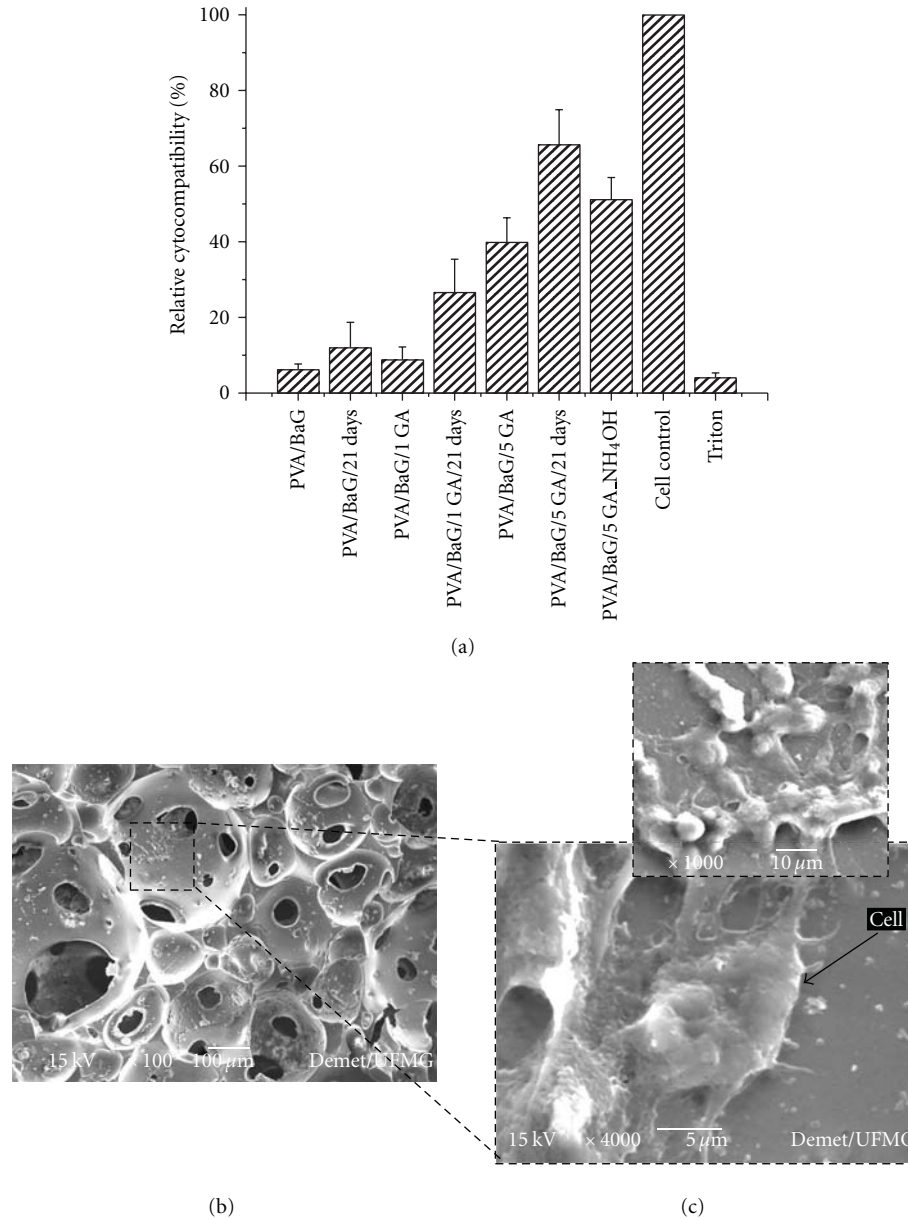


FIGURE 9: (a) Typical cell viability response of MTT assay of PVA/BaG and PVA/BaG/GA hybrids crosslinked with 1.0% and 5.0% GA before and after *in vitro* degradation (21 days). Also, PVA/BaG/GA (5.0%) with NH₄OH stabilization process. SEM images of hybrid scaffolds crosslinked at different magnifications with evidence of cell adhesion/spreading (b, c) (*see [38]).

contact with PVA/BaG/GA hybrid crosslinked with 5.0% GA samples via adhesion and spreading behavior.

It could be verified that the VERO cells seeded onto PVA/BaG/GA hybrid matrices showed a good adhesion and spreading morphology, that is, well matched to this fibroblastic lineage (Figure 9(b)). Since cellular attachment, adhesion, and spreading belong to the first phase of cell/material interactions, the quality of this phase will influence the proliferation and differentiation of cells on biomaterials surfaces. Based on the SEM results, one may attribute the VERO cell spreading and adhesion verified in the PVA/BaG/GA hybrid to be an important response regarding the biocompatibility and noncytotoxicity of the investigated samples. According to the literature [30, 36, 38], cell spreading is generally

divided into three main interaction levels: (a) unspread: cells were still spherical in appearance, and protrusions or lamellipodia were not yet produced; (b) partially spread: at this stage, cells began to spread laterally on one or more sides, but the extensions of the plasma membrane were not completely confluent; (c) fully spread. The final model (c) would represent the best result for material cell hosting. These morphological aspects are accredited to healthy VERO cell cultures giving clear evidence of hybrids produced cytocompatibility. Additionally, the selected cell line (VERO) used as a model in this research plays a role in producing many of the components that are essential to the connective tissue, for example, extracellular components, such as glycosaminoglycans, and fibrous tissue, such as

collagen. In summary, cell adhesion and spreading are of vital importance in living biological processes and are involved in various natural phenomena, such as embryogenesis, the maintenance of tissue structure, wound healing, immune response, metastasis, and tissue integration of biomaterials [30, 36, 38, 42, 43].

4. Conclusions

Three-dimensional interconnected porous structures comprised of PVA/BaG were obtained with varying structural and mechanical properties for different degrees of network crosslinking. A decrease in the medium pore and interconnection size and a more homogeneous pore size distribution, with 80% within the range of 100–450 μm , was observed for larger concentrations of glutaraldehyde. In addition, an increase in the yield strength and in the deformation at the yield stress, with an increase in crosslinking, could be observed, which proved to be more pronounced for the sample crosslinked with 5.0% GA. The synthesized organic-inorganic hybrids based on PVA/BaG have presented different degradation kinetics due to the degree of chemical crosslinking which altered the nanostructure of the network. Finally, these engineered hybrids have shown a preliminary cell viability behavior that, when combined with appropriate mechanical and morphological properties, can be considered potential biomaterials for tissue engineering applications.

Acknowledgments

They acknowledge the financial support from CAPES, FAPEMIG, and CNPq. The authors would like to express their special gratitude to Professor Edel F. Barbosa-Stancioli (ICB-UFMG Brazil) for the MTT cytotoxicity assays and Dr. Julian R. Jones (Imperial College London UK) for the μCT analysis.

References

- [1] J. D. Kretlow and A. G. Mikos, "From material to tissue: biomaterial development, scaffold fabrication, and tissue engineering," *AIChE Journal*, vol. 54, no. 12, pp. 3048–3067, 2008.
- [2] U. A. Stock and J. P. Vacanti, "Tissue engineering: current state and prospects," *Annual Review of Medicine*, vol. 52, pp. 443–451, 2001.
- [3] J. J. Blaker, S. N. Nazhat, V. Maquet, and A. R. Boccaccini, "Long-term in vitro degradation of PDLA/Bioglass® bone scaffolds in acellular simulated body fluid," *Acta Biomaterialia*, vol. 7, no. 2, pp. 829–840, 2011.
- [4] Y. Chen, S. Zhou, and Q. Li, "Mathematical modeling of degradation for bulk-erosive polymers: applications in tissue engineering scaffolds and drug delivery systems," *Acta Biomaterialia*, vol. 7, no. 3, pp. 1140–1149, 2011.
- [5] P. Fabbri, V. Cannillo, A. Sola, A. Dorigato, and F. Chiellini, "Highly porous polycaprolactone-45S5 Bioglass® scaffolds for bone tissue engineering," *Composites Science and Technology*, vol. 70, no. 13, pp. 1869–1878, 2010.
- [6] Y. Minaberry and M. Jobbágy, "Macroporous bioglass scaffolds prepared by coupling sol-gel with freeze drying," *Chemistry of Materials*, vol. 23, no. 9, pp. 2327–2332, 2011.
- [7] L.-C. Gerhardt and A. R. Boccaccini, "Bioactive glass and glass-ceramic scaffolds for bone tissue engineering," *Materials*, vol. 3, pp. 3867–3910, 2010.
- [8] J. J. Blaker, A. Bismarck, A. R. Boccaccini, A. M. Young, and S. N. Nazhat, "Premature degradation of poly(α -hydroxyesters) during thermal processing of Bioglass®-containing composites," *Acta Biomaterialia*, vol. 6, no. 3, pp. 756–762, 2010.
- [9] Q. Tan, S. Li, J. Ren, and C. Chen, "Fabrication of porous scaffolds with a controllable microstructure and mechanical properties by porogen fusion technique," *International Journal of Molecular Sciences*, vol. 12, no. 2, pp. 890–904, 2011.
- [10] E. M. Valliant and J. R. Jones, "Softening bioactive glass for bone regeneration: sol-gel hybrid materials," *Soft Matter*, vol. 7, no. 11, pp. 5083–5095, 2011.
- [11] Q. Fu, M. N. Rahaman, H. Fu, and X. Liu, "Silicate, borosilicate, and borate bioactive glass scaffolds with controllable degradation rate for bone tissue engineering applications. I. Preparation and in vitro degradation," *Journal of Biomedical Materials Research—Part A*, vol. 95, no. 1, pp. 164–171, 2010.
- [12] K. J. L. Burg, S. Porter, and J. F. Kellam, "Biomaterial developments for bone tissue engineering," *Biomaterials*, vol. 21, no. 23, pp. 2347–2359, 2000.
- [13] D. W. Hutmacher, J. T. Schantz, C. X. Lam, K. C. Tan, and T. C. Lim, "State of the art and future directions of scaffold-based bone engineering from a biomaterials perspective," *Journal of Tissue Engineering and Regenerative Medicine*, vol. 1, no. 4, pp. 245–260, 2007.
- [14] V. Olivier, N. Fauchoux, and P. Hardouin, "Biomaterial challenges and approaches to stem cell use in bone reconstructive surgery," *Drug Discovery Today*, vol. 9, no. 18, pp. 803–811, 2004.
- [15] J. R. Jones and L. L. Hench, "Regeneration of trabecular bone using porous ceramics," *Current Opinion in Solid State and Materials Science*, vol. 7, no. 4–5, pp. 301–307, 2003.
- [16] M. Vallet-Regí and J. M. González-Calbet, "Calcium phosphates as substitution of bone tissues," *Progress in Solid State Chemistry*, vol. 32, no. 1–2, pp. 1–31, 2004.
- [17] W. Paul and P. Sharma, "Nanoceramic matrices: biomedical applications," *American Journal of Biochemistry and Biotechnology*, vol. 2, pp. 41–48, 2006.
- [18] J. R. Jones, L. M. Ehrenfried, and L. L. Hench, "Optimising bioactive glass scaffolds for bone tissue engineering," *Biomaterials*, vol. 27, no. 7, pp. 964–973, 2006.
- [19] S. Padilla, S. Sánchez-Salcedo, and M. Vallet-Regí, "Bioactive glass as precursor of designed-architecture scaffolds for tissue engineering," *Journal of Biomedical Materials Research—Part A*, vol. 81, no. 1, pp. 224–232, 2007.
- [20] X. Yan, C. Yu, X. Zhou, J. Tang, and D. Zhao, "Highly ordered mesoporous bioactive glasses with superior in vitro bone-forming bioactivities," *Angewandte Chemie—International Edition*, vol. 43, no. 44, pp. 5980–5984, 2004.
- [21] J. E. Gough, J. R. Jones, and L. L. Hench, "Nodule formation and mineralisation of human primary osteoblasts cultured on a porous bioactive glass scaffold," *Biomaterials*, vol. 25, no. 11, pp. 2039–2046, 2004.
- [22] P. Valerio, M. M. Pereira, A. M. Goes, and M. F. Leite, "The effect of ionic products from bioactive glass dissolution on osteoblast proliferation and collagen production," *Biomaterials*, vol. 25, no. 15, pp. 2941–2948, 2004.
- [23] I. D. Xynos, A. J. Edgar, L. D. K. Buttery, L. L. Hench, and J. M. Polak, "Ionic products of bioactive glass dissolution increase

- proliferation of human osteoblasts and induce insulin-like growth factor II mRNA expression and protein synthesis," *Biochemical and Biophysical Research Communications*, vol. 276, no. 2, pp. 461–465, 2000.
- [24] H. Mansur, R. Oréfice, M. Pereira, Z. Lobato, W. Vasconcelos, and L. Machado, "FTIR and UV-vis study of chemically engineered biomaterial surfaces for protein immobilization," *Spectroscopy*, vol. 16, no. 3-4, pp. 351–360, 2002.
- [25] G. Andrade, E. F. Barbosa-Stancioli, A. A. Piscitelli Mansur, W. L. Vasconcelos, and H. S. Mansur, "Design of novel hybrid organic-inorganic nanostructured biomaterials for immunoassay applications," *Biomedical Materials*, vol. 1, no. 4, article 008, pp. 221–234, 2006.
- [26] V. M. Bispo, A. A. P. Mansur, E. F. Barbosa-Stancioli, and H. S. Mansur, "Biocompatibility of nanostructured chitosan/poly(vinyl alcohol) blends chemically crosslinked with genipin for biomedical applications," *Journal of Biomedical Nanotechnology*, vol. 6, no. 2, pp. 166–175, 2010.
- [27] K. Rezwani, Q. Z. Chen, J. J. Blaker, and A. R. Boccaccini, "Biodegradable and bioactive porous polymer/inorganic composite scaffolds for bone tissue engineering," *Biomaterials*, vol. 27, no. 18, pp. 3413–3431, 2006.
- [28] S. Verrier, J. J. Blaker, V. Maquet, L. L. Hench, and A. R. Boccaccini, "PDLLA/Bioglass® composites for soft-tissue and hard-tissue engineering: an in vitro cell biology assessment," *Biomaterials*, vol. 25, no. 15, pp. 3013–3021, 2004.
- [29] A. Stein, B. J. Melde, and R. C. Schroden, "Hybrid inorganic-organic mesoporous silicates-nanoscale reactors coming of age," *Advanced Materials*, vol. 12, no. 19, pp. 1403–1419, 2000.
- [30] H. S. Mansur and H. S. Costa, "Nanostructured poly(vinyl alcohol)/bioactive glass and poly(vinyl alcohol)/chitosan/bioactive glass hybrid scaffolds for biomedical applications," *Chemical Engineering Journal*, vol. 137, no. 1, pp. 72–83, 2008.
- [31] J. R. Jones, "New trends in bioactive scaffolds: the importance of nanostructure," *Journal of the European Ceramic Society*, vol. 29, no. 7, pp. 1275–1281, 2009.
- [32] T. Yamaoka, Y. Tabata, and Y. Ikada, "Comparison of body distribution of poly(vinyl alcohol) with other water-soluble polymers after intravenous administration," *Journal of Pharmacy and Pharmacology*, vol. 47, no. 6, pp. 479–486, 1995.
- [33] E. Chiellini, A. Corti, S. D'Antone, and R. Solaro, "Biodegradation of poly (vinyl alcohol) based materials," *Progress in Polymer Science*, vol. 28, no. 6, pp. 963–1014, 2003.
- [34] H. S. Mansur, C. M. Sadahira, A. N. Souza, and A. A. P. Mansur, "FTIR spectroscopy characterization of poly (vinyl alcohol) hydrogel with different hydrolysis degree and chemically crosslinked with glutaraldehyde," *Materials Science and Engineering C*, vol. 28, no. 4, pp. 539–548, 2008.
- [35] M. M. Pereira, J. R. Jones, and L. L. Hench, "Bioactive glass and hybrid scaffolds prepared by sol-gel method for bone tissue engineering," *Advances in Applied Ceramics*, vol. 104, no. 1, pp. 35–42, 2005.
- [36] H. S. Costa, M. F. Rocha, G. I. Andrade et al., "Sol-gel derived composite from bioactive glass-polyvinyl alcohol," *Journal of Materials Science*, vol. 43, no. 2, pp. 494–502, 2008.
- [37] A. A. R. De Oliveira, V. Ciminelli, M. S. S. Dantas, H. S. Mansur, and M. M. Pereira, "Acid character control of bioactive glass/polyvinyl alcohol hybrid foams produced by sol-gel," *Journal of Sol-Gel Science and Technology*, vol. 47, no. 3, pp. 335–346, 2008.
- [38] H. S. Costa, E. F. B. Stancioli, M. M. Pereira, R. L. Oréfice, and H. S. Mansur, "Synthesis, neutralization and blocking procedures of organic/inorganic hybrid scaffolds for bone tissue engineering applications," *Journal of Materials Science*, vol. 20, no. 2, pp. 529–535, 2009.
- [39] E. S. Costa-Júnior, E. F. Barbosa-Stancioli, A. A. P. Mansur, W. L. Vasconcelos, and H. S. Mansur, "Preparation and characterization of chitosan/poly(vinyl alcohol) chemically crosslinked blends for biomedical applications," *Carbohydrate Polymers*, vol. 76, no. 3, pp. 472–481, 2009.
- [40] J. A. Burdick, C. Chung, X. Jia, M. A. Randolph, and R. Langer, "Controlled degradation and mechanical behavior of photopolymerized hyaluronic acid networks," *Biomacromolecules*, vol. 6, no. 1, pp. 386–391, 2005.
- [41] H. S. Mansur, R. L. Oréfice, and A. A. P. Mansur, "Characterization of poly(vinyl alcohol)/poly(ethylene glycol) hydrogels and PVA-derived hybrids by small-angle X-ray scattering and FTIR spectroscopy," *Polymer*, vol. 45, no. 21, pp. 7193–7202, 2004.
- [42] P. Estacia, A. S. Rodrigues Junior, P. L. Moreira, and S. C. Genari, "The cytotoxicity in vero cells of a perfluorocarbon used in vitreoretinal surgery," *Brazilian Journal of Morphological Sciences*, vol. 19, no. 2, pp. 41–47, 2002.
- [43] T. Mosmann, "Rapid colorimetric assay for cellular growth and survival: application to proliferation and cytotoxicity assays," *Journal of Immunological Methods*, vol. 65, no. 1-2, pp. 55–63, 1983.
- [44] J. Coates, "Encyclopedia of analytical chemistry: interpretation of infrared spectra, a practical approach," in *Encyclopedia of Analytical Chemistry*, R. A. Meyers, Ed., pp. 10815–10837, John Wiley & Sons, Chichester, UK, 2000.
- [45] R. M. Almeida and C. G. Pantano, "Structural investigation of silica gel films by infrared spectroscopy," *Journal of Applied Physics*, vol. 68, no. 8, article 4225, 8 pages, 1990.
- [46] J. Román, S. Padilla, and M. Vallet-Regí, "Sol-gel glasses as precursors of bioactive glass ceramics," *Chemistry of Materials*, vol. 15, no. 3, pp. 798–806, 2003.
- [47] A. I. Martín, A. J. Salinas, and M. Vallet-Regí, "Bioactive and degradable organic-inorganic hybrids," *Journal of the European Ceramic Society*, vol. 25, no. 16, pp. 3533–3538, 2005.
- [48] T. Wang, M. Turhan, and S. Gunasekaran, "Selected properties of pH-sensitive, biodegradable chitosan-poly(vinyl alcohol) hydrogel," *Polymer International*, vol. 53, no. 7, pp. 911–918, 2004.
- [49] S.-H. Shin and H.-I. Kim, "Contribution of hydrogen bond and coupling reaction improvement in compatibility of organic polymer/silica nanocomposites," *Industrial & Engineering Chemistry Research*, vol. 7, pp. 147–152, 2001.
- [50] S. T. Ho and D. W. Huttmacher, "A comparison of micro CT with other techniques used in the characterization of scaffolds," *Biomaterials*, vol. 27, no. 8, pp. 1362–1376, 2006.
- [51] L. J. Gibson, "Biomechanics of cellular solids," *Journal of Biomechanics*, vol. 38, no. 3, pp. 377–399, 2005.
- [52] H. S. Costa, A. A. R. De Oliveira, R. L. Oréfice, H. S. Mansur, and M. M. Pereira, "Tailoring mechanical behavior of PVA-bioactive glass hybrid foams," *Key Engineering Materials*, vol. 361–363, pp. 289–292, 2008.
- [53] M. Vert, S. M. Li, G. Spenlehauer, and P. Guerin, "Bioresorbability and biocompatibility of aliphatic polyesters," *Journal of Materials Science*, vol. 3, no. 6, pp. 432–446, 1992.

Review Article

Topical Review: Design, Fabrication, and Applications of Hybrid Nanostructured Array

Shaoli Zhu and Wei Zhou

School of Mechanical and Aerospace Engineering, Nanyang Technological University, 50 Nanyang Avenue, Singapore 639798

Correspondence should be addressed to Shaoli Zhu, s.zhu2@uq.edu.au

Received 20 July 2011; Accepted 31 August 2011

Academic Editor: Hui Wang

Copyright © 2012 S. Zhu and W. Zhou. This is an open access article distributed under the Creative Commons Attribution License, which permits unrestricted use, distribution, and reproduction in any medium, provided the original work is properly cited.

Nanohybrid materials have been widely used in the material chemistry research areas. In this paper, we mainly discussed the hybrid nanostructures used for nanobiosensor applications. It is one of the most promising and rapidly emerging research areas in nanotechnology field. Design, fabrication, and applications of hybrid nanostructures are reviewed, respectively. Finite difference time domain (FDTD) methods are applied to design different materials of hybrid nanostructures. Nanosphere lithography (NSL) is used to fabricate our designed hybrid nanostructures. Moreover, protein A and staphylococcal enterotoxin B (SEB), an enterotoxin, are detected by our designed hybrid nanostructures. From all the experiment results, we can see that our designed hybrid nanostructures are one of important nanohybrid materials. They have many potential applications in the nanobiosensor in the future.

1. Introduction

Localized surface plasmon resonance- (LSPR-) based nanobiosensors are of great interest in various applications such as environmental protection [3–5], biotechnology [6–8], and food safety [8]. It is well known that LSPR can be excited when the incident photon frequency is resonant with the collective oscillation of the conduction electrons. It is named as the LSPR effect. Transmission peaks of LSPR-related spectra are sensitive to the electric medium on surface of metal films. The LSPR-based nano-biosensor is a refractive index-based sensing device which relies on the extraordinary optical properties of noble metal (e.g., Ag, Au, and Cu, etc.) nanoparticles [9, 10]. The sensing capability of the LSPR sensor can be modified by tuning shape, size, and material composition of the nanoparticles. The nanoparticles are effective for quantitative detection of chemical and biological targets [4]. The sensing principle employed in these experiments relies on the high sensitivity of the LSPR spectrum of the noble metal nanoparticles due to an absorbate-induced change occurring in the dielectric constant of the surrounding environment. The local environment that surrounds the nanoparticles can be modified by means of binding of

the biological molecular. The extinction spectrum of the nanosensor can be derived using a spectrophotometer [11].

Many biological and chemical agents such as bacteria, algae, fungi, viruses, and toxins are capable of extensively affecting humans and animals [12–15]. Staphylococcus aureus enterotoxin B (SEB), a small protein toxin [12, 16], was selected as a typical small protein toxin in our experiments. SEB with 28.4 kDa protein toxin is one of a group of five major serological types of related proteins with molecular weights ranging from 26 kDa to 29.6 kDa. SEB is an incapacitating toxin, but it is rarely lethal. Detection and quantification of SEB in buffer were demonstrated using the LSPR-based nano-biosensor. Theoretically, the detection concentration of SEB can reach to nanogramme per milliliter level. The methods used to detect SEB include enzyme-linked immunosorbent assays (ELISAs) [17], light addressable potentiometric sensors (LAPSS) [18], array biosensors [19], immunomagnetic separation electro-chemiluminescence and fluorescence procedures (IMS-ECL and IMS-FCL) [20] or rapid chromatographic assays (RCA) [21], and Surface Plasmon Resonance (SPR) sensors [22]. In our previous research work, we have designed and explored some nanohybrid materials to detect the different refractive index

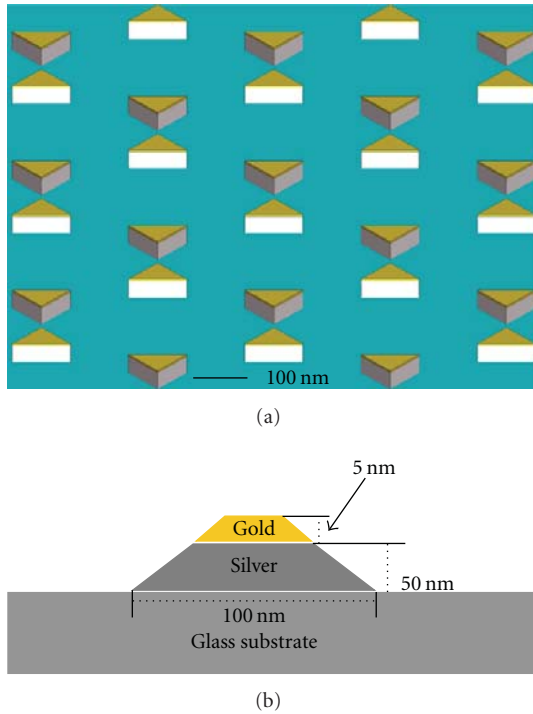


FIGURE 1: (a) Three-dimensional geometrical model of triangular hybrid Au-Ag nanostructures, (b) cross-section of a single hybrid Au-Ag triangular nanostructures. From [1, 2].

of chemical materials and the various kinds of biomolecules [1, 2, 23–27]. In this paper, we reviewed the design, fabrication, and applications of hybrid nanostructured array. The paper is divided into the following three parts: (1) finite-difference and time-domain (FDTD) algorithm was used to design the hybrid nanostructured array. (2) Nanosphere lithography was employed to fabricate our designed array. (3) The functionalized nanostructures are used for detection of proteins A and SEB.

2. Design Methods for Hybrid Nanostructures

There are many design methods to aid in deciding the parameters of the nanostructured array. For example, Mie scattering theory [28] discrete dipole approximation (DDA) [29], finite integration technique (FIT) [30], finite difference time domain (FDTD) [31] method, and the finite element method [32] are widely used for the design of the nanoparticles. FDTD is a commercial software to design arbitrary shapes, sizes and periods of nanostructures. The following parts are our design model and method. The triangular hybrid Au-Ag nanostructure array was proposed as a sensitive cell of the LSPR-based nano-biosensor. Using FDTD algorithm [33], we designed and calculated the refractive index sensitivity of the hybrid nanostructures. The corresponding model of the triangular hybrid Au-Ag nanostructure array is shown in Figure 1(a). A cross-section of a single particle labeling the materials of the substrate and particle and their thicknesses is shown in Figure 1(b).

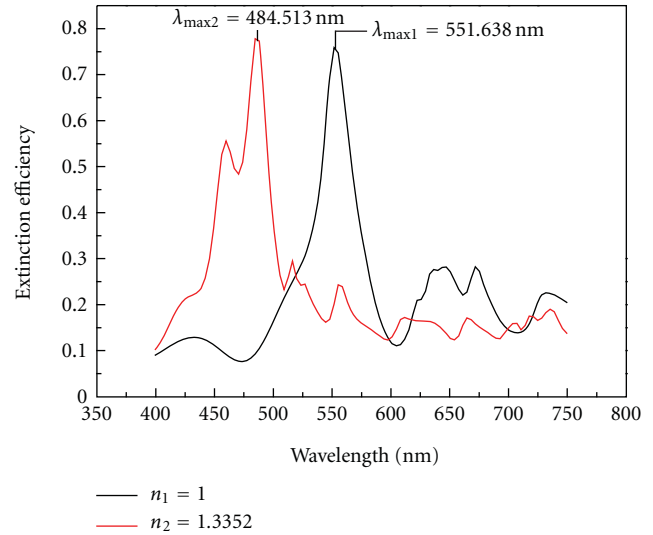


FIGURE 2: FDTD solution calculation results when the refractive index medium surrounding this hybrid nanostructures are 1.0 and 1.3352, respectively. From [1].

The out-of plane heights of the Ag nanostructures under the Au layer is 50 nm and the top Au nanostructures is 5 nm only. The in-plane widths of each nanostructures are 100 nm. The period of the nanostructure array is 400 nm. In order to investigate the effectiveness of mediums with different refractive index surrounding the hybrid nanostructures, we selected the air ($n_1 = 1.0$) and Protein A (Protein A: PBS (0.01 M, pH = 7.4) = 1 : 100, $n_2 = 1.3352$) surrounding the nanostructures. When the refractive index of the mediums surrounding this hybrid nanostructures is 1.0 and 1.3352, respectively, the FDTD algorithm-based calculation results can be obtained, as shown in Figure 2. From the results, we can calculate the sensitivity of the hybrid Au-Ag triangular nanostructure array as $S = (\lambda_{\max 1} - \lambda_{\max 2}) / (n_2 - n_1) = (551.638 - 484.513) / (1.3352 - 1.0) = 200 \text{ nm/RIU}$. It can realize a detection of SEB with higher sensitivity.

3. Fabrication of Nanostructures

An NSL technique [34] was employed to create the surface-confined hybrid Au-Ag triangular nanostructures supported on a glass substrate (see Figure 3). NSL process begins from the self-assembly of size-monodisperse nanospheres into a two-dimensional (2D) colloidal crystal. As the solvent of the nanosphere solution evaporates, capillary forces draw the nanospheres together, thereby crystallizing them into a hexagonally close-packed pattern on the substrate. Following self-assembly of the nanosphere mask, some silver and gold metals are deposited onto the nanosphere-coated substrate, respectively. Metal deposition parameters and vacuum condition are listed as follows: vacuum $2 \times e - 6$ Torr, deposition rate 0.4 A/sec. After the metals deposition, the nanosphere mask is removed via sonication in ethanol resulting in surface-confined nanostructures with triangular footprints. The nanostructures have out-of plane heights of silver

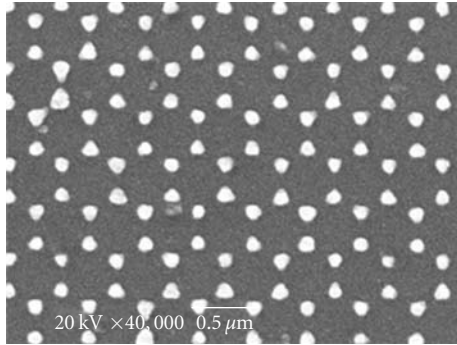


FIGURE 3: SEM image of topography of the triangular hybrid Au-Ag nanostructures fabricated by NSL. From [1].

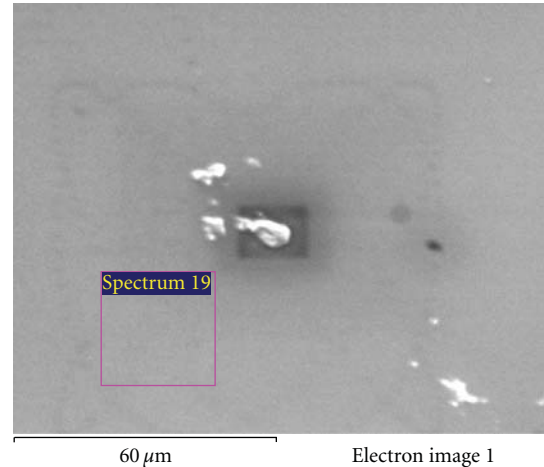
nanostructures ~ 50 nm and the upper gold nanostructures ~ 5 nm in thickness, and ~ 100 nm in plane widths of each nanostructure and ~ 400 nm period of the nanostructure array as measured using JSM-5900 LA scanning electron microscope (SEM). In order to approve the existence of Au cap layer, we used EDX to analyse the materials of hybrid nanostructured array. Figure 4 shows the EDX results for all the elements for the hybrid nanostructured array. EDX analysis results are based on the same materials as the hybrid Au and Ag film. From these results, we can see that there are Au in the cap layer in the hybrid materials. More details for NSL fabrication information are listed in [1, 35].

4. Applications of Hybrid Nanostructures

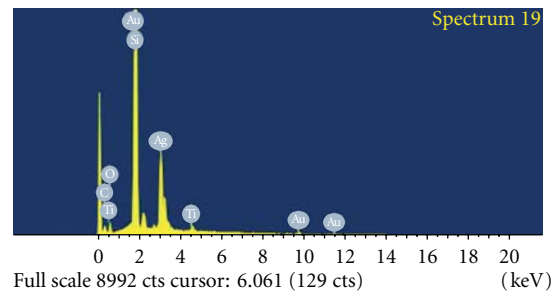
There are many applications for the hybrid nanomaterials. They are widely used as polymers [36, 37]. Polymers can be made into various bulk forms and thin films and widely applied to optical and electronic materials, biomaterials, catalysis, sensing, coating, and energy storage, and so forth fields. Here, we only focus on our research groups' applications such as protein A and SEB detection based on our designed nanostructured array.

4.1. Detecting Protein A. The LSPR-based nanobiosensors are extremely sensitive to variation of refractive index (RI) within a few hundred nanometers of gold surface. Capture of the target analyte (Protein A, from Sigma-Aldrich) by the specific reaction between the metal Au and the Protein A. Protein A bound to the sensing face changes the apparent RI due to solution displacement by the analytes of higher refractive index. To test the detection capability of the hybrid Au-Ag nano-biosensors, experiments were performed using solutions of Protein A in PBS buffer (1 : 100, 0.01 M, pH 7.4, from Jinshan Chemical Analyte Pte. Ltd.), and the refractive index of Protein A (1.3352) was detected by Abbe refractometer ZWA-J (temperature 20°C , $\Delta n = \pm 0.0002$). All the buffer used in the experiments was prepared using double glass-distilled water.

Resonant wavelength λ_{\max} of the bare hybrid Au-Ag nanostructures (see Figure 5, black line) was measured to be 575.99 nm. Exposure to 1 : 100 Protein A resolution resulted



(a)



(b)

FIGURE 4: EDX analysis results for hybrid nanostructured array, (a) spectrum area captured by DEX, (b) EDX elements results of hybrid materials.

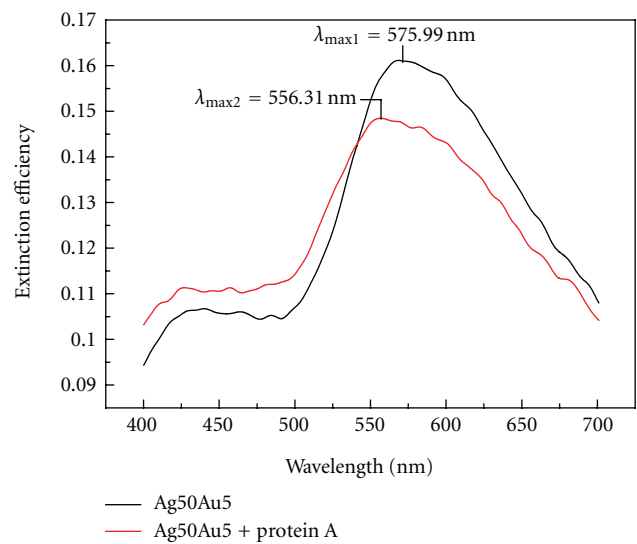


FIGURE 5: Measured spectra for both pure hybrid Au-Ag (thickness of the Ag and Au is 50 nm and 5 nm, resp.) nanostructure array and binding with protein A. From [1].

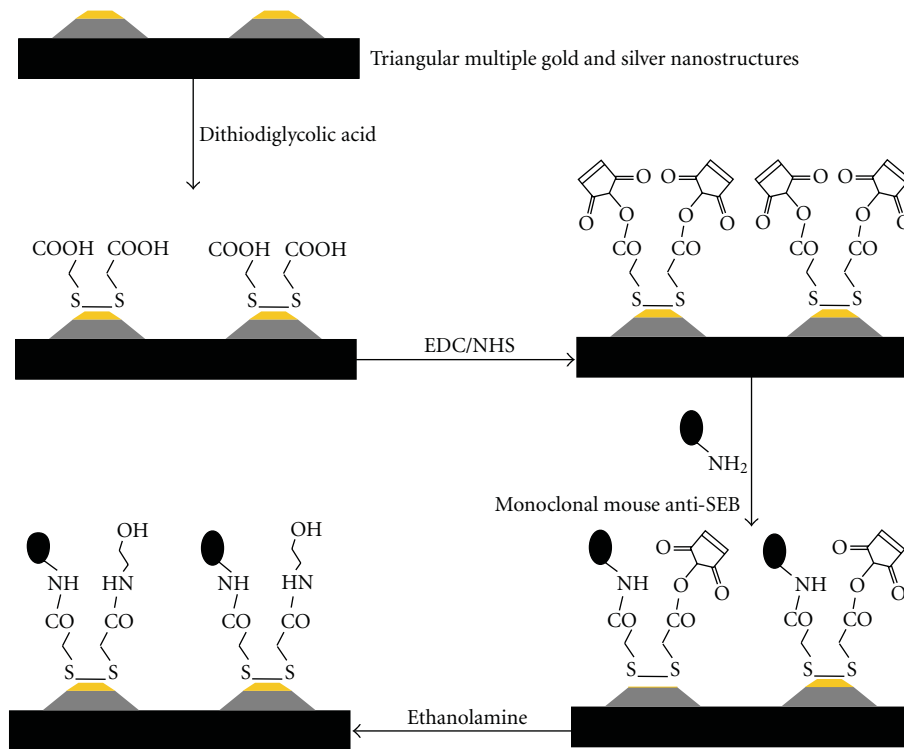


FIGURE 6: Schematic illustration of prefunctionalization for the nanostructure surface. From [2].

in $\lambda_{\max} = 556.31$ nm (see Figure 5, red line), corresponding to a -19.68 nm shift. It should be noted that $\Delta\lambda_{\max} = -19.68$ nm is smaller than the calculated result of the FDTD. It attributes the experiment defects caused by the NSL fabrication technique. The blue shift is caused by the scattered radiation from the incident radiation (ω) less than the vibrational frequencies of the molecules (ω_{vib}).

4.2. Detecting SEB. For SEB detection, Our experiments were carried out using home-made SEB prepared by our collaborator (Chinese Academy of Chemical Defence). Monoclonal mouse anti-SEB was purchased from Chemicon; 1-Ethyl-3-(3-dimethylaminopropyl) carbodiimide-HCl (EDC) and Sulfo-Nhydroxysuccinimide (S-NHS) from Pierce; ethanolamine from Sigma-Aldrich; dithiodiglycolic acid from Sigma; and phosphate buffer solution (PBS, 0.01 M, pH7.4) from Jinshan Chemical analyte Pte. Ltd. The buffer used in the experiments was prepared using double glass-distilled water.

Functionalization of the sensor is a multistep process that prepares the surface for specific detection applications. Prior to each experiment, the triangular hybrid Au-Ag nanostructure array was cleaned and prefunctionalized according to the following protocol: (1) the hybrid nanostructures were cleaned by sonicating the sample in ethanol in 3 min.; (2) dithiodiglycolic acid (2 mM) aqueous solution was dropped to the surface of the samples and reacting in 30 min.; (3) the carboxyl groups on dithiodiglycolic acid were activated in 30 min. using the same volume of EDC (0.4 M) and S-NHS (0.1 M); (4) the samples were thoroughly rinsed with

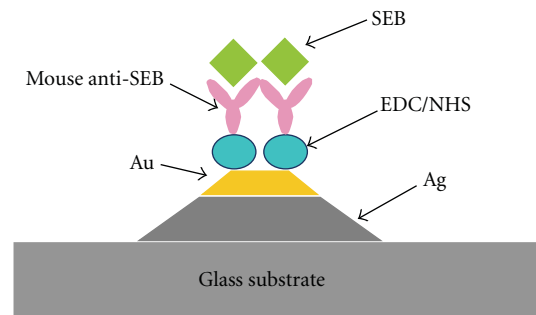


FIGURE 7: Schematic diagram of LSPR-sensor. From [2].

0.01 M PBS buffer and then dried by N_2 blowing with high-pressure; (5) monoclonal mouse anti-SEB IgG antibodies were coupled to the surface of the nanostructures by dropping $10 \mu\text{g}/\text{mL}$ solution in PBS buffer through chemical reaction between amidogen beside the alkaline aminophenol (Arg and Lys) of IgG and the active carboxyl; (6) redundant active ester groups were enclosed by 1 M ethanolamine aqueous solution. Finally, the samples were rinsed by 0.01 M PBS buffer and a hybrid Au-Ag SEB nano-biosensor was formed. A schematic illustration of the prefunctionalization for the nanostructures surface and a description (with figure) of the LSPR-sensor are shown in Figures 6 and 7, respectively.

The LSPR nano-biosensors are extremely sensitive to a change of refractive index (RI) within the range of a few hundred nanometers from the Au surface. Capturing of the target analyte (SEB) by homologous antibody (monoclonal

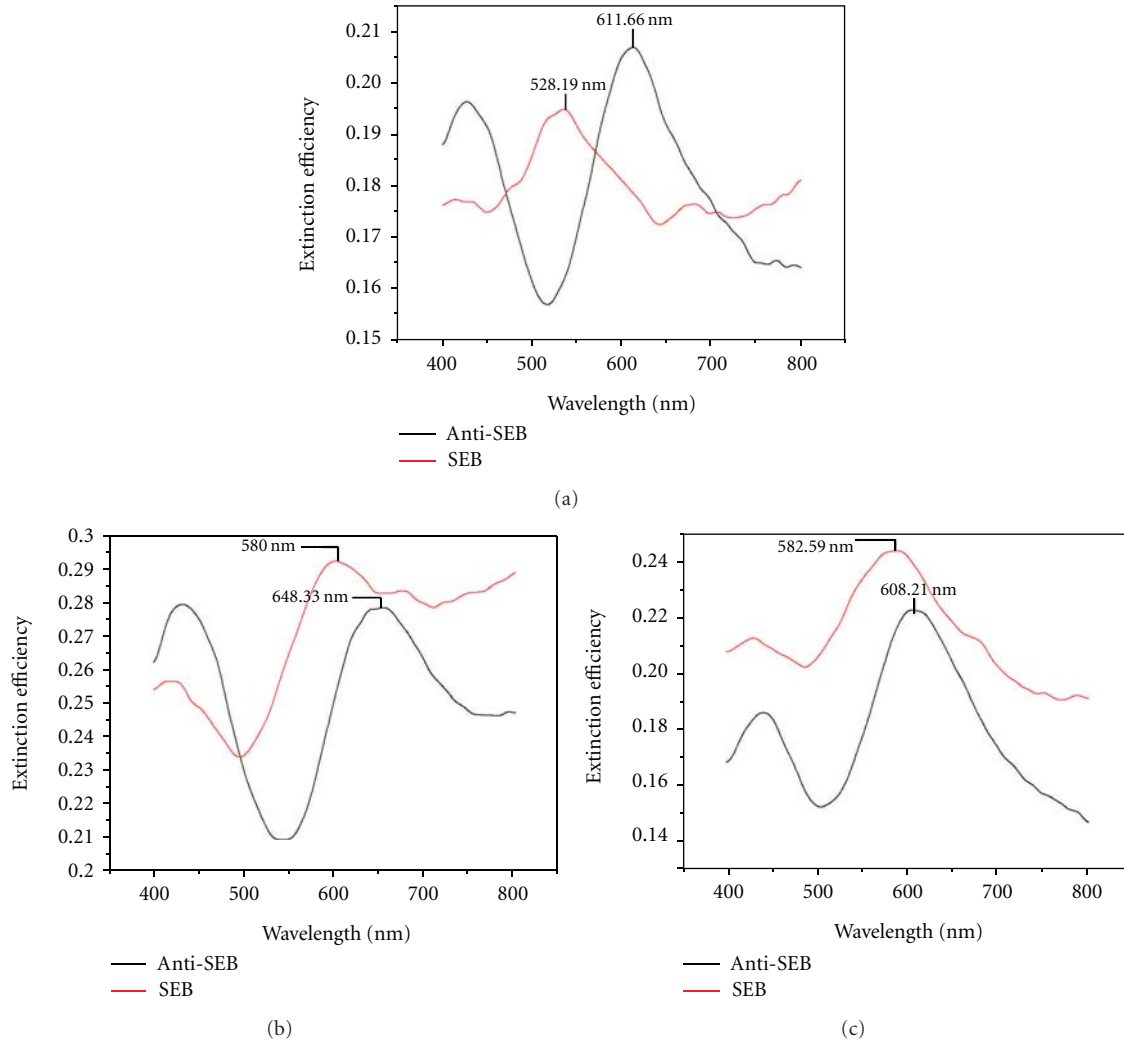


FIGURE 8: Measured spectra of the LSPR-based hybrid Au-Ag nanobiosensor for specific binding detection with detection concentration of (a) 10 $\mu\text{g/mL}$ SEB, (b) 1 $\mu\text{g/mL}$ SEB, and (c) 100 ng/mL SEB. From [2].

mouse anti-SEB antibody) bound to the sensing surface varies the RI significantly due to a solution displacement by the analytes with higher refractive index. To test the detection capability of the hybrid Au-Ag triangular particle-based nano-biosensors, experiments were carried out on the basis of the SEB solutions of various concentrations in PBS buffer. Three independent experiments were performed for the SEB solutions in different concentrations of 10 $\mu\text{g/mL}$, 1 $\mu\text{g/mL}$, and 100 ng/mL SEB, respectively. In this study, the LSPR spectra for the specific binding signals were measured using the integrated LSPR biosensor (see Figure 8(a)). The LSPR λ_{\max} after monoclonal mouse anti-SEB antibody attachment (see Figure 8(a), black line) was measured to be 611.66 nm. Exposure to 10 $\mu\text{g/mL}$ SEB, corresponding peak wavelength of LSPR $\lambda_{\max} = 528.19$ nm (see Figure 8(a), red line), which corresponds to a $\Delta\lambda_{\max} = -83.47$ nm peak shift. Hereinafter, “+” denotes a red-shift and “-” a blue-shift. When the concentration of the SEB solution is changed to be 1 $\mu\text{g/mL}$ and 100 ng/mL, the corresponding peak shift-

ing of LSPR is $\Delta\lambda_{\max} = -68.33$ nm (see Figure 8(b)), and $\Delta\lambda_{\max} = -25.62$ nm (see Figure 8(c)), respectively. The main absorbance peak for the anti-SEB drifting from sample to sample (Figures 8(a)–8(c)) attributes to the changing of effective refractive index of the surrounding medium due to binding of SEB and anti-SEB. It should be noted that $\Delta\lambda_{\max} = -25.62$ nm is greatly larger than the resolving power of the integrated LSPR sensor (spectrum resolving power of the spectrometer is 1.7 nm). Therefore, it is reasonable to believe that even the SEB solution in lower concentration can be detected by the integrated LSPR biosensor. These will be performed in our next research project. All the extinction measurements were collected at atmosphere environment. To further explore detection performance of the SEB sensors, the concentration of SEB as low as 1 ng/mL was applied on the biochips. Figure 9 is the measured spectra of the LSPR-based hybrid Au-Ag nano-biosensor for the specific binding detection with detection concentration of 1 ng/mL SEB. It can be seen that the peak wavelength blue shifts

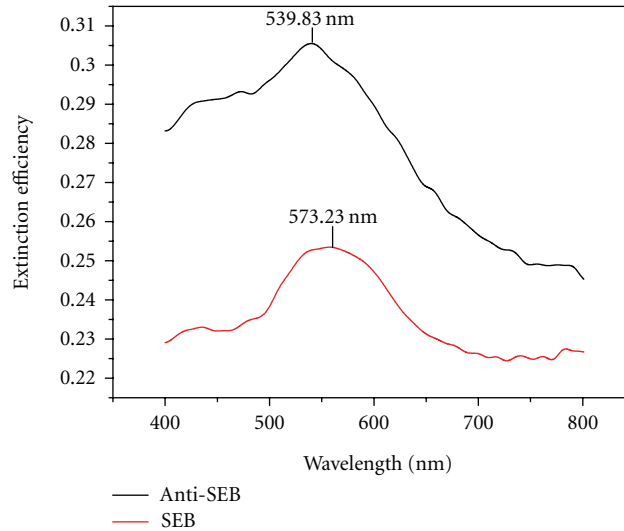


FIGURE 9: Measured spectra of the LSPR-based hybrid Au-Ag nanobiosensor for specific binding detection with detection concentration of 1 ng/mL SEB. From [2].

are $\Delta\lambda_{\max} = 539.83 \text{ nm} - 573.23 \text{ nm} = -33.4 \text{ nm}$. Actually, the differences of the resonance peak position are caused by different refractive index materials around the Ag nanostructures. The refractive index of materials changed can influence the resonance peak position. When the concentration of the SEB changed, the peak shifts will change. The red and blue shifts are caused by the scattered radiation from the incident radiation (ω) by an amount that corresponds to vibrational frequencies of the molecules (ω_{vib}). The frequency emitted by the photo $\omega_R = \omega \pm \omega_{\text{vib}}$. If $\omega > \omega_{\text{vib}}$, it causes red shift; if $\omega < \omega_{\text{vib}}$ (smaller SEB concentration), it leads to blue shift.

Our Ag-Au composite structures can be verified by our binding detection results, as shown in Figure 8. If the structure does not involve Au, dithiodiglycolic acid (see Figure 6) cannot bind with the nanostructures because it binds with Au only [38]. Dithiodiglycolic acid derivatives have a thiol group that reacts with Au atoms. Therefore, the immobilization process of dithiodiglycolic acid derivatives on the Au surface occurred spontaneously. The pure Ag particles bind with $-\text{OH}-$ only [11]. The binding detection spectra cannot be obtained without the hybrid structure with Au capped on the Ag particles. Compared to conventional SPR systems, at the same detection level, our presented LSPR-based biosensor is far simpler than the traditional SPR systems (e.g., Biacore system, etc.). The LSPR system is cost-effective, small volume, light weight, and portable because some subsystems such as temperature control, pressure control, and precise incident angle control are not necessary. The important advantages of our approach include that: (1) it can provide good selectivity and sensitivity without the labeling process. Our LSPR biosensor assay can detect SEB at approximately 1 ng/mL rapidly within 1 min; (2) spatial resolution of our detect approach is a single nanostructure while SPR sensors require at least a $10 \times 10 \mu\text{m}$ area for sensing experiments; (3) our LSPR nanobiosensor does not have temperature control, which can reduce the weight

and the volume of the detected spectrometric system; (4) The detected spectrometric system costs only 1/30 of the commercialized SPR instruments.

5. Summary

We reviewed the design, fabricate, and applications of our proposed hybrid Au-Ag triangular nanostructures. The refractive index sensitivity of hybrid Au-Ag triangular nanostructures is calculated by FDTD method. And we detected the sensitivity in experiment using protein A. This hybrid Au-Ag nanostructures are used to detect SEB solution. The detection sensitivity for SEB is nanogramme per milliliter level. All the design and experiment results show that the hybrid nanostructures are useful in the nanobiosensor research field. It has many potential applications in chemical material research fields.

References

- [1] S. L. Zhu, C. L. Du, and Y. Q. Fu, "Hybridization of localized surface plasmon resonance-based Au-Ag nanoparticles," *Biomedical Microdevices*, vol. 11, no. 3, pp. 579–583, 2009.
- [2] S. L. Zhu, C. L. Du, and Y. Q. Fu, "Localized surface plasmon resonance-based hybrid Au-Ag nanoparticles for detection of *Staphylococcus aureus* enterotoxin B," *Optical Materials*, vol. 31, no. 11, pp. 1608–1613, 2009.
- [3] H. Nakamura, Y. Mogi, T. Akimoto et al., "An enzyme-chromogenic surface plasmon resonance biosensor probe for hydrogen peroxide determination using a modified Trinder's reagent," *Biosensors and Bioelectronics*, vol. 24, no. 3, pp. 455–460, 2008.
- [4] J. Yuan, R. Oliver, J. Li, J. Lee, M. Aguilar, and Y. Wu, "Sensitivity enhancement of SPR assay of progesterone based on mixed self-assembled monolayers using nanoAu particles," *Biosensors and Bioelectronics*, vol. 23, no. 1, pp. 144–148, 2007.

- [5] A. J. Haes and R. P. van Duyne, "Nanosensors enable portable detectors for environmental and medical applications," *Laser Focus World*, vol. 39, no. 5, pp. 153–156, 2003.
- [6] F. C. Chien, C. Y. Lin, J. N. Yih et al., "Coupled waveguide-surface plasmon resonance biosensor with subwavelength grating," *Biosensors and Bioelectronics*, vol. 22, no. 11, pp. 2737–2742, 2007.
- [7] G. Rong, H. Wang, L. R. Skewis, and B. M. Reinhard, "Resolving Sub-Diffraction limit encounters in nanoparticle tracking using live cell plasmon coupling microscopy," *Nano Letters*, vol. 8, no. 10, pp. 3386–3393, 2008.
- [8] H. Uzawa, K. Ohga, Y. Shinozaki et al., "A novel sugar-probe biosensor for the deadly plant proteinous toxin, ricin," *Biosensors and Bioelectronics*, vol. 24, no. 4, pp. 923–927, 2008.
- [9] C. R. Yonzon, E. Jeoung, S. Zou, G. C. Schatz, M. Mrksich, and R. P. van Duyne, "A comparative analysis of localized and propagating surface plasmon resonance sensors: the binding of Concanavalin A to a monosaccharide functionalized self-assembled monolayer," *Journal of the American Chemical Society*, vol. 126, no. 39, pp. 12669–12676, 2004.
- [10] J. C. Riboh, A. J. Haes, A. D. McFarland, C. R. Yonzon, and R. P. van Duyne, "A nanoscale optical biosensor: real-time immunoassay in physiological buffer enabled by improved nanoparticle adhesion," *Journal of Physical Chemistry B*, vol. 107, no. 8, pp. 1772–1780, 2003.
- [11] A. J. Haes, S. Zou, G. C. Schatz, and R. P. van Duyne, "A nanoscale optical biosensor: the long range distance dependence of the localized surface plasmon resonance of noble metal nanoparticles," *Journal of Physical Chemistry B*, vol. 108, no. 1, pp. 109–116, 2004.
- [12] D. R. Franz, P. B. Jahrling, A. M. Friedlander et al., "Clinical recognition and management of patients exposed to biological warfare agents," *Journal of the American Medical Association*, vol. 278, no. 5, pp. 399–411, 1997.
- [13] T. Yoshida, "Sarin poisoning in Matsumoto, Nagano prefecture," *Journal of Toxicological Sciences*, vol. 19, no. 3, pp. 85–88, 1994.
- [14] T. Suzuki, H. Morita, K. Ono et al., "Sarin poisoning in Tokyo subway," *The Lancet*, vol. 345, no. 8955, pp. 980–981, 1995.
- [15] H. C. Holloway, A. E. Norwood, C. S. Fullerton, C. C. Engel, and R. J. Ursano Jr., "The threat of biological weapons: prophylaxis and mitigation of psychological and social consequences," *Journal of the American Medical Association*, vol. 278, no. 5, pp. 425–427, 1997.
- [16] T. R. Jensen, M. L. Duval, K. L. Kelly, A. Lazarides, G. C. Schatz, and R. P. van Duyne, "Nanosphere lithography: effect of the external dielectric medium on the surface plasmon resonance spectrum of a periodic array of silver nanoparticles," *Journal of Physical Chemistry B*, vol. 103, no. 45, pp. 9846–9853, 1999.
- [17] P. A. Emanuel, J. Dang, J. S. Gebhardt et al., "Recombinant antibodies: a new reagent for biological agent detection," *Biosensors and Bioelectronics*, vol. 14, no. 10–11, pp. 751–759, 2000.
- [18] K. A. Uithoven, J. C. Schmidt, and M. E. Ballman, "Rapid identification of biological warfare agents using an instrument employing a light addressable potentiometric sensor and a flow-through immunofiltration-enzyme assay system," *Biosensors and Bioelectronics*, vol. 14, no. 10–11, pp. 761–770, 2000.
- [19] C. A. Rowe-Taitt, J. P. Golden, M. J. Feldstein, J. J. Cras, K. E. Hoffman, and F. S. Ligler, "Array biosensor for detection of biohazards," *Biosensors and Bioelectronics*, vol. 14, no. 10–11, pp. 785–794, 2000.
- [20] H. Yu, J. W. Raymond, T. M. McMahon, and A. A. Campagnari, "Detection of biological threat agents by immunomagnetic microsphere-based solid phase fluorogenic- and electrochemiluminescence," *Biosensors and Bioelectronics*, vol. 14, no. 10–11, pp. 829–840, 2000.
- [21] T. O'Brien, L. H. Johnson III, J. L. Aldrich et al., "The development of immunoassays to four biological threat agents in a bidiffractive grating biosensor," *Biosensors and Bioelectronics*, vol. 14, no. 10–11, pp. 815–828, 2000.
- [22] N. N. Alexei, D. S. Scott, K. N. Di et al., "Detection of Staphylococcus aureus enterotoxin B at femtomolar levels with a miniature integrated two-channel surface plasmon resonance (SPR) sensor," *Biosensors and Bioelectronics*, vol. 17, no. 6–7, pp. 573–584, 2002.
- [23] S. L. Zhu, X. G. Luo, C. L. Du et al., "Hybrid metallic nanoparticles for excitation of surface plasmon resonance," *Journal of Applied Physics*, vol. 101, no. 6, Article ID 064701, 2007.
- [24] S. L. Zhu, C. L. Du, Y. Q. Fu, and A. Liu, "Tuning optical properties of rhombic hybrid Au-Ag nanoparticles: a discrete dipole approximation calculation," *Journal of Computational and Theoretical Nanoscience*, vol. 6, no. 5, pp. 1034–1038, 2009.
- [25] S. L. Zhu and W. Zhou, "Effect of gold coating on sensitivity of rhombic silver nanostructure array," *Plasmonics*, vol. 4, no. 4, pp. 303–306, 2009.
- [26] S. L. Zhu and W. Zhou, "Optical characteristics of rhombic hybrid Au-Ag nanostructures calculated by discrete dipole approximation method," *Journal of Computational and Theoretical Nanoscience*, vol. 7, no. 3, pp. 634–637, 2010.
- [27] S. L. Zhu and W. Zhou, "Sensitivity of triangular hybrid Au-Ag nanostructure array," *Journal of Computational and Theoretical Nanoscience*, vol. 7, no. 8, pp. 1414–1517, 2010.
- [28] A. L. Aden and M. Kerker, "Scattering of electromagnetic waves from two concentric spheres," *Journal of Applied Physics*, vol. 22, no. 10, pp. 1242–1246, 1951.
- [29] B. T. Draine and P. J. Flatau, "Discrete-dipole approximation for scattering calculations," *Journal of the Optical Society of America A*, vol. 11, no. 4, pp. 1491–1499, 1994.
- [30] A. Skarlatos, R. Schuhmann, and T. Weiland, "Solution of radiation and scattering problems in complex environments using a hybrid finite integration technique-uniform theory of diffraction approach," *IEEE Transactions on Antennas and Propagation*, vol. 53, no. 10, pp. 3347–3357, 2005.
- [31] C. Oubre and P. Nordlander, "Optical properties of metallo-dielectric nanostructures calculated using the finite difference time domain method," *The Journal of Physical Chemistry B*, vol. 108, no. 46, pp. 17740–17747, 2004.
- [32] A. A. Pisano, A. Sofi, and P. Fuschi, "Finite element solutions for Eringen-type nonlocal elastic 2D problems," *International Journal of Solids and Structures*, vol. 46, no. 21, pp. 3836–3849, 2009.
- [33] S. Kawata, M. Ohtsu, and M. Irie, *Nano-Optics*, Springer, Heidelberg, Germany, 2002.
- [34] A. J. Haes and R. P. van Duyne, "A nanoscale optical biosensor: sensitivity and selectivity of an approach based on the localized surface plasmon resonance spectroscopy of triangular silver nanoparticles," *Journal of the American Chemical Society*, vol. 124, no. 35, pp. 10596–10604, 2002.
- [35] S. Zhu, C. Du, and Y. Fu, "Fabrication and characterization of rhombic silver nanoparticles for biosensing," *Optical Materials*, vol. 31, no. 6, pp. 769–774, 2009.
- [36] Z. Merican, T. L. Schiller, C. J. Hawker, P. M. Fredericks, and I. Blakey, "Self-assembly and encoding of polymer-stabilized

- gold nanoparticles with surface-enhanced Raman reporter molecules,” *Langmuir*, vol. 23, no. 21, pp. 10539–10545, 2007.
- [37] K. J. Thurecht, I. Blakey, H. Peng et al., “Functional hyper-branched polymers: toward targeted in vivo ^{19}F magnetic resonance imaging using designed macromolecules,” *Journal of the American Chemical Society*, vol. 132, no. 15, pp. 5336–5337, 2010.
- [38] M. Lee, Y. Hur, T. Kim et al., “Surface plasmon resonance study on the interaction between the fructose and phenylboronic acid monolayer,” *Microchemical Journal*, vol. 72, no. 3, pp. 315–321, 2002.

Research Article

Making Organic-Inorganic Nanocomposites via Selective Dispersion of PS-Tethered SiO₂ Particles in Polystyrene-Block-Polymethylmethacrylate Copolymer

Chia-Hong Liu, Li-Ko Chiu, Je-Yuan Yeh, and Raymond Chien-Chao Tsiang

Department of Chemical Engineering, National Chung Cheng University, Chiayi 621, Taiwan

Correspondence should be addressed to Raymond Chien-Chao Tsiang, chmct@ccu.edu.tw

Received 6 June 2011; Accepted 10 August 2011

Academic Editor: Hui Wang

Copyright © 2012 Chia-Hong Liu et al. This is an open access article distributed under the Creative Commons Attribution License, which permits unrestricted use, distribution, and reproduction in any medium, provided the original work is properly cited.

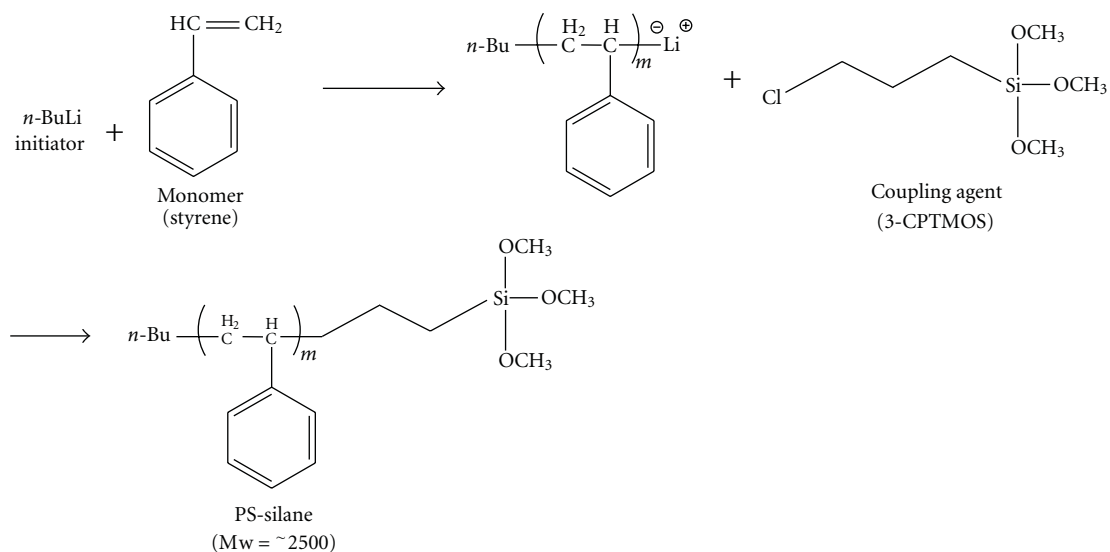
SiO₂ nanoparticles have been dispersed selectively in the polystyrene (PS) microdomain of polystyrene-*block*-polymethylmethacrylate (PS-*b*-PMMA) block copolymer via the blending of PS-*b*-PMMA with PS-tethered SiO₂. As observed by atomic force microscopy and scanning electron microscopy, the incorporation of SiO₂ particles not only enlarges the PS microdomain but also reduces the surface energy of the PS microdomain and transforms the morphology from either lamellar layers or cylinders to islanded bicontinuous microstructures. Blending SiO₂ particles with an excessive amount or with a particle size larger than that of the PS microdomain would pose an extreme constraint on the molecular rearrangement, unbalance the microdomain separation, and even make the microdomain separation unobservable. The nanosize and the uniform distribution of the PS microdomain in the PS-*b*-PMMA polymer have thus enabled us to achieve a uniform distribution of the inorganic SiO₂ particles in the organic polymeric matrix.

1. Introduction

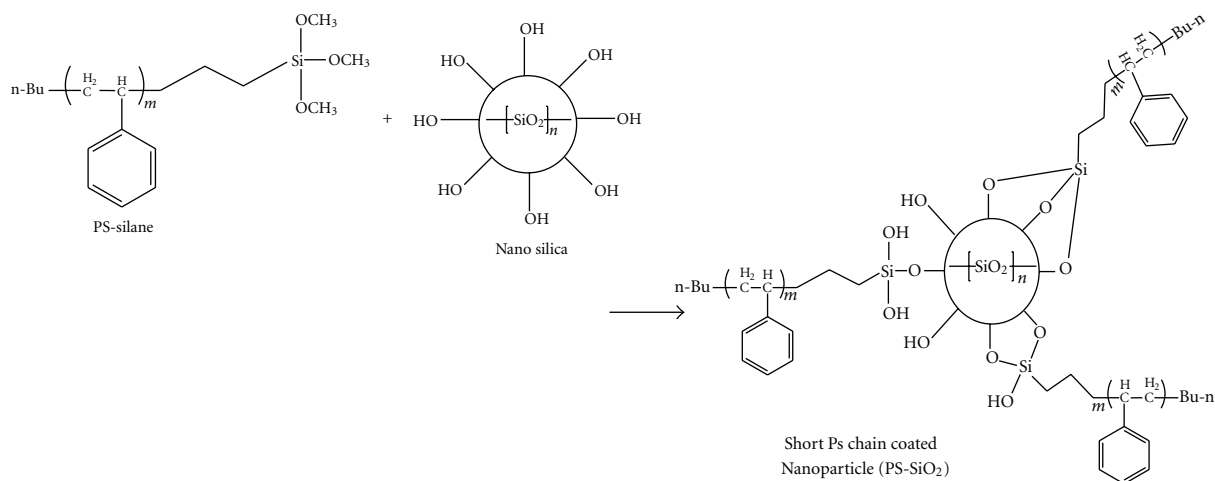
Block copolymers are known for their microdomain separation which attains various periodic nanostructures under proper compositions and conditions [1–8]. In recent years, nanotemplating studies involving block copolymers have gained extensive interest. Nanowires such as Co, Ag, and Au or nanoparticles such as CdSe, Pd, and TiO₂ have been reported either to grow in or to be blended into a specific microdomain [9–15]. The selective dispersion of nanoparticles in one of the microdomains has great potential in applications such as photonic crystals with enhanced refractive index contrast between microdomains [9–11], and nanoporous hybrid membranes after etching one of the microdomains [16–34]. The growth of nanoparticles in one of the microdomains of a diblock copolymer often requires the functionalization of that specific microdomain with precursor complexes followed by an in situ reduction of that precursor complexes to form nanoparticles. On the other hand, the blending of nanoparticles into one of the microdomains requires the pretreatment of nanoparticles with

various surfactants, such as ionic or nonionic types, or functioning agents containing functional groups compatible with the targeted microdomain.

Recently, it has been reported that blending a homopolymer hA into a block copolymer A-*b*-B would result in changes in the microdomain separation depending upon the temperature, the wt% of homopolymer, the molecular weight ratio of homopolymer to the corresponding block, and the overall volume ratio of constituting species [35–38]. Under proper conditions, homopolymer hA could be solubilized in the A block either locally or uniformly. These studies have prompted us to explore another approach to selectively disperse SiO₂ nanoparticles in a PS-*b*-PMMA diblock copolymer. Here, in the current study, we have synthesized two PS-*b*-PMMA diblock copolymers with different ratios of PS to PMMA block lengths, having either an alternating lamellar layers or cylindrical microstructures, as well as a trimethoxysilane-terminated homopolystyrene (PS-silane). This PS-silane was thereafter tethered to SiO₂ nanoparticles to form PS-SiO₂ particles, and these PS-SiO₂ particles were then blended quantitatively with PS-*b*-PMMA to make an



SCHEME 1: Synthesis of PS-silane.

SCHEME 2: Synthesis of PS-SiO₂.

organic-inorganic nanocomposite material with a targeted PS/PMMA volume ratios. We envisioned that the compatibility between PS-SiO₂ and the PS-*b*-PMMA would result in a dispersion of SiO₂ nanoparticles exclusively in the PS microdomain and thus enable a uniform distribution of the inorganic SiO₂ particles in the organic polymeric matrix.

2. Experimental

2.1. Materials. Styrene (S) and methyl methacrylate (MMA) (both with a purity of 99%) were acquired from Aldrich and predistilled with CaH₂ to remove the inhibitor before use. *n*-Butyllithium (*n*-BuLi) was obtained from Taiwan Synthetic Rubber Corp. 1,1-Diphenylethylene (DPE) purchased from Alfa Aesar had a purity of 98% and was diluted in toluene at a concentration of 0.6M before use. (3-Chloropropyl) trimethoxysilane (3-CPTMOS) was acquired from Aldrich at 97% purity. Colloidal nanosized silica (SiO₂) of a diameter of

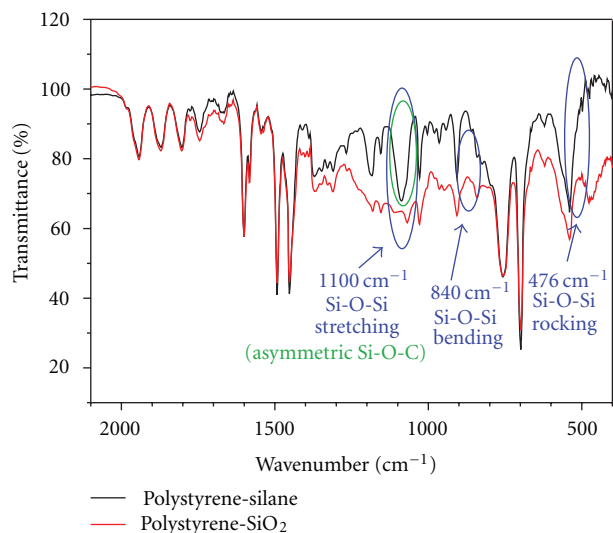
10~20 nm was supplied by Echo Nano-bio Co., Ltd., Taiwan as a clear suspension in isopropanol (IPA) with a solid content of 30%. Other chemicals were purchased from J. T. Baker and used as received.

2.2. Measurements. The molecular structures of PS-*b*-PMMA samples were determined from ¹HNMR (Varian-Unity INOVA-500 MHz) spectra of samples in deuterated chloroform (CDCl₃) at 30°C. The functional groups of samples were analyzed with a Shimadzu SSU-8000 FTIR spectrophotometer. Scanning electron microscope (SEM) images were obtained on a Hitachi S4800 Type I SEM system for samples spin-coated on a silicon wafer. The atomic force microscope (AFM) height-mode micrographs were obtained from the Quesant Universal SPM Instruments, using as the AFM tip a silicon nitride-based cantilever coated with a magnetic film.

TABLE 1: Molecular characteristics of PS-*b*-PMMA samples.

	Mol% of styrene	M _w absolute of PS	M _w absolute of PS- <i>b</i> -PMMA	Vol% of Styrene	PDI
Sample(1)	36.67	8655	23037	40.57	1.21
Sample(2)	25.53	17750	67535	28.79	1.26

(The absolute molecular weights of PS and PS-*b*-PMMA were measured by GPC and ¹HNMR, resp.).

FIGURE 1: FTIR spectra for PS-silane and PS-SiO₂.

2.3. Synthesis and Characterization of PS-*b*-PMMA. The synthesis of PS-*b*-PMMA was accomplished via a sequential anionic polymerization in toluene. The choice of toluene as the solvent was due to the need of a polar environment for the polymerization of MMA. The PS-*b*-PMMA was synthesized following typical anionic polymerization procedures [39, 40]. A total of 150 mL of toluene, 5 mL styrene monomer, and 0.2 mL of tetrahydrofuran (THF) (to accelerate the polymerization) were charged into a 250 mL pressure vessel under a slight nitrogen overpressure. Afterwards styrene was polymerized at room temperature for 1 hr with the addition of 0.202 mL *n*-BuLi as the initiator. The color turned to reddish orange indicating the presence of living polystyryl-lithium anions. Next, DPE was added, and the reaction continued for another 1 hr. Thus, the living PS chain was capped by the DPE molecule (or a few DPE molecules) so as to provide the steric hindrance required for the following MMA polymerization. Thereafter, the reactor temperature was lower to -78°C , and 4 mL of MMA monomer was added to continue the polymerization reaction for 1 hr, forming the final product PS-*b*-PMMA. The low polymerization temperature, that is, -78°C , was necessary in order to minimize the unwanted side reactions. At the completion of the reaction, methanol was added to quench the reaction and the vessel content was poured into a large amount of deionized water under vigorous stirring to extract residual salts into the aqueous phase. The organic phase containing the dissolved PS-*b*-PMMA was then separated from the aqueous phase. The

extraction step was repeated three times, and the final organic phase was poured into methanol for the precipitation of PS-*b*-PMMA. The precipitated PS-*b*-PMMA was then dried at 40°C in a vacuum. The control of the block lengths of PS-*b*-PMMA has been achieved by the precise control of the feed amount of styrene and MMA.

2.4. Synthesis and Characterization of PS-Silane. In order to blend the hydrophilic SiO₂ into PS-*b*-PMMA matrix, PS-silane was first prepared via Scheme 1.

A total of 100 mL cyclohexane, 0.2 mL THF, and 5 mL styrene monomer was charged into a 250 mL glass reactor, followed by the addition of 2 mL *n*-BuLi. The reaction was allowed to proceed for 1 hr before termination with 3-CPTMOS. The PS-silane was precipitated in methanol and dried. A low molecular weight PS (MW = 2200, PDI = 1.10) was synthesized by controlling the ratio of *n*-BuLi to styrene. At the end of polymerization, 3-CPTMOS was added to terminate the living PS chain forming the PS-silane.

2.5. Functionalization of SiO₂ by Anchoring PS-Silane onto Nanosilica via the Sol-Gel Reaction to (Making PS-SiO₂). The hydrophilic nanosilica particles contain inherent hydroxyls at the surface and can hardly react with the hydrophobic PS-silane. Fortunately, a mixture of dichlorobenzene (DCB) and IPA at 3 : 2 volume ratio is able to dissolve both of them. Thus, the sol-gel reaction occurs (with an addition of 0.1 M HCl to maintain the pH at 3 ~ 4) between the nanosilica and PS-silane in the mixed solvent as in Scheme 2.

In this work, a total of 0.5 g of PS-silane was dissolved in 15 g of DCB followed by the addition of 10 g of IPA and 0.09 g of 30 wt% SiO₂ in IPA solution. The mixture was agitated at 75°C for 3 mins, and then 2 g of 0.1 M HCl was added. The sol-gel reaction was allowed to take place for 2 hrs before the PS-SiO₂ was precipitated out in methanol.

2.6. Blending of PS-*b*-PMMA with PS-SiO₂ to Make a Hybrid Film. PS-*b*-PMMA and PS-SiO₂ were mixed at various weight ratios in toluene for preparing a solution of 1 wt% concentration. Afterwards, 9 drops of solution were added onto the surface of a 2 cm × 2 cm wafer which had been cleaned with acetone, IPA, and deionized water sequentially and dried before use. The hybrid film was made after 60 sec spin coating at 4000 rpm. Thereafter, the wafer was put together with the film in a vacuum oven at 180°C for annealing and self-assembling. After 24 hrs, the temperature was lowered to 30°C , and the drying continued for another 24 hrs.

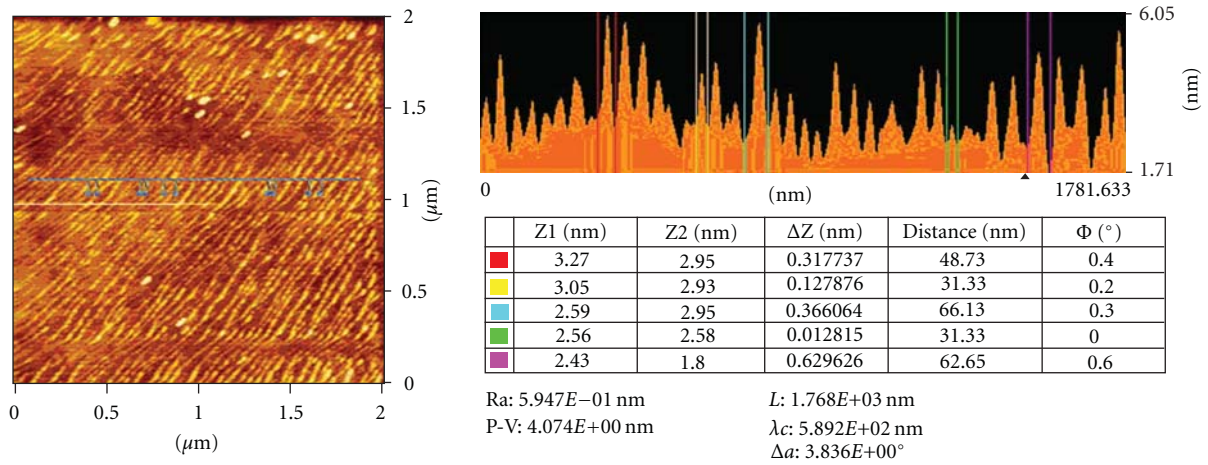
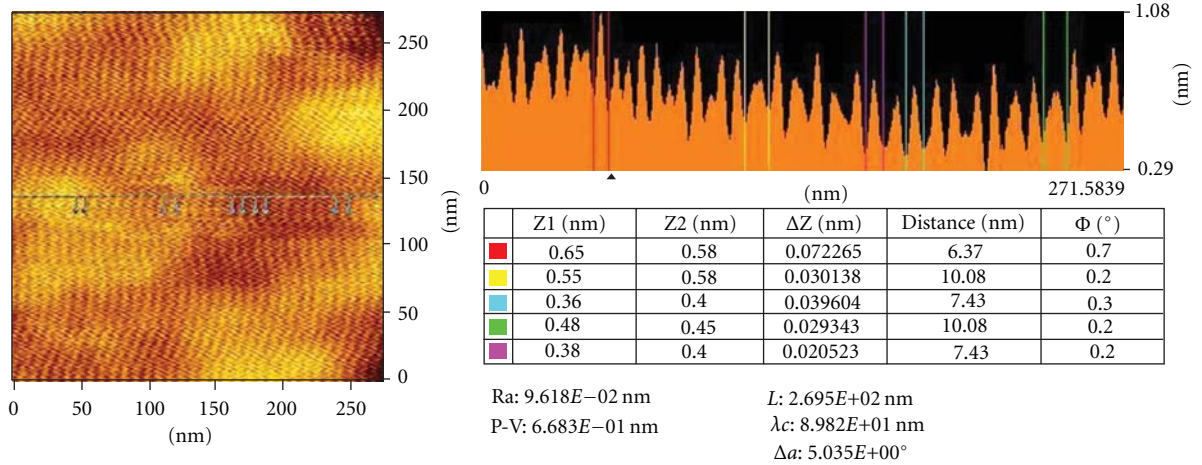


FIGURE 2: (a) AFM image of sample(1), and (b) AFM image of sample(1)/PS-SiO₂.

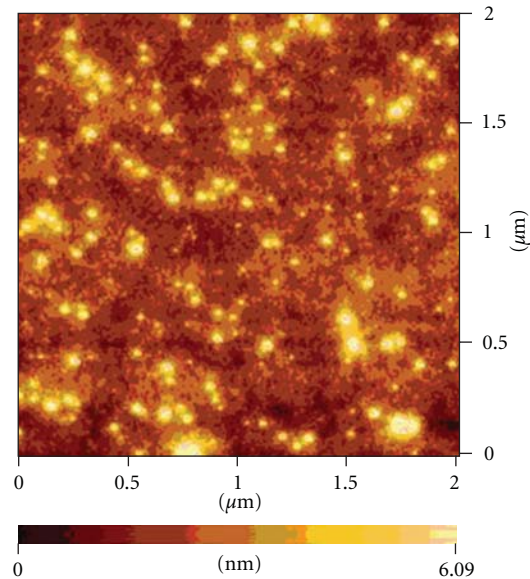


FIGURE 3: AFM image of sample(1)/PS-SiO₂ with 7:3 volume ratio of PS to PMMA.

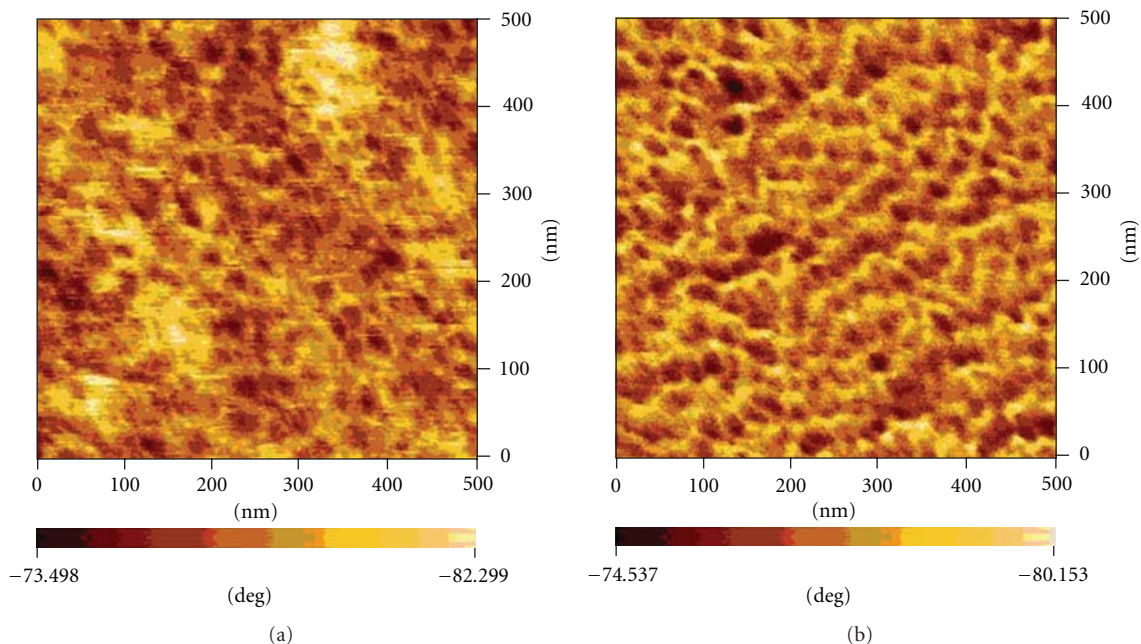


FIGURE 4: (a) AFM image of sample(2), and (b) AFM image of sample(2)/PS-SiO₂ with 5 : 5 volume ratio of PS to PMMA.

3. Results and Discussion

Two, PS-*b*-PMMA samples have been synthesized in this work and the polymers are characterized by GPC(SEC) and ¹HNMR as shown in Table 1. Based on the measured molecular weights of PS block and PS-*b*-PMMA, the molecular weight of PMMA block is calculated. Afterwards, the volume fraction of PS and PMMA blocks are calculated by dividing the molecular weights of each block by the well-known density of corresponding PS and PMMA homopolymer, ρ_{PS} ($= 1.05 \text{ g/cm}^3$) and ρ_{PMMA} ($= 1.19 \text{ g/cm}^3$).

The synthesized PS-silane has been verified by GPC and ¹HNMR to have a molecular weight of 2363 (PDI: 1.10) which comprises a PS chain length of 2200 and a terminal 3-CPTMOS (molecular weight: 163 after the elimination of chlorine atom).

The successful completion of the sol-gel reaction between PS-silane and SiO₂ has been verified by the disappearance of Si-O-C stretches and the generation of Si-O-Si stretches in the PS-SiO₂ spectrum (as shown in Figure 1).

While the sol-gel reaction occurs between PS-silane and the nanosilica particle, sol-gel reaction can also occur between nanosilica particles owing to the silanol groups on the surface of these particles. As a result, it is difficult either to analyze the number of PS-silane molecules bound to each nanosilica particle or to achieve a uniform size of the final PS-SiO₂ particles. Nevertheless, despite a few aggregates, the particle size of PS-SiO₂ observed under AFM is largely within a range of 15 ~ 40 nm. Blending various amounts of these PS-SiO₂ particles into the aforementioned PS-*b*-PMMA samples enables us to make composite materials with various PS to PMMA ratios, which indirectly affects the morphologies. All samples, either the pristine PS-*b*-PMMA or the PS-*b*-PMMA/PS-SiO₂ composites, after being spin-coated as

films on silicon wafer and annealed at 180°C for 24 hrs, were examined under AFM. The AFM image of sample(1), having a nearly 4 : 6 PS/PMMA volume ratio, exhibits phase separation of a lamellar type (shown in Figure 2(a)). The size of each microdomain (either PS or PMMA layer thickness) is approximately 6–10 nm. In contrast, the composite, comprising 0.018 g of PS-SiO₂ and 0.1 g of sample(1), has a 5 : 5 volume ratio and displays a markedly different phase morphology (shown in Figure 2(b)).

In these AFM images, the bright yellow layers represent the PMMA microdomains, the dark brown areas represent the PS microdomains, and the bright spots represent SiO₂ particles. Because the PS-SiO₂ particles are compatible with the PS microdomain of sample(1), they tend to reside in the PS microdomain. However, because the size of PS-SiO₂ particles (15 ~ 40 nm) is larger than the microdomain size of sample(1) (6–10 nm), PS-SiO₂ particles has enlarged the PS microdomain and caused a rearrangement of PMMA microdomains. Because the size of the PMMA microdomain has been measured as 30 ~ 70 nm, the incorporation of PS-SiO₂ into the PS microdomain thereby has also enlarged the size of the PMMA microdomain.

Furthermore, when sample(1) is blended with PS-SiO₂ to make a composite with 7 : 3 PS to PMMA volume ratio, the number of bright spots increases as a result of an increase in the amount of PS-SiO₂ (Figure 3). It is worthy to note that the phase separation which used to be seen clearly in sample(1) now disappears. Apparently, the excessive amount of PS-SiO₂ poses an extreme constraint on the molecular rearrangement and makes the microdomain separation unobservable.

Similar investigations have been conducted on sample (2). At a nearly 3 : 7 PS to PMMA volume ratio, sample(2) exhibits a cylindrical morphology for PS microdomain

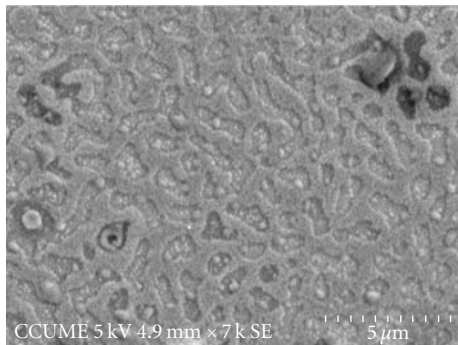


FIGURE 5: SEM micrograph of sample(2)/PS-SiO₂ at 5 : 5 PS/PMMA volume ratio.

oriented in either the vertical or the horizontal direction (shown in Figure 4(a)). The size of the PS microdomain is approximately 20–30 nm.

0.1 g of sample(2) has also been blended with 0.039 g of PS-SiO₂, that is, 39% addition, to make a composite sample with a 5 : 5 PS to PMMA volume ratio. Because the PS microdomain size is larger than the particle size of PS-SiO₂, it is theoretically easier to have all the PS-SiO₂ particles embedded in the PS microdomain during the blending of PS-SiO₂ with PS-*b*-PMMA. Therefore, it would be difficult to distinguish the SiO₂ particles from the PS microdomains (as shown in Figure 4(b)). In order to observe the distribution of PS-SiO₂ particles and examine whether there is any microdomain changes after the blending of PS-SiO₂ with PS-*b*-PMMA, SEM has been used. The SEM micrograph for a composite sample with a 5 : 5 PS to PMMA volume ratio is shown in Figure 5.

Owing to the indistinguishable electron densities of PS and PMMA, RuO₄ has been used for the dyeing of PS microdomain to facilitate the microscopy analysis [41–43]. It is clearly seen that all PS-SiO₂ particles are selectively residing in the islanded PS microdomains and the PS microdomains are enlarged by the incorporation of PS-SiO₂ particles (presumably caused by the molecular chain rearrangement during the domain formation). Furthermore, the incorporation of PS-SiO₂ particles also transforms the morphology from cylinders to islanded bicontinuous microstructures because of the inherent low surface energy of SiO₂.

4. Conclusion

With PS-tethering, SiO₂ nanoparticles can be dispersed selectively in the PS microdomain of PS-*b*-PMMA block copolymer. Despite the change in size and morphology of microdomains, the uniform distribution of the PS microdomain in the PS-*b*-PMMA polymer enables us to achieve a uniform distribution of the inorganic SiO₂ particles in the organic polymeric matrix.

Acknowledgment

Financial support provided by the National Science Council of the Republic of China under the program NSC97-2221-E-194-002-MY3 is greatly appreciated.

References

- [1] F. S. Bates, "Polymer-polymer phase behavior," *Science*, vol. 251, no. 4996, pp. 898–905, 1991.
- [2] E. L. Thomas, "The ABCs of self-assembly," *Science*, vol. 286, no. 5443, p. 1307, 1999.
- [3] L. Zhu, S. Z. D. Cheng, P. Huang et al., "Nanoconfined polymer crystallization in the hexagonally perforated layers of a self-assembled PS-*b*-PEO diblock copolymer," *Advanced Materials*, vol. 14, no. 1, pp. 31–34, 2002.
- [4] S. Choi, K. M. Lee, C. D. Han, N. Sota, and T. Hashimoto, "Phase transitions in sphere-forming polystyrene-block-polyisoprene-block-polystyrene copolymer and its blends with homopolymer," *Macromolecules*, vol. 36, no. 3, pp. 793–803, 2003.
- [5] E. Buck and J. Fuhrmann, "Surface-induced microphase separation in spin-cast ultrathin diblock copolymer films on silicon substrate before and after annealing," *Macromolecules*, vol. 34, no. 7, pp. 2172–2178, 2001.
- [6] Y. L. Loo, R. A. Register, and A. J. Ryan, "Modes of crystallization in block copolymer microdomains: breakout, templated, and confined," *Macromolecules*, vol. 35, no. 6, pp. 2365–2374, 2002.
- [7] Y. L. Loo, R. A. Register, A. J. Ryan, and G. T. Dee, "Polymer crystallization confined in one, two, or three dimensions," *Macromolecules*, vol. 34, no. 26, pp. 8968–8977, 2001.
- [8] A. Röttele, T. Thurn-Albrecht, J. U. Sommer, and G. Reiter, "Thermodynamics of formation, reorganization, and melting of confined nanometer-sized polymer crystals," *Macromolecules*, vol. 36, no. 4, pp. 1257–1260, 2003.
- [9] C. C. Weng and K. H. Wei, "Selective distribution of surface-modified TiO₂ nanoparticles in polystyrene-*b*-poly(methyl methacrylate) diblock copolymer," *Chemistry of Materials*, vol. 15, no. 15, pp. 2936–2941, 2003.
- [10] Y. Fink, A. M. Urbas, M. G. Bawendi, J. D. Joannopoulos, and E. L. J. Thomas, "Block copolymers as photonic bandgap materials," *Journal of Lightwave Technology*, vol. 17, no. 11, pp. 1963–1969, 1999.
- [11] A. C. Edrington, A. M. Urbas, P. DeRege et al., "Polymer-based photonic crystals," *Advanced Materials*, vol. 13, no. 6, pp. 421–425, 2001.
- [12] S. W. Yeh, K. H. Wei, Y. S. Sun, U. S. Jeng, and K. S. Liang, "Morphological transformation of PS-*b*-PEO diblock copolymer by selectively dispersed colloidal CdS quantum dots," *Macromolecules*, vol. 36, no. 21, pp. 7903–7907, 2003.
- [13] B. J. Kim, J. J. Chiu, G. R. Yi, D. J. Pine, and E. J. Kramer, "Nanoparticle-induced phase transitions in diblock-copolymer films," *Advanced Materials*, vol. 17, no. 21, pp. 2618–2622, 2005.
- [14] S. C. Park, B. J. Kim, C. J. Hawker, E. J. Kramer, J. Bang, and J. S. Ha, "Controlled ordering of block copolymer thin films by the addition of hydrophilic nanoparticles," *Macromolecules*, vol. 40, no. 22, pp. 8119–8124, 2007.
- [15] C. P. Li, C. H. Wu, K. H. Wei et al., "The effect of nanoscale confinement on the collective electron transport behavior in Au nanoparticles self-assembled in a nanostructured polystyrene-block-poly(4-vinylpyridine) diblock copolymer ultrathin film," *Advanced Functional Materials*, vol. 17, no. 14, pp. 2283–2290, 2007.
- [16] V. Z.-H. Chan, J. Hoffman, V. Y. Lee et al., "Ordered bicontinuous nanoporous and nanorelief ceramic films from self-assembling polymer precursors," *Science*, vol. 286, no. 5445, pp. 1716–1719, 1999.

- [17] T. Hashimoto, K. Tsutsumi, and Y. Funaki, "Nanoprocessing based on bicontinuous microdomains of block copolymers: nanochannels coated with metals," *Langmuir*, vol. 13, no. 26, pp. 6869–6872, 1997.
- [18] K. W. Ho, "Ozonation of hydrocarbon diene elastomers: a mechanistic study," *Journal of Polymer Science Part A: Polymer Chemistry*, vol. 24, no. 10, pp. 2467–2482, 2003.
- [19] J. T. Goldbach, K. A. Lavery, J. Penelle, and T. P. Russell, "Nano- to macro-sized heterogeneities using cleavable diblock copolymers," *Macromolecules*, vol. 37, no. 25, pp. 9639–9645, 2004.
- [20] K. W. Guarini, C. T. Black, and S. H. I. Yeung, "Optimization of diblock copolymer thin film self assembly," *Advanced Materials*, vol. 14, no. 18, pp. 1290–1294, 2002.
- [21] E. Huang, P. Mansky, T. P. Russell et al., "Mixed lamellar films: evolution, commensurability effects, and preferential defect formation," *Macromolecules*, vol. 33, no. 1, pp. 80–88, 2000.
- [22] E. Jeoung, T. H. Galow, J. Schotter et al., "Fabrication and characterization of nanoelectrode arrays formed via block copolymer self-assembly," *Langmuir*, vol. 17, no. 21, pp. 6396–6398, 2001.
- [23] B. J. Melde, S. L. Burkett, T. Xu, J. T. Goldbach, T. P. Russell, and C. J. Hawker, "Silica nanostructures templated by oriented block copolymer thin films using pore-filling and selective-mineralization routes," *Chemistry of Materials*, vol. 17, no. 18, pp. 4743–4749, 2005.
- [24] Q. Ren, H. J. Zhang, X. K. Zhang, and B. T. Huang, "Hydrogenated polybutadiene-polymethyl methacrylate (HPB-PMMA) block copolymer. I. Synthesis of polybutadiene-polymethyl methacrylate (PB-PMMA) block copolymer," *Journal of Polymer Science Part A: Polymer Chemistry*, vol. 31, no. 4, pp. 847–851, 1993.
- [25] L. Rockford, S. G. J. Mochrie, and T. P. Russell, "Propagation of nanopatterned substrate templated ordering of block copolymers in thick films," *Macromolecules*, vol. 34, no. 5, pp. 1487–1492, 2001.
- [26] T. Thurn-Albrecht, J. Schotter, G. A. Kästle et al., "Ultra-high-density nanowire arrays grown in self-assembled diblock copolymers templates," *Science*, vol. 290, no. 5499, pp. 2126–2129, 2000.
- [27] T. Thurn-Albrecht, R. Steiner, J. DeRouchey et al., "Nanoscale templates from oriented block copolymer films," *Advanced Materials*, vol. 12, no. 11, pp. 787–791, 2000.
- [28] S. Wei, B. Vaidya, A. B. Patel, S. A. Soper, and R. L. McCarley, "Photochemically patterned poly(methyl methacrylate) surfaces used in the fabrication of microanalytical devices," *Journal of Physical Chemistry B*, vol. 109, no. 35, pp. 16988–16996, 2005.
- [29] J. O. Choi, J. A. Moore, J. C. Moore, J. C. Corelli, J. P. Silverman, and H. Bakhru, "Degradation of poly(methylmethacrylate) by deep ultraviolet, x-ray, electron beam, and proton beam irradiations," *Journal of Vacuum Science and Technology B: Microelectronics Processing and Phenomena*, vol. 6, no. 6, pp. 2286–2289, 1988.
- [30] R. B. Fox, "Photodegradation of high polymers," in *Progress in Polymer Science*, A. D. Jenkins, Ed., pp. 47–89, Pergamon Press, London, UK, 1967.
- [31] R. B. Fox, L. G. Isaacs, and S. Stokes, "Photolytic degradation of poly(methyl methacrylate)," *Journal of Polymer Science Part A: Polymer Chemistry*, vol. 1, no. 3, pp. 1079–1086, 1963.
- [32] E. J. Harbron, V. P. McCaffrey, R. Xu, and M. D. E. Forbes, "Stereochemistry and pseudosymmetries in main chain polymeric free radicals," *Journal of the American Chemical Society*, vol. 122, no. 38, pp. 9182–9188, 2000.
- [33] B. Rånby and J. F. Rabek, *Photodegradation, Photo-oxidation and Photostabilization of Polymers*, Wiley, London, UK, 1975.
- [34] B. Rånby and J. F. Rabek, *ESR Spectroscopy in Polymer Research*, Springer-Verlag, Berlin, Germany, 1977.
- [35] K. Kimishima, T. Hashimoto, and D. H. Chang, "Spatial distribution of added homopolymer within the microdomains of a mixture consisting of an ABA-type triblock copolymer and a homopolymer," *Macromolecules*, vol. 28, no. 11, pp. 3842–3853, 1995.
- [36] K. I. Winey, E. L. Thomas, and L. J. Fetters, "Isothermal morphology diagrams for binary blends of diblock copolymer and homopolymer," *Macromolecules*, vol. 25, no. 10, pp. 2645–2650, 1992.
- [37] R. J. Spontak, S. D. Smith, and A. Ashraf, "Linear multiblock copolymer/homopolymer blends of constant composition. 1. Low-molecular-weight homopolymers," *Macromolecules*, vol. 26, no. 19, pp. 5118–5124, 1993.
- [38] N. Y. Vaidya, C. D. Han, D. Kim, N. Sakamoto, and T. Hashimoto, "Microdomain structures and phase transitions in binary blends consisting of a highly asymmetric block copolymer and a homopolymer," *Macromolecules*, vol. 34, no. 2, pp. 222–234, 2001.
- [39] H. Hückstädt, V. Abetz, and R. Stadler, "Synthesis of a polystyrene-arm -polybutadiene-arm-poly(methyl methacrylate) triarm star copolymer," *Macromolecular Rapid Communications*, vol. 17, no. 8, pp. 599–606, 1996.
- [40] K. Sugiyama, T. Oie, A. A. Ei-Magd, and A. Hirao, "Synthesis of well-defined (AB)_n multiblock copolymers composed of polystyrene and poly(methyl methacrylate) segments using specially designed living AB diblock copolymer anion," *Macromolecules*, vol. 43, no. 3, pp. 1403–1410, 2010.
- [41] Y. Sun, M. Steinhart, D. Zschech, R. Adhikari, G. H. Michler, and U. Gösele, "Diameter-dependence of the morphology of PS-b-PMMA nanorods confined within ordered porous alumina templates," *Macromolecular Rapid Communications*, vol. 26, no. 5, pp. 369–375, 2005.
- [42] T. M. Chou, P. Prayoonthong, A. Aitouchen, and M. Libera, "Nanoscale artifacts in RuO₄-stained poly(styrene)," *Polymer*, vol. 43, no. 7, pp. 2085–2088, 2002.
- [43] B. Ohlsson and B. Törnell, "Use of RuO₄ in studies of polymer blends by scanning electron microscopy," *Journal of Applied Polymer Science*, vol. 41, no. 5-6, pp. 1189–1196, 1990.

Review Article

A Review on Nanofluids: Preparation, Stability Mechanisms, and Applications

Wei Yu and Huaqing Xie

School of Urban Development and Environmental Engineering, Shanghai Second Polytechnic University, Shanghai 201209, China

Correspondence should be addressed to Huaqing Xie, hqxie@eed.sspu.cn

Received 21 April 2011; Accepted 11 July 2011

Academic Editor: Li-Hong Liu

Copyright © 2012 W. Yu and H. Xie. This is an open access article distributed under the Creative Commons Attribution License, which permits unrestricted use, distribution, and reproduction in any medium, provided the original work is properly cited.

Nanofluids, the fluid suspensions of nanomaterials, have shown many interesting properties, and the distinctive features offer unprecedented potential for many applications. This paper summarizes the recent progress on the study of nanofluids, such as the preparation methods, the evaluation methods for the stability of nanofluids, and the ways to enhance the stability for nanofluids, the stability mechanisms of nanofluids, and presents the broad range of current and future applications in various fields including energy and mechanical and biomedical fields. At last, the paper identifies the opportunities for future research.

1. Introduction

Nanofluids are a new class of fluids engineered by dispersing nanometer-sized materials (nanoparticles, nanofibers, nanotubes, nanowires, nanorods, nanosheet, or droplets) in base fluids. In other words, nanofluids are nanoscale colloidal suspensions containing condensed nanomaterials. They are two-phase systems with one phase (solid phase) in another (liquid phase). Nanofluids have been found to possess enhanced thermophysical properties such as thermal conductivity, thermal diffusivity, viscosity, and convective heat transfer coefficients compared to those of base fluids like oil or water. It has demonstrated great potential applications in many fields.

For a two-phase system, there are some important issues we have to face. One of the most important issues is the stability of nanofluids, and it remains a big challenge to achieve desired stability of nanofluids. In this paper, we will review the new progress in the methods for preparing stable nanofluids and summarize the stability mechanisms.

In recent years, nanofluids have attracted more and more attention. The main driving force for nanofluids research lies in a wide range of applications. Although some review articles involving the progress of nanofluid investigation were published in the past several years [1–6], most of the reviews are concerned of the experimental and theoretical studies of the thermophysical properties or the convective heat transfer

of nanofluids. The purpose of this paper will focus on the new preparation methods and stability mechanisms, especially the new application trends for nanofluids in addition to the heat transfer properties of nanofluids. We will try to find some challenging issues that need to be solved for future research based on the review on these aspects of nanofluids.

2. Preparation Methods for Nanofluids

2.1. Two-Step Method. Two-step method is the most widely used method for preparing nanofluids. Nanoparticles, nanofibers, nanotubes, or other nanomaterials used in this method are first produced as dry powders by chemical or physical methods. Then, the nanosized powder will be dispersed into a fluid in the second processing step with the help of intensive magnetic force agitation, ultrasonic agitation, high-shear mixing, homogenizing, and ball milling. Two-step method is the most economic method to produce nanofluids in large scale, because nanopowder synthesis techniques have already been scaled up to industrial production levels. Due to the high surface area and surface activity, nanoparticles have the tendency to aggregate. The important technique to enhance the stability of nanoparticles in fluids is the use of surfactants. However, the functionality of the surfactants under high temperature is also a big concern, especially for high-temperature applications.

Due to the difficulty in preparing stable nanofluids by two-step method, several advanced techniques are developed to produce nanofluids, including one-step method. In the following part, we will introduce one-step method in detail.

2.2. One-Step Method. To reduce the agglomeration of nanoparticles, Eastman et al. developed a one-step physical vapor condensation method to prepare Cu/ethylene glycol nanofluids [7]. The one-step process consists of simultaneously making and dispersing the particles in the fluid. In this method, the processes of drying, storage, transportation, and dispersion of nanoparticles are avoided, so the agglomeration of nanoparticles is minimized, and the stability of fluids is increased [5]. The one-step processes can prepare uniformly dispersed nanoparticles, and the particles can be stably suspended in the base fluid. The vacuum-SANSS (submerged arc nanoparticle synthesis system) is another efficient method to prepare nanofluids using different dielectric liquids [8, 9]. The different morphologies are mainly influenced and determined by various thermal conductivity properties of the dielectric liquids. The nanoparticles prepared exhibit needle-like, polygonal, square, and circular morphological shapes. The method avoids the undesired particle agglomeration fairly well.

One-step physical method cannot synthesize nanofluids in large scale, and the cost is also high, so the one-step chemical method is developing rapidly. Zhu et al. presented a novel one-step chemical method for preparing copper nanofluids by reducing $\text{CuSO}_4 \cdot 5\text{H}_2\text{O}$ with $\text{NaH}_2\text{PO}_2 \cdot \text{H}_2\text{O}$ in ethylene glycol under microwave irradiation [10]. Well-dispersed and stably suspended copper nanofluids were obtained. Mineral oil-based nanofluids containing silver nanoparticles with a narrow-size distribution were also prepared by this method [11]. The particles could be stabilized by Korantin, which coordinated to the silver particle surfaces via two oxygen atoms forming a dense layer around the particles. The silver nanoparticle suspensions were stable for about 1 month. Stable ethanol-based nanofluids containing silver nanoparticles could be prepared by microwave-assisted one-step method [12]. In the method, polyvinylpyrrolidone (PVP) was employed as the stabilizer of colloidal silver and reducing agent for silver in solution. The cationic surfactant octadecylamine (ODA) is also an efficient phase-transfer agent to synthesize silver colloids [13]. The phase transfer of the silver nanoparticles arises due to coupling of the silver nanoparticles with the ODA molecules present in organic phase via either coordination bond formation or weak covalent interaction. Phase transfer method has been developed for preparing homogeneous and stable graphene oxide colloids. Graphene oxide nanosheets (GONs) were successfully transferred from water to n-octane after modification by oleylamine, and the schematic illustration of the phase transfer process is shown in Figure 1 [14].

However, there are some disadvantages for one-step method. The most important one is that the residual reactants are left in the nanofluids due to incomplete reaction or stabilization. It is difficult to elucidate the nanoparticle effect without eliminating this impurity effect.

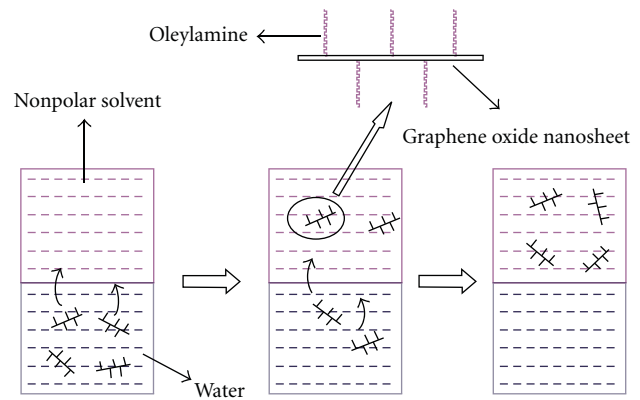


FIGURE 1: Schematic illustration of the phase transfer process.

2.3. Other Novel Methods. Wei et al. developed a continuous-flow microfluidic microreactor to synthesize copper nanofluids. By this method, copper nanofluids can be continuously synthesized, and their microstructure and properties can be varied by adjusting parameters such as reactant concentration, flow rate, and additive. CuO nanofluids with high solid volume fraction (up to 10 vol%) can be synthesized through a novel precursor transformation method with the help of ultrasonic and microwave irradiation [15]. The precursor $\text{Cu}(\text{OH})_2$ is completely transformed to CuO nanoparticle in water under microwave irradiation. The ammonium citrate prevents the growth and aggregation of nanoparticles, resulting in a stable CuO aqueous nanofluid with higher thermal conductivity than those prepared by other dispersing methods. Phase-transfer method is also a facile way to obtain monodisperse noble metal colloids [16]. In a water-cyclohexane two-phase system, aqueous formaldehyde is transferred to cyclohexane phase via reaction with dodecylamine to form reductive intermediates in cyclohexane. The intermediates are capable of reducing silver or gold ions in aqueous solution to form dodecylamine-protected silver and gold nanoparticles in cyclohexane solution at room temperature. Feng et al. used the aqueous organic phase-transfer method for preparing gold, silver, and platinum nanoparticles on the basis of the decrease of the PVP's solubility in water with the temperature increase [17]. Phase-transfer method is also applied for preparing stable kerosene-based Fe_3O_4 nanofluids. Oleic acid is successfully grafted onto the surface of Fe_3O_4 nanoparticles by chemisorbed mode, which lets Fe_3O_4 nanoparticles have good compatibility with kerosene [18]. The Fe_3O_4 nanofluids prepared by phase-transfer method do not show the previously reported "time dependence of the thermal conductivity characteristic". The preparation of nanofluids with controllable microstructure is one of the key issues. It is well known that the properties of nanofluids strongly depend on the structure and shape of nanomaterials. The recent research shows that nanofluids synthesized by chemical solution method have both higher conductivity enhancement and better stability than those produced by the other methods [19]. This method is distinguished from the others by its controllability. The nanofluid microstructure can be varied

and manipulated by adjusting synthesis parameters such as temperature, acidity, ultrasonic and microwave irradiation, types and concentrations of reactants and additives, and the order in which the additives are added to the solution.

3. The Stability of Nanofluid

The agglomeration of nanoparticles results in not only the settlement and clogging of microchannels but also the decreasing of thermal conductivity of nanofluids. So, the investigation on stability is also a key issue that influences the properties of nanofluids for application, and it is necessary to study and analyze influencing factors to the dispersion stability of nanofluids. This section will contain (a) the stability evaluation methods for nanofluids, (b) the ways to enhance the stability of nanofluids, and (c) the stability mechanisms of nanofluids.

3.1. The Stability Evaluation Methods for Nanofluids

3.1.1. Sedimentation and Centrifugation Methods. Many methods have been developed to evaluate the stability of nanofluids. The simplest method is sedimentation method [20, 21]. The sediment weight or the sediment volume of nanoparticles in a nanofluid under an external force field is an indication of the stability of the characterized nanofluid. The variation of concentration or particle size of supernatant particle with sediment time can be obtained by special apparatus [5]. The nanofluids are considered to be stable when the concentration or particle size of supernatant particles keeps constant. Sedimentation photograph of nanofluids in test tubes taken by a camera is also a usual method for observing the stability of nanofluids [5]. Zhu et al. used a sedimentation balance method to measure the stability of the graphite suspension [22]. The tray of sedimentation balance immersed in the fresh graphite suspension. The weight of sediment nanoparticles during a certain period was measured. The suspension fraction of graphite nanoparticles at a certain time could be calculated. For the sedimentation method, long period for observation is the defect. Therefore, centrifugation method is developed to evaluate the stability of nanofluids. Singh et al. applied the centrifugation method to observe the stability of silver nanofluids prepared by the microwave synthesis in ethanol by reduction of AgNO_3 with PVP as stabilizing agent [12]. It has been found that the obtained nanofluids are stable for more than 1 month in the stationary state and more than 10 h under centrifugation at 3,000 rpm without sedimentation. Excellent stability of the obtained nanofluid is due to the protective role of PVP, as it retards the growth and agglomeration of nanoparticles by steric effect. Li prepared the aqueous polyaniline colloids and used the centrifugation method to evaluate the stability of the colloids [23]. Electrostatic repulsive forces between nanofibers enabled the long-term stability of the colloids.

3.1.2. Zeta Potential Analysis. Zeta potential is electric potential in the interfacial double layer at the location of the slipping plane versus a point in the bulk fluid away from

the interface, and it shows the potential difference between the dispersion medium and the stationary layer of fluid attached to the dispersed particle. The significance of zeta potential is that its value can be related to the stability of colloidal dispersions. So, colloids with high zeta potential (negative or positive) are electrically stabilized, while colloids with low zeta potentials tend to coagulate or flocculate. In general, a value of 25 mV (positive or negative) can be taken as the arbitrary value that separates low-charged surfaces from highly charged surfaces. The colloids with zeta potential from 40 to 60 mV are believed to be good stable, and those with more than 60 mV have excellent stability. Kim et al. prepared Au nanofluids with an outstanding stability even after 1 month although no dispersants were observed [24]. The stability is due to a large negative zeta potential of Au nanoparticles in water. The influence of pH and sodium dodecylbenzene sulfonate (SDBS) on the stability of two water-based nanofluids was studied [25], and zeta potential analysis was an important technique to evaluate the stability. Zhu et al. [26] measured the zeta potential of $\text{Al}_2\text{O}_3\text{-H}_2\text{O}$ nanofluids under different pH values and different SDBS concentration. The Derjaguin-Landau-Verwey-Overbeek (DLVO) theory was used to calculate attractive and repulsive potentials. Cationic gemini surfactant as stabilizer was used to prepare stable water-based nanofluids containing MWNTs [27]. Zeta potential measurements were employed to study the absorption mechanisms of the surfactants on the MWNT surfaces with the help of Fourier transformation infrared spectra.

3.1.3. Spectral Absorbency Analysis. Spectral absorbency analysis is another efficient way to evaluate the stability of nanofluids. In general, there is a linear relationship between the absorbency intensity and the concentration of nanoparticles in fluid. Huang et al. evaluated the dispersion characteristics of alumina and copper suspensions using the conventional sedimentation method with the help of absorbency analysis by using a spectrophotometer after the suspensions deposited for 24 h [28]. The stability investigation of colloidal FePt nanoparticle systems was done via spectrophotometer analysis [29]. The sedimentation kinetics could also be determined by examining the absorbency of particle in solution [26].

If the nanomaterials dispersed in fluids have characteristic absorption bands in the wavelength 190–1100 nm, it is an easy and reliable method to evaluate the stability of nanofluids using UV-vis spectral analysis. The variation of supernatant particle concentration of nanofluids with sediment time can be obtained by the measurement of absorption of nanofluids, because there is a linear relation between the supernatant nanoparticle concentration and the absorbance of suspended particles. The outstanding advantage comparing to other methods is that UV-vis spectral analysis can present the quantitative concentration of nanofluids. Hwang et al. [30] studied the stability of nanofluids with the UV-vis spectrophotometer. It was believed that the stability of nanofluids was strongly affected by the characteristics of the suspended particles and the base fluid such as particle morphology. Moreover, the

addition of a surfactant could improve the stability of the suspensions. The relative stability of MWNT nanofluids [27] could be estimated by measuring the UV-vis absorption of the MWNT nanofluids at different sediment times. From the above relation between MWNT concentration and its UV-vis absorbance value, the concentration of the MWNT nanofluids at different sediment times could be obtained. The above three methods can be united to investigate the stability of nanofluids. For example, Li et al. evaluated the dispersion behavior of the aqueous copper nanosuspensions under different pH values, different dispersant type, and concentration by the method of zeta potential, absorbency, and sedimentation photographs [21].

3.2. The Ways to Enhance the Stability of Nanofluids

3.2.1. Surfactants Used in Nanofluids. Surfactants used in nanofluids are also called dispersants. Adding dispersants in the two-phase systems is an easy and economic method to enhance the stability of nanofluids. Dispersants can markedly affect the surface characteristics of a system in small quantity. Dispersants consists of a hydrophobic tail portion, usually a long-chain hydrocarbon, and a hydrophilic polar head group. Dispersants are employed to increase the contact of two materials, sometimes known as wettability. In a two-phase system, a dispersant tends to locate at the interface of the two phases, where it introduces a degree of continuity between the nanoparticles and fluids. According to the composition of the head, surfactants are divided into four classes: nonionic surfactants without charge groups in its head (include polyethylene oxide, alcohols, and other polar groups), anionic surfactants with negatively charged head groups (anionic head groups include long-chain fatty acids, sulfosuccinates, alkyl sulfates, phosphates, and sulfonates), cationic surfactants with positively charged head groups (cationic surfactants may be protonated long-chain amines and long-chain quaternary ammonium compounds), and amphoteric surfactants with zwitterionic head groups (charge depends on pH. The class of amphoteric surfactants is represented by betaines and certain lecithins). How to select suitable dispersants is a key issue. In general, when the base fluid of nanofluids is polar solvent, we should select water-soluble surfactants; otherwise, we will select oil-soluble ones. For nonionic surfactants, we can evaluate the solubility through the term hydrophilic/lipophilic balance (HLB) value. The lower the HLB number, the more oil-soluble the surfactants, and in turn, the higher the HLB number, the more water-soluble the surfactants is. The HLB value can be obtained easily by many handbooks. Although surfactant addition is an effective way to enhance the dispersibility of nanoparticles, surfactants might cause several problems [31]. For example, the addition of surfactants may contaminate the heat transfer media. Surfactants may produce foams when heating, while heating and cooling are routine processes in heat exchange systems. Furthermore, surfactant molecules attaching on the surfaces of nanoparticles may enlarge the thermal resistance between the nanoparticles and the base fluid, which may limit the enhancement of the effective thermal conductivity.

3.2.2. Surface Modification Techniques: Surfactant-Free Method. Use of functionalized nanoparticles is a promising approach to achieve long-term stability of nanofluid. It represents the surfactant-free technique. Yang and Liu presented a work on the synthesis of functionalized silica (SiO_2) nanoparticles by grafting silanes directly to the surface of silica nanoparticles in original nanoparticle solutions [32]. One of the unique characteristics of the nanofluids was that no deposition layer formed on the heated surface after a pool boiling process. Hwang et al. introduced hydrophilic functional groups on the surface of the nanotubes by mechanochemical reaction [30]. The prepared nanofluids, with no contamination to medium, good fluidity, low viscosity, high stability, and high thermal conductivity, would have potential applications as coolants in advanced thermal systems. A wet mechanochemical reaction was applied to prepare surfactant-free nanofluids containing double- and single-walled CNTs. Results from the infrared spectrum and zeta potential measurements showed that the hydroxyl groups had been introduced onto the treated CNT surfaces [33]. The chemical modification to functionalize the surface of carbon nanotubes is a common method to enhance the stability of carbon nanotubes in solvents. Here, we present a review about the surface modification of carbon nanotubes [34]. Plasma treatment was used to modify the surface characteristics of diamond nanoparticles [35]. Through plasma treatment using gas mixtures of methane and oxygen, various polar groups were imparted on the surface of the diamond nanoparticles, improving their dispersion property in water. A stable dispersion of titania nanoparticles in an organic solvent of diethylene glycol dimethylether (diglyme) was successfully prepared using a ball milling process [36]. In order to enhance dispersion stability of the solution, surface modification of dispersed titania particles was carried out during the centrifugal bead mill process. Surface modification was utilized with silane coupling agents, (3-acryl-oxypopyl) trimethoxysilane and trimethoxypropylsilane. Zinc oxide nanoparticles could be modified by polymethacrylic acid (PMAA) in aqueous system [37]. The hydroxyl groups of nano-ZnO particle surface could interact with carboxyl groups of PMAA and form poly (zinc methacrylate) complex on the surface of nano-ZnO. PMAA enhanced the dispersibility of nano-ZnO particles in water. The modification did not alter the crystalline structure of the ZnO nanoparticles.

3.2.3. Stability Mechanisms of Nanofluids. Particles in dispersion may adhere together and form aggregates of increasing size which may settle out due to gravity. Stability means that the particles do not aggregate at a significant rate. The rate of aggregation is in general determined by the frequency of collisions and the probability of cohesion during collision. Derjaguin, Verway, Landau, and Overbeek (DVLO) developed a theory which dealt with colloidal stability [38, 39]. DLVO theory suggests that the stability of a particle in solution is determined by the sum of van der Waals attractive and electrical double layer repulsive forces that exist between particles as they approach each other due to the Brownian motion they are undergoing. If the attractive force is larger

TABLE 1: Properties of oxides and their nanofluids.

	Thermal conductivity* W/(m·K)	Density (g/cm ³)	Crystalline	Viscosity (Cp) with 5.0 vol. % 30	Thermal conductivity enhancement of nanofluids (%) with 5.0 vol. %
MgO	48.4	2.9	Cubic	17.4	40.6
TiO ₂	8.4	4.1	Anatase	31.2	27.2
ZnO	13.0	5.6	Wurtzite	129.2	26.8
Al ₂ O ₃	36.0	3.6	γ	28.2	28.2
SiO ₂	10.4	2.6	noncrystalline	31.5	25.3

*Thermal conductivities of the oxides are for the corresponding bulk materials

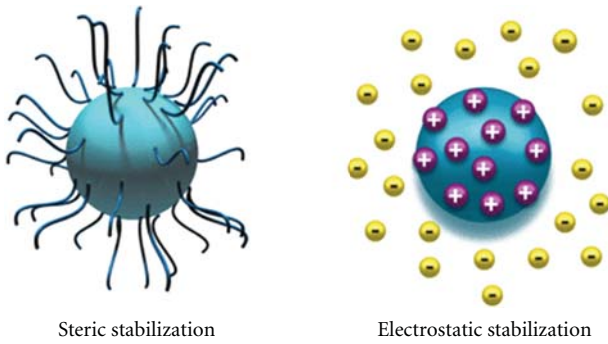


FIGURE 2: Types of colloidal stabilization.

than the repulsive force, the two particles will collide, and the suspension is not stable. If the particles have a sufficient high repulsion, the suspensions will exist in stable state. For stable nanofluids or colloids, the repulsive forces between particles must be dominant. According to the types of repulsion, the fundamental mechanisms that affect colloidal stability are divided into two kinds, one is steric repulsion, and another is electrostatic (charge) repulsion, shown in Figure 2. For steric stabilization, polymers are always involved into the suspension system, and they will adsorb onto the particles surface, producing an additional steric repulsive force. For example, Zinc oxide nanoparticles modified by PMAA have good compatibility with polar solvents [37]. Silver nanofluids are very stable due to the protective role of PVP, as it retards the growth and agglomeration of nanoparticles by steric effect. PVP is an efficient agent to improve the stability of graphite suspension [22]. The steric effect of polymer dispersant is determined by the concentration of the dispersant. If the PVP concentration is low, the surface of the graphite particles is gradually coated by PVP molecules with the increase of PVP. Kamiya et al. studied the effect of polymer dispersant structure on electrosteric interaction and dense alumina suspension behavior [40]. An optimum hydrophilic to hydrophobic group ratio was obtained from the maximum repulsive force and minimum viscosity. For electrostatic stabilization, surface charge will be developed through one or more of the following mechanisms: (1) preferential adsorption of ions, (2) dissociation of surface charged species, (3) isomorphic substitution of ions, (4) accumulation or depletion of electrons at the surface, and (5) physical adsorption of charged species onto the surface.

4. Application of Nanofluids

4.1. Heat Transfer Intensification. Since the origination of the nanofluid concept about a decade ago, the potentials of nanofluids in heat transfer applications have attracted more and more attention. Up to now, there are some review papers which present overviews of various aspects of nanofluids [1, 3–6, 41–46], including preparation and characterization, techniques for the measurements of thermal conductivity, theory and model, thermophysical properties, and convective heat transfer. Our group studied the thermal conductivities of ethylene glycol- (EG-) based nanofluids containing oxides including MgO, TiO₂, ZnO, Al₂O₃, and SiO₂ nanoparticles [47], and the results (Table 1) demonstrated that MgO-EG nanofluid was found to have superior features with the highest thermal conductivity and lowest viscosity. In this part, we will summarize the applications of nanofluids in heat transfer enhancement.

4.1.1. Electronic Applications. Due to higher density of chips, design of electronic components with more compact makes heat dissipation more difficult. Advanced electronic devices face thermal management challenges from the high level of heat generation and the reduction of available surface area for heat removal. So, the reliable thermal management system is vital for the smooth operation of the advanced electronic devices. In general, there are two approaches to improve the heat removal for electronic equipment. One is to find an optimum geometry of cooling devices; another is to increase the heat transfer capacity. Nanofluids with higher thermal conductivities are predicated convective heat transfer coefficients compared to those of base fluids. Recent researches illustrated that nanofluids could increase the heat transfer coefficient by increasing the thermal conductivity of a coolant. Jang and Choi designed a new cooler, combined microchannel heat sink with nanofluids [48]. Higher cooling performance was obtained when compared to the device using pure water as working medium. Nanofluids reduced both the thermal resistance and the temperature difference between the heated microchannel wall and the coolant. A combined microchannel heat sink with nanofluids had the potential as the next-generation cooling devices for removing ultrahigh heat flux. Nguyen et al. designed a closed liquid-circuit to investigate the heat transfer enhancement of a liquid cooling system by replacing the base fluid (distilled water) with a nanofluid composed of distilled

water and Al_2O_3 nanoparticles at various concentrations [49]. Measured data have clearly shown that the inclusion of nanoparticles within the distilled water has produced a considerable enhancement in convective heat transfer coefficient of the cooling block. With particle loading 4.5 vol%, the enhancement is up to 23% with respect to that of the base fluid. It has also been observed that an augmentation of particle concentration has produced a clear decrease of the junction temperature between the heated component and the cooling block. Silicon microchannel heat sink performance using nanofluids containing Cu nanoparticles was analyzed [50]. It was found that nanofluids could enhance the performance as compared with that using pure water as the coolant. The enhancement was due to the increase in thermal conductivity of coolant and the nanoparticle thermal dispersion effect. The other advantage was that there was no extra pressure drop, since the nanoparticle was small, and particle volume fraction was low.

The thermal requirements on the personal computer become much stricter with the increase in thermal dissipation of CPU. One of the solutions is the use of heat pipes. Nanofluids, employed as working medium for conventional heat pipe, have shown higher thermal performances, having the potential as a substitute for conventional water in heat pipe. At a same charge volume, there is a significant reduction in thermal resistance of heat pipe with nanofluid containing gold nanoparticles as compared with water [51]. The measured results also show that the thermal resistance of a vertical meshed heat pipe varies with the size of gold nanoparticles. The suspended nanoparticles tend to bombard the vapor bubble during the bubble formation. Therefore, it is expected that the nucleation size of vapor bubble is much smaller for fluid with suspended nanoparticles than that without them. This may be the major reason for reducing the thermal resistance of heat pipe. Chen et al. studied the effect of a nanofluid on flat heat pipe (FHP) thermal performance [52], using silver nanofluid as the working fluid. The temperature difference and the thermal resistance of the FHP with the silver nanoparticle solution were lower than those with pure water. The plausible reasons for enhancement of the thermal performance of the FHP using the nanofluid can be explained by the critical heat flux enhancement by higher wettability and the reduction of the boiling limit. Nanofluid oscillating heat pipe with ultrahigh-performance was developed by Ma et al. [53]. They combined nanofluids with thermally excited oscillating motion in an oscillating heat pipe, and heat transport capability significantly increased. For example, at the input power of 80.0 W, diamond nanofluid could reduce the temperature difference between the evaporator and the condenser from 40.9 to 24.3°C. This study would accelerate the development of a highly efficient cooling device for ultrahigh-heat-flux electronic systems. The thermal performance investigation of heat pipe indicated that nanofluids containing silver or titanium nanoparticles could be used as an efficient cooling fluid for devices with high energy density. For a silver nanofluid, the temperature difference decreased 0.56–0.65 compared to water at an input power of 30–50 W [54]. For the heat pipe with titanium nanoparticles at a volume

concentration of 0.10%, the thermal efficiency is 10.60% higher than that with the based working fluid [55]. These positive results are promoting the continued research and development of nanofluids for such applications.

4.1.2. Transportation. Nanofluids have great potentials to improve automotive and heavy-duty engine cooling rates by increasing the efficiency, lowering the weight and reducing the complexity of thermal management systems. The improved cooling rates for automotive and truck engines can be used to remove more heat from higher horsepower engines with the same size of cooling system. Alternatively, it is beneficial to design more compact cooling system with smaller and lighter radiators. It is, in turn, beneficial the high performance and high fuel economy of car and truck. Ethylene glycol-based nanofluids have attracted much attention in the application as engine coolant [56–58] due to the low-pressure operation compared with a 50/50 mixture of ethylene glycol and water, which is the nearly universally used automotive coolant. The nanofluids has a high boiling point, and it can be used to increase the normal coolant operating temperature and then reject more heat through the existing coolant system [59]. Kole et al. prepared car engine coolant (Al_2O_3 nanofluid) using a standard car engine coolant (HP KOOLGARD) as the base fluid [60] and studied the thermal conductivity and viscosity of the coolant. The prepared nanofluid, containing only 3.5% volume fraction of Al_2O_3 nanoparticles, displayed a fairly higher thermal conductivity than the base fluid, and a maximum enhancement of 10.41% was observed at room temperature. Tzeng et al. [61] applied nanofluids to the cooling of automatic transmissions. The experimental platform was the transmission of a four-wheel drive vehicle. The used nanofluids were prepared by dispersing CuO and Al_2O_3 nanoparticles into engine transmission oil. The results showed that CuO nanofluids produced the lower transmission temperatures both at high and low rotating speeds. From the thermal performance viewpoint, the use of nanofluid in the transmission has a clear advantage.

The researchers of Argonne National Laboratory have assessed the applications of nanofluids for transportation [62]. The use of high-thermal conductive nanofluids in radiators can lead to a reduction in the frontal area of the radiator up to 10%. The fuel saving is up to 5% due to the reduction in aerodynamic drag. It opens the door for new aerodynamic automotive designs that reduce emissions by lowering drag. The application of nanofluids also contributed to a reduction of friction and wear, reducing parasitic losses, operation of components such as pumps and compressors, and subsequently leading to more than 6% fuel savings. In fact, nanofluids not only enhance the efficiency and economic performance of car engine, but also will greatly influence the structure design of automotives. For example, the engine radiator cooled by a nanofluid will be smaller and lighter. It can be placed elsewhere in the vehicle, allowing for the redesign of a far more aerodynamic chassis. By reducing the size and changing the location of the radiator, a reduction in weight and wind resistance could enable greater fuel efficiency and subsequently lower exhaust

emissions. Computer simulations from the US department of energy's office of vehicle technology showed that nanofluid coolants could reduce the size of truck radiators by 5%. This would result in a 2.5% fuel saving at highway speeds.

The practical applications are on the road. In USA, car manufacturers GM and Ford are running their own research programs on nanofluid applications. A €8.3 million FP7 project, named NanoHex (Nanofluid Heat Exchange), began to run. It involved 12 organizations from Europe and Israel ranging from Universities to SMEs and major companies. NanoHex is overcoming the technological challenges faced in development and application of reliable and safe nanofluids for more sophisticated, energy efficient, and environmentally friendly products and services [63].

4.1.3. Industrial Cooling Applications. The application of nanofluids in industrial cooling will result in great energy savings and emissions reductions. For US industry, the replacement of cooling and heating water with nanofluids has the potential to conserve 1 trillion Btu of energy [41, 64]. For the US electric power industry, using nanofluids in closed loop cooling cycles could save about 10–30 trillion Btu per year (equivalent to the annual energy consumption of about 50,000–150,000 households). The associated emissions reductions would be approximately 5.6 million metric tons of carbon dioxide, 8,600 metric tons of nitrogen oxides, and 21,000 metric tons of sulfur dioxide [65].

Experiments were performed using a flow-loop apparatus to explore the performance of polyalphaolefin nanofluids containing exfoliated graphite nanoparticle fibers in cooling [66]. It was observed that the specific heat of nanofluids was found to be 50% higher for nanofluids compared with polyalphaolefin, and it increased with temperature. The thermal diffusivity was found to be 4 times higher for nanofluids. The convective heat transfer was enhanced by 10% using nanofluids compared with using polyalphaolefin. Ma et al. proposed the concept of nanoliquid-metal fluid, aiming to establish an engineering route to make the highest conductive coolant with about several dozen times larger thermal conductivity than that of water [45]. The liquid metal with low melting point is expected to be an idealistic base fluid for making superconductive solution, which may lead to the ultimate coolant in a wide variety of heat transfer enhancement area. The thermal conductivity of the liquid-metal fluid can be enhanced through the addition of more conductive nanoparticles.

4.1.4. Heating Buildings and Reducing Pollution. Nanofluids can be applied in the building heating systems. Kulkarni et al. evaluated how they perform heating buildings in cold regions [67]. In cold regions, it is a common practice to use ethylene or propylene glycol mixed with water in different proportions as a heat transfer fluid. So, 60:40 ethylene glycol/water (by weight) was selected as the base fluid. The results showed that using nanofluids in heat exchangers could reduce volumetric and mass flow rates, resulting in an overall pumping power savings. Nanofluids necessitate smaller heating systems, which are capable of

delivering the same amount of thermal energy as larger heating systems but are less expensive. This lowers the initial equipment cost excluding nanofluid cost. This will also reduce environmental pollutants, because smaller heating units use less power, and the heat transfer unit has less liquid and material waste to discard at the end of its life cycle.

4.1.5. Nuclear Systems Cooling. The Massachusetts Institute of Technology has established an interdisciplinary center for nanofluid technology for the nuclear energy industry. The researchers are exploring the nuclear applications of nanofluids, specifically the following three [68]: (1) main reactor coolant for pressurized water reactors (PWRs). It could enable significant power uprates in current and future PWRs, thus enhancing their economic performance. Specifically, the use of nanofluids with at least 32% higher critical heat flux (CHF) could enable a 20% power density uprate in current plants without changing the fuel assembly design and without reducing the margin to CHF; (2) coolant for the emergency core cooling systems (ECCSs) of both PWRs and boiling water reactors. The use of a nanofluid in the ECCS accumulators and safety injection can increase the peak-cladding-temperature margins (in the nominal-power core) or maintain them in uprated cores if the nanofluid has a higher post-CHF heat transfer rate; (3) coolant for in-vessel retention of the molten core during severe accidents in high-power-density light water reactors. It can increase the margin to vessel breach by 40% during severe accidents in high-power density systems such as Westinghouse APR1000 and the Korean APR1400. While there exist several significant gaps, including the nanofluid thermal-hydraulic performance at prototypical reactor conditions and the compatibility of the nanofluid chemistry with the reactor materials. Much work should be done to overcome these gaps before any applications can be implemented in a nuclear power plant.

4.1.6. Space and Defense. Due to the restriction of space, energy, and weight in space station and aircraft, there is a strong demand for high efficient cooling system with smaller size. You et al. [69] and Vassalo et al. [70] have reported order of magnitude increases in the critical heat flux in pool boiling with nanofluids compared to the base fluid alone. Further research of nanofluids will lead to the development of next generation of cooling devices that incorporate nanofluids for ultrahigh-heat-flux electronic systems, presenting the possibility of raising chip power in electronic components or simplifying cooling requirements for space applications. A number of military devices and systems require high-heat flux cooling to the level of tens of MW/m². At this level, the cooling of military devices and system is vital for the reliable operation. Nanofluids with high critical heat fluxes have the potential to provide the required cooling in such applications as well as in other military systems, including military vehicles, submarines, and high-power laser diodes. Therefore, nanofluids have wide application in space and defense fields, where power density is very high and the components should be smaller and weight less.

4.2. Mass Transfer Enhancement. Several researches have studied the mass transfer enhancement of nanofluids. Kim et al. initially examined the effect of nanoparticles on the bubble type absorption for $\text{NH}_3/\text{H}_2\text{O}$ absorption system [71]. The addition of nanoparticles enhances the absorption performance up to 3.21 times. Then, they visualized the bubble behavior during the $\text{NH}_3/\text{H}_2\text{O}$ absorption process and studied the effect of nanoparticles and surfactants on the absorption characteristics [72]. The results show that the addition of surfactants and nanoparticles improved the absorption performance up to 5.32 times. The addition of both surfactants and nanoparticles enhanced significantly the absorption performance during the ammonia bubble absorption process. The theoretical investigations of thermodiffusion and diffusionthermo on convective instabilities in binary nanofluids for absorption application were conducted. Mass diffusion is induced by thermal gradient. Diffusionthermo implies that heat transfer is induced by concentration gradient [73]. Ma et al. studied the mass transfer process of absorption using CNTs-ammonia nanofluids as the working medium [74, 75]. The absorption rates of the CNTs-ammonia binary nanofluids were higher than those of ammonia solution without CNTs. The effective absorption ratio of the CNTs-ammonia binary nanofluids increased with the initial concentration of ammonia and the mass fraction of CNTs. Komati et al. studied CO_2 absorption into amine solutions, and the addition of ferrofluids increased the mass transfer coefficient in gas/liquid mass transfer [76], and the enhancement extent depended on the amount of ferrofluid added. The enhancement in mass transfer coefficient was 92.8% for a volume fraction of the fluid of about 50% (solid magnetite volume fraction of about 0.39%). The research about the influence of Al_2O_3 nanofluid on the falling film absorption with ammonia water showed that the sorts of nanoparticles and surfactants in the nanofluid and the concentration of ammonia in the basefluid were the key parameters influencing the absorption effect of ammonia [77].

So far, the mechanism leading to mass transfer enhancement is still unclear. The existing research work on the mass transfer in nanofluids is not enough. Much experimental and simulation work should be carried out to clarify some important influencing factors.

4.3. Energy Applications. For energy applications of nanofluids, two remarkable properties of nanofluids are utilized, one is the higher thermal conductivities of nanofluids, enhancing the heat transfer, another is the absorption properties of nanofluids.

4.3.1. Energy Storage. The temporal difference of energy source and energy needs made necessary the development of storage system. The storage of thermal energy in the form of sensible and latent heat has become an important aspect of energy management with the emphasis on efficient use and conservation of the waste heat and solar energy in industry and buildings [78]. Latent heat storage is one of the most efficient ways of storing thermal energy. Wu et al. evaluated

the potential of $\text{Al}_2\text{O}_3\text{-H}_2\text{O}$ nanofluids as a new phase change material (PCM) for the thermal energy storage of cooling systems. The thermal response test showed the addition of Al_2O_3 nanoparticles remarkably decreased the supercooling degree of water, advanced the beginning freezing time, and reduced the total freezing time. Only adding 0.2 wt% Al_2O_3 nanoparticles, the total freezing time of $\text{Al}_2\text{O}_3\text{-H}_2\text{O}$ nanofluids could be reduced by 20.5%. Liu et al. prepared a new sort of nanofluid phase change materials (PCMs) by suspending small amount of TiO_2 nanoparticles in saturated BaCl_2 aqueous solution [79]. The nanofluids PCMs possessed remarkably high thermal conductivities compared to the base material. The cool storage/supply rate and the cool storage/supply capacity all increased greatly than those of BaCl_2 aqueous solution without added nanoparticles. The higher thermal performances of nanofluids PCMs indicate that they have a potential for substituting conventional PCMs in cool storage applications. Copper nanoparticles are efficient additives to improve the heating and cooling rates of PCMs [80]. For composites with 1 wt % copper nanoparticle, the heating and cooling times could be reduced by 30.3 and 28.2%, respectively. The latent heats and phase-change temperatures changed very little after 100 thermal cycles.

4.3.2. Solar Absorption. Solar energy is one of the best sources of renewable energy with minimal environmental impact. The conventional direct absorption solar collector is a well-established technology, and it has been proposed for a variety of applications such as water heating; however, the efficiency of these collectors is limited by the absorption properties of the working fluid, which is very poor for typical fluids used in solar collectors. Recently, this technology has been combined with the emerging technologies of nanofluids and liquid-nanoparticle suspensions to create a new class of nanofluid-based solar collectors. Otanicar et al. reported the experimental results on solar collectors based on nanofluids made from a variety of nanoparticles (CNTs, graphite, and silver) [81]. The efficiency improvement was up to 5% in solar thermal collectors by utilizing nanofluids as the absorption media. In addition, they compared the experimental data with a numerical model of a solar collector with direct absorption nanofluids. The experimental and numerical results demonstrated an initial rapid increase in efficiency with volume fraction, followed by a leveling off in efficiency as volume fraction continues to increase. Theoretical investigation on the feasibility of using a nonconcentrating direct absorption solar collector showed that the presence of nanoparticles increased the absorption of incident radiation by more than nine times over that of pure water [82]. Under the similar operating conditions, the efficiency of an absorption solar collector using nanofluid as the working fluid was found to be up to 10% higher (on an absolute basis) than that of a flat-plate collector. Otanicar and Golden evaluated the overall economic and environmental impacts of the technology in contrast with conventional solar collectors using the life-cycle assessment methodology [83]. Results showed that for the current cost of nanoparticles the nanofluid-based solar collector had a slightly longer payback period but at the end of its useful life has the

same economic saving as a conventional solar collector. Sani et al. investigated the optical and thermal properties of nanofluids consisting of aqueous suspensions of single-wall carbon nanohorns [84]. The observed nanoparticle-induced differences in optical properties appeared promising, leading to a considerably higher sunlight absorption. Both these effects, together with the possible chemical functionalization of carbon nanohorns, make this new kind of nanofluids very interesting for increasing the overall efficiency of the sunlight exploiting device.

4.4. Mechanical Applications. Why nanofluids have great friction reduction properties? Nanoparticles in nanofluids form a protective film with low hardness and elastic modulus on the worn surface can be considered as the main reason that some nanofluids exhibit excellent lubricating properties.

Magnetic fluids are kinds of special nanofluids. Magnetic liquid rotary seals operate with no maintenance and extremely low leakage in a very wide range of applications, and it utilizing the property magnetic properties of the magnetic nanoparticles in liquid.

4.4.1. Friction Reduction. Advanced lubricants can improve productivity through energy saving and reliability of engineered systems. Tribological research heavily emphasizes reducing friction and wear. Nanoparticles have attracted much interest in recent years due to their excellent load-carrying capacity, good extreme pressure and friction reducing properties. Zhou et al. evaluated the tribological behavior of Cu nanoparticles in oil on a four-ball machine. The results showed that Cu nanoparticles as an oil additive had better friction-reduction and antiwear properties than zinc dithiophosphate, especially at high applied load. Meanwhile, the nanoparticles could also strikingly improve the load-carrying capacity of the base oil [85]. Dispersion of solid particles was found to play an important role, especially when a slurry layer was formed. Water-based Al_2O_3 and diamond nanofluids were applied in the minimum quantity lubrication (MQL) grinding process of cast iron. During the nanofluid MQL grinding, a dense and hard slurry layer was formed on the wheel surface and could benefit the grinding performance. Nanofluids showed the benefits of reducing grinding forces, improving surface roughness, and preventing workpiece burning. Compared to dry grinding, MQL grinding could significantly reduce the grinding temperature [86]. Wear and friction properties of surface modified Cu nanoparticles, as 50CC oil additive were studied. The higher the oil temperature applied, the better the tribological properties of Cu nanoparticles were. It could be inferred that a thin copper protective film with lower elastic modulus and hardness was formed on the worn surface, which resulted in the good tribological performances of Cu nanoparticles, especially when the oil temperature was higher [87]. Yu et al. firstly reported that room temperature ionic liquid multiwalled carbon nanotubes composite was evaluated as lubricant additive in ionic liquid due to their excellent dispersibility and that the composite showed good friction-reduction and antiwear properties in friction process [88].

Wang et al. studied the tribological properties of ionic liquid-based nanofluids containing functionalized MWNTs under loads in the range of 200–800 N [89], indicating that the nanofluids exhibited preferable friction-reduction properties under 800 N and remarkable antiwear properties with use of reasonable concentrations. Magnetic nanoparticle $\text{Mn}_{0.78}\text{Zn}_{0.22}\text{Fe}_2\text{O}_4$ was also an efficient lubricant additive. When used as a lubricant additive in 46 turbine oil, it could improve the wear resistance, load-carrying capacity, and antifriction ability of base oil, and the decreasing percentage of wear scar diameter was 25.45% compared to the base oil. This was a typical self-repair phenomenon [90]. Chen et al. reported on dispersion stability enhancement and self-repair principle discussion of ultrafine-tungsten disulfide in green lubricating oil [91]. Ultrafine-tungsten disulfide particulates could fill and level up the furrows on abrasive surfaces, repairing abrasive surface well. What is more, ultrafine-tungsten disulfide particulates could form a WS_2 film with low shear stress by adsorbing and depositing in the hollowness of abrasive surface, making the abrasive surface be more smooth, and the FeS film formed in tribochemical reaction could protect the abrasive surface further, all of which realize the self-repair to abrasive surface. The tribological properties of liquid paraffin with SiO_2 nanoparticles additive made by a sol-gel method was investigated by Peng et al. [92]. The optimal concentrations of SiO_2 nanoparticles in liquid paraffin was associated with better tribological properties than pure paraffin oil, and an antiwear ability that depended on the particle size, and oleic acid surface-modified SiO_2 nanoparticles with an average diameter of 58 nm provided better tribological properties in load-carrying capacity, antiwear and friction-reduction than pure liquid paraffin. Nanoparticles can easily penetrate into the rubbing surfaces because of their nanoscale. During the frictional process, the thin physical tribofilm of the nanoparticles forms between rubbing surfaces, which cannot only bear the load, but also separates the rubbing surfaces. The spherical SiO_2 nanoparticles could roll between the rubbing surfaces in sliding friction, and the originally pure sliding friction becomes mixed sliding and rolling friction. Therefore, the friction coefficient declines markedly and then remains constant.

4.4.2. Magnetic Sealing. Magnetic fluids (ferromagnetic fluid) are kinds of special nanofluids. They are stable colloidal suspensions of small magnetic particles such as magnetite (Fe_3O_4). The properties of the magnetic nanoparticles, the magnetic component of magnetic nanofluids, may be tailored by varying their size and adapting their surface coating in order to meet the requirements of colloidal stability of magnetic nanofluids with nonpolar and polar carrier liquids [93]. Comparing with the mechanical sealing, magnetic sealing offers a cost-effective solution to environmental and hazardous-gas sealing in a wide variety of industrial rotation equipment with high-speed capability, low-friction power losses, and long life and high reliability [94]. A ring magnet forms part of a magnetic circuit in which an intense magnetic field is established in the gaps between the teeth on a magnetically permeable shaft and the

surface of an opposing pole block. Ferrofluid introduced into the gaps forms discrete liquid rings capable of supporting a pressure difference while maintaining zero leakage. The seals operate without wear as the shaft rotates, because the mechanical moving parts do not touch. With these unique characteristics, sealing liquids with magnetic fluids can be applied in many application areas. It is reported that an iron particle dispersed magnetic fluids was utilized in the sealing of a high-rotation pump. The sealing holds pressure of 618 kPa with a 1800 r/min [95]. Mitamura et al. studied the application of a magnetic fluid seal to rotary blood pumps. The developed magnetic fluid seal worked for over 286 days in a continuous flow condition, for 24 days (ongoing) in a pulsatile flow condition and for 24 h (electively terminated) in blood flow [96]. Ferrocobalt magnetic fluid was used for oil sealing, and the holding pressure is 25 times as high as that of a conventional magnetite sealing [97].

4.5. Biomedical Application. For some special kinds of nanoparticles, they have antibacterial activities or drug-delivery properties, so the nanofluids containing these nanoparticles will exhibit some relevant properties.

4.5.1. Antibacterial Activity. Organic antibacterial materials are often less stable particularly at high temperatures or pressures. As a consequence, inorganic materials such as metal and metal oxides have attracted lots of attention over the past decade due to their ability to withstand harsh process conditions. The antibacterial behaviour of ZnO nanofluids shows that the ZnO nanofluids have bacteriostatic activity against [98]. Electrochemical measurements suggest some direct interaction between ZnO nanoparticles and the bacteria membrane at high ZnO concentrations. Jalal et al. prepared ZnO nanoparticles via a green method. The antibacterial activity of suspensions of ZnO nanoparticles against *Escherichia coli* (*E. coli*) has been evaluated by estimating the reduction ratio of the bacteria treated with ZnO. Survival ratio of bacteria decreases with increasing the concentrations of ZnO nanofluids and time [99]. Further investigations have clearly demonstrated that ZnO nanoparticles have a wide range of antibacterial effects on a number of other microorganisms. The antibacterial activity of ZnO may be dependent on the size and the presence of normal visible light [100]. Recent research showed that ZnO nanoparticles exhibited impressive antibacterial properties against an important foodborne pathogen, *E. coli* O157:H7, and the inhibitory effects increased as the concentrations of ZnO nanoparticles increased. ZnO nanoparticles changed the cell membrane components including lipids and proteins. ZnO nanoparticles could distort bacterial cell membrane, leading to loss of intracellular components, and ultimately the death of cells, considered as an effective antibacterial agent for protecting agricultural and food safety [101].

The antibacterial activity research of CuO nanoparticles showed that they possessed antibacterial activity against four bacterial strains. The size of nanoparticles was less than that of the pore size in the bacteria, and thus, they had a unique property of crossing the cell membrane without any hindrance. It could be hypothesized that these

nanoparticles formed stable complexes with vital enzymes inside cells which hampered cellular functioning resulting in their death [102]. Bulk equivalents of these products showed no inhibitory activity, indicating that particle size was determinant in activity [103]. Lee et al. reported the antibacterial efficacy of nanosized silver colloidal solution on the cellulosic and synthetic fabrics [104]. The antibacterial treatment of the textile fabrics was easily achieved by padding them with nanosized silver colloidal solution. The antibacterial efficacy of the fabrics was maintained after many times laundering. Silver colloid is an efficient antibacterial agent. The silver colloid prepared by a one-step synthesis showed high antimicrobial and bactericidal activity against Gram-positive and Gram-negative bacteria, including highly multi-resistant strains such as methicillin-resistant staphylococcus aureus. The antibacterial activity of silver nanoparticles was found to be dependent on the size of silver particles. A very low concentration of silver gave antibacterial performance [105]. The aqueous suspensions of fullerenes and nano-TiO₂ can produce reactive oxygen species (ROS). Bacterial (*E. coli*) toxicity tests suggested that unlike nano-TiO₂ which was exclusively phototoxic, the antibacterial activity of fullerene suspensions was linked to ROS production. Nano-TiO₂ may be more efficient for water treatment involving UV or solar energy, to enhance contaminant oxidation and perhaps for disinfection. However, fullerol and PVP/C₆₀ may be useful as water treatment agents targeting specific pollutants or microorganisms that are more sensitive to either superoxide or singlet oxygen [106]. Lyon and Alvarez proposed that C₆₀ suspensions exerted ROS-independent oxidative stress in bacteria, with evidence of protein oxidation, changes in cell membrane potential, and interruption of cellular respiration. This mechanism requires direct contact between the nanoparticle and the bacterial cell and differs from previously reported nanomaterial antibacterial mechanisms that involve ROS generation (metal oxides) or leaching of toxic elements (nanosilver) [107].

4.5.2. Nanodrug Delivery. Over the last few decades, colloidal drug delivery systems have been developed in order to improve the efficiency and the specificity of drug action [108]. The small-size, customized surface improved solubility, and multifunctionality of nanoparticles opens many doors and creates new biomedical applications. The novel properties of nanoparticles offer the ability to interact with complex cellular functions in new ways [109]. Gold nanoparticles provide nontoxic carriers for drug- and gene-delivery applications. With these systems, the gold core imparts stability to the assembly, while the monolayer allows tuning of surface properties such as charge and hydrophobicity. Another attractive feature of gold nanoparticles is their interaction with thiols, providing an effective and selective means of controlled intracellular release [110]. Nakano et al. proposed the drug-delivery system using nanomagnetic fluid [111], which targeted and concentrated drugs using a ferrofluid cluster composed of magnetic nanoparticles. The potential of magnetic nanoparticles stems from the intrinsic properties of their magnetic cores combined with their drug-loading capability and the biochemical properties

that can be bestowed on them by means of a suitable coating. CNT has emerged as a new alternative and efficient tool for transporting and translocating therapeutic molecules. CNT can be functionalised with bioactive peptides, proteins, nucleic acids, and drugs and used to deliver their cargos to cells and organs. Because functionalised CNT display low toxicity and are not immunogenic, such systems hold great potential in the field of nanobiotechnology and nanomedicine [112, 113]. Pastorin et al. have developed a novel strategy for the functionalisation of CNTs with two different molecules using the 1,3-dipolar cycloaddition of azomethine ylides [114]. The attachment of molecules that will target specific receptors on tumour cells will help improve the response to anticancer agents. Liu et al. have found that prefunctionalized CNTs can adsorb widely used aromatic molecules by simple mixing, forming “forest-scrub”-like assemblies on CNTs with PEG extending into water to impart solubility and aromatic molecules densely populating CNT sidewalls. The work establishes a novel, easy-to-make formulation of a SWNT-doxorubicin complex with extremely high drug loading efficiency [115].

In recent years, graphene based drug delivery systems have attracted more and more attention. In 2008, Sun et al. firstly reported the application of nanographene oxide (NGO) for cellular imaging and drug delivery [116]. They have developed functionalization chemistry in order to impart solubility and compatibility of NGO in biological environments. Simple physisorption via π -stacking can be used for loading doxorubicin, a widely used cancer drug onto NGO functionalized with antibody for selective killing of cancer cells in vitro. Functional nanoscale graphene oxide is found to be a novel nanocarrier for the loading and targeted delivery of anticancer drugs [117]. Controlled loading of two anticancer drugs onto the folic acid-conjugated NGO via π - π stacking and hydrophobic interactions demonstrated that NGO loaded with the two anticancer drugs showed specific targeting to MCF-7 cells (human breast cancer cells with folic acid receptors), and remarkably high cytotoxicity compared to NGO loaded with either doxorubicin or camptothecin only. The PEGylated (PEG: polyethylene glycol) nanographene oxide could be used for the delivery of water-insoluble cancer drugs [118]. PEGylated NGO readily complexes with a water-insoluble aromatic molecule SN38, a camptothecin analogue, via noncovalent van der Waals interaction. The NGO-PEG-SN38 complex exhibits excellent aqueous solubility and retains the high potency of free SN38 dissolved in organic solvents. Yang *et al.* found GO-Fe₃O₄ hybrid could be loaded with anticancer drug doxorubicin hydrochloride with a high loading capacity [119]. This GO-Fe₃O₄ hybrid showed superparamagnetic property and could congregate under acidic conditions and be redispersed reversibly under basic conditions. This pH-triggered controlled magnetic behavior makes this material a promising candidate for controlled targeted drug delivery.

4.6. Other Applications

4.6.1. Intensify Microreactors. The discovery of high enhancement of heat transfer in nanofluids can be applicable

to the area of process intensification of chemical reactors through integration of the functionalities of reaction and heat transfer in compact multifunctional reactors. Fan et al. studied a nanofluid based on benign TiO₂ material dispersed in ethylene glycol in an integrated reactor-heat exchanger [120]. The overall heat transfer coefficient increase was up to 35% in the steady state continuous experiments. This resulted in a closer temperature control in the reaction of selective reduction of an aromatic aldehyde by molecular hydrogen and very rapid change in the temperature of reaction under dynamic reaction control.

4.6.2. Nanofluids as Vehicular Brake Fluids. A vehicle's kinetic energy is dispersed through the heat produced during the process of braking and this is transmitted throughout the brake fluid in the hydraulic braking system [39], and now, there is a higher demand for the properties of brake oils. Copper-oxide and aluminum-oxide based brake nanofluids were manufactured using the arc-submerged nanoparticle synthesis system and the plasma charging arc system, respectively [121, 122]. The two kinds of nanofluids both have enhanced properties such as a higher boiling point, higher viscosity, and a higher conductivity than that of traditional brake fluid. By yielding a higher boiling point, conductivity, and viscosity, the nanofluid brake oil will reduce the occurrence of vapor-lock and offer increased safety while driving.

4.6.3. Nanofluids-Based Microbial Fuel Cell. Microbial fuel cells (MFC) that utilize the energy found in carbohydrates, proteins, and other energy-rich natural products to generate electrical power have a promising future. The excellent performance of MFC depends on electrodes and electron mediator. Sharma et al. constructed a novel microbial fuel cell (MFC) using novel electron mediators and CNT-based electrodes [123]. The novel mediators are nanofluids which were prepared by dispersing nanocrystalline platinum anchored CNTs in water. They compared the performance of the new *E. coli*-based MFC to the previously reported *E. coli*-based microbial fuel cells with neutral red and methylene blue electron mediators. The performance of the MFC using CNT-based nanofluids and CNT-based electrodes has been compared against plain graphite electrode-based MFC. CNT-based electrodes showed as high as ~6-fold increase in the power density compared to graphite electrodes. The work demonstrates the potential of noble metal nanoparticles dispersed on CNT-based MFC for the generation of high energies from even simple bacteria like *E. coli*.

4.6.4. Nanofluids with Unique Optical Properties. Optical filters are used to select different wavelengths of light. The ferrofluid-based optical filter has tunable properties. The desired central wavelength region can be tuned by an external magnetic field. Philip et al. developed a ferrofluid-based emulsion for selecting different bands of wavelengths in the UV, visible, and IR regions [124]. The desired range

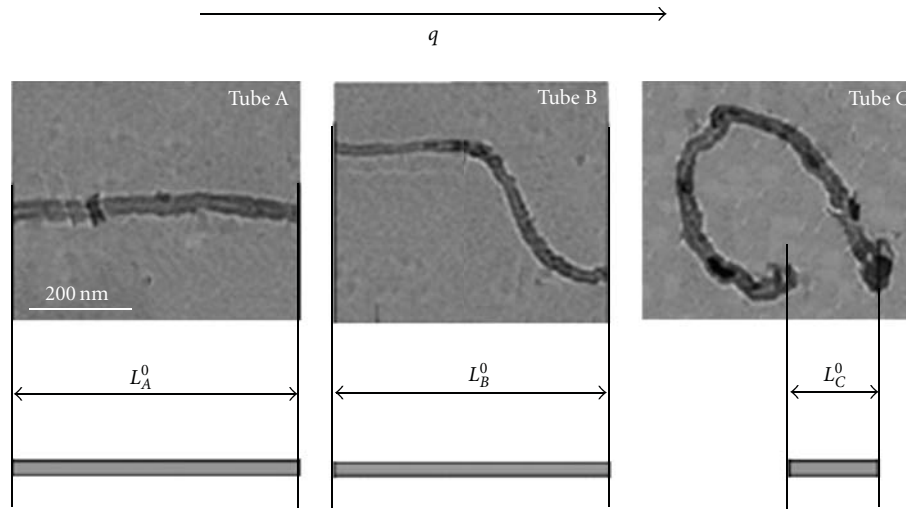


FIGURE 3: Actual nonstraight CNTs (left two) and equivalent straight thermal passages (right).

of wavelengths, bandwidth, and percentage of reflectivity could be easily controlled by using suitably tailored ferrofluid emulsions. Mishra et al. developed nanofluids with selective visible colors in gold nanoparticles embedded in polymer molecules of polyvinyl pyrrolidone (PVP) in water [125]. They compared the developments in the apparent visible colors in forming the Au-PVP nanofluids of 0.05, 0.10, 0.50, and 1.00 wt% Au contents. The surface plasmon bands, which occurs over 480–700 nm, varies sensitively in its position as well as the intensity when varying the Au content 0–1 wt%.

5. Conclusions and Future Work

Many interesting properties of nanofluids have been reported in the past decades. This paper presents an overview of the recent developments in the study of nanofluids, including the preparation methods, the evaluation methods for their stability, the ways to enhance their stability, the stability mechanisms, and their potential applications in heat transfer intensification, mass transfer enhancement, energy fields, mechanical fields, biomedical fields, and so forth.

Although nanofluids have displayed enormously exciting potential applications, some vital hinders also exist before commercialization of nanofluids. The following key issues should receive greater attention in the future. Firstly, further experimental and theoretical research is required to find the major factors influencing the performance of nanofluids. Up to now, there is a lack of agreement between experimental results from different groups, so it is important to systematically identify these factors. The detailed and accurate structure characterizations of the suspensions may be the key to explain the discrepancy in the experimental data. Secondly, increase in viscosity by the use of nanofluids is an important drawback due to the associated increase in pumping power. The applications for nanofluids with low viscosity and high conductivity are promising. Enhancing

the compatibility between nanomaterials and the base fluids through modifying the interface properties of two phases may be one of the solution routes. Thirdly, the shape of the additives in nanofluids is very important for the properties; therefore, the new nanofluid synthesis approaches with controllable microscope structure will be an interesting research work. Fourthly, stability of the suspension is a crucial issue for both scientific research and practical applications. The stability of nanofluids, especially the long-term stability, the stability in the practical conditions, and the stability after thousands of thermal cycles should be paid more attention. Fifthly, there is a lack of investigation of the thermal performance of nanofluids at high temperatures, which may widen the possible application areas of nanofluids, like in high-temperature solar energy absorption and high-temperature energy storage. At the same time, high temperature may accelerate the degradation of the surfactants used as dispersants in nanofluids and may produce more foams. These factors should be taken into account. Finally, the properties of nanofluids strongly depend on the shape and property of the additive. Xie's findings indicated that thermal conductivity enhancement was adjusted by ball milling and cutting the treated CNTs suspended in the nanofluids to relatively straight CNTs with an appropriate length distribution. They proposed the concept of straightness ratio to explain the facts (Figure 3). Nanofluid research can be enriched and extended through exploring new nanomaterials. For example, the newly discovered 2D monatomic sheet graphene is a promising candidate material to enhance the thermal conductivity of the base fluid [126, 127], as shown in Figure 4. The concept of nanofluids is extended by the use of phase change materials, which goes well beyond simply increasing the thermal conductivity of a fluid [128]. It is found that the indium/polyalphaolefin phase change nanofluid exhibits simultaneously enhanced thermal conductivity and specific heat.

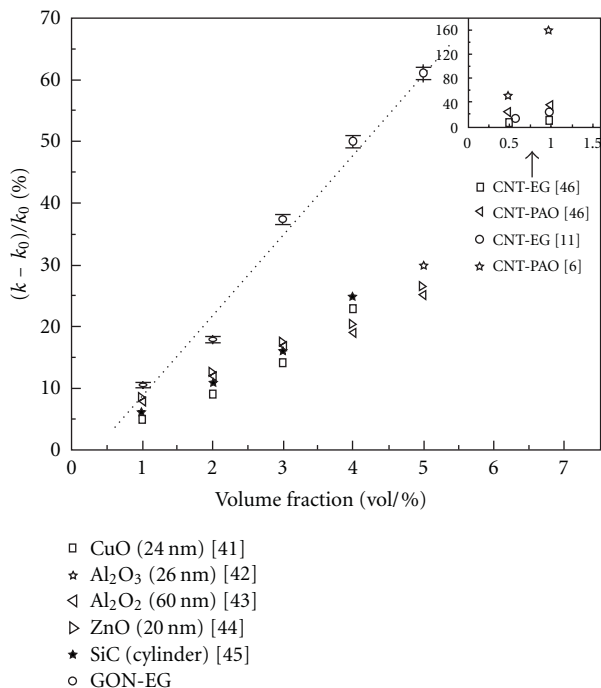


FIGURE 4: Thermal conductivity enhancement ratios of EG-based nanofluids as a function of loading. The inset shows the thermal conductivity enhancement ratios of nanofluids containing CNTs.

Acknowledgments

The work was supported by New Century Excellent Talents in University (NECT-10-883), the Program for Professor of Special Appointment (Eastern Scholar) at Shanghai Institutions of Higher Learning, and partly by National Natural Science Foundation of China (51106093).

References

- [1] V. Trisaksri and S. Wongwises, "Critical review of heat transfer characteristics of nanofluids," *Renewable and Sustainable Energy Reviews*, vol. 11, no. 3, pp. 512–523, 2007.
- [2] S. Özerinç, S. Kakaç, and A. G. Yazlıoğlu, "Enhanced thermal conductivity of nanofluids: a state-of-the-art review," *Microfluidics and Nanofluidics*, vol. 8, no. 2, pp. 145–170, 2010.
- [3] X. Q. Wang and A. S. Mujumdar, "Heat transfer characteristics of nanofluids: a review," *International Journal of Thermal Sciences*, vol. 46, no. 1, pp. 1–19, 2007.
- [4] X. Q. Wang and A. S. Mujumdar, "A review on nanofluids—part I: theoretical and numerical investigations," *Brazilian Journal of Chemical Engineering*, vol. 25, no. 4, pp. 613–630, 2008.
- [5] Y. Li, J. Zhou, S. Tung, E. Schneider, and S. Xi, "A review on development of nanofluid preparation and characterization," *Powder Technology*, vol. 196, no. 2, pp. 89–101, 2009.
- [6] S. Kakaç and A. Pramuanjaroenkij, "Review of convective heat transfer enhancement with nanofluids," *International Journal of Heat and Mass Transfer*, vol. 52, no. 13–14, pp. 3187–3196, 2009.
- [7] J. A. Eastman, S. U. S. Choi, S. Li, W. Yu, and L. J. Thompson, "Anomalous increase in effective thermal conductivities of ethylene glycol-based nanofluids containing copper nanoparticles," *Applied Physics Letters*, vol. 78, no. 6, pp. 718–720, 2001.
- [8] C. H. Lo, T. T. Tsung, and L. C. Chen, "Shape-controlled synthesis of Cu-based nanofluid using submerged arc nanoparticle synthesis system (SANSS)," *Journal of Crystal Growth*, vol. 277, no. 1–4, pp. 636–642, 2005.
- [9] C. H. Lo, T. T. Tsung, L. C. Chen, C. H. Su, and H. M. Lin, "Fabrication of copper oxide nanofluid using submerged arc nanoparticle synthesis system (SANSS)," *Journal of Nanoparticle Research*, vol. 7, no. 2–3, pp. 313–320, 2005.
- [10] H. T. Zhu, Y. S. Lin, and Y. S. Yin, "A novel one-step chemical method for preparation of copper nanofluids," *Journal of Colloid and Interface Science*, vol. 277, no. 1, pp. 100–103, 2004.
- [11] H. Bönnemann, S. S. Botha, B. Bladergroen, and V. M. Linkov, "Monodisperse copper- and silver-nanocolloids suitable for heat-conductive fluids," *Applied Organometallic Chemistry*, vol. 19, no. 6, pp. 768–773, 2005.
- [12] A. K. Singh and V. S. Raykar, "Microwave synthesis of silver nanofluids with polyvinylpyrrolidone (PVP) and their transport properties," *Colloid and Polymer Science*, vol. 286, no. 14–15, pp. 1667–1673, 2008.
- [13] A. Kumar, H. Joshi, R. Pasricha, A. B. Mandale, and M. Sastry, "Phase transfer of silver nanoparticles from aqueous to organic solutions using fatty amine molecules," *Journal of Colloid and Interface Science*, vol. 264, no. 2, pp. 396–401, 2003.
- [14] W. Yu, H. Xie, X. Wang, and X. Wang, "Highly efficient method for preparing homogeneous and stable colloids containing graphene oxide," *Nanoscale Research Letters*, vol. 6, p. 47, 2011.
- [15] H. T. Zhu, C. Y. Zhang, Y. M. Tang, and J. X. Wang, "Novel synthesis and thermal conductivity of CuO nanofluid," *Journal of Physical Chemistry C*, vol. 111, no. 4, pp. 1646–1650, 2007.
- [16] Y. Chen and X. Wang, "Novel phase-transfer preparation of monodisperse silver and gold nanoparticles at room temperature," *Materials Letters*, vol. 62, no. 15, pp. 2215–2218, 2008.
- [17] X. Feng, H. Ma, S. Huang et al., "Aqueous-organic phase-transfer of highly stable gold, silver, and platinum nanoparticles and new route for fabrication of gold nanofilms at the oil/water interface and on solid supports," *Journal of Physical Chemistry B*, vol. 110, no. 25, pp. 12311–12317, 2006.
- [18] W. Yu, H. Xie, L. Chen, and Y. Li, "Enhancement of thermal conductivity of kerosene-based Fe₃O₄ nanofluids prepared via phase-transfer method," *Colloids and Surfaces A*, vol. 355, no. 1–3, pp. 109–113, 2010.
- [19] L. Wang and J. Fan, "Nanofluids research: key issues," *Nanoscale Research Letters*, vol. 5, no. 8, pp. 1241–1252, 2010.
- [20] X. Wei and L. Wang, "Synthesis and thermal conductivity of microfluidic copper nanofluids," *Particuology*, vol. 8, no. 3, pp. 262–271, 2010.
- [21] X. Li, D. Zhu, and X. Wang, "Evaluation on dispersion behavior of the aqueous copper nano-suspensions," *Journal of Colloid and Interface Science*, vol. 310, no. 2, pp. 456–463, 2007.
- [22] H. Zhu, C. Zhang, Y. Tang, J. Wang, B. Ren, and Y. Yin, "Preparation and thermal conductivity of suspensions of graphite nanoparticles," *Carbon*, vol. 45, no. 1, pp. 226–228, 2007.

- [23] D. Li and R. B. Kaner, "Processable stabilizer-free polyaniline nanofiber aqueous colloids," *Chemical Communications*, vol. 14, no. 26, pp. 3286–3288, 2005.
- [24] H. J. Kim, I. C. Bang, and J. Onoe, "Characteristic stability of bare Au-water nanofluids fabricated by pulsed laser ablation in liquids," *Optics and Lasers in Engineering*, vol. 47, no. 5, pp. 532–538, 2009.
- [25] X. J. Wang, X. Li, and S. Yang, "Influence of pH and SDBS on the stability and thermal conductivity of nanofluids," *Energy and Fuels*, vol. 23, no. 5, pp. 2684–2689, 2009.
- [26] D. Zhu, X. Li, N. Wang, X. Wang, J. Gao, and H. Li, "Dispersion behavior and thermal conductivity characteristics of Al_2O_3 - H_2O nanofluids," *Current Applied Physics*, vol. 9, no. 1, pp. 131–139, 2009.
- [27] L. Chen and H. Xie, "Properties of carbon nanotube nanofluids stabilized by cationic gemini surfactant," *Thermochimica Acta*, vol. 506, no. 1-2, pp. 62–66, 2010.
- [28] J. Huang, X. Wang, Q. Long, X. Wen, Y. Zhou, and L. Li, "Influence of pH on the stability characteristics of nanofluids," in *Proceedings of the Symposium on Photonics and Optoelectronics (SPO '09)*, 2009.
- [29] M. Farahmandjou, S. A. Sebt, S. S. Parhizgar, P. Aberomand, and M. Akhavan, "Stability investigation of colloidal FePt nanoparticle systems by spectrophotometer analysis," *Chinese Physics Letters*, vol. 26, no. 2, Article ID 027501, 2009.
- [30] Y. Hwang, J. K. Lee, C. H. Lee et al., "Stability and thermal conductivity characteristics of nanofluids," *Thermochimica Acta*, vol. 455, no. 1-2, pp. 70–74, 2007.
- [31] L. Chen, H. Xie, Y. Li, and W. Yu, "Nanofluids containing carbon nanotubes treated by mechanochemical reaction," *Thermochimica Acta*, vol. 477, no. 1-2, pp. 21–24, 2008.
- [32] X. Yang and Z. H. Liu, "A kind of nanofluid consisting of surface-functionalized nanoparticles," *Nanoscale Research Letters*, vol. 5, no. 8, pp. 1324–1328, 2010.
- [33] L. Chen and H. Xie, "Surfactant-free nanofluids containing double- and single-walled carbon nanotubes functionalized by a wet-mechanochemical reaction," *Thermochimica Acta*, vol. 497, no. 1-2, pp. 67–71, 2010.
- [34] K. A. Wepasnick, B. A. Smith, J. L. Bitter, and D. H. Fairbrother, "Chemical and structural characterization of carbon nanotube surfaces," *Analytical and Bioanalytical Chemistry*, vol. 396, no. 3, pp. 1003–1014, 2010.
- [35] Q. Yu, Y. J. Kim, and H. Ma, "Nanofluids with plasma treated diamond nanoparticles," *Applied Physics Letters*, vol. 92, no. 10, Article ID 103111, 2008.
- [36] I. M. Joni, A. Purwanto, F. Iskandar, and K. Okuyama, "Dispersion stability enhancement of titania nanoparticles in organic solvent using a bead mill process," *Industrial and Engineering Chemistry Research*, vol. 48, no. 15, pp. 6916–6922, 2009.
- [37] E. Tang, G. Cheng, X. Ma, X. Pang, and Q. Zhao, "Surface modification of zinc oxide nanoparticle by PMAA and its dispersion in aqueous system," *Applied Surface Science*, vol. 252, no. 14, pp. 5227–5232, 2006.
- [38] T. Missana and A. Adell, "On the applicability of DLVO theory to the prediction of clay colloids stability," *Journal of Colloid and Interface Science*, vol. 230, no. 1, pp. 150–156, 2000.
- [39] I. Popa, G. Gillies, G. Papastavrou, and M. Borkovec, "Attractive and repulsive electrostatic forces between positively charged latex particles in the presence of anionic linear polyelectrolytes," *Journal of Physical Chemistry B*, vol. 114, no. 9, pp. 3170–3177, 2010.
- [40] H. Kamiya, Y. Fukuda, Y. Suzuki, M. Tsukada, T. Kakui, and M. Naito, "Effect of polymer dispersant structure on electrosteric interaction and dense alumina suspension behavior," *Journal of the American Ceramic Society*, vol. 82, no. 12, pp. 3407–3412, 1999.
- [41] K. V. Wong and O. de Leon, "Applications of nanofluids: current and future," *Advances in Mechanical Engineering*, vol. 2010, Article ID 519659, 11 pages, 2010.
- [42] G. Donzelli, R. Cerbino, and A. Vailati, "Bistable heat transfer in a nanofluid," *Physical Review Letters*, vol. 102, no. 10, Article ID 104503, 2009.
- [43] M. Arruebo, R. Fernández-Pacheco, M. R. Ibarra, and J. Santamaría, "Magnetic nanoparticles for drug delivery," *Nano Today*, vol. 2, no. 3, pp. 22–32, 2007.
- [44] W. Yu, D. M. France, D. Singh, E. V. Timofeeva, D. S. Smith, and J. L. Routbort, "Mechanisms and models of effective thermal conductivities of nanofluids," *Journal of Nanoscience and Nanotechnology*, vol. 10, no. 8, pp. 4824–4849, 2010.
- [45] K. Q. Ma and J. Liu, "Nano liquid-metal fluid as ultimate coolant," *Physics Letters Section A*, vol. 361, no. 3, pp. 252–256, 2007.
- [46] G. Paul, M. Chopkar, I. Manna, and P. K. Das, "Techniques for measuring the thermal conductivity of nanofluids: a review," *Renewable and Sustainable Energy Reviews*, vol. 14, p. 1913, 2010.
- [47] H. Xie, W. Yu, and W. Chen, "MgO nanofluids: higher thermal conductivity and lower viscosity among ethylene glycol-based nanofluids containing oxide nanoparticles," *Journal of Experimental Nanoscience*, vol. 5, no. 5, pp. 463–472, 2010.
- [48] S. P. Jang and S. U. S. Choi, "Cooling performance of a microchannel heat sink with nanofluids," *Applied Thermal Engineering*, vol. 26, no. 17-18, pp. 2457–2463, 2006.
- [49] C. T. Nguyen, G. Roy, N. Galanis, and S. Suiro, "Heat transfer enhancement by using Al_2O_3 -water nanofluid in a liquid cooling system for microprocessors," in *Proceedings of the 4th WSEAS International Conference on Heat Transfer, Thermal Engineering and Environment*, pp. 103–108, Elounda, Greece, August 2006.
- [50] H. Shokouhmand, M. Ghazvini, and J. Shabanian, "Performance analysis of using nanofluids in microchannel heat sink in different flow regimes and its simulation using artificial neural network," in *Proceedings of the World Congress on Engineering (WCE '08)*, vol. 3, London, UK, July 2008.
- [51] C. Y. Tsai, H. T. Chien, P. P. Ding, B. Chanc, T. Y. Luh, and P. H. Chena, "Effect of structural character of gold nanoparticles in nanofluid on heat pipe thermal performance," *Materials Letters*, vol. 58, p. 1461, 2004.
- [52] Y. T. Chen, W. C. Wei, S. W. Kang, and C. S. Yu, "Effect of nanofluid on flat heat pipe thermal performance," in *Proceedings of the 24th IEEE Semiconductor Thermal Measurement and Management Symposium (SEMI-THERM '08)*, March 2006.
- [53] H. B. Ma, C. Wilson, B. Borgmeyer et al., "Effect of nanofluid on the heat transport capability in an oscillating heat pipe," *Applied Physics Letters*, vol. 88, no. 14, Article ID 143116, 2006.
- [54] S. W. Kang, W. C. Wei, S. H. Tsai, and C. C. Huang, "Experimental investigation of nanofluids on sintered heat pipe thermal performance," *Applied Thermal Engineering*, vol. 29, no. 5-6, pp. 973–979, 2009.
- [55] P. Naphon, P. Assadamongkol, and T. Borirak, "Experimental investigation of titanium nanofluids on the heat pipe thermal

- efficiency," *International Communications in Heat and Mass Transfer*, vol. 35, no. 10, pp. 1316–1319, 2008.
- [56] H. Xie and L. Chen, "Adjustable thermal conductivity in carbon nanotube nanofluids," *Physics Letters Section A*, vol. 373, no. 21, pp. 1861–1864, 2009.
- [57] H. Xie, W. Yu, and Y. Li, "Thermal performance enhancement in nanofluids containing diamond nanoparticles," *Journal of Physics D*, vol. 42, no. 9, Article ID 095413, 2009.
- [58] W. Yu, H. Xie, L. Chen, and Y. Li, "Investigation of thermal conductivity and viscosity of ethylene glycol based ZnO nanofluid," *Thermochimica Acta*, vol. 491, no. 1-2, pp. 92–96, 2009.
- [59] W. Yu, D. M. France, S. U. S. Choi, and J. L. Routbort, "Review and assessment of nanofluid technology for transportation and other applications," Tech. Rep. 78, ANL/ESD/07-9, Argonne National Laboratory, 2007.
- [60] M. Kole and T. K. Dey, "Thermal conductivity and viscosity of Al₂O₃ nanofluid based on car engine coolant," *Journal of Physics D*, vol. 43, no. 31, Article ID 315501, 2010.
- [61] S. C. Tzeng, C. W. Lin, and K. D. Huang, "Heat transfer enhancement of nanofluids in rotary blade coupling of four-wheel-drive vehicles," *Acta Mechanica*, vol. 179, no. 1-2, pp. 11–23, 2005.
- [62] D. Singh, J. Toutbort, G. Chen et al., "Heavy vehicle systems optimization merit review and peer evaluation," Annual Report, Argonne National Laboratory, 2006.
- [63] http://www.labnews.co.uk/feature_archive.php/5449/5/keeping-it-cool.
- [64] J. Routbort et al., Argonne National Lab, Michellin North America, St. Gobain Corp., 2009, <http://www1.eere.energy.gov/industry/nanomanufacturing/pdfs/nanofluidsindustrialcooling.pdf>.
- [65] <http://96.30.12.13/execsumm/VU0319-Nanofluid%20for%20Cooling%20Enhancement%20of%20Electrical%20Power%20Equipment.pdf>.
- [66] I. C. Nelson, D. Banerjee, and R. Ponnappan, "Flow loop experiments using polyalphaolefin nanofluids," *Journal of Thermophysics and Heat Transfer*, vol. 23, no. 4, pp. 752–761, 2009.
- [67] D. P. Kulkarni, D. K. Das, and R. S. Vajjha, "Application of nanofluids in heating buildings and reducing pollution," *Applied Energy*, vol. 86, no. 12, pp. 2566–2573, 2009.
- [68] J. Bongiorno, L. W. Hu, S. J. Kim, R. Hannink, B. Truong, and E. Forrest, "Nanofluids for enhanced economics and safety of nuclear reactors: an evaluation of the potential features issues, and research gaps," *Nuclear Technology*, vol. 162, no. 1, pp. 80–91, 2008.
- [69] S. M. You, J. H. Kim, and K. H. Kim, "Effect of nanoparticles on critical heat flux of water in pool boiling heat transfer," *Applied Physics Letters*, vol. 83, no. 16, pp. 3374–3376, 2003.
- [70] P. Vassallo, R. Kumar, and S. D'Amico, "Pool boiling heat transfer experiments in silica-water nano-fluids," *International Journal of Heat and Mass Transfer*, vol. 47, no. 2, pp. 407–411, 2004.
- [71] J. K. Kim, J. Y. Jung, and Y. T. Kang, "The effect of nanoparticles on the bubble absorption performance in a binary nanofluid," *International Journal of Refrigeration*, vol. 29, no. 1, pp. 22–29, 2006.
- [72] J. K. Kim, J. Y. Jung, and Y. T. Kang, "Absorption performance enhancement by nano-particles and chemical surfactants in binary nanofluids," *International Journal of Refrigeration*, vol. 30, no. 1, pp. 50–57, 2007.
- [73] J. Kim, Y. T. Kang, and C. K. Choi, "Soret and Dufour effects on convective instabilities in binary nanofluids for absorption application," *International Journal of Refrigeration*, vol. 30, no. 2, pp. 323–328, 2007.
- [74] X. Ma, F. Su, J. Chen, and Y. Zhang, "Heat and mass transfer enhancement of the bubble absorption for a binary nanofluid," *Journal of Mechanical Science and Technology*, vol. 21, p. 1813, 2007.
- [75] X. Ma, F. Su, J. Chen, T. Bai, and Z. Han, "Enhancement of bubble absorption process using a CNTs-ammonia binary nanofluid," *International Communications in Heat and Mass Transfer*, vol. 36, no. 7, pp. 657–660, 2009.
- [76] S. Komati and A. K. Suresh, "CO₂ absorption into amine solutions: a novel strategy for intensification based on the addition of ferrofluids," *Journal of Chemical Technology and Biotechnology*, vol. 83, no. 8, pp. 1094–1100, 2008.
- [77] L. Yang, K. Du, B. Cheng, and Y. Jiang, "The influence of Al₂O₃ nanofluid on the falling film absorption with ammonia-water," in *Proceedings of the Asia-Pacific Power and Energy Engineering Conference (APPEEC '10)*, 2010.
- [78] M. F. Demirbas, "Thermal energy storage and phase change materials: an overview," *Energy Sources Part B*, vol. 1, no. 1, pp. 85–95, 2006.
- [79] S. Wu, D. Zhu, X. Zhang, and J. Huang, "Preparation and melting/freezing characteristics of Cu/paraffin nanofluid as phase-change material (PCM)," *Energy and Fuels*, vol. 24, no. 3, pp. 1894–1898, 2010.
- [80] Y. D. Liu, Y. G. Zhou, M. W. Tong, and X. S. Zhou, "Experimental study of thermal conductivity and phase change performance of nanofluids PCMs," *Microfluidics and Nanofluidics*, vol. 7, no. 4, pp. 579–584, 2009.
- [81] T. P. Otanicar, P. E. Phelan, R. S. Prasher, G. Rosengarten, and R. A. Taylor, "Nanofluid-based direct absorption solar collector," *Journal of Renewable and Sustainable Energy*, vol. 2, no. 3, Article ID 033102, 13 pages, 2010.
- [82] H. Tyagi, P. Phelan, and R. Prasher, "Predicted efficiency of a low-temperature Nanofluid-based direct absorption solar collector," *Journal of Solar Energy Engineering*, vol. 131, no. 4, pp. 0410041–0410047, 2009.
- [83] T. P. Otanicar and J. S. Golden, "Comparative environmental and economic analysis of conventional and nanofluid solar hot water technologies," *Environmental Science and Technology*, vol. 43, no. 15, pp. 6082–6087, 2009.
- [84] E. Sani, S. Barison, C. Pagura et al., "Carbon nanohorns-based nanofluids as direct sunlight absorbers," *Optics Express*, vol. 18, p. 4613, 2010.
- [85] J. Zhou, Z. Wu, Z. Zhang, W. Liu, and Q. Xue, "Tribological behavior and lubricating mechanism of Cu nanoparticles in oil," *Tribology Letters*, vol. 8, no. 4, pp. 213–218, 2000.
- [86] B. Shen, A. J. Shih, and S. C. Tung, "Application of nanofluids in minimum quantity lubrication grinding," *Tribology Transactions*, vol. 51, no. 6, pp. 730–737, 2008.
- [87] H. L. Yu, Y. Xu, P. J. Shi, B. S. Xu, X. L. Wang, and Q. Liu, "Tribological properties and lubricating mechanisms of Cu nanoparticles in lubricant," *Transactions of Nonferrous Metals Society of China*, vol. 18, no. 3, pp. 636–641, 2008.
- [88] B. Yu, Z. Liu, F. Zhou, W. Liu, and Y. Liang, "A novel lubricant additive based on carbon nanotubes for ionic liquids," *Materials Letters*, vol. 62, no. 17-18, pp. 2967–2969, 2008.
- [89] B. Wang, X. Wang, W. Lou, and J. Hao, "Rheological and tribological properties of ionic liquid-based nanofluids

- containing functionalized multi-walled carbon nanotubes," *Journal of Physical Chemistry C*, vol. 114, no. 19, pp. 8749–8754, 2010.
- [90] L. J. Wang, C. W. Guo, and R. Yamane, "Experimental research on tribological properties of $Mn_{0.78}Zn_{0.22}Fe_2O_4$ magnetic fluids," *Journal of Tribology*, vol. 130, no. 3, Article ID 031801, 2008.
- [91] S. Chen and D. H. Mao, "Study on dispersion stability and self-repair principle of ultrafine-tungsten disulfide particulates," *Advanced Tribology*, vol. 995, 2010.
- [92] D. X. Peng, C. H. Chen, Y. Kang, Y. P. Chang, and S. Y. Chang, "Size effects of SiO_2 nanoparticles as oil additives on tribology of lubricant," *Industrial Lubrication and Tribology*, vol. 62, no. 2, pp. 111–120, 2010.
- [93] L. Vékás, D. Bica, and M. V. Avdeev, "Magnetic nanoparticles and concentrated magnetic nanofluids: synthesis, properties and some applications," *China Particuology*, vol. 5, no. 1-2, pp. 43–49, 2007.
- [94] R. E. Rosensweig, "Magnetic fluids," *Annual Review of Fluid Mechanics*, vol. 19, pp. 437–463, 1987.
- [95] Y. S. Kim, K. Nakatsuka, T. Fujita, and T. Atarashi, "Application of hydrophilic magnetic fluid to oil seal," *Journal of Magnetism and Magnetic Materials*, vol. 201, no. 1–3, pp. 361–363, 1999.
- [96] Y. Mitamura, S. Arioka, D. Sakota, K. Sekine, and M. Azegami, "Application of a magnetic fluid seal to rotary blood pumps," *Journal of Physics Condensed Matter*, vol. 20, no. 20, Article ID 204145, 2008.
- [97] Y. S. Kim and Y. H. Kim, "Application of ferro-cobalt magnetic fluid for oil sealing," *Journal of Magnetism and Magnetic Materials*, vol. 267, no. 1, pp. 105–110, 2003.
- [98] L. Zhang, Y. Jiang, Y. Ding, M. Povey, and D. York, "Investigation into the antibacterial behaviour of suspensions of ZnO nanoparticles (ZnO nanofluids)," *Journal of Nanoparticle Research*, vol. 9, no. 3, pp. 479–489, 2007.
- [99] R. Jalal, E. K. Goharshadi, M. Abareshi, M. Moosavi, A. Yousefi, and P. Nancarrow, "ZnO nanofluids: green synthesis, characterization, and antibacterial activity," *Materials Chemistry and Physics*, vol. 121, no. 1-2, pp. 198–201, 2010.
- [100] N. Jones, B. Ray, K. T. Ranjit, and A. C. Manna, "Antibacterial activity of ZnO nanoparticle suspensions on a broad spectrum of microorganisms," *FEMS Microbiology Letters*, vol. 279, no. 1, pp. 71–76, 2008.
- [101] Y. Liu, L. He, A. Mustapha, H. Li, Z. Q. Hu, and M. Lin, "Antibacterial activities of zinc oxide nanoparticles against *Escherichia coli* O157:H7," *Journal of Applied Microbiology*, vol. 107, no. 4, pp. 1193–1201, 2009.
- [102] O. Mahapatra, M. Bhagat, C. Gopalakrishnan, and K. D. Arunachalam, "Ultrafine dispersed CuO nanoparticles and their antibacterial activity," *Journal of Experimental Nanoscience*, vol. 3, no. 3, pp. 185–193, 2008.
- [103] P. Gajjar, B. Pettee, D. W. Britt, W. Huang, W. P. Johnson, and A. J. Anderson, "Antimicrobial activities of commercial nanoparticles against an environmental soil microbe, *Pseudomonas putida* KT2440," *Journal of Biological Engineering*, vol. 3, p. 9, 2009.
- [104] H. J. Lee, S. Y. Yeo, and S. H. Jeong, "Antibacterial effect of nanosized silver colloidal solution on textile fabrics," *Polymer Journal*, vol. 8, p. 2199, 2003.
- [105] A. Panáček, L. Kvítek, R. Prucek et al., "Silver colloid nanoparticles: synthesis, characterization, and their antibacterial activity," *Journal of Physical Chemistry B*, vol. 110, no. 33, pp. 16248–16253, 2006.
- [106] L. Brunet, D. Y. Lyon, E. M. Hotze, P. J. J. Alvarez, and M. R. Wiesner, "Comparative photoactivity and antibacterial properties of C60 fullerenes and titanium dioxide nanoparticles," *Environmental Science and Technology*, vol. 43, no. 12, pp. 4355–4360, 2009.
- [107] D. Y. Lyon and P. J. J. Alvarez, "Fullerene water suspension (nC₆₀) exerts antibacterial effects via ROS-independent protein oxidation," *Environmental Science and Technology*, vol. 42, no. 21, pp. 8127–8132, 2008.
- [108] A. Vonarbourg, C. Passirani, P. Saulnier, and J. P. Benoit, "Parameters influencing the stealthiness of colloidal drug delivery systems," *Biomaterials*, vol. 27, no. 24, pp. 4356–4373, 2006.
- [109] R. Singh and J. W. Lillard, "Nanoparticle-based targeted drug delivery," *Experimental and Molecular Pathology*, vol. 86, no. 3, pp. 215–223, 2009.
- [110] P. Ghosh, G. Han, M. De, C. K. Kim, and V. M. Rotello, "Gold nanoparticles in delivery applications," *Advanced Drug Delivery Reviews*, vol. 17, p. 1307, 2008.
- [111] M. Nakano, H. Matsuura, D. Ju et al., "Drug delivery system using nano-magnetic fluid," in *Proceedings of the 3rd International Conference on Innovative Computing, Information and Control (ICICIC '08)*, Dalian, China, June 2008.
- [112] A. Bianco, K. Kostarelos, and M. Prato, "Applications of carbon nanotubes in drug delivery," *Current Opinion in Chemical Biology*, vol. 9, no. 6, pp. 674–679, 2005.
- [113] C. Tripisciano, K. Kraemer, A. Taylor, and E. Borowiak-Palen, "Single-wall carbon nanotubes based anticancer drug delivery system," *Chemical Physics Letters*, vol. 478, no. 4–6, pp. 200–205, 2009.
- [114] G. Pastorin, W. Wu, S. Wieckowski et al., "Double functionalisation of carbon nanotubes for multimodal drug delivery," *Chemical Communications*, no. 11, pp. 1182–1184, 2006.
- [115] Z. Liu, X. Sun, N. Nakayama-Ratchford, and H. Dai, "Supramolecular chemistry on water-soluble carbon nanotubes for drug loading and delivery," *ACS nano*, vol. 1, no. 1, pp. 50–56, 2007.
- [116] X. Sun, Z. Liu, J. T. Robinson et al., "Nano-graphene oxide for cellular imaging and drug delivery," *Nano Research*, vol. 1, p. 203, 2008.
- [117] L. Zhang, J. Xia, Q. Zhao, L. Liu, and Z. Zhang, "Functional graphene oxide as a nanocarrier for controlled loading and targeted delivery of mixed anticancer drugs," *Small*, vol. 6, no. 4, pp. 537–544, 2010.
- [118] Z. Liu, J. T. Robinson, X. Sun, and H. Dai, "PEGylated nanographene oxide for delivery of water-insoluble cancer drugs," *Journal of the American Chemical Society*, vol. 130, no. 33, pp. 10876–10877, 2008.
- [119] X. Yang, X. Zhang, Y. Ma, Y. Huang, Y. Wang, and Y. Chen, "Superparamagnetic graphene oxide- Fe_3O_4 nanoparticles hybrid for controlled targeted drug carriers," *Journal of Materials Chemistry*, vol. 19, no. 18, pp. 2710–2714, 2009.
- [120] X. Fan, H. Chen, Y. Ding, P. K. Plucinski, and A. A. Lapkin, "Potential of 'nanofluids' to further intensify microreactors," *Green Chemistry*, vol. 10, no. 6, pp. 670–677, 2008.
- [121] M. J. Kao, C. H. Lo, T. T. Tsung, Y. Y. Wu, C. S. Jwo, and H. M. Lin, "Copper-oxide brake nanofluid manufactured using arc-submerged nanoparticle synthesis system," *Journal of Alloys and Compounds*, vol. 434–435, pp. 672–674, 2007.
- [122] M. J. Kao, H. Chang, Y. Y. Wu, T. T. Tsung, and H. M. Lin, "Producing Aluminum-oxide brake nanofluids derived using plasma charging system," *Journal of the Chinese Society of Mechanical Engineers*, vol. 28, p. 123, 2007.

- [123] T. Sharma, A. L. M. Reddy, T. S. Chandra, and S. Ramaprabhu, "Development of carbon nanotubes and nanofluids based microbial fuel cell," *International Journal of Hydrogen Energy*, vol. 33, no. 22, pp. 6749–6754, 2008.
- [124] J. Philip, T. Jaykumar, P. Kalyanasundaram, and B. Raj, "A tunable optical filter," *Measurement Science and Technology*, vol. 14, no. 8, pp. 1289–1294, 2003.
- [125] A. Mishra, P. Tripathy, S. Ram, and H. J. Fecht, "Optical properties in nanofluids of gold nanoparticles in poly(vinylpyrrolidone)," *Journal of Nanoscience and Nanotechnology*, vol. 9, no. 7, pp. 4342–4347, 2009.
- [126] W. Yu, H. Xie, and D. Bao, "Enhanced thermal conductivities of nanofluids containing graphene oxide nanosheets," *Nanotechnology*, vol. 21, no. 5, Article ID 055705, 2010.
- [127] W. Yu, H. Xie, and W. Chen, "Experimental investigation on thermal conductivity of nanofluids containing graphene oxide nanosheets," *Journal of Applied Physics*, vol. 107, no. 9, Article ID 094317, 2010.
- [128] Z. H. Han, F. Y. Cao, and B. Yang, "Synthesis and thermal characterization of phase-changeable indium/polyaluminum phaeofin nanofluids," *Applied Physics Letters*, vol. 92, no. 24, Article ID 243104, 2008.